

**NUMERICAL PREDICTION OF FREE-SURFACE
WAVE INDUCED SEPARATION ON A 3D FLOATING
BODY**

by

MD. HABIBUR RAHMAN

MASTER OF SCIENCE

in

NAVAL ARCHITECTURE AND MARINE ENGINEERING



Department of Naval Architecture and Marine Engineering
BANGLADESH UNIVERSITY OF ENGINEERING AND TECHNOLOGY

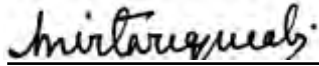
The thesis titled “**Numerical Prediction of Free–Surface Wave Induced Separation on A 3D Floating Body**”, submitted by MD. HABIBUR RAHMAN, Roll No. 0416122010, Session October 2017, to the Department of Naval Architecture and Marine Engineering, Bangladesh University of Engineering and Technology, has been accepted as satisfactory in partial fulfillment of the requirements for the degree of Master of Science in Naval Architecture and Marine Engineering on October 12, 2019.

BOARD OF EXAMINERS



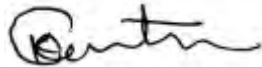
Chairman
(Supervisor)

1. **Dr. Md Mashud Karim**
Professor
Department of Naval Architecture and Marine Engineering
Bangladesh University of Engineering and Technology, Dhaka



Member
(Ex-Officio)

2. **Dr. Mir Tareque Ali**
Professor and Head
Department of Naval Architecture and Marine Engineering
Bangladesh University of Engineering and Technology, Dhaka



Member

3. **Dr. Goutam Kumar Saha**
Professor
Department of Naval Architecture and Marine Engineering
Bangladesh University of Engineering and Technology, Dhaka



Member
(External)

4. **Dr. Mohammad Ali**
Professor
Department of Department of Mechanical Engineering
Bangladesh University of Engineering and Technology, Dhaka

DECLARATION

It is hereby declared that this thesis or any part of it has not been submitted elsewhere for the award of any degree or diploma.



Md. Habibur Rahman

Roll No.: 0416122010

Dedicated

To

My Parents and All my Respected Teachers

ACKNOWLEDGEMENT

I would like to acknowledge the blessings of almighty Allah. The Beneficent and the Merciful for His divine help in completing my thesis successfully.

I wish to convey regards to my supervisor, Dr. Md. Mashud Karim, Professor of the department of Naval Architecture and Marine Engineering for his continuous support and encouragement throughout the preparation of the thesis. I am extremely thankful and indebted to him for providing me all necessary supports to perform my thesis efficiently. Without his guidance, wise suggestions, great assistance and all the given amenities this thesis may not be completed.

I am thankful to Salman Yasin for helping me with my study.

I also want to thank the members of my thesis committee for their invaluable suggestions. I thank Dr. Mir Tareque Ali, Dr. Goutam Kumar Saha, and the external member Dr. Mohammad Ali.

Finally, I want to express my deepest gratitude to my parents who have always encouraged me and made me what I am today. They always inspire me to give my best. It would be impossible for me to do anything without their support and prayer.

ABSTRACT

In this research, the effects of free-surface wave and wave induced separation on a 3D surface piercing floating body has been studied. The simulation has been performed using a commercial Computational Fluid Dynamics (CFD) code ANSYS Fluent based on Finite Volume Method (FVM). The predicted results for several Froude numbers ($Fr = 0.19, 0.37, \text{ and } 0.55$) have been studied for surface piercing body with NACA 0024 airfoil section and validated with both the experimental data and the previous numerical result. The thickness effects on the wave-induced separation have been evaluated for surface piercing bodies with NACA 0012 and NACA 0018 airfoil sections, whereas surface piercing bodies with cylindrical, elliptical and rectangular cross-sections have been used to evaluate the shape effects. It has been found that the wave height, wave steepness, and distortion in the separation region changes abruptly with the change in Froude number. The wave patterns are dependent on Froude number rather than thickness or shape of the floating body at higher Froude number but the thickness or shape effects become dominant at lower Froude number. The thickness or shape effects are noticeable in the bow wave peak, extent of the free – surface, at the wake region, and also in the separation region. Free-surface elevations and other flow characteristics have also been studied for the surface piercing bodies with NACA 0012, NACA 0018, NACA 0024, cylindrical, elliptical, and rectangular sections.

TABLE OF CONTENTS

ACKNOWLEDGEMENT	v
ABSTRACT	vi
LIST OF FIGURES	x
NOMENCLATURE.....	xx
CHAPTER 1 Introduction.....	1
1.1 Introduction	1
1.2 Literature Review	1
1.3 Objective of the Research.....	6
1.4 Outline of Methodology	7
CHAPTER 2 Theoretical Background.....	8
2.1 NACA Airfoils	8
2.1.1 Four Digit Series	8
2.1.2 Shape for the NACA Airfoils.....	9
2.2 Computational Fluid Dynamics (CFD).....	10
2.2.1 Governing Equations.....	12
2.3 Finite Volume Method (FVM).....	13
2.3.1 Different Versions of Finite Volume Method.....	14
2.4 Multiphase Flow Theory	15
2.5 Different modeling Approaches to Describe Multiphase Flow Theory	17
2.6 Overview of VOF model.....	17
2.6.1 Limitations of the VOF Model.....	18
2.6.2 Steady – State and Transient VOF Calculation.....	18
2.7 Turbulent Flow	20
2.8 Turbulence models	21
2.9 Shear – Stress Transport (SST) $k - \omega$ Model.....	21

2.9.1	Transport Equations for the (SST) $k - \omega$ Model.....	22
2.9.2	Modeling the Effective Diffusivity	23
2.9.3	Modeling the Turbulence Production.....	24
2.9.4	Modeling the Turbulence Dissipation.....	24
2.9.5	Cross – Diffusion Modification	26
2.9.6	Model Constants	26
CHAPTER 3 Numerical Solution		28
3.1	Geometry Profile	28
3.2	Grid Generation.....	32
3.3	Simulation Using ANSYS Fluent.....	36
3.4	Grid Study	37
CHAPTER 4 Result and Discussion		39
4.1	Validation	39
4.2	Wave Profile for Different Surface Piercing Body	41
4.3	Comparison of Wave Profile	49
4.4	Comparison of Thickness Effects for Different NACA Airfoil sections	51
4.5	Comparison of Shape Effects for Different Sections	53
4.6	Free Surface Elevation Contour	55
4.7	Contour of Pressure	64
4.8	Contour of X-Wall Shear Stress.....	92
4.9	Velocity Vector	101
4.10	Streamline along Different Bodies	111
4.11	3D Views of Free Surface of Different Bodies	120
CONCLUSIONS.....		123
REFERENCES.....		124
Appendix A Basic profile of NACA 0024 airfoil of chord length 1.0 m.....		127

Appendix B Detailed procedure to simulate flow around a surface piercing body 128

LIST OF FIGURES

Figure 2.3.1	Visualization of typical flow patterns for flow in horizontal pipes	16
Figure 2.3.2	Example of flow map for two phase flow in horizontal pipes	16
Figure 2.5.1	Advection of fluid	19
Figure 3.2.1	Geometry for surface piercing body with NACA 0024 airfoil section	28
Figure 3.2.2	Geometry for surface piercing body with NACA 0012 airfoil section	29
Figure 3.2.3	Geometry for surface piercing body with NACA 0018 airfoil section	30
Figure 3.2.4	Geometry for surface piercing body with cylindrical cross – section	30
Figure 3.2.5	Geometry for surface piercing body with elliptical cross – section	31
Figure 3.2.6	Geometry for surface piercing body with rectangular cross – section	31
Figure 3.3.1	3D grid generation for surface piercing body with NACA 0024 airfoil section	33
Figure 3.3.2	3D grid generation for surface piercing body with NACA 0012 airfoil section	33
Figure 3.3.3	3D grid generation for surface piercing body with NACA 0018 airfoil section	34
Figure 3.3.4	3D grid generation for surface piercing body with cylindrical cross – section	34
Figure 3.3.5	3D grid generation for surface piercing body with elliptical cross – section	35
Figure 3.3.6	3D grid generation for surface piercing body with rectangular cross – section	35
Figure 4.1.1	Wave profile along the NACA 0024 airfoil for $Fr = 0.19$	39
Figure 4.1.2	Wave profile along the NACA 0024 airfoil for $Fr = 0.37$	40

Figure 4.1.3	Wave profile along the NACA 0024 airfoil for $Fr = 0.55$	40
Figure 4.2.1	Wave profile along the NACA 0012 airfoil for $Fr = 0.19$ ($t = 8.2s$)	41
Figure 4.2.2	Wave profile along the NACA 0018 airfoil for $Fr = 0.19$ ($t = 3.3s$)	41
Figure 4.2.3	Wave profile along the NACA 0012 airfoil for $Fr = 0.37$ ($t = 8.2s$)	42
Figure 4.2.4	Wave profile along the NACA 0018 airfoil for $Fr = 0.37$ ($t = 3.3s$)	43
Figure 4.2.5	Wave profile along the NACA 0012 airfoil for $Fr = 0.55$ ($t = 8.2s$)	43
Figure 4.2.6	Wave profile along the NACA 0018 airfoil for $Fr = 0.55$ ($t = 3.3s$)	44
Figure 4.2.7	Wave profile along circular cylinder section at $Fr = 0.19$ ($t = 3.3s$)	44
Figure 4.2.8	Wave profile along circular cylinder section at $Fr = 0.37$ ($t = 3.3s$)	45
Figure 4.2.9	Wave profile along circular cylinder section at $Fr = 0.55$ ($t = 3.3s$)	45
Figure 4.2.10	Wave profile along elliptical section at $Fr = 0.19$ ($t = 3.3s$)	46
Figure 4.2.11	Wave profile along elliptical section at $Fr = 0.37$ ($t = 3.3s$)	46
Figure 4.2.12	Wave profile along elliptical section at $Fr = 0.55$ ($t = 3.3s$)	47
Figure 4.2.13	Wave profile along rectangular section at $Fr = 0.19$ ($t = 3.3s$)	47
Figure 4.2.14	Wave profile along rectangular section at $Fr = 0.37$ ($t = 3.3s$)	48
Figure 4.2.15	Wave profile along rectangular section at $Fr = 0.55$ ($t = 3.3s$)	48
Figure 4.3.1	Comparison of wave profiles along the NACA 0024 airfoil for different Froude numbers	49
Figure 4.3.2	Comparison of wave profiles along the NACA 0012 airfoil for different Froude numbers	50
Figure 4.3.3	Comparison of wave profiles along the NACA 0018 airfoil for different Froude numbers	51

Figure 4.4.1	Comparison of thickness effects for different NACA airfoil sections at $Fr = 0.19$	51
Figure 4.4.2	Comparison of thickness effects for different NACA airfoil sections at $Fr = 0.37$	52
Figure 4.4.3	Comparison of thickness effects for different NACA airfoil sections at $Fr = 0.55$	52
Figure 4.5.1	Comparison of shape effects for different sections at $Fr = 0.19$	53
Figure 4.5.2	Comparison of shape effects for different sections at $Fr = 0.37$	54
Figure 4.5.3	Comparison of shape effects for different sections at $Fr = 0.55$	54
Figure 4.6.1	Free surface elevation contour along NACA 0012 airfoil section with $Fr = 0.19$	55
Figure 4.6.2	Free surface elevation contour along NACA 0012 airfoil section with $Fr = 0.37$	55
Figure 4.6.3	Free surface elevation contour along NACA 0012 airfoil section with $Fr = 0.55$	56
Figure 4.6.4	Free surface elevation contour along NACA 0018 airfoil section with $Fr = 0.19$	56
Figure 4.6.5	Free surface elevation contour along NACA 0018 airfoil section with $Fr = 0.37$	57
Figure 4.6.6	Free surface elevation contour along NACA 0018 airfoil section with $Fr = 0.55$	57
Figure 4.6.7	Free surface elevation contour along NACA 0024 airfoil section with $Fr = 0.19$	58
Figure 4.6.8	Free surface elevation contour along NACA 0024 airfoil section with $Fr = 0.37$	58
Figure 4.6.9	Free surface elevation contour along NACA 0024 airfoil section with $Fr = 0.55$	59
Figure 4.6.10	Free surface elevation contour along circular cylindrical section with $Fr = 0.19$	59
Figure 4.6.11	Free surface elevation contour along circular cylindrical section with $Fr = 0.37$	60

Figure 4.6.12	Free surface elevation contour along circular cylindrical section with $Fr = 0.55$	60
Figure 4.6.13	Free surface elevation contour along elliptical section with $Fr = 0.19$	61
Figure 4.6.14	Free surface elevation contour along elliptical section with $Fr = 0.37$	61
Figure 4.6.15	Free surface elevation contour along elliptical section with $Fr = 0.55$	62
Figure 4.6.16	Free surface elevation contour along rectangular section with $Fr = 0.19$	62
Figure 4.6.17	Free surface elevation contour along rectangular section with $Fr = 0.37$	63
Figure 4.6.18	Free surface elevation contour along rectangular section with $Fr = 0.55$	63
Figure 4.7.1	Pressure contour on the free surface along NACA 0024 airfoil section with $Fr = 0.19$	64
Figure 4.7.2	Pressure contour on the free surface along NACA 0024 airfoil section with $Fr = 0.37$	64
Figure 4.7.3	Pressure contour on the free surface along NACA 0024 airfoil section with $Fr = 0.55$	65
Figure 4.7.4	Pressure contour on the free surface along NACA 0012 airfoil section with $Fr = 0.19$	65
Figure 4.7.5	Pressure contour on the free surface along NACA 0012 airfoil section with $Fr = 0.37$	66
Figure 4.7.6	Pressure contour on the free surface along NACA 0012 airfoil section with $Fr = 0.55$	66
Figure 4.7.7	Pressure contour on the free surface along NACA 0018 airfoil section with $Fr = 0.19$	67
Figure 4.7.8	Pressure contour on the free surface along NACA 0018 airfoil section with $Fr = 0.37$	68
Figure 4.7.9	Pressure contour on the free surface along NACA 0018 airfoil section with $Fr = 0.55$	68

Figure 4.7.10	Pressure contour on the free surface along circular cylinder section with $Fr = 0.19$	69
Figure 4.7.11	Pressure contour on the free surface along circular cylinder section with $Fr = 0.37$	69
Figure 4.7.12	Pressure contour on the free surface along circular cylinder section with $Fr = 0.55$	70
Figure 4.7.13	Pressure contour on the free surface along elliptical section with $Fr = 0.19$	70
Figure 4.7.14	Pressure contour on the free surface along elliptical section with $Fr = 0.37$	71
Figure 4.7.15	Pressure contour on the free surface along elliptical section with $Fr = 0.55$	71
Figure 4.7.16	Pressure contour on the free surface along rectangular section with $Fr = 0.19$	72
Figure 4.7.17	Pressure contour on the free surface along rectangular section with $Fr = 0.37$	72
Figure 4.7.18	Pressure contour on the free surface along rectangular section with $Fr = 0.55$	73
Figure 4.7.19	Pressure contour at $z = 0.5$ m along NACA 0012 airfoil section with $Fr = 0.19$	74
Figure 4.7.20	Pressure contour at $z = 0.5$ m along NACA 0012 airfoil section with $Fr = 0.37$	74
Figure 4.7.21	Pressure contour at $z = 0.5$ m along NACA 0012 airfoil section with $Fr = 0.55$	75
Figure 4.7.22	Pressure contour at $z = 0.5$ m along NACA 0018 airfoil section with $Fr = 0.19$	75
Figure 4.7.23	Pressure contour at $z = 0.5$ m along NACA 0018 airfoil section with $Fr = 0.37$	76
Figure 4.7.24	Pressure contour at $z = 0.5$ m along NACA 0018 airfoil section with $Fr = 0.55$	76
Figure 4.7.25	Pressure contour at $z = 0.5$ m along NACA 0024 airfoil section with $Fr = 0.19$	77

Figure 4.7.26	Pressure contour at $z = 0.5$ m along NACA 0024 airfoil section with $Fr = 0.37$	77
Figure 4.7.27	Pressure contour at $z = 0.5$ m along NACA 0024 airfoil section with $Fr = 0.55$	78
Figure 4.7.28	Pressure contour at $z = 0.5$ m along circular cylinder section with $Fr = 0.19$	78
Figure 4.7.29	Pressure contour at $z = 0.5$ m along circular cylinder section with $Fr = 0.37$	79
Figure 4.7.30	Pressure contour at $z = 0.5$ m along circular cylinder section with $Fr = 0.55$	79
Figure 4.7.31	Pressure contour at $z = 0.5$ m along elliptical section with $Fr = 0.19$	80
Figure 4.7.32	Pressure contour at $z = 0.5$ m along elliptical section with $Fr = 0.37$	80
Figure 4.7.33	Pressure contour at $z = 0.5$ m along elliptical section with $Fr = 0.55$	81
Figure 4.7.34	Pressure contour at $z = 0.5$ m along rectangular section with $Fr = 0.19$	81
Figure 4.7.35	Pressure contour at $z = 0.5$ m along rectangular section with $Fr = 0.37$	82
Figure 4.7.36	Pressure contour at $z = 0.5$ m along rectangular section with $Fr = 0.55$	82
Figure 4.7.37	Pressure contour on the body of NACA 0012 airfoil section at $Fr = 0.19$	83
Figure 4.7.38	Pressure contour on the body of NACA 0012 airfoil section at $Fr = 0.37$	83
Figure 4.7.39	Pressure contour on the body of NACA 0012 airfoil section at $Fr = 0.55$	84
Figure 4.7.40	Pressure contour on the body of NACA 0018 airfoil section at $Fr = 0.19$	84
Figure 4.7.41	Pressure contour on the body of NACA 0018 airfoil section at $Fr = 0.37$	85

Figure 4.7.42	Pressure contour on the body of NACA 0018 airfoil section at $Fr = 0.55$	85
Figure 4.7.43	Pressure contour on the body of NACA 0024 airfoil section at $Fr = 0.19$	86
Figure 4.7.44	Pressure contour on the body of NACA 0024 airfoil section at $Fr = 0.37$	86
Figure 4.7.45	Pressure contour on the body of NACA 0024 airfoil section at $Fr = 0.55$	87
Figure 4.7.46	Pressure contour on the body of circular cylindrical section at $Fr = 0.19$	87
Figure 4.7.47	Pressure contour on the body of circular cylindrical section at $Fr = 0.37$	88
Figure 4.7.48	Pressure contour on the body of circular cylindrical section at $Fr = 0.55$	88
Figure 4.7.49	Pressure contour on the body of elliptical section at $Fr = 0.19$	89
Figure 4.7.50	Pressure contour on the body of elliptical section at $Fr = 0.37$	89
Figure 4.7.51	Pressure contour on the body of elliptical section at $Fr = 0.55$	90
Figure 4.7.52	Pressure contour on the body of rectangular section at $Fr = 0.19$	90
Figure 4.7.53	Pressure contour on the body of rectangular section at $Fr = 0.37$	91
Figure 4.7.54	Pressure contour on the body of rectangular section at $Fr = 0.55$	91
Figure 4.8.1	X-wall shear stress along NACA 0024 airfoil section at $Fr = 0.19$	92
Figure 4.8.2	X-wall shear stress along NACA 0024 airfoil section at $Fr = 0.37$	92
Figure 4.8.3	X-wall shear stress along NACA 0024 airfoil section at $Fr = 0.55$	93
Figure 4.8.4	X-wall shear stress along NACA 0012 airfoil section at $Fr = 0.19$	93

Figure 4.8.5	X-wall shear stress along NACA 0012 airfoil section at $Fr = 0.37$	94
Figure 4.8.6	X-wall shear stress along NACA 0012 airfoil section at $Fr = 0.55$	94
Figure 4.8.7	X-wall shear stress along NACA 0018 airfoil section at $Fr = 0.19$	95
Figure 4.8.8	X-wall shear stress along NACA 0018 airfoil section at $Fr = 0.37$	96
Figure 4.8.9	X-wall shear stress along NACA 0018 airfoil section at $Fr = 0.55$	96
Figure 4.8.10	X-wall shear stress along circular cylinder section at $Fr = 0.19$	97
Figure 4.8.11	X-wall shear stress along circular cylinder section at $Fr = 0.37$	97
Figure 4.8.12	X-wall shear stress along circular cylinder section at $Fr = 0.55$	98
Figure 4.8.13	X-wall shear stress along elliptical section at $Fr = 0.19$	98
Figure 4.8.14	X-wall shear stress along elliptical section at $Fr = 0.37$	99
Figure 4.8.15	X-wall shear stress along elliptical section at $Fr = 0.55$	99
Figure 4.8.16	X-wall shear stress along rectangular section at $Fr = 0.19$	100
Figure 4.8.17	X-wall shear stress along rectangular section at $Fr = 0.37$	100
Figure 4.8.18	X-wall shear stress along rectangular section at $Fr = 0.55$	101
Figure 4.9.1	Velocity vector for surface piercing body with NACA 0012 airfoil section at $Fr = 0.19$	102
Figure 4.9.2	Velocity vector for surface piercing body with NACA 0012 airfoil section at $Fr = 0.37$	102
Figure 4.9.3	Velocity vector for surface piercing body with NACA 0012 airfoil section at $Fr = 0.55$	103
Figure 4.9.4	Velocity vector for surface piercing body with NACA 0018 airfoil section at $Fr = 0.19$	103
Figure 4.9.5	Velocity vector for surface piercing body with NACA 0018 airfoil section at $Fr = 0.37$	104
Figure 4.9.6	Velocity vector for surface piercing body with NACA 0018 airfoil section at $Fr = 0.55$	104

Figure 4.9.7	Velocity vector for surface piercing body with NACA 0024 airfoil section at $Fr = 0.19$	105
Figure 4.9.8	Velocity vector for surface piercing body with NACA 0024 airfoil section at $Fr = 0.37$	105
Figure 4.9.9	Velocity vector for surface piercing body with NACA 0024 airfoil section at $Fr = 0.55$	106
Figure 4.9.10	Velocity vector for surface piercing body with cylindrical cross – section at $Fr = 0.19$	106
Figure 4.9.11	Velocity vector for surface piercing body with cylindrical cross – section at $Fr = 0.37$	107
Figure 4.9.12	Velocity vector for surface piercing body with cylindrical cross – section at $Fr = 0.55$	107
Figure 4.9.13	Velocity vector for surface piercing body with elliptical cross – section at $Fr = 0.19$	108
Figure 4.9.14	Velocity vector for surface piercing body with elliptical cross – section at $Fr = 0.37$	108
Figure 4.9.15	Velocity vector for surface piercing body with elliptical cross – section at $Fr = 0.55$	109
Figure 4.9.16	Velocity vector for surface piercing body with rectangular cross – section at $Fr = 0.19$	109
Figure 4.9.17	Velocity vector for surface piercing body with rectangular cross – section at $Fr = 0.37$	110
Figure 4.9.18	Velocity vector for surface piercing body with rectangular cross – section at $Fr = 0.55$	110
Figure 4.10.1	Streamline along NACA 0012 airfoil section at $Fr = 0.19$	111
Figure 4.10.2	Streamline along NACA 0012 airfoil section at $Fr = 0.37$	111
Figure 4.10.3	Streamline along NACA 0012 airfoil section at $Fr = 0.55$	112
Figure 4.10.4	Streamline along NACA 0018 airfoil section at $Fr = 0.19$	112
Figure 4.10.5	Streamline along NACA 0018 airfoil section at $Fr = 0.37$	113
Figure 4.10.6	Streamline along NACA 0018 airfoil section at $Fr = 0.55$	113
Figure 4.10.7	Streamline along NACA 0024 airfoil section at $Fr = 0.19$	114
Figure 4.10.8	Streamline along NACA 0024 airfoil section at $Fr = 0.37$	114

Figure 4.10.9	Streamline along NACA 0024 airfoil section at $Fr = 0.55$	115
Figure 4.10.10	Streamline along circular cylindrical section at $Fr = 0.19$	115
Figure 4.10.11	Streamline along circular cylindrical section at $Fr = 0.37$	116
Figure 4.10.12	Streamline along circular cylindrical section at $Fr = 0.55$	116
Figure 4.10.13	Streamline along elliptical section at $Fr = 0.19$	117
Figure 4.10.14	Streamline along elliptical section at $Fr = 0.37$	117
Figure 4.10.15	Streamline along elliptical section at $Fr = 0.55$	118
Figure 4.10.16	Streamline along rectangular section at $Fr = 0.19$	118
Figure 4.10.17	Streamline along rectangular section at $Fr = 0.37$	119
Figure 4.10.18	Streamline along rectangular section at $Fr = 0.55$	119
Figure 4.11.1	3D view of free surface for surface piercing body with NACA 0012 airfoil section at $Fr = 0.55$	120
Figure 4.11.2	3D view of free surface for surface piercing body with NACA 0018 airfoil section at $Fr = 0.55$	120
Figure 4.11.3	3D view of free surface for surface piercing body with NACA 0024 airfoil section at $Fr = 0.55$	121
Figure 4.11.4	3D view of free surface for surface piercing body with cylindrical cross – section at $Fr = 0.55$	121
Figure 4.11.5	3D view of free surface for surface piercing body with elliptical cross – section at $Fr = 0.55$	122
Figure 4.11.6	3D view of free surface for surface piercing body with rectangular cross – section at $Fr = 0.55$	122

NOMENCLATURE

Acronyms

Symbols	Description
CFD	Computational Fluid Dynamics
DES	Detached Eddy Simulation
EFD	Experimental Fluid Dynamics
FVM	Finite Volume Method
HRIC	High – Resolution Interface Capturing
IBEM	Iterative Boundary Element Method
KCS	KRISO Container ship
LES	Large Eddy Simulation
NACA	National Advisory Committee for Aeronautics
NASA	National Aeronautics and Space Administration
PISO	Pressure – Implicit with Splitting of Operators
PIV	Particle Image Velocimetry
PDE	Partial Differential Equation
RANS	Reynolds Averaged Navier – Stokes
SIMPLE	Semi-Implicit Method for Pressure Linked Equations
SST	Shear Stress Transport
SAS	Scale – Adaptive Simulation
URANS	Unsteady Reynolds Averaged Navier – Stokes
UDF	User – Defined Function
VOF	Volume of Fluid

Latin Symbols

Symbols	Description
F_1, F_2	Blending functions defined in eqn. 2.14 and 2.17
G	Production of turbulence kinetic energy
Y	Dissipation
D	Cross – diffusion
S_k	Source term for k
k	Turbulence kinetic energy
S	Strain rate magnitude defined in equation 2.10
D_ω^+	Positive portion of the cross-diffusion term in eqn. 2.16
f	Mixing function
Re	Reynolds number
C_D	Drag coefficient
C_L	Lift coefficient
Fr	Froude number
Ma	Mach number
u	Velocity magnitude
$a_1, R_\beta, R_k, R_\omega, M_{t0}, f_\beta, f_\beta^*$	Model constants

Greek Symbols

Symbols	Description
α	Volume fraction
τ_{ij}	Stress tensor
ρ	Density
Γ	Effective diffusivity
ω	Specific dissipation rate
σ	Turbulent Prandtl number

μ	Turbulent viscosity
Φ	Generic transport variable
ν	Kinematic viscosity
α^*	Constant defined in eqn. 2.13
$\sigma_{k,1}, \sigma_{\omega,1}, \sigma_{k,2}, \sigma_{\omega,2}, \beta_{i,1},$ $\beta_{i,2}, \alpha_{\infty}^*, \alpha_{\infty}, \alpha_0, \beta_{\infty}^*, \zeta^*$	Model constants

Subscripts

Symbols	Description
w	Water
a	Air

CHAPTER 1

Introduction

1.1 Introduction

When a body moves through the free-surface of water, gravity wave is generated around the body due to the pressure variation. Separation of flow occurs at the crest of the wave due to the adverse pressure gradient and extends to the wave trough near the wake of the body. This free-surface wave induced separation is very important in naval architecture, ocean and offshore engineering (Iafrati, 2017). Separation due to the free-surface wave deals with the complexities of free-surface deformation, vorticity, turbulence including the 3D boundary layer separation. The free surface wave induced separation was first identified by Chow (1967) using vertical (surface piercing) and horizontal (submerged) foils, designed for insignificant separation at large depths. It was found that the regions of separated flow originated just beyond the wave trough, and, in some cases, beyond the trailing edge. This phenomenon was also studied by Stern et al. (1996) using a free – surface piercing flat plate with a horizontal submerged foil (foil – plate model). These studies showed the dependence of the separation region on the Froude number (Fr) and wave steepness.

1.2 Literature Review

Zhang and Stern (1996) used RANS equations and Baldwin – Lomax turbulence model to analyze free – surface wave induced separation for a surface piercing NACA 0024 airfoil for different Froude numbers ($Fr = 0, 0.20, 0.37, \text{ and } 0.55$). They transformed the unsteady RANS and continuity equations from Cartesian coordinates to curvilinear coordinates in the computational domain. They analyzed the steady – flow results with regard to the wave and viscous flow and the nature of the separation.

Adjali et al. (2015) used VOF method for determining the free – surface impact of a submerged airfoil. They validated the simulation result with an earlier experimental result using NACA 0012 foil. They used Shear Stress Transport (SST) $k - \omega$ model and SIMPLE algorithm for the simulation. Different methods were used to find the least amount of error of drag and lift coefficient. They used the same method to hypothesis for NACA 0015 foil. Their work is focused for 2D analysis of the free – surface effects only. In both the simulation and experimental case, the airfoil was completely submerged. The impact of the depth is not clearly explained in this research.

Pogozelski et al. (1996) performed experiment in towing tank to analyze the flow past a rudder shaped strut. Particle Image Velocimetry (PIV) method had been used to visualize the wake, vorticity distribution and velocity profile above and below the free – surface. They found that, at low Froude numbers, the bow wave has a series of capillary waves that become increasingly unstable with the increase in Froude number.

Banks et al. (2010) used a commercial RANS code to investigate the multiphase flow field around KRISO Container Ships (KCS) full form. They analyzed the wave pattern, dynamic sinkage, trim and self-propulsion parameters for the hull using a body force propeller model. They compared the results with model tests performed by towing tanks on the KCS. They experienced problems with air ventilation on the wetted surface of the hull. They found that when the entire topside of the hull geometry was modeled, the air drag equated to 2 – 5% of the hull drag raising into the question the common assumption that air phase can be neglected in CFD simulation.

Wei and Ao-de (2007) employed Large Eddy Simulation (LES) model to observe the variation of the free – surface around a circular pier. They approached a two – steps method using user – defined function (UDF), since multiphase flow models cannot be performed with the LES model in Fluent CFD, in which the 2D compressible ideal gas equations and the LES model combined to calculate the 3D flow field with free – surface around the 3D surface piercing pier. They found that, with the increase

in velocity, the water level increases gradually in the area ahead of the pier until it reaches the maximum at the stagnation point of the upstream face. At the two sides of the pier the water level falls, whereas it increases, in the wake region, away from the pier until it reaches the flow depth not influenced by the presence of the pier. The variation of the wake level around the pier is significant with the increase in approaching velocity.

Ahmed et al. (2013) studied 2D flow around a NACA 0012 airfoil wing flapped at different flap angles (30° , 40° , and 50°) with varying Mach numbers (Ma) using Shear Stress Transport (SST) $k - \omega$ model in ANSYS Fluent solver with turbulence intensities 1% and 5% at velocity inlet and pressure outlet respectively. They validated the results with NASA Langley Research Center validation cases. They used the results to analyze aerodynamic characteristics of plain flapped NACA 0012 airfoil. They found that, with increase in Mach number (Ma), lift coefficient (C_L) increases but drag coefficient (C_D) remains approximately constant. They observed a rapid drastic decrease in C_L and an abrupt upsurge in C_D with velocity approaching to the sonic velocity. They showed that if the both values of C_L/C_D and $\sqrt{C_L/C_D}$ are declined, range and endurance are decreased in all cases. They also found that, at high flap angles, flow is very unstable and it remains unconverged even after larger iteration period in ANSYS Fluent flow solver.

Metcalf et al. (2005) delivered detailed experimental data documentation of the wave elevations and surface pressures for a surface piercing NACA 0024 hydrofoil. Test conditions were selected for minimal, reattaching and non-reattaching separation using different Reynolds numbers. It was found that mean wave elevations in the separation region were relatively constant at lower Reynolds numbers but bow wave is tremendous, at higher Reynolds numbers, and the separation region is shifted towards the trailing edge with increased splashing and bubbles. The work is mainly focused on a steady state condition. Unsteady wave elevation had not been analyzed in this study.

Liu et al. (2016) studied two-dimensional transient simulations to analyze the flow characteristics around a plate normal to the stream. The variation of force coefficients and vortex shedding patterns were investigated at different plate depths. The characteristics of free-surface flow were evaluated using $k - \omega$ Shear Stress Transport ($k - \omega$ SST) turbulence model and Volume of Fluid (VOF) multiphase model. It was found that, with the increase in Froude number, the drag coefficient decreases when the plate gets closer to the free surface and a jet - like flow form from the surface was observed on the top of the plate and vortices from the plate top surface dissipate into smaller eddies because of the presence of the free surface.

Raza et al. (2013) performed numerical simulation to study the free - surface effects on a moving hydrofoil near free - surface using unsteady Reynolds average Navier - Stokes code with a $k - \varepsilon$ turbulence model and free - surface Volume of Fluid (VOF) tracking method. Dynamic mesh technique was executed for the grid generation during body motion. It was found that lift and drag coefficients of hydrofoil increase and there is a suction area which pull the submerged body up near the free - surface.

Karim et al. (2014) investigated the surface wave generated by flow past a NACA 0015 hydrofoil normal to the stream near the free surface of water. Reynolds Averaged Navier - Stokes (RANS) equations were solved using two - dimensional implicit Finite Volume Method (FVM) and turbulent flow around the hydrofoil near the free - surface was captured using realizable $k - \varepsilon$ turbulence model. The effects of free surface on water was studied by Volume of Fluid (VOF) method. Lift and drag coefficients were studied and the hydrodynamic forces near the free surface were also calculated.

Uslu and Bal (2008) studied wave drag, lift, wave pattern and pressure distribution around 2 - D and 3 - D bodies moving steadily under or on a free surface. The iterative boundary element method (IBEM), originally developed for both 2 - D and 3 - D cavitating hydrofoils and ship - like bodies moving with constant speed under or on the free surface, was applied here in the case of a 2 - D hydrofoil with an angle of attack, and some extended results were given. The effects of Froude Number

and the depth of submergence of hydrofoil from the free surface on the pressure distribution and lift and wave drag values and the free surface wave elevation were discussed.

Kandasamy et al. (2008) investigated the vortical structures and instability mechanisms of the unsteady free surface wave – induced separation around a surface piercing NACA 0024 foil at a Froude number (Fr) of 0.37 and a Reynolds number (Re) of 1.52×10^6 using a Unsteady Reynolds Averaged Navier – Stokes (URANS) code with a blended $k - \varepsilon$ and $k - \omega$ turbulence model and a free surface tracking method. The mean flow solutions for the free surface wave – elevation and foil surface pressure showed good correspondence with the experimental fluid dynamics (EFD), the main shortcoming being that URANS predicts higher wave – elevation magnitudes and predicts a quicker pressure recovery pressure after separation. At the free surface, the separated flow reattached to the foil surface with wall – bounded separation bubble. The mean and instantaneous flow topologies in the separation region were similar to the owl – face pattern. The initial shear – layer instability, the Karmen – like instability, and the flapping instability were identified and their scaling and physical mechanisms were studied.

Rhee (2009) performed the numerical simulation of free – surface wave flows around surface – piercing cylindrical structures using an unstructured grid – based Unsteady Reynolds Averaged Navier – Stokes (URANS) method. The Volume of Fluid (VOF) method was implemented in the CFD code based on the finite volume discretization method. The modified High – Resolution Interface Capturing (HRIC) scheme was employed to calculate the face fluxes for the VOF model. The computational method was applied for two problems: (1) the free – surface wave flow around a surface – piercing NACA 0024 hydrofoil, and (2) the free – surface wave flow around a surface – piercing circular cylinder that involve the Kelvin waves, spilling breaking waves, bubbly free – surface in the separated region, and interaction between free surface waves and underlying viscous flow. It was observed that the free – surface turbulence and turbulence transition are deemed to play a significant role in

the film development, bubble generation or transport, and vortex shedding behavior and eventually vortex – induced vibration modes.

Koo et al. (2013) studied the two – phase turbulent flow past an interface – piercing circular cylinder using a high – fidelity orthogonal curvilinear grid solver. The large – eddy simulation was carried out by a Lagrangian dynamic subgrid – scale model. A coupled level set and Volume of Fluid (VOF) method was used to track the air – water interface. The simulation covered the sub – critical and critical and post critical regimes of the Reynolds. Significant changes in flow features near the air – water interface was observed as the Reynolds number was increased from the sub – critical to the critical regime. The interface makes the separation point near the interface much delayed for all Reynolds numbers. The separation region at intermediate depths is remarkably reduced for the critical Reynolds number regime. At different Froude numbers, the air – water interface exhibits significantly changed structures, including breaking bow waves with splashes and bubbles at high Froude numbers. Instantaneous and mean flow features such as interface structures, vortex shedding, Reynolds stresses, and vorticity transport are also analyzed in this study.

In the present study the free – surface effects will be analyzed in order to explain the flow features due to wave induced separation, free – surface elevations, surface pressures around a three-dimensional surface piercing floating body.

1.3 Objective of the Research

The present study is concerned with the numerical simulation of free-surface waves and wave-induced separation due to the flow past a 3D floating body. The objectives of the present research are as follows:

- To study the effect of free-surface on wave-induced separation of flow past a 3D floating body with NACA 0024 hydrofoil section for different Froude Numbers (0.19, 0.37, and 0.55).

- To validate the computed results comparing with both the available experimental data and the previous numerical results.
- To investigate the thickness effect on the wave-induced separation using 3D floating body with NACA 0012 and NACA 0018 hydrofoil section.
- To investigate the effect of shape on the wave-induced separation using 3D floating body with circular and elliptical cross-section.

1.4 Outline of Methodology

In this research, the effects of free-surface on wave-induced separation of flow past a 3D floating body will be studied using a commercial CFD code ANSYS Fluent. Structured grid will be adopted for 3D floating body with NACA 0012, NACA 0018, NACA 0024 hydrofoil sections and surface piercing body with rectangular section. An unstructured grid will be used for floating body with circular and elliptical cross-section. A fine grid will be applied near the free-surface and the bodies whereas the grid will be coarse in rest of the domain.

The equations governing the flow past the floating body are the RANS equations. These equations will be discretized by the Finite Volume Method (FVM), and the solution will be carried out using the Pressure-Implicit with Splitting of Operators (PISO) algorithm. For time discretization, the first order implicit scheme will be employed. The Shear-Stress Transport (SST) $k-\omega$ turbulence model will be used to capture the boundary layer and the Volume of Fluid (VOF) technique will be adopted to track the free-surface of water. As for boundary conditions, the upstream will be modeled as pressure inlet, the downstream as pressure outlet, the surface of the body as wall and the sides as symmetry.

CHAPTER 2

Theoretical Background

2.1 NACA Airfoils

The word NACA means National Advisory Committee for Aeronautics. The airfoil shapes that are developed by NACA are mainly for aircraft wings. But these shapes are also used as airfoils, rudder sections and so on. Every NACA airfoil has a distinctive name, which is a series of digits following the name “NACA”. The shape of the airfoil depends on this series of digits.

2.1.1 Four Digit Series

The NACA four – digit wing sections defined by the profile as (Rahman et al., 2016):

1. First digit describes maximum camber as percentage of the chord length.
2. Second digit describes the distance of the maximum camber from the airfoil leading edge in terms of the percentage of the chord length.
3. Last two digits describe the maximum thickness of the airfoil as percentage of the chord length.

In this study, NACA 0012, NACA 0018, and NACA 0024 airfoil sections have been used, where the first two digits describe that there is no camber in the airfoil and the last two digits describe that the maximum thickness of the airfoil as a percentage of the chord length.

2.1.2 Shape for the NACA Airfoils

The thickness distribution for the NACA four-digit sections is given by the following formula (Abbott et al., 1959):

$$\pm y_t = \frac{t}{0.2} \left[0.2969 \sqrt{\frac{x}{c}} - 0.126 \left(\frac{x}{c} \right) - 0.3516 \left(\frac{x}{c} \right)^2 + 0.2843 \left(\frac{x}{c} \right)^3 - 0.1015 \left(\frac{x}{c} \right)^4 \right] \dots (2.1)$$

Where, c is the chord length, x is the position along the chord from 0 to c , y is the half thickness at a given value of x (centerline to surface), and t is the maximum thickness as a fraction of the chord (so $100t$ gives the last two digits in the NACA-4-digit denomination).

The leading-edge radius is given by the following formula (Abbott et al., 1959):

$$r = 1.1019t^2 \dots \dots \dots (2.2)$$

It will be noted from equations (2.1) and (2.2) that the ordinate at any point is directly proportional to the thickness ratio and that the leading-edge radius varies as the square of the thickness ratio.

Hence, the coordinates of the upper surface of the airfoil (x_u, y_u), and the lower surface of the airfoil (x_l, y_l) can be formulate as (Abbott et al., 1959):

$$x_u = x_l = x, \quad y_u = +y_t \quad \text{and} \quad y_l = -y_t \dots \dots \dots (2.3)$$

2.2 Computational Fluid Dynamics (CFD)

Modern fluid mechanical problems would be impossible to solve without the help of Computational Fluid Dynamics (CFD). CFD is a robust method which simulates a model with its actual environment long before it has been practically made. CFD solves the numerical governing equations with the help of computer. These governing equations are:

- Conservation of mass (Continuity equation)
- Conservation of momentum (Navier-Stokes equations)
- Conservation of energy (The first law of thermodynamics)
- Simplified boundary layer equations

The scope of analytical solutions to fundamental equations of fluid dynamics is very limited and, once a more difficult and complex geometry is introduced, we usually have to choose a given numerical method for obtaining a solution. With the advancements in computer hardware technology enables researchers to develop new computational and numerical techniques, which leads designers to come up with novel designs through varying the geometry and flow conditions easily. The new computational techniques aided by computer are mainly:

- Finite Difference Method (FDM)
- Finite Volume Method (FVM)
- Finite Element Method (FEM)

The governing equations that are usually composed of partial differentials need to be stated approximately, so that in the digital environment (can only cover analytical and logical operations), the algebraic or analytical methods, just mentioned above, can be utilized to approach the solution considering accuracy. However, one should also remember that the more accurate the computation of flow is and the more complex shape the sample over which the fluid has flown, the more computer performance and

the more time and intelligence are necessary. In this particular research, the solution is carried out using the Pressure-Implicit with Splitting of Operators (PISO) algorithm. For time discretization, the first order implicit scheme is employed. This study has been carried out using ANSYS Fluent software, version 2019 R2, to solve the numerical equations. The grids are generated by this software in order to discretize the physical domain.

Nevertheless, computational fluid dynamics method has some shortcomings. One of those is basically lack of distinguishing the boundaries, for example, in transition between laminar and turbulent flow. It may be easier to explicitly distinguish flow transition around corners of a simple shaped box but can be very complicated for the flow transition over a 2D or 3D rudder. Another shortcoming is that CFD method requires very high performance-computer to numerically resolve the very complex Navier-Stokes equations and still might be very time-consuming process in comparison to theoretical and experimental approach.

The computational investigations have been done using turbulence modeling through Reynolds averaged Navier-Stokes equations (RANS). Turbulence modeling is a wide subject offering many kinds of models such as the one-equation Spallart-Allmaras model, the Standard $k - \varepsilon$ model, the $k - \omega$ SST model, the $k - \varepsilon$ RNG model, the Realizable $k - \varepsilon$ model, the Transitional $k - kl - \omega$ model and the Standard $k - \omega$ model. The accuracy and the compatibility of the results from each computational model with the corresponding experiment results is another field of study and it is not discussed here. In this research, the $k - \omega$ SST model has been used to study the numerical simulation of free-surface waves and wave-induced separation due to the flow past a surface piercing body.

2.2.1 Governing Equations

The CFD (Computational Fluid Dynamics) results are obtained by solving RANS equations using the finite volume method. The governing equations, continuity and momentum are, as follows (Sadathosseini et al., 2008):

- *Continuity Equations:*

$$\frac{\partial U_i}{\partial x_j} = 0 \dots\dots\dots (2.4)$$

- *Equation of momentum:*

$$\frac{\partial}{\partial x_j} (\rho U_i U_j) = -\frac{\partial P}{\partial x_j} - \frac{\partial}{\partial x_j} (\tau_{ij} + \rho \overline{u_i' u_j'}) \dots\dots\dots (2.5)$$

where $\tau_{ij} = \mu \left(\frac{\partial U_i}{\partial x_j} + \frac{\partial U_j}{\partial x_i} \right)$ is the stress tensor. The treatment for the free-surface flow uses Volume of Fluid (VOF) method (Karim, 2014) for interface tracking. In this method, an additional transport equation is solved for the volume fraction of water in each cell. If the volume fractions of water and air in each cell are denoted as α_w and α_a respectively, the tracking of the interface between the phases is accomplished by the solution of a continuity equation for the volume fraction of water. This equation has the following form:

$$\frac{\partial \alpha_w}{\partial t} + \vec{U} \cdot \nabla \alpha_w = 0 \dots\dots\dots (2.6)$$

The volume fraction equation will not be solved for air; the volume fraction of air will be computed based on the following constraint:

$$\alpha_w + \alpha_a = 1 \dots\dots\dots (2.7)$$

The properties appearing in the transport equations are determined by the presence of the component phases in each control volume. For example, the density in each cell is given by the following:

$$\rho = \alpha_w \rho_w + \alpha_a \rho_a \dots\dots\dots (2.8)$$

The viscosity is also computed using similar manner.

A single momentum equation is solved throughout the domain and the resulting velocity field is shared among the phases. The momentum equation is dependent on the volume fractions of all phases through the properties, ρ and μ .

2.3 Finite Volume Method (FVM)

A method for discretizing the transport equations commonly implemented in CFD codes is the finite volume method (FVM). The finite volume method (FVM) is an increasingly popular numerical method for the approximate solution of partial differential equations (PDEs). Most of the authors' research work has been based on the FVM. Compared to the classical finite difference method (FDM) has the following advantages:

- Spatial discretization is totally flexible. The mesh can accommodate to irregular shaped boundaries to reduce geometric errors and the mesh refined locally to give more resolution in regions of particular interest.
- Equations are presented in integral form which is often how they are derived from the underlying physical laws.
- A larger class of problem can be solved.

- The FVM method naturally conserves conserved variables when applied to PDEs expressing conservation laws since, as two neighboring cells share a common interface, the total flow of a conserved quantity out of one cell will be the same as the entering the other cell.
- FVM is especially powerful on course of non-uniform grids and in calculations where the mesh moves to track interfaces or shocks

2.3.1 Different Versions of Finite Volume Method

2.3.1.1 Centre node based FVM

In center node based FVM approach, the computational domain is divided into a mesh. One set of algebraic equations is obtained for each control volume or cell by integrating the transport equations over each control volume. The value of each variable is stored in a node in the center of the cell. However, the discretized equations also include values for the cell faces. Therefore, interpolation methods are used to approximate values at these positions. Interpolation method creates a great impact on numerical stability, convergence rate and accuracy.

2.3.1.2 Vertex based FMV

In the vertex based FVM approach, control volumes are constructed around each mesh vertex (each cell corner). The mesh vertices are also used to store the variables. Just as in the center node based FVM approach, the governing equations are integrated over each control volume. However, discretization is done within each element since a control volume lies within several mesh elements. Then the properties are distributed to the corresponding control volume. To solve the discretized equations, properties are needed for other locations than the mesh vertices. Approximations are needed and, in the vertex based, approach the concept of finite element shape functions is used to

obtain these approximations. The appearance of the shape functions depends on the element type.

2.4 Multiphase Flow Theory

Multiphase flow is a flow with simultaneous presence of different phases, where phase refers to solid, liquid or vapor state of matter. There are four main categories of multiphase flows:

- Gas – Liquid;
- Gas – Solid;
- Liquid – Solid and
- Three – phase flows.

Further characterization is commonly done according to the visual appearance of the flow as separated, mixed or dispersed flow. These are called flow patterns or flow regimes and the categorization of a multiphase flow into a certain flow regime is comparable to the importance of knowing if a flow is laminar or turbulent in single – phase flow analysis (Stenmark, 2013).

A flow pattern describes the geometrical distribution of the phases and the flow pattern greatly affects phase distribution, velocity distribution etc. for a certain flow situation. A number of flow regimes exist and the possible flow patterns differ depending on the geometry of the flow domain. For some simple shapes, for example horizontal and vertical pipes, the flow patterns that occur for different phase velocities have been summarized in the flow map. Figure 2.1 visualizes the flow configuration for some possible flow regimes and Figure 2.2 shows an example of a flow map for horizontal pipe flow (Stenmark, 2013).

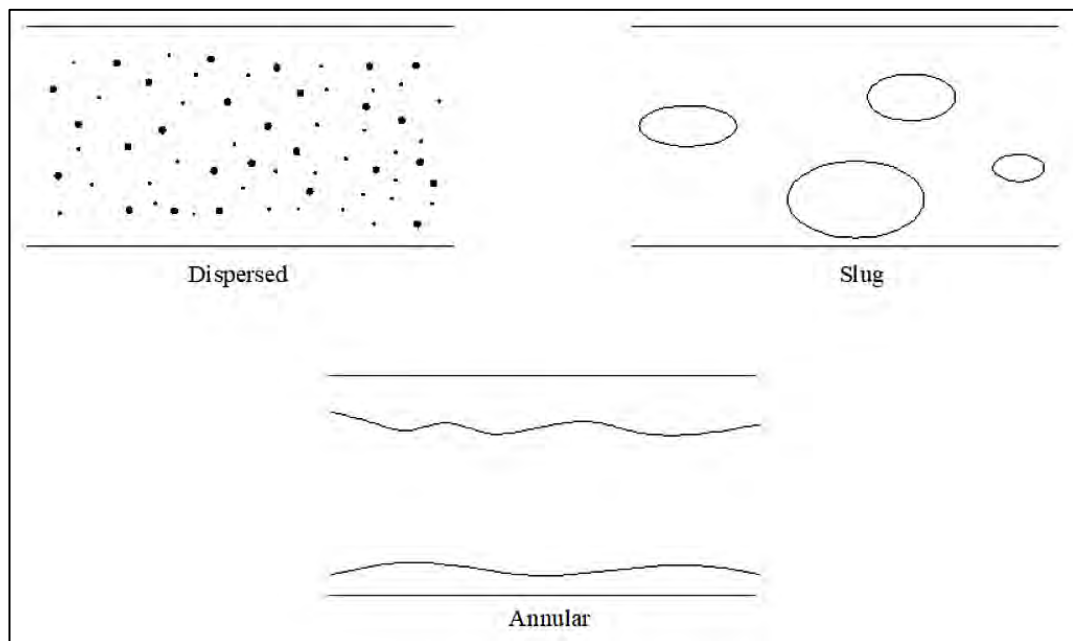


Figure 2.1: Visualization of typical flow patterns for flow in horizontal pipes

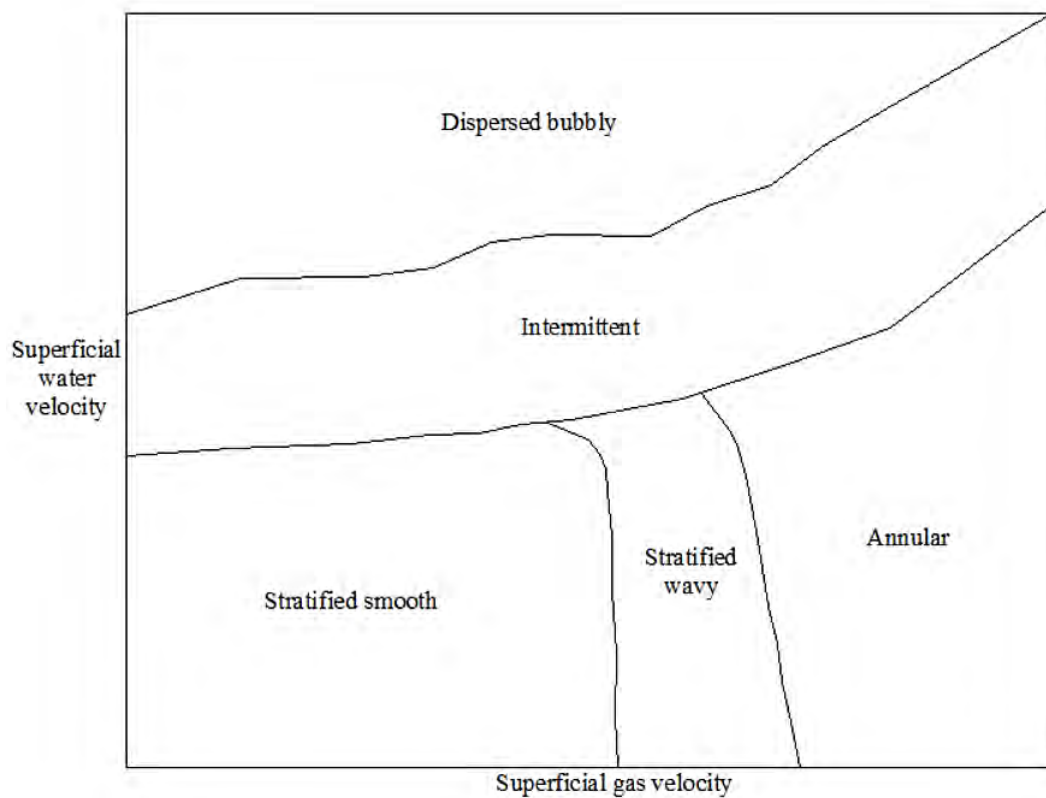


Figure 2.2: Example of flow map for two phase flow in horizontal pipes

The two extremes on a flow map is dispersed flow and separated flow. In separated flow there is a distinct boundary between the phases. Examples of separated flow is stratified flow where one phase is flowing on top of another or annular flow in a pipe with a liquid film along the pipe and a gas core in the middle. Dispersed flow is flow where one phase is widely distributed as solid particles or bubbles in another continuous phase. Several intermediate regimes also exist, which contain both separated and dispersed phases such as for example annular bubbly flow. Due to growing instabilities in one regime, transition to another regime can occur. This phenomenon complicated the modeling of multiphase flow even further as the transition is unpredicted and the different flow regimes are to some extent governed by different physics.

2.5 Different modeling Approaches to Describe Multiphase Flow Theory

- Euler – Lagrange Approach
- Euler – Euler Approach
- Volume of Fluid Approach (VOF)

2.6 Overview of VOF model

The VOF model can model two or more immiscible fluids by solving a single set of momentum equations and tracing the volume fraction of each of the fluids throughout the domain. Typical applications include the prediction of jet breakup, the motion of large bubbles in a liquid, the motion of liquid after a dam break, and the steady or transient tracking of any liquid-gas interface.

2.6.1 Limitations of the VOF Model

The following restrictions apply to the VOF model in ANSYS Fluent:

- Pressure based solver must be used. The VOF model is not available with the density-based solver.
- All control volumes must be filled with either a single fluid phase or a combination of phases. The VOF model does not allow for void regions where no fluid of any type is present.
- Only one of the phases can be defined as a compressible ideal gas. There is no limitation on using compressible liquids using user-defined functions.
- Stream wise periodic flow (either specified mass flow rate or specified pressure drop) cannot be modeled when the VOF model is used.
- The second-order implicit time-stepping formulation cannot be used with the VOF explicit scheme.
- When tracking particles in parallel, the DPM model cannot be used with the VOF model if the shared memory option is enabled.

2.6.2 Steady – State and Transient VOF Calculation

The VOF formation in ANSYS Fluent is generally used to compute a time-dependent solution, but for problems in which a steady-state solution is considered, it is possible to perform a steady-state calculate. A steady-state VOF calculation is sensible only when the solution is independent of the initial conditions and there are distinct inflow boundaries for the individual phases. For example, since the shape of the free surface inside a rotating cup depends on the initial level of the fluid, such a problem must be solved using the time-dependent formulation. On the other hand, the flow of water in a channel with a region of air on tip and a separate air inlet can be solved with the steady – state formulation.

The VOF formulation relies on the fact that two or more fluids (or phases) are not interpenetrating. For each additional phase that is added to the model, a variable is introduced: the volume fraction of the phase in the computational cell. In each control volume, the volume fractions of all phases sum to unity. The fields for all variables and properties are shared by the phases and represent volume-averaged values, as long as the volume fraction of each of the phases is known at each location. Thus the variables and properties in any given cell are either purely representative of one of the phases, or of a mixture of the phases, depending upon the volume fraction values.

In other words, if the fluid's volume fraction in the cell is denoted as, then the following three conditions are possible:

- $\alpha_w = 0$, the cell is empty (of the fluid)
- $\alpha_w = 1$, the cell is full (of the fluid)
- $0 < \alpha < 1$, the cell contains fluid interface

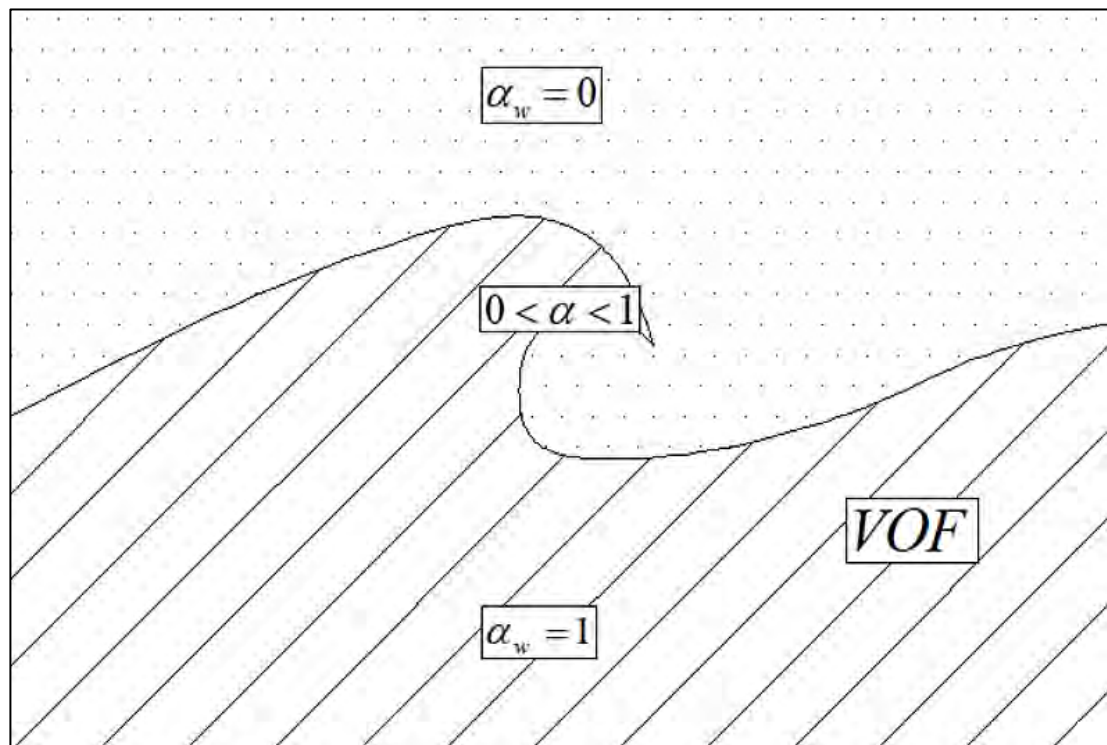


Figure 2.3: Advection of fluid

2.7 Turbulent Flow

Most flows encountered in engineering practice are turbulent and therefore require different treatment. Turbulent flows are characterized by the following properties:

- Turbulence flows are highly unsteady. A plot of the velocity as a function of time at most points in the flow would appear random to an observer unfamiliar with these flows. The word, 'chaotic' could be used but it has been given another definition in recent years.
- They are three dimensional. The time-averaged velocity may be a function of only two coordinates, but the instantaneous field fluctuates rapidly in all three dimensions.
- They contain great deal of vorticity. Indeed, vortex stretching in one of the principal mechanisms by which the intensity of turbulence is increased.
- Turbulence increases the rate at which conserved quantities are stirred. Stirring is a process in which parcels of fluid with differing concentration of at least one of the conserved properties are brought into contact. The actual mixing is accomplished by diffusion. Nonetheless, the process is often called turbulent diffusion.
- By means of the processes just mentioned, turbulence brings fluids of differing momentum content into contact. The reduction of velocity gradients due to the actions of viscosity reduces the kinetic energy of the flow; in other words, mixing is a dissipative process. The lost energy is irreversibly converted into internal energy of the fluid.
- Turbulent flows fluctuate on a broad range of length and time scales. This property makes direct numerical simulation of turbulent flows very difficult.

2.8 Turbulence models

A turbulence model is a computational procedure to close the system of mean flow equations so that a more or less wide variety of flow problems can be calculated. For most engineering purposes, it is unnecessary to resolve the details of the turbulent fluctuations. Only the effects of the turbulence on the mean flow are usually sought. For a turbulence model to be useful in a general CFD code, it must have wide applicability, be accurate, simple and economical to run. The turbulence models that are used in commercial CFD code ANSYS Fluent are given below:

- Spallart – Allmaras (1 equation model)
- K – epsilon (2 equations model)
- K – omega (2 equations model)
- Transition k – kl – omega (3 equations model)
- Transition SST model (4 equations model)
- Reynolds Stress (4 equations model)
- Scale – Adaptive Simulation (SAS)
- Detached Eddy Simulation (DES)
- Large Eddy Simulation (LES)

2.9 Shear – Stress Transport (SST) $k - \omega$ Model

The shear – stress transport (SST) $k - \omega$ model was developed by Menter (2004) to effectively blend the robust and accurate formulation of the $k - \omega$ model in the near-wall region with the freestream independence of the $k - \omega$ model in the far field. To achieve this, the $k - \epsilon$ model is converted into a $k - \omega$ formulation. The SST $k - \omega$ model is similar to the standard $k - \omega$ model, but includes the following refinements:

- The standard $k - \omega$ model and the transformed $k - \varepsilon$ model are both multiplied by a blending function and both models are added together. The blending function is designed to be one in the near – wall region, which activated the standard $k - \omega$ model, and zero away from the surface, which activates the transformed $k - \varepsilon$ model.
- The SST model incorporates a damped cross – diffusion derivative term in the ω equation.
- The definition of the turbulent viscosity is modified to account for the transport of the turbulent shear stress.
- The modeling constants are different.

These features make the SST $k - \omega$ model more accurate and reliable for a wider class of flows (adverse pressure gradient flows, airfoils, transonic shock waves) than the standard $k - \omega$ model.

2.9.1 Transport Equations for the (SST) $k - \omega$ Model

The turbulence kinetic energy, k , and the specific dissipation rate, ω , are obtained from the following transport equations (Fluent, 2015):

$$\frac{\partial}{\partial t}(\rho k) + \frac{\partial}{\partial x_i}(\rho k u_i) = \frac{\partial}{\partial x_i} \left(\Gamma_k \frac{\partial k}{\partial x_i} \right) + G_k - Y_k + S_k \dots\dots\dots (2.9)$$

$$\frac{\partial}{\partial t}(\rho \omega) + \frac{\partial}{\partial x_j}(\rho \omega u_j) = \frac{\partial}{\partial x_j} \left(\Gamma_\omega \frac{\partial \omega}{\partial x_j} \right) + G_\omega - Y_\omega + D_\omega + S_k \dots\dots\dots (2.10)$$

In these equations, the term G_k represents the production of turbulence kinetic energy. G_ω represents the generation of ω . Γ_k and Γ_ω represent the effective diffusivity of k and ω , respectively. Y_k and Y_ω represent the dissipation of k and ω due to turbulence. D_ω represents the cross – diffusion term. S_k and S_ω are used – defined source terms.

2.9.2 Modeling the Effective Diffusivity

The effective diffusivities of the SST model are given by (Fluent, 2015)

$$\Gamma_k = \mu + \frac{\mu_t}{\sigma_k} \dots\dots\dots (2.11)$$

$$\Gamma_\omega = \mu + \frac{\mu_t}{\sigma_\omega} \dots\dots\dots (2.12)$$

where σ_k and σ_ω are the turbulent Prandtl numbers for k and ω , respectively. The turbulent viscosity μ_t is computed as follows:

$$\mu_t = \frac{\rho k}{\omega} \frac{1}{\max\left[\frac{1}{\alpha^*}, \frac{S F_2}{a_1 \omega}\right]} \dots\dots\dots (2.13)$$

where S is the strain rate magnitude and

$$\sigma_k = \frac{1}{F_1 / \sigma_{k,1} + (1 - F_1) / \sigma_{k,2}} \dots\dots\dots (2.14)$$

$$\sigma_\omega = \frac{1}{F_1 / \sigma_{\omega,1} + (1 - F_1) / \sigma_{\omega,2}} \dots\dots\dots (2.15)$$

The coefficient α^* damps the turbulent viscosity causing a low – Reynolds number correction. It is given by

$$\alpha^* = \alpha_\infty^* \left(\frac{\alpha_0^* + \text{Re}_t / R_k}{1 + \text{Re}_t / R_k} \right) \dots\dots\dots (2.16)$$

where $\text{Re}_t = \frac{\rho k}{\mu \omega}$, $R_k = 6$, $\alpha_0^* = \frac{\beta_i}{3}$, $\beta_i = 0.072$.

The blending functions, F_1 and F_2 , are given by

$$F_1 = \tanh(\Phi_1^4) \dots\dots\dots (2.17)$$

$$\Phi_1 = \min \left[\max \left(\frac{\sqrt{k}}{0.09 \omega y}, \frac{500 \mu}{\rho y^2 \omega} \right), \frac{4 \rho k}{\sigma_{\omega,2} D_\omega^+ y^2} \right] \dots\dots\dots (2.18)$$

$$D_\omega^+ = \max \left[2 \rho \frac{1}{\sigma_{\omega,2}} \frac{1}{\omega} \frac{\partial k}{\partial x_j} \frac{\partial \omega}{\partial x_j}, 10^{-10} \right] \dots\dots\dots (2.19)$$

$$F_2 = \tanh(\Phi_2^2) \dots\dots\dots (2.20)$$

$$\Phi_2 = \max \left[2 \frac{\sqrt{k}}{0.09\omega y}, \frac{500\mu}{\rho y^2 \omega} \right] \dots\dots\dots (2.21)$$

where y is the distance to the next surface and D_ω^+ is the positive portion of the cross – diffusion term.

2.9.3 Modeling the Turbulence Production

2.9.3.1 Production of k

The term G_k represents the production of turbulence kinetic energy. From the exact equation for the transport of k , this term may be defined as (Fluent, 2015)

$$G_k = -\overline{\rho u_i' u_j'} \frac{\partial u_j}{\partial x_i} \dots\dots\dots (2.22)$$

2.9.3.2 Production of ω

The term G_ω represents the production of ω and is given by (Fluent, 2015)

$$G_\omega = \frac{\alpha}{\nu_t} G_k \dots\dots\dots (2.23)$$

2.9.4 Modeling the Turbulence Dissipation

2.9.4.1 Dissipation of k

The term Y_k represents the dissipation of turbulence kinetic energy, and is defined by (Fluent, 2015)

$$Y_k = \rho \beta^* f_{\beta^*} k \omega \dots\dots\dots (2.24)$$

where

$$\beta^* = \beta_i^* [1 + \zeta^* F(M_t)] \dots\dots\dots (2.25)$$

$$\beta_i^* = \beta_\infty^* \left(\frac{4/15 + (\text{Re}_t / R_\beta)^4}{1 + (\text{Re}_t / R_\beta)^4} \right) \dots\dots\dots (2.26)$$

$$f_{\beta^*} = 1 \dots\dots\dots (2.27)$$

$$\zeta^* = 1.50 \dots\dots\dots (2.28)$$

$$R_\beta = 8.0 \dots\dots\dots (2.29)$$

$$\beta_\infty^* = 0.09 \dots\dots\dots (2.30)$$

2.9.4.2 Dissipation of ω

The Y_ω represents the dissipation of ω and is defined by (Fluent, 2015)

$$Y_\omega = \rho \beta f_\beta \omega^2 \dots\dots\dots (2.31)$$

where

$$\beta = \beta_i \left[1 - \frac{\beta_i^*}{\beta_i} \zeta^* F(M_t) \right] \dots\dots\dots (2.32)$$

$$\beta_i = F_1 \beta_{i,1} + (1 - F_1) \beta_{i,2} \dots\dots\dots (2.33)$$

$$f_\beta = 1.0 \dots\dots\dots (2.34)$$

$F(M_t)$ is the compressibility function and is given by

$$F(M_t) = \begin{cases} 0 & M_t \leq M_{t0} \\ M_t^2 - M_{t0}^2 & M_t > M_{t0} \end{cases} \dots\dots\dots (2.35)$$

$$M_t^2 \equiv \frac{2k}{a^2} \dots\dots\dots (2.36)$$

$$M_{t0} = 0.25 \dots\dots\dots (2.37)$$

$$a = \sqrt{\gamma RT} \dots\dots\dots (2.38)$$

In the high – Reynolds number form of the $k - \omega$ model, $\beta_i^* = \beta_\infty^*$. In the compressible form, $\beta^* = \beta_i^*$.

2.9.5 Cross – Diffusion Modification

The SST $k - \omega$ model is based on both the standard $k - \omega$ model and the standard $k - \varepsilon$ model. To blend these two models together, the standard $k - \varepsilon$ model has been transformed into equations based on k and ω , which leads to the introduction of a cross – diffusion term D_ω . D_ω is defined as (Fluent, 2015)

$$D_\omega = 2(1 - F_1)\rho \frac{1}{\omega\sigma_{\omega,2}} \frac{\partial k}{\partial x_j} \frac{\partial \omega}{\partial x_j} \dots\dots\dots (2.39)$$

2.9.6 Model Constants

The model constants for Shear Stress Transport (SST) $k - \omega$ model are (Fluent, 2015):

$$\sigma_{k,1} = 1.176$$

$$\sigma_{\omega,1} = 2.0$$

$$\sigma_{k,2} = 1.0$$

$$\sigma_{\omega,2} = 1.168$$

$$a_1 = 0.31$$

$$\beta_{i,1} = 0.075$$

$$\beta_{i,2} = 0.0828$$

$$\alpha_\infty^* = 1.0$$

$$\alpha_\infty = 0.52$$

$$\alpha_0 = 1/9$$

$$\beta_\infty^* = 0.09$$

$$R_\beta = 8.0$$

$$R_k = 6.0$$

$$R_\omega = 2.95$$

$$\zeta^* = 1.5$$

$$M_{t_0} = 0.25$$

CHAPTER 3

Numerical Solution

For numerical simulation the computational domain is created and simulations are run with different 3D surface piercing bodies.

3.1 Geometry Profile

The flow field around different surface piercing bodies is modeled in three dimensions. The simulations have been performed for three different Froude numbers ($Fr = 0.19, 0.37, \text{ and } 0.55$). Only half the domain is solved, since the geometries are symmetrical. Different boundaries of the domain are velocity inlet upstream, pressure outlet downstream, symmetry and wall.

The first case is surface piercing rudder with NACA 0024 airfoil cross – section, with 1.0 m chord length, L and 1.0 m span (50% under the incompressible fluid which is water). The leading edge of the surface piercing rudder with NACA 0024 airfoil section is positioned at a distance of 3.90 m right from the inlet boundary and the trailing edge is at a distance of 5.10 m left from the outlet boundary in the x – axis.

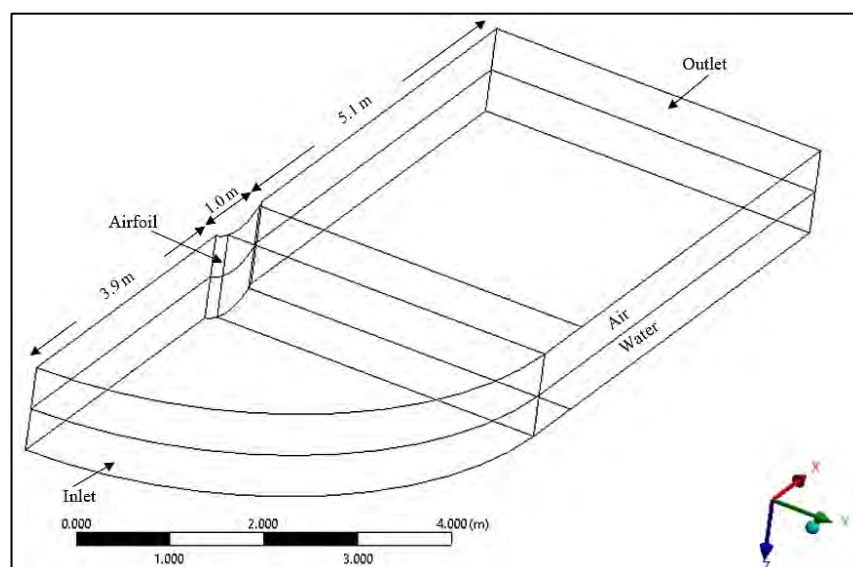


Figure 3.2.1: Geometry for surface piercing body with NACA 0024 airfoil section

The second case is a surface piercing rudder with NACA 0012 airfoil cross – section, with a chord length of 1.0 m and a span of 1.0 m (0.5 m in water). The leading edge is 3.90 m right from the inlet boundary and the trailing edge is 4.10 m left from the outlet boundary.

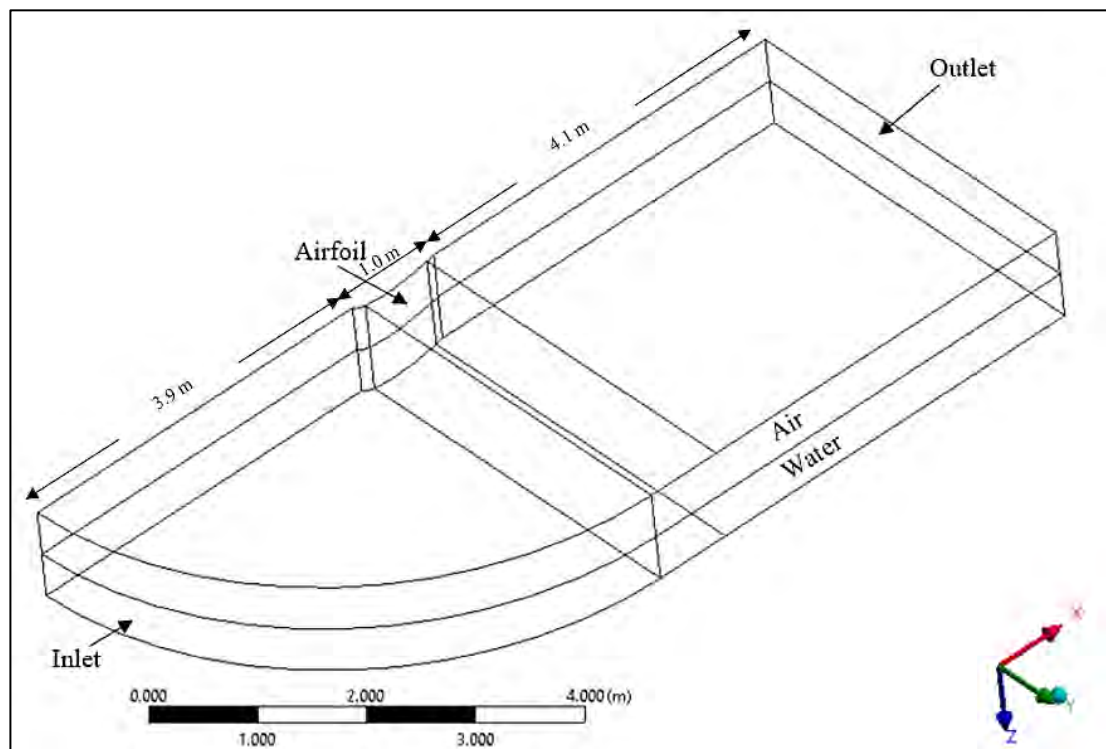


Figure 3.2.2: Geometry for surface piercing body with NACA 0012 airfoil section

The third case has been performed with a surface piercing rudder having NACA 0018 airfoil cross – section. It consists of 1.0 m chord length and 1.0 m span (50% in water). The leading edge is at a distance of 3.90 m right from the inlet boundary and the trailing edge is at a distance of 4.10 m left from the outlet boundary.

The fourth case is a surface piercing body with cylindrical cross – section having a diameter of 1.0 m and a height of 1.0 m (50% in air). This circular cross – sectional surface piercing body is at a distance of 3.0 m right from the inlet boundary and 4.0 m left from the outlet boundary.

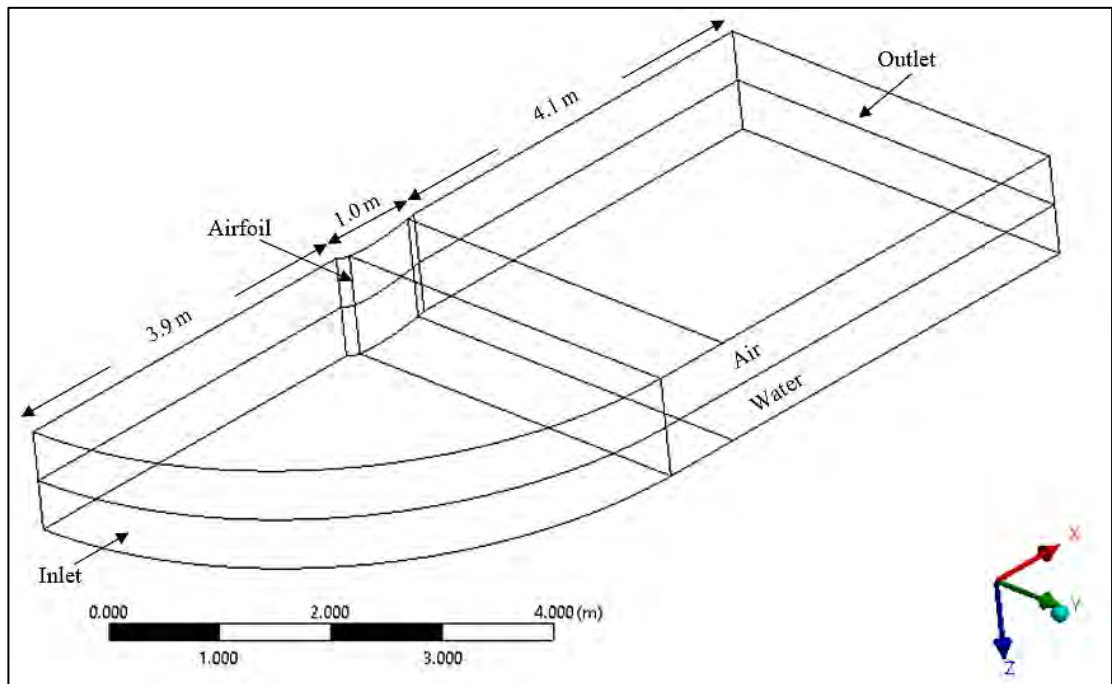


Figure 3.2.3: Geometry for surface piercing body with NACA 0018 airfoil section

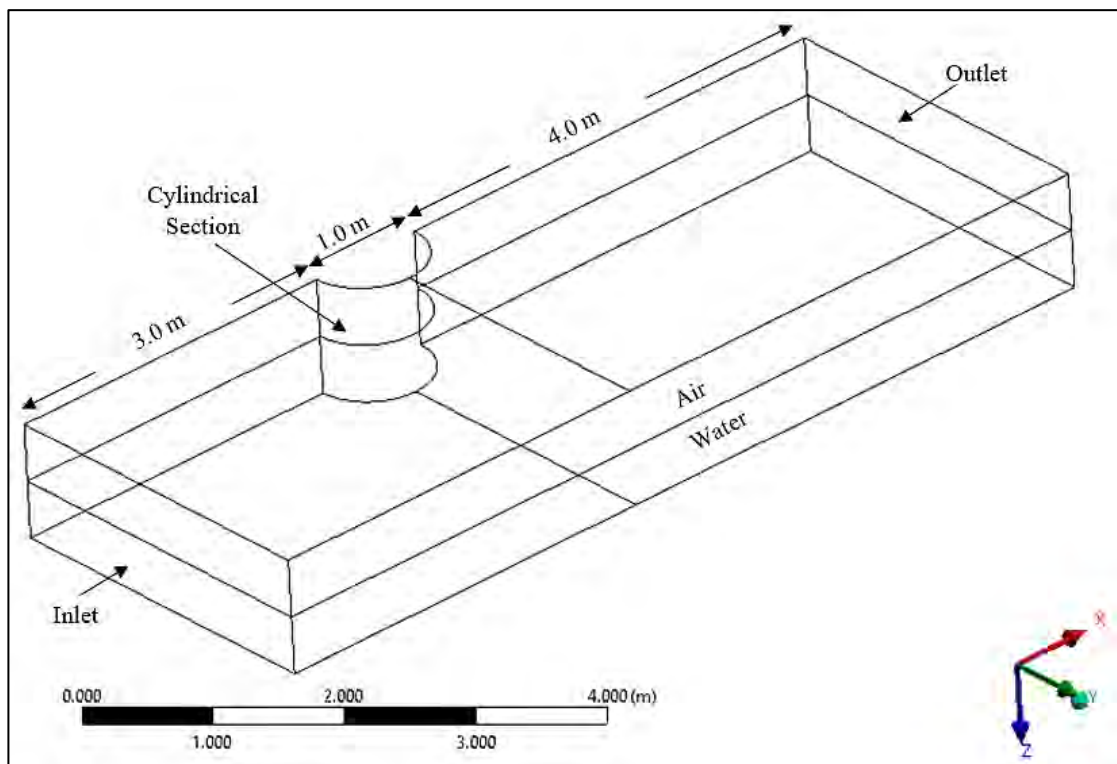


Figure 3.2.4: Geometry for surface piercing body with cylindrical cross – section

The fifth case has been studied with a surface piercing body having elliptical cross – section. This surface piercing body has a major axis of 1.0 m, a minor axis of 0.75 m and a height of 1.0 m (50% in water). The body is 3.0 m right from the inlet boundary and 4.0 m left from the outlet boundary.

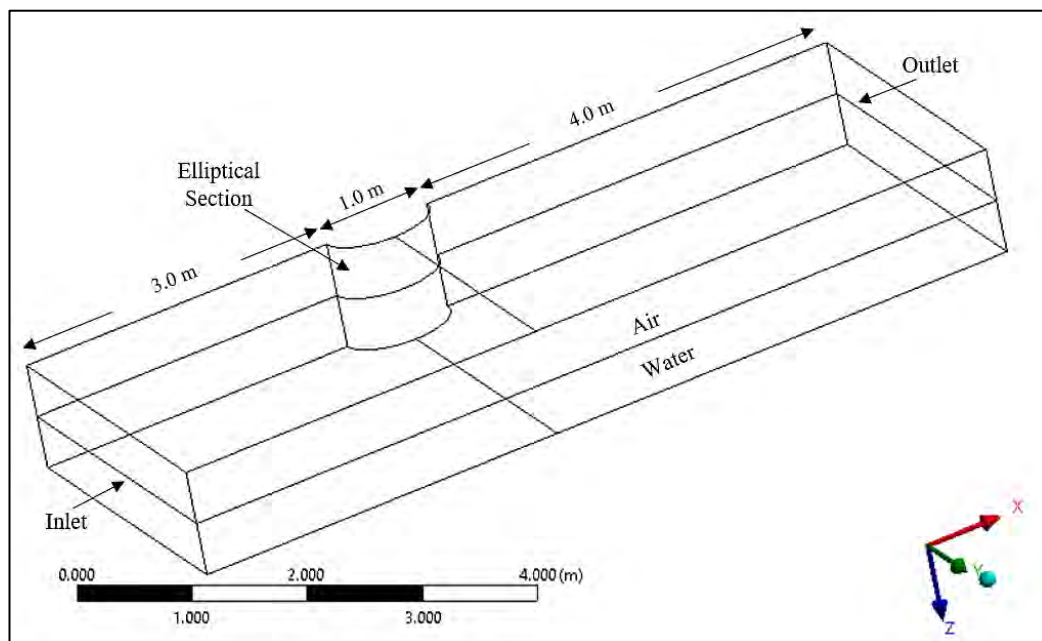


Figure 3.2.5: Geometry for surface piercing body with elliptical cross – section

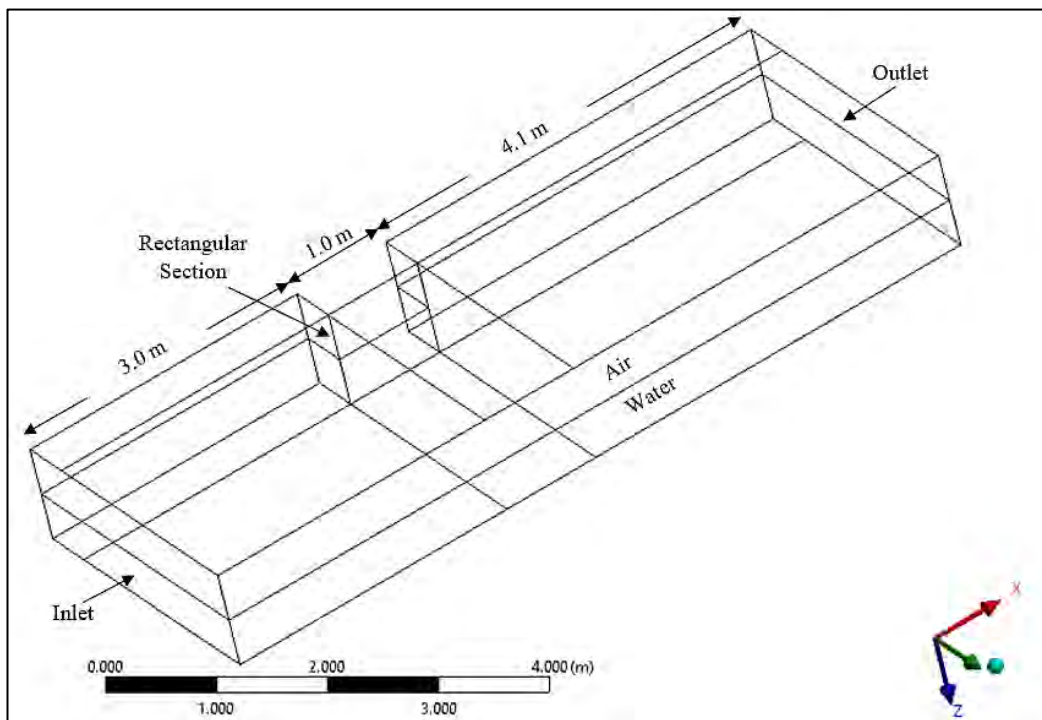


Figure 3.2.6: Geometry for surface piercing body with rectangular cross – section

The final case is a surface piercing body with a rectangular cross – section of length 1.0 m, width 1.0 m and height 1.0 m (50% in water). The surface piercing body is 3.0 m right from the inlet boundary and 4.10 m left from the outlet boundary.

Overall design of the computational domain is carried out using ANSYS Workbench. The second and third case have been performed to evaluate the thickness effects on the free surface wave and wave induced separation whereas the last three cases have been studied to analyze the shape effects on the free surface wave and wave induced separation.

3.2 Grid Generation

A grid is a small-sized geometrical shape that covers the physical domain, whose objective is to identify the discrete volumes or elements where conservation laws can be applied. Grid generation is the first process involved in computing numerical solutions to the equations that describe a physical process. The result of the solution depends upon the quality of grid. A well-constructed grid can improve the quality of solution whereas, deviations from the numerical solution can be observed with poorly constructed grid. Techniques for creating the cell forms the basis of grid generation.

The structured grid has adopted to develop the domain around the surface piercing rudder with NACA 0024 airfoil section containing 343356 nodes and 325500 hexahedral structured cells. The domain is also structured for the surface piercing bodies with NACA 0012 and 0018 airfoil cross – sectional each with 343356 nodes and 325500 hexahedral structured cells. Fine grids are used near the body and the free-surface whereas the rest of the domain is coarse.

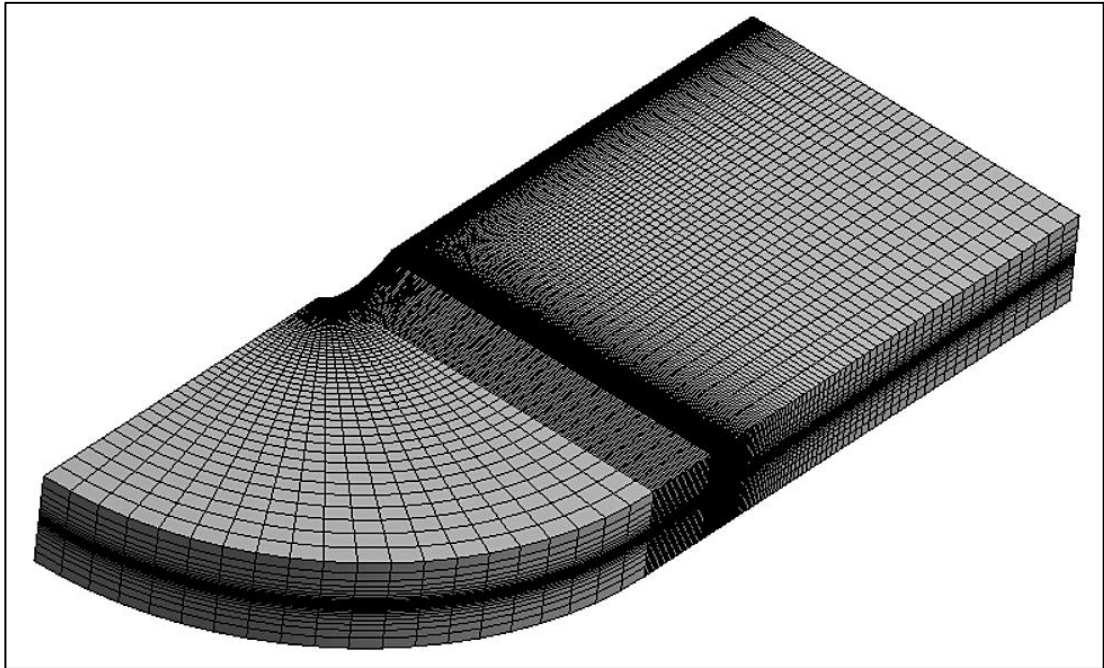


Figure 3.3.1: 3D grid generation for surface piercing body with NACA 0024 airfoil section

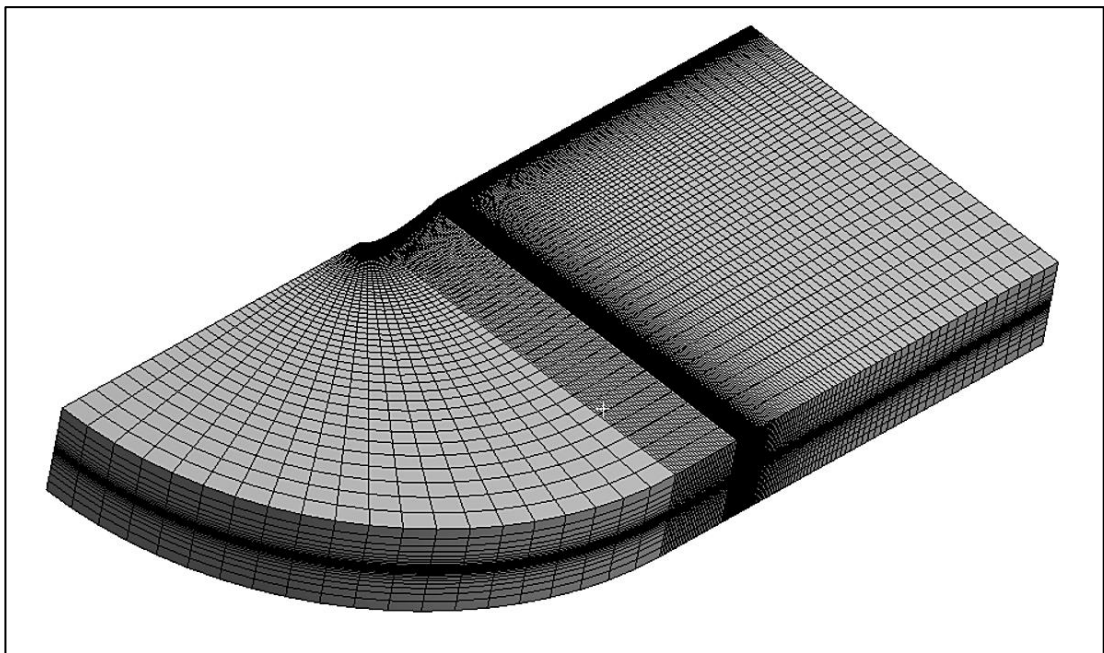


Figure 3.3.2: 3D grid generation for surface piercing body with NACA 0012 airfoil section

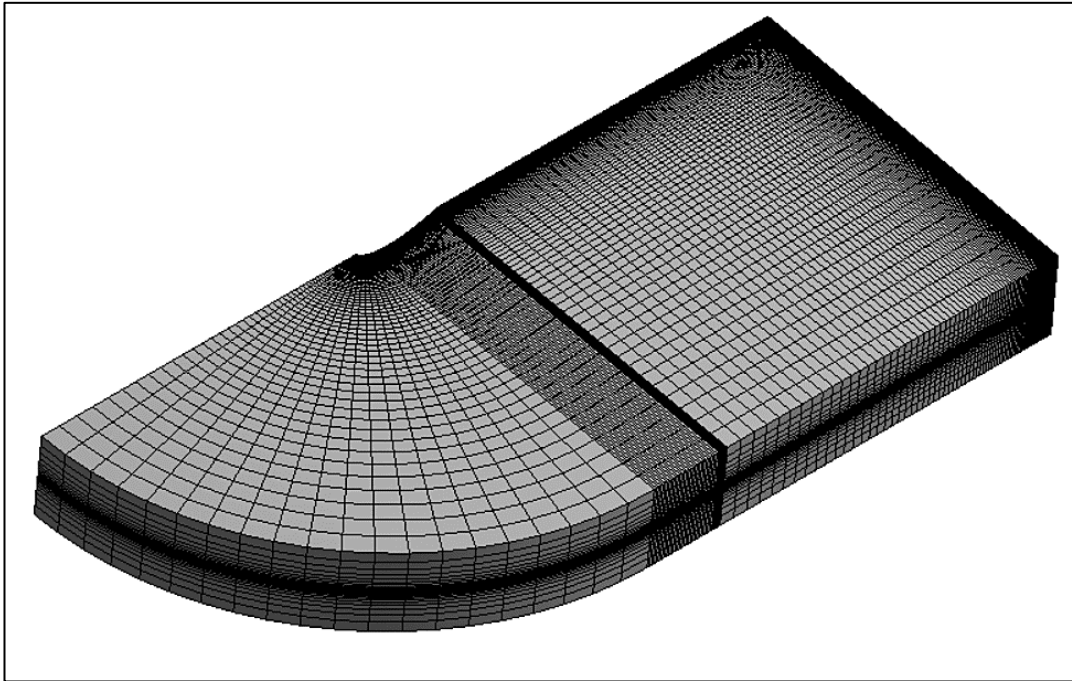


Figure 3.3.3: 3D grid generation for surface piercing body with NACA 0018 airfoil section

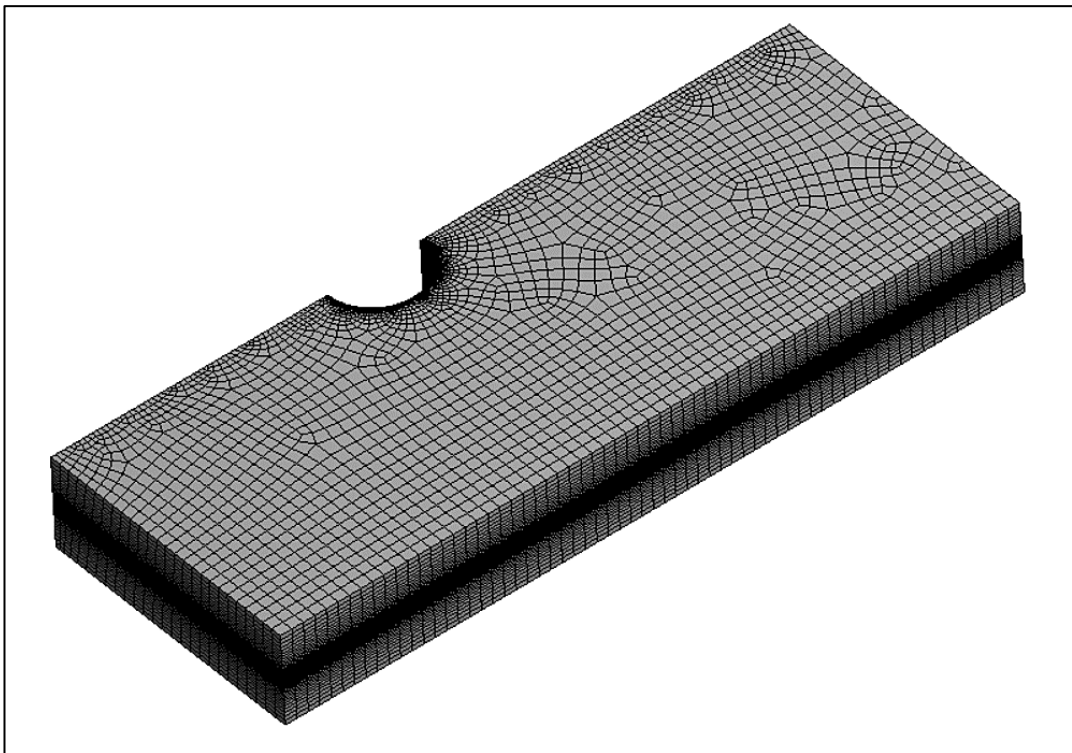


Figure 3.3.4: 3D grid generation for surface piercing body with cylindrical cross – section

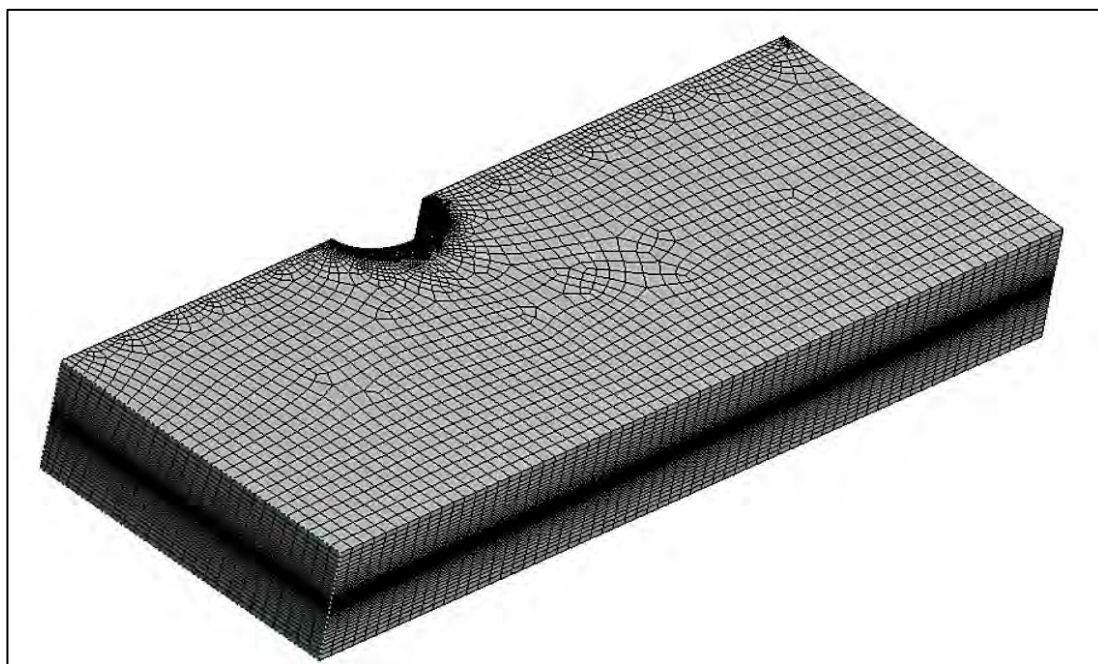


Figure 3.3.5: 3D grid generation for surface piercing body with elliptical cross – section

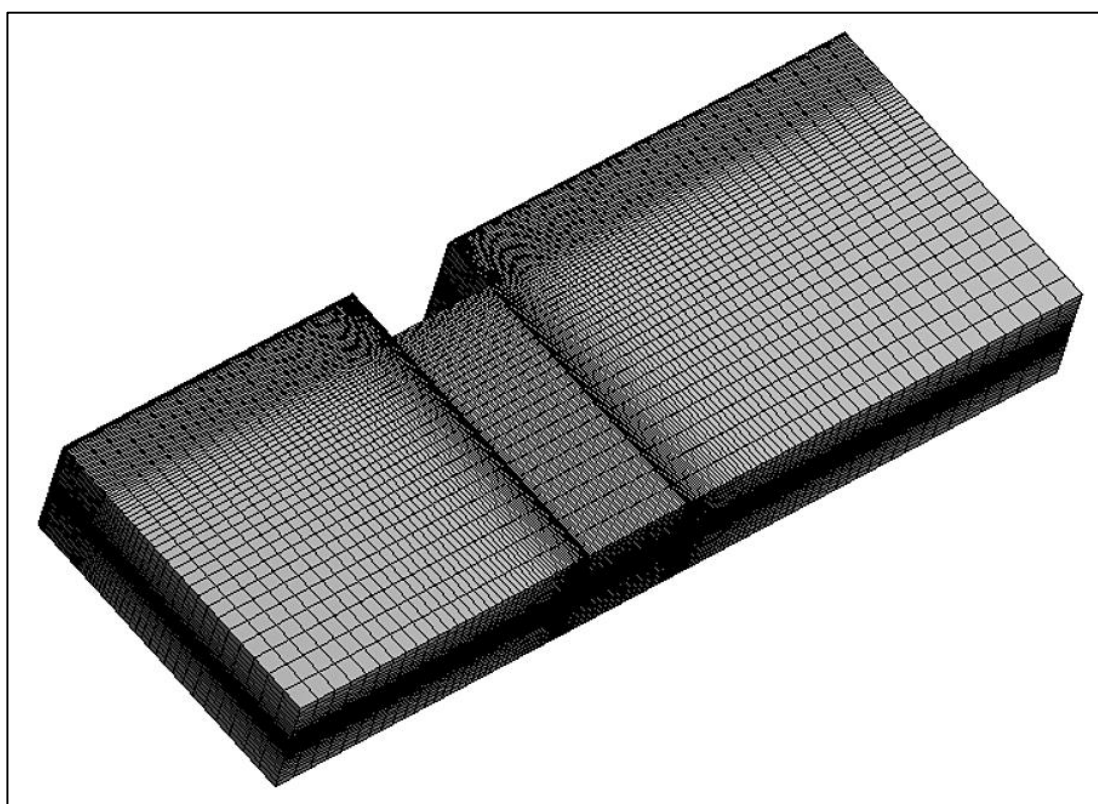


Figure 3.3.6: 3D grid generation for surface piercing body with rectangular cross – section

The domain of the surface piercing body with cylindrical cross – section is unstructured with 203031 nodes and 188500 unstructured cells. Like circular cylinder section, the surface piercing body with elliptical cross – section has as unstructured domain with 213690 nodes and 198650 unstructured cells. A structured grid system is adopted for surface piercing body with rectangular cross – section is structured with 314675 nodes and 297600 hexahedral structured cells.

3.3 Simulation Using ANSYS Fluent

Fluent uses a finite volume – based algorithm to transform the governing physical equations to algebraic equations that can be solved numerically (Fluent, 2015). In such an approach, the computational domain is subdivided into individual, discrete volume, or cells. The governing equations about each cell are then integrated, yielding discrete equations that conserve each quantity on a control – volume basis. Let us consider the following steady – state conservation equation for transport of a scalar φ written in integral form for an arbitrary control volume V :

$$\int \rho \varphi \bar{v} \cdot d\bar{A} = \int \Gamma_{\varphi} \bar{\nabla} \varphi \cdot d\bar{A} + \int S_{\varphi} dV \dots\dots\dots (3.1)$$

where ρ is the density, v is the velocity vector $u_i + v_j + w_z$, A is the surface area vector, Γ_{φ} is the diffusion coefficient for φ , $\bar{\nabla} \varphi$ is the gradient of φ and S_{φ} is the source of φ per unit volume.

The equation is applied to each cell in the computational domain. Fluent discretizes this integral equation as:

$$\sum_f^{n_f} \bar{v}_f \varphi_f A_f = \sum_f^{n_f} \Gamma_{\varphi} (\bar{\nabla} \varphi)_n A_f + S_{\varphi} \dots\dots\dots (3.2)$$

where n_f is the number of faces enclosing the cell,

\bar{v}_f is the mass flux through the face,

A_f is the area of face,

$(\bar{\nabla}\phi)_n$ is the magnitude of $\bar{\nabla}\phi$ normal to the face f and V is the cell volume.

3.4 Grid Study

After the grids are constructed, the next step is to import them into ANSYS Fluent, the numerical solver. A detailed grid study is carried out for the flow past the surface piercing bodies. This can be done by checking grid size. After checking the quality of the grids using ANSYS Fluent, we get the quality report as:

For surface piercing body with NACA 0012 airfoil section –

- Minimum orthogonal quality = 0.0012389
- Maximum ortho skew = 0.29968
- Maximum aspect ratio = 106.39

For surface piercing body with NACA 0018 airfoil section –

- Minimum orthogonal quality = 0.0012388
- Maximum ortho skew = 0.26639
- Maximum aspect ratio = 106.39

For surface piercing body with NACA 0024 airfoil section –

- Minimum orthogonal quality = 0.0014217
- Maximum ortho skew = 0.21418

- Maximum aspect ratio = 106.39

For surface piercing body with cylindrical cross – section –

- Minimum orthogonal quality = 0.016781
- Maximum ortho skew = 0.64285
- Maximum aspect ratio = 54.484

For surface piercing body with elliptical cross – section –

- Minimum orthogonal quality = 0.051115
- Maximum ortho skew = 0.89563
- Maximum aspect ratio = 37.475

For surface piercing body with rectangular cross – section –

- Minimum orthogonal quality = 0.006841
- Maximum ortho skew = 0.85899
- Maximum aspect ratio = 34.039

From the above quality report, it has been shown that the produced grid for different surface piercing bodies is fine enough to perform the simulation.

CHAPTER 4

Result and Discussion

4.1 Validation

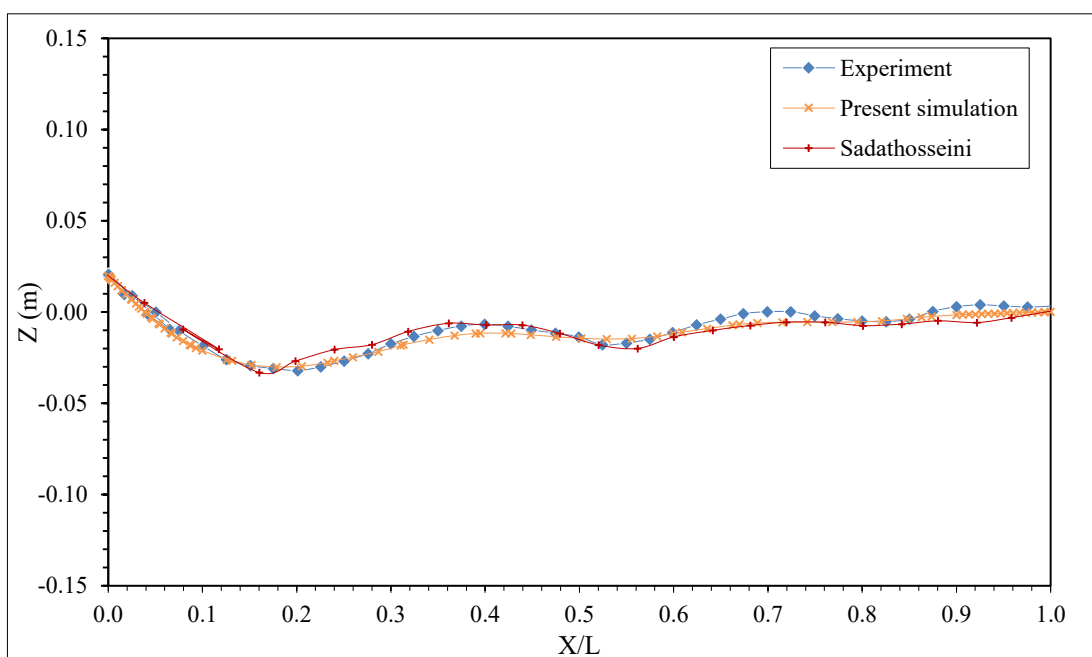


Figure 4.1.1: Wave profile along the NACA 0024 airfoil for $Fr = 0.19$

Figure 4.1.1 shows the wave profile along the NACA 0024 airfoil section for $Fr = 0.19$ and validates with Zhang and Stern experimental data and Sadathosseini numerical result. The wave pattern in this case agrees with both the experimental and numerical results showing that the effect of air is negligible for lower Froude number. The wave length is slightly greater than the Kelvin wave length and the wave pattern is linear in the separation region from $x/L = 0.40$ to $x/L = 1.00$. The bow wave peak is at about 2.0% of chord length, L .

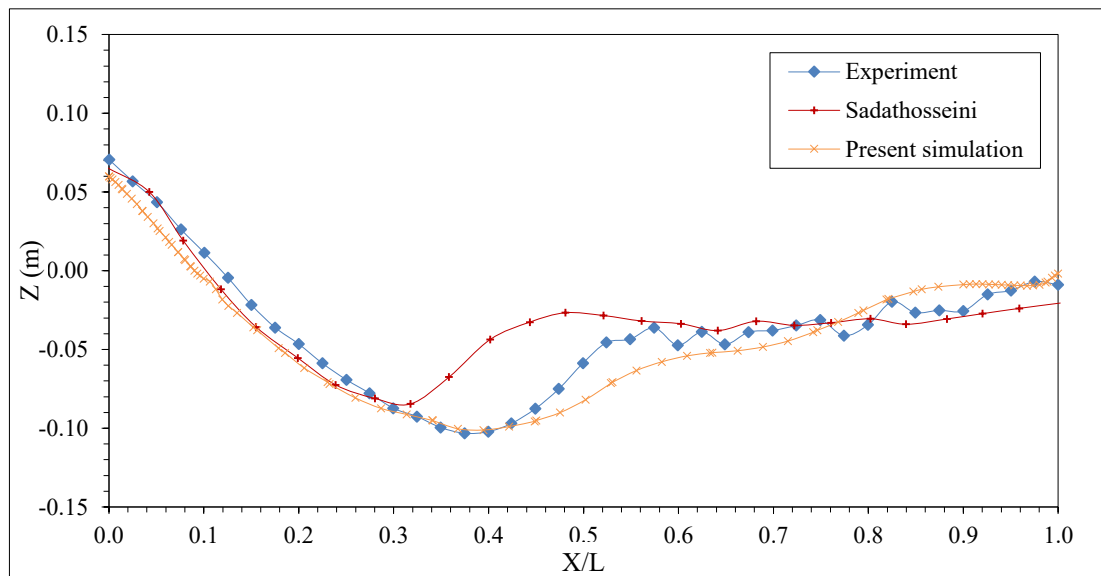


Figure 4.1.2: Wave profile along the NACA 0024 airfoil for $Fr = 0.37$

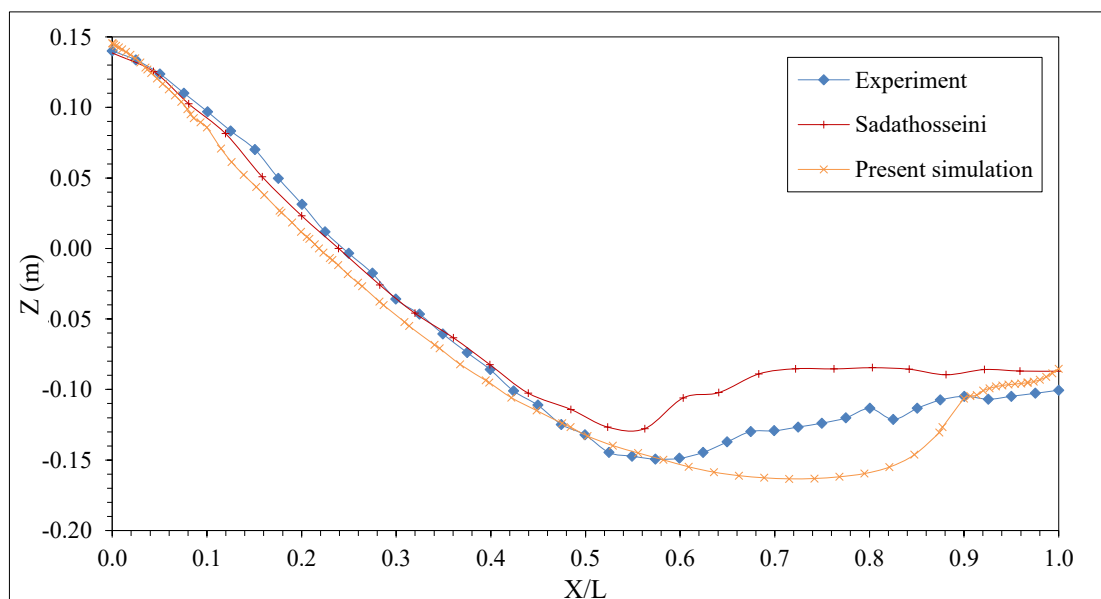


Figure 4.1.3: Wave profile along the NACA 0024 airfoil for $Fr = 0.55$

Figure 4.1.2 and 4.1.3 show the wave profile for $Fr = 0.37$ and $Fr = 0.55$ along NACA 0024 airfoil sections respectively. The results agree with the experimental and numerical data. The wave steepness, wave height, and the distortion in the separation region at $Fr = 0.55$ are larger than those at $Fr = 0.19$ and the free surface effects dominate the wave profile. The free-surface elevation increases. The bow wave peak for $Fr = 0.37$ and $Fr = 0.55$ are at about 6% and 14.5% of L respectively.

4.2 Wave Profile for Different Surface Piercing Body

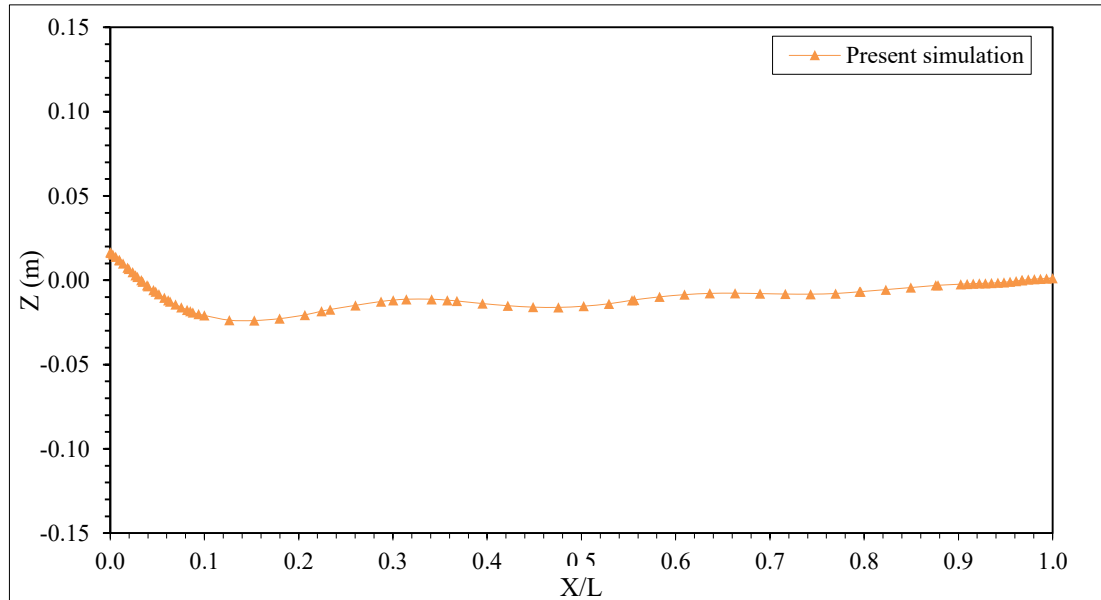


Figure 4.2.1: Wave profile along the NACA 0012 airfoil for $Fr = 0.19$ ($t = 8.2s$)

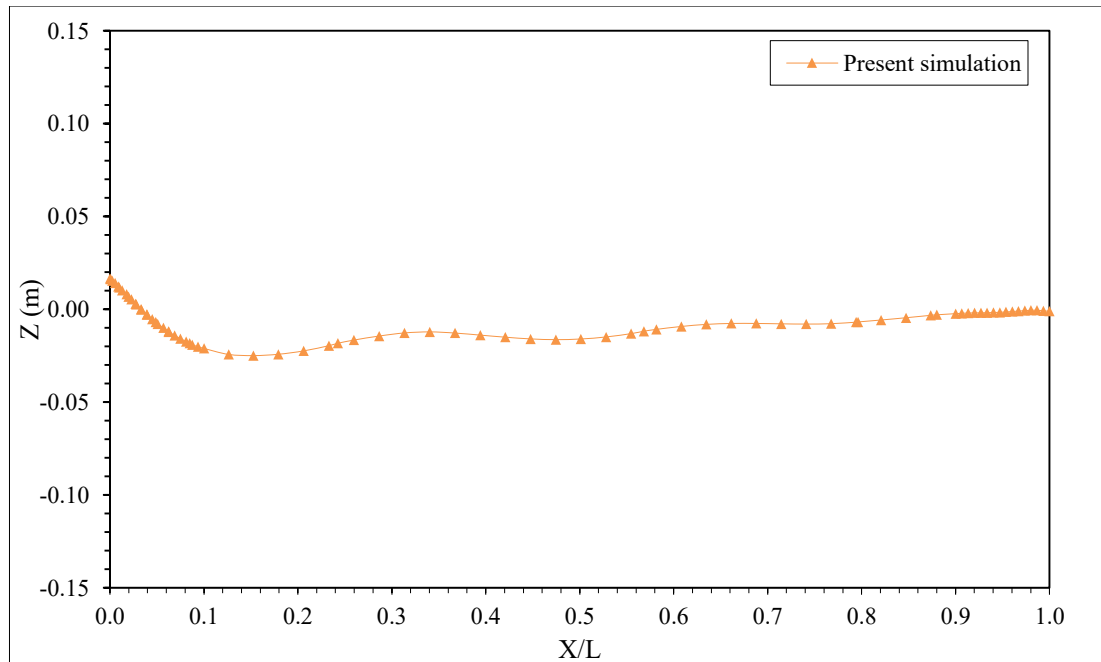


Figure 4.2.2: Wave profile along the NACA 0018 airfoil for $Fr = 0.19$ ($t = 3.3s$)

Figure 4.2.1 represents the wave profile along NACA 0012 airfoil section for $Fr = 0.19$. The wave pattern shows no change due to the thickness effect. The wave height,

wave steepness and the distortion in the separation region are all function of Fr . The wave pattern is linear from $x/L = 0.30$ to $x/L = 1.00$. The bow wave peak is at about 1.7% of L .

Figure 4.2.2 represents the wave elevation along NACA 0018 airfoil section for $Fr = 0.19$. The wave pattern is linear from $x/L = 0.35$ to $x/L = 1.00$. The bow wave peak is at about 1.7% of L .

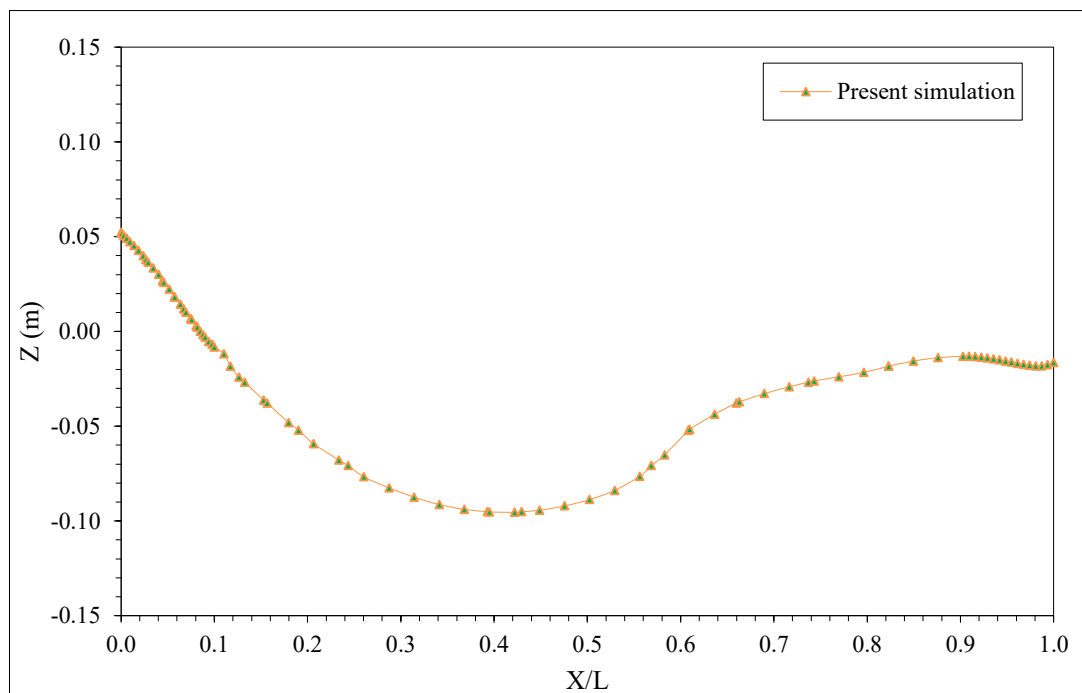


Figure 4.2.3: Wave profile along the NACA 0012 airfoil for $Fr = 0.37$ ($t = 8.2s$)

Figure 4.2.3 and 4.2.4 show the wave profile for $Fr = 0.37$ and $Fr = 0.55$ along NACA 0012 airfoil section respectively. The free-surface elevation is greater at $Fr = 0.37$ and $Fr = 0.55$ than that at $Fr = 0.19$. The wave pattern, i.e. the wave height, wave steepness, and the distortion in the separation region, is affected by strong pressure at stagnation point and increases with higher Froude number. Thus the effects of air become significant. The bow wave peaks for $Fr = 0.37$ and $Fr = 0.55$ are at about 5.2% and 13.9% of L respectively.

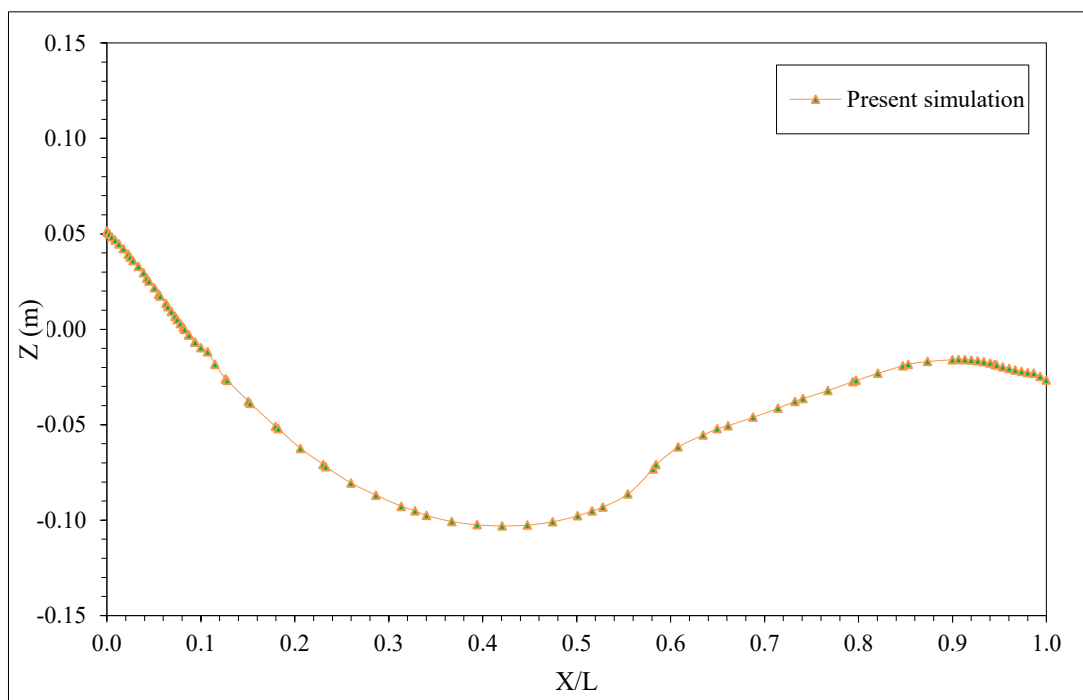


Figure 4.2.4: Wave profile along the NACA 0018 airfoil for $Fr = 0.37$ ($t = 3.3s$)

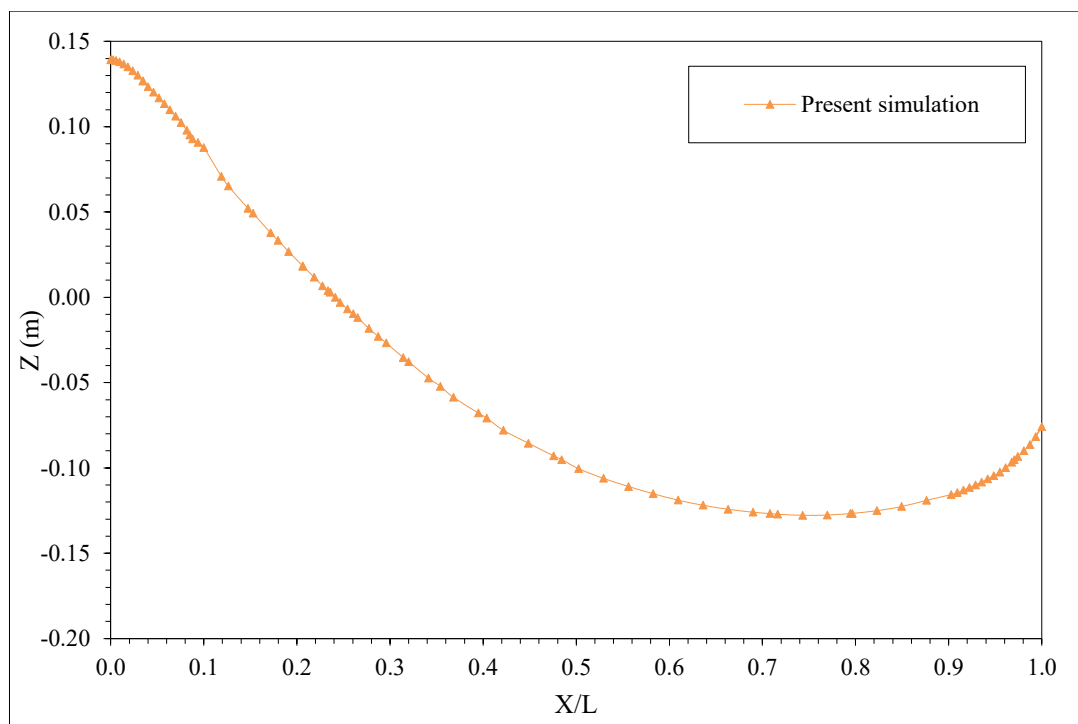


Figure 4.2.5: Wave profile along the NACA 0012 airfoil for $Fr = 0.55$ ($t = 8.2s$)

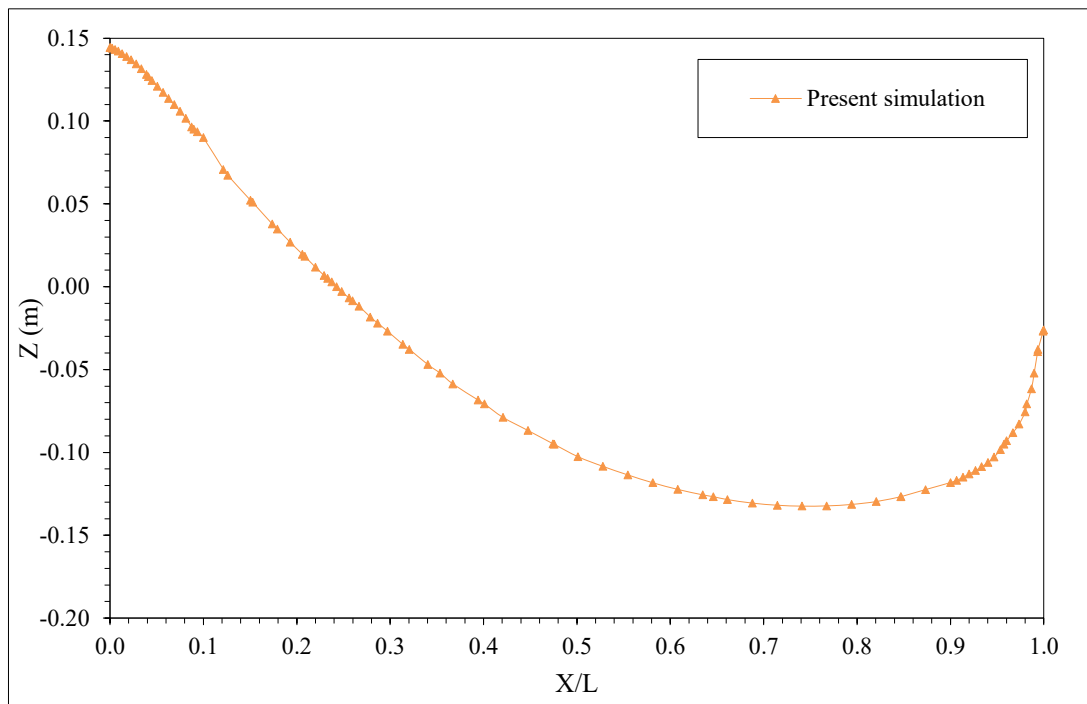


Figure 4.2.6: Wave profile along the NACA 0018 airfoil for $Fr = 0.55$ ($t = 3.3s$)

Figure 4.2.5 and 4.2.6 show the wave profile for $Fr = 0.37$ and $Fr = 0.55$ along NACA 0018 airfoil section respectively. The wave pattern becomes complicated with higher Froude number and the free surface effects dominate the wave profile. The bow wave peak for $Fr = 0.37$ and $Fr = 0.55$ are at about 5.1% and 14.4% of L respectively.

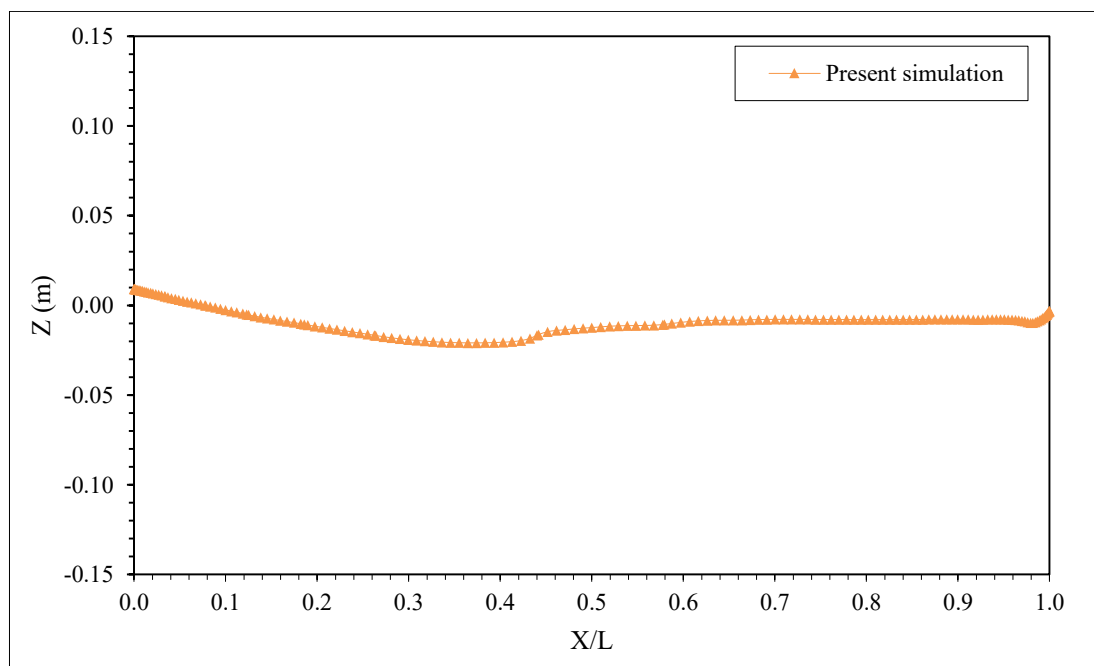


Figure 4.2.7: Wave profile along circular cylinder section at $Fr = 0.19$ ($t = 3.3s$)

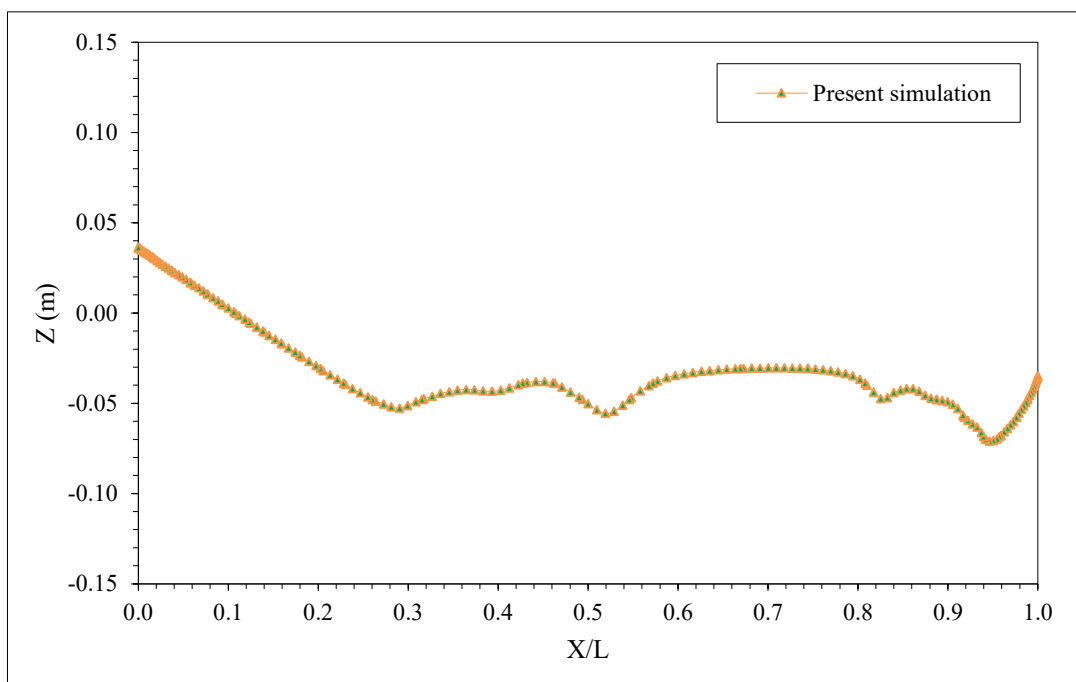


Figure 4.2.8: Wave profile along circular cylinder section at $Fr = 0.37$ ($t = 3.3s$)

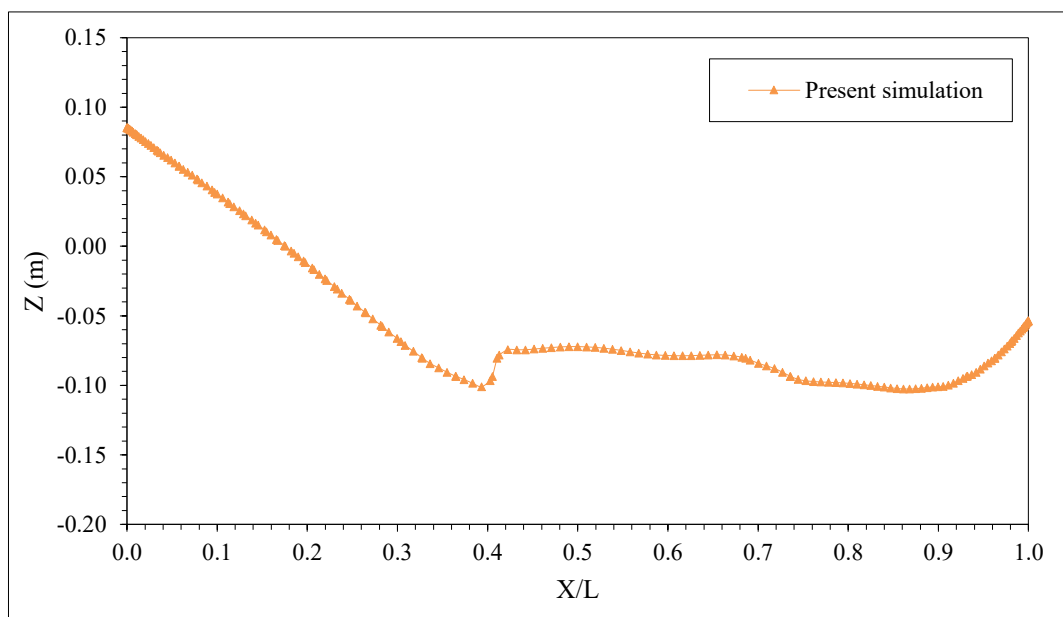


Figure 4.2.9: Wave profile along circular cylinder section at $Fr = 0.55$ ($t = 3.3s$)

Figure 4.2.7, 4.2.8 and 4.2.9 show the wave profiles along circular cylinder section at different Froude numbers. For $Fr = 0.19$, the bow wave peak is at about 0.9% of L . The free-surface elevation is small and the effects of air are negligible. The wave pattern becomes complicated at higher Froude number. The free surface elevation

increases with a constant steepness with the increase in Froude number and depends on Fr but not on shape. The bow wave peaks for $Fr = 0.37$ and $Fr = 0.55$ are at about 3.6% and 8.5% of L respectively.

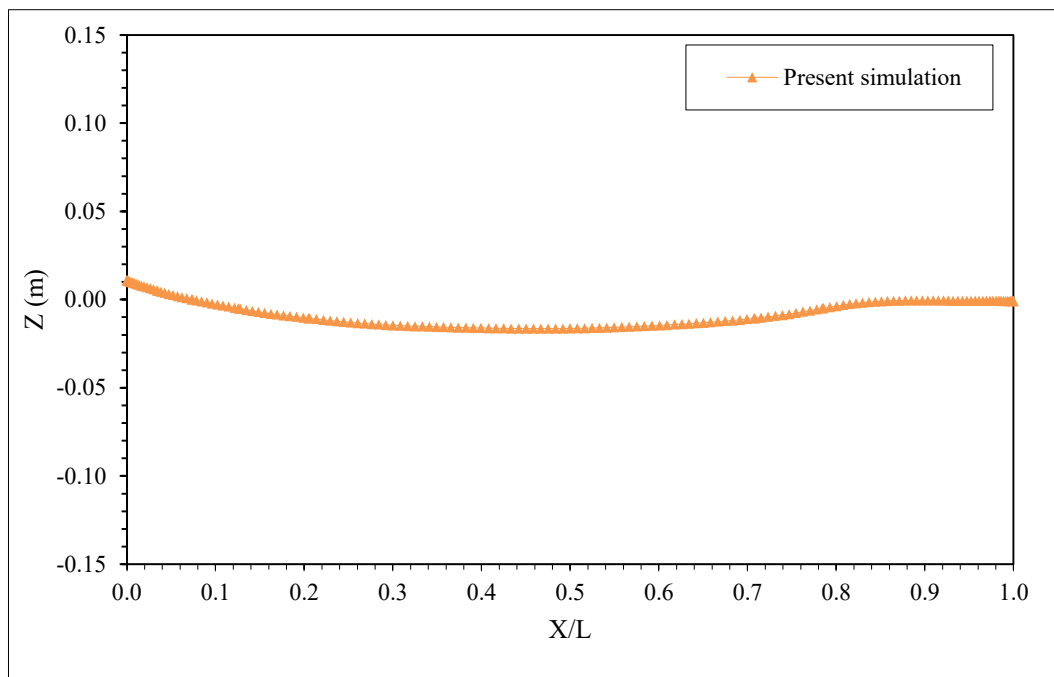


Figure 4.2.10: Wave profile along elliptical section at $Fr = 0.19$ ($t = 3.3s$)

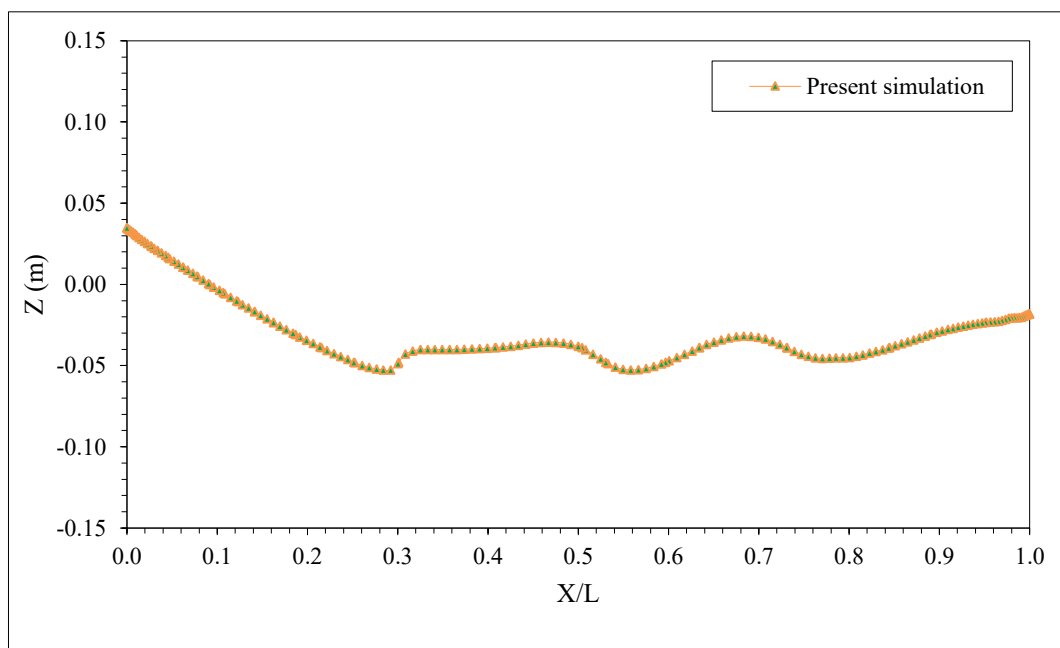


Figure 4.2.11: Wave profile along elliptical section at $Fr = 0.37$ ($t = 3.3s$)

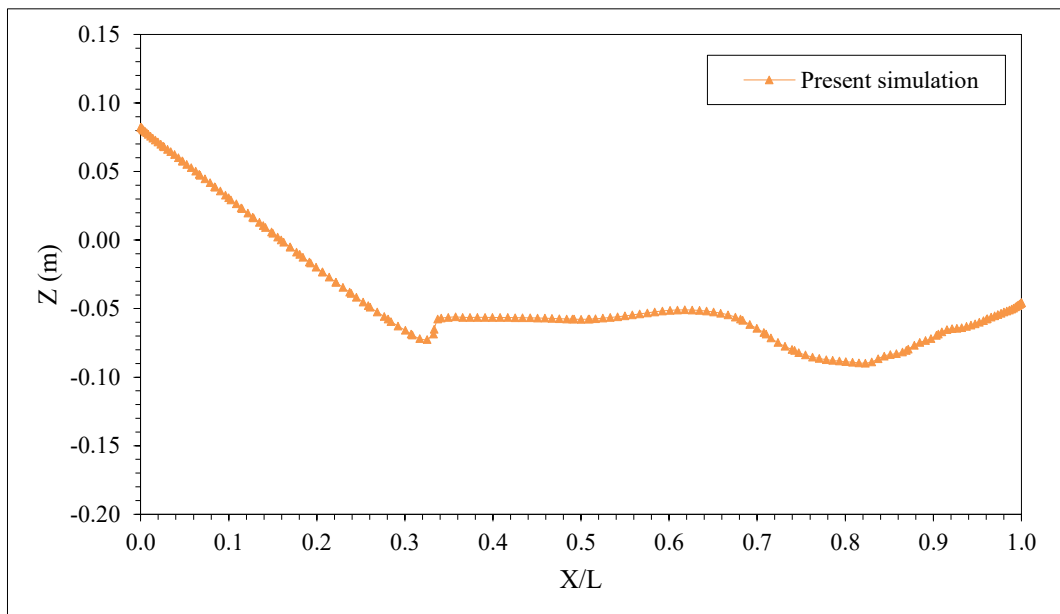


Figure 4.2.12: Wave profile along elliptical section at $Fr = 0.55$ ($t = 3.3s$)

Figure 4.2.10, 4.2.11 and 4.2.12 represent the wave profiles along elliptical section at different Froude numbers. The bow wave peak for $Fr = 0.19$ is at about 1.1% of L and it increases with the increase in Froude number due to the blunt shape of the body. The separation region is linear from $x/L = 0.86$ to $x/L = 1.00$ for $Fr = 0.19$ but it changes abruptly with the increase in Froude number due to the strong pressure distribution.

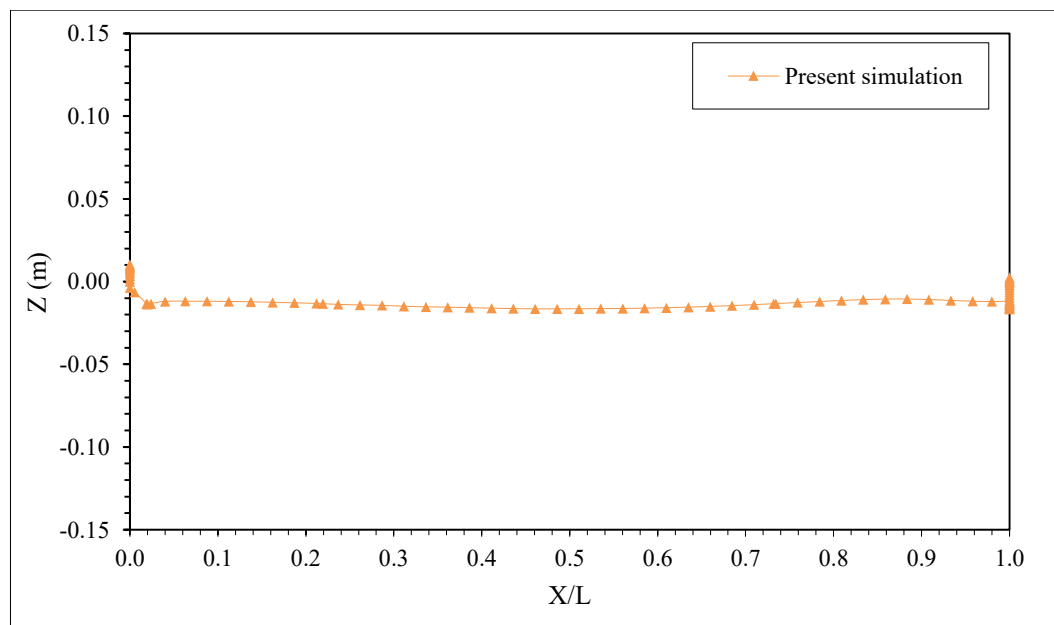


Figure 4.2.13: Wave profile along rectangular section at $Fr = 0.19$ ($t = 3.3s$)

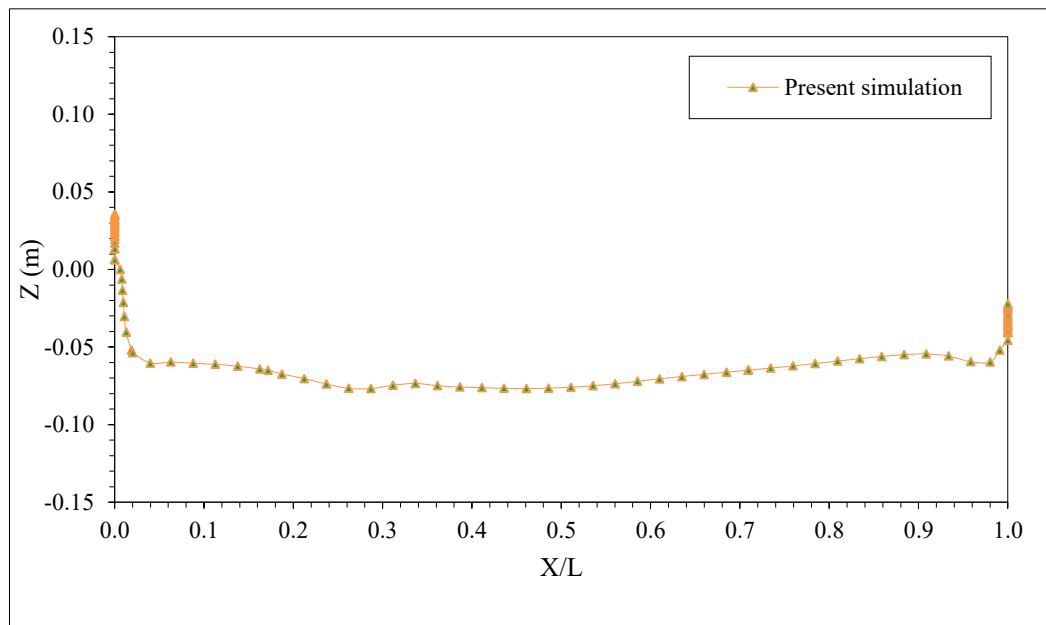


Figure 4.2.14: Wave profile along rectangular section at $Fr = 0.37$ ($t = 3.3s$)

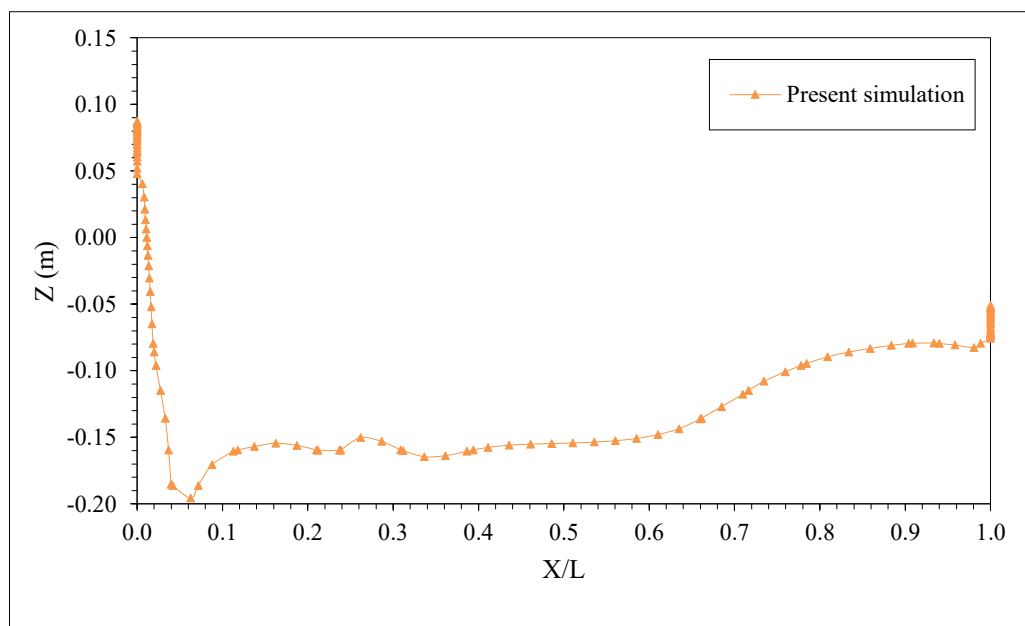


Figure 4.2.15: Wave profile along rectangular section at $Fr = 0.55$ ($t = 3.3s$)

Figure 4.2.13, 4.2.14 and 4.2.15 show the wave profile along rectangular section at different Froude numbers. The separation region is linear from $x/L = 0.03$ to $x/L = 0.95$, but with the increase in Froude number it decreases. For $Fr = 0.37$, the separation region is linear from $x/L = 0.32$ to $x/L = 0.90$. At lower Froude number, the shape of

the body dominates the flow but with the increase in Froude number, the flow becomes dependent on Fr instead of shape.

4.3 Comparison of Wave Profile

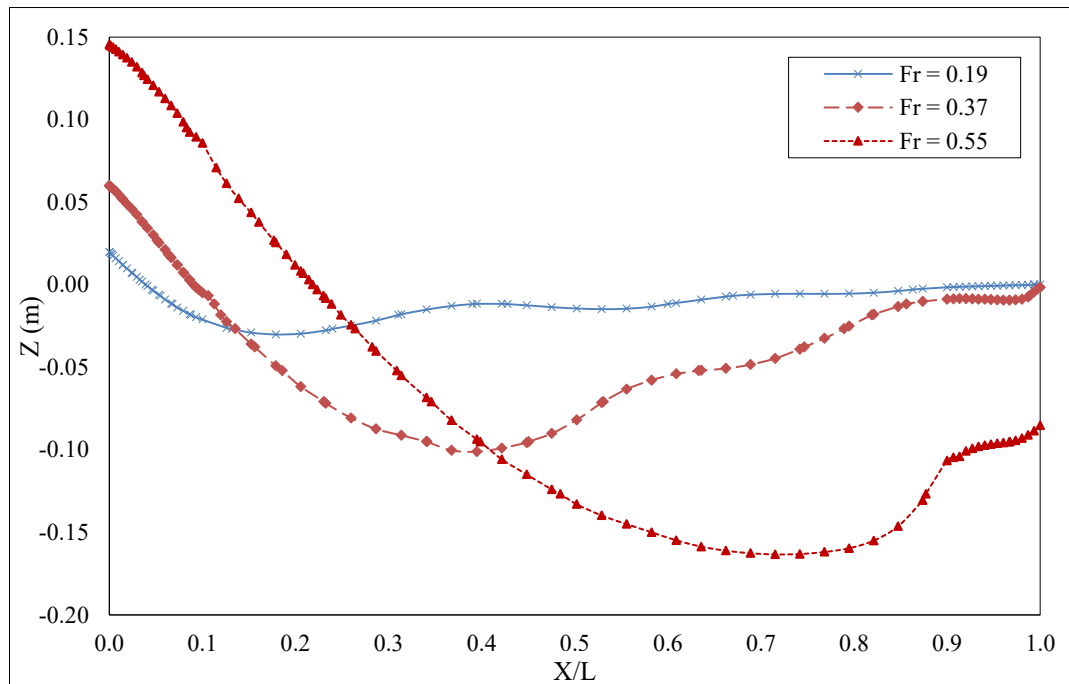


Figure 4.3.1: Comparison of wave profiles along the NACA 0024 airfoil for different Froude numbers

Figure 4.3.1 shows the comparison of wave profiles along the NACA 0024 airfoil section at different Froude numbers. For $Fr = 0.19$, the free-surface elevation is small which shows the insignificance of free surface effects. With the increase in Froude number, the wave-surface elevation increases with a constant steepness and the effects of air dominate the wave profile. The wave pattern becomes more complicated for higher Froude number. The wave profile is negative in the wake section and also behind the separation for $Fr = 0.55$. The wave steepness and the wave height are greater in $Fr = 0.55$ than $Fr = 0.37$.

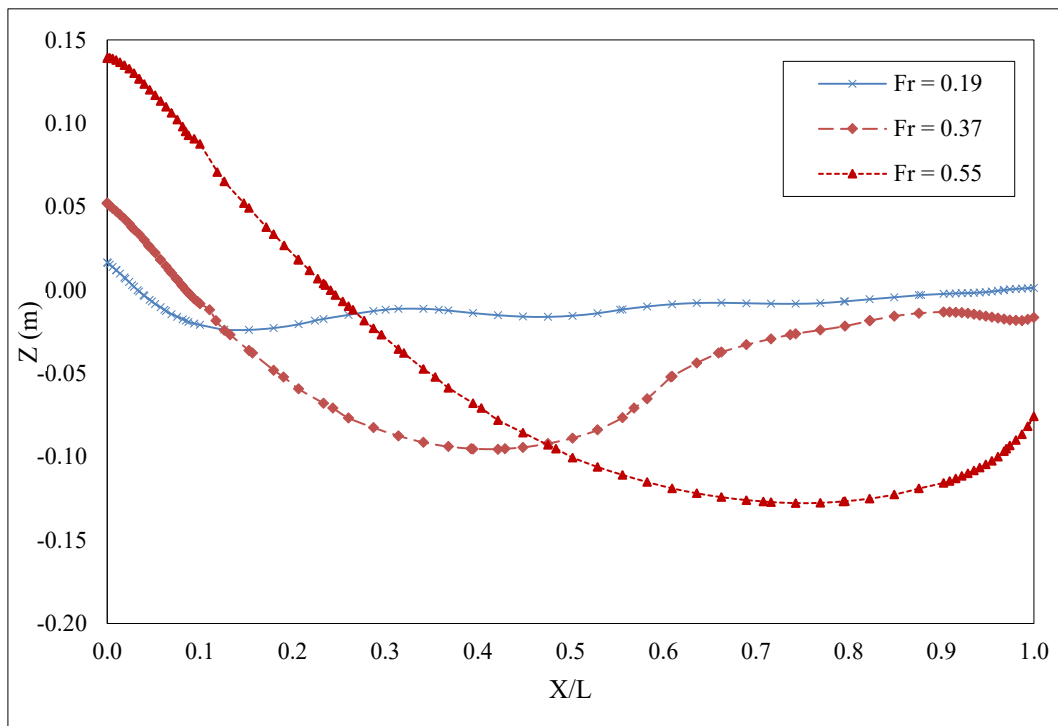


Figure 4.3.2: Comparison of wave profiles along the NACA 0012 airfoil for different Froude numbers

Figure 4.3.2 represents the wave profile for NACA 0012 airfoil section at different Froude numbers. With the increase in Froude number, the strong pressure stagnation point affects the flow and the wave steepness, wave height, free-surface elevations and the distortion in the separation region becomes larger at $Fr = 0.37$ and $Fr = 0.55$. The profile is linear in the separation region for $Fr = 0.37$ but decreases with a constant steepness for $Fr = 0.55$.

Figure 4.3.3 shows the wave profiles for NACA 0018 airfoil section at different Froude numbers. The effects of air are negligible for $Fr = 0.19$, but dominate the wave profile with the increase in Froude number. For $Fr = 0.37$ and $Fr = 0.5$, the free-surface elevation and wave steepness is greater than $Fr = 0.19$. The wave profile is dependent on Fr at higher Froude numbers. The wave pattern is linear from $x/L = 0.35$ to $x/L = 1.00$ and from $x/L = 0.90$ to $x/L = 1.00$ for $Fr = 0.19$ and $Fr = 0.37$ respectively.

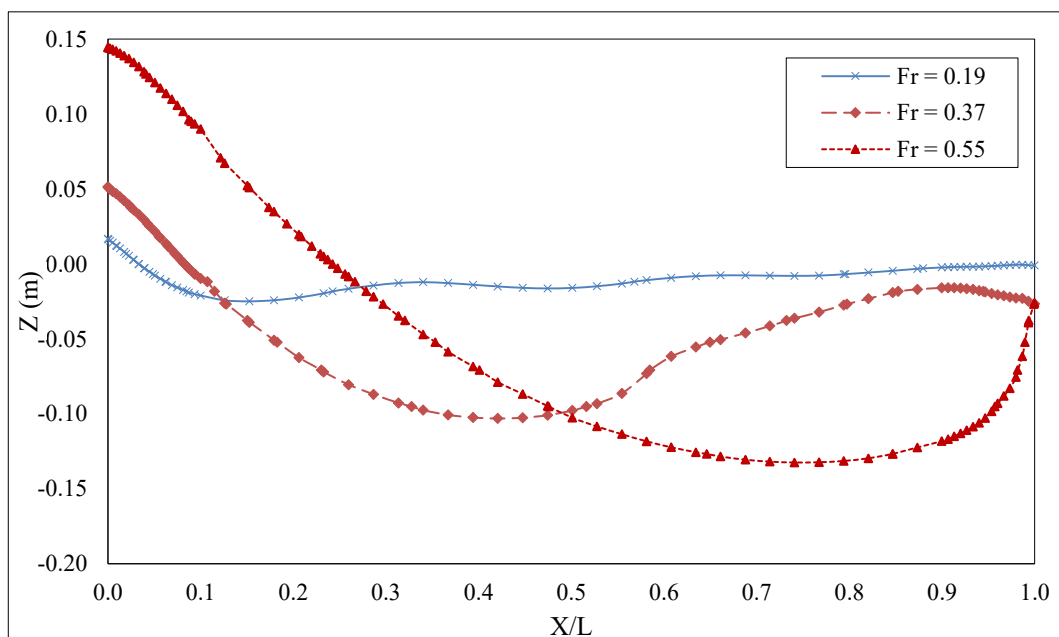


Figure 4.3.3: Comparison of wave profiles along the NACA 0018 airfoil for different Froude numbers

4.4 Comparison of Thickness Effects for Different NACA Airfoil sections

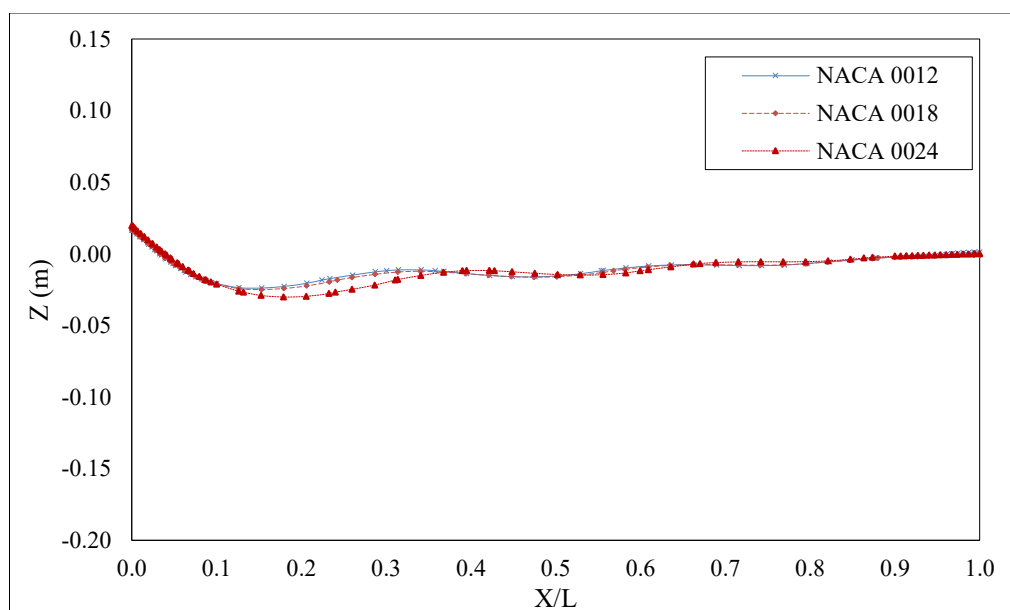


Figure 4.4.1: Comparison of thickness effects for different NACA airfoil sections at $Fr = 0.19$

Figure 4.4.1, 4.4.2, and 4.4.3 show the comparison of the wave profiles along different airfoil sections for different Froude numbers. For $Fr = 0.19$, the free-surface elevation is small and agrees well with the experimental results which shows the insignificance of free surface effects. With the increase in Froude number, the free-surface elevation increases with a constant steepness and the free surface effects dominate the wave profile.

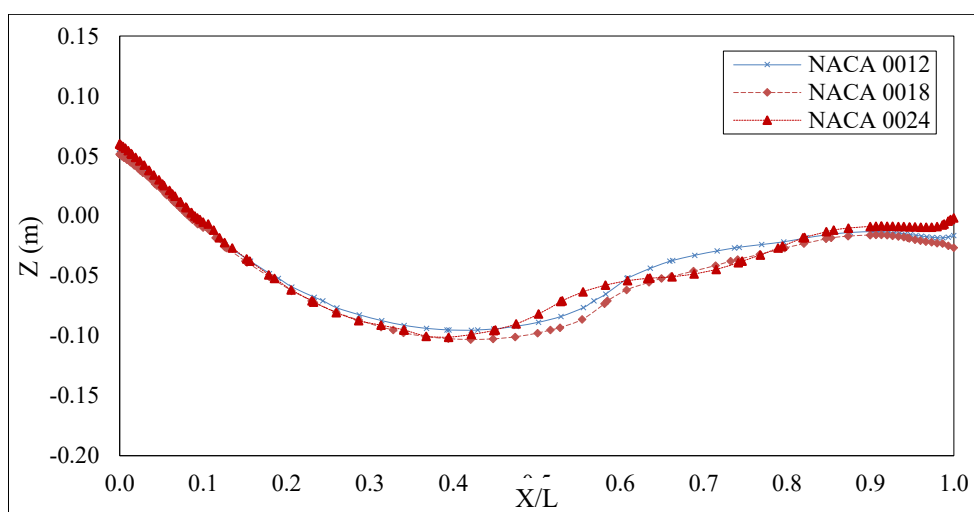


Figure 4.4.2: Comparison of thickness effects for different NACA airfoil sections at $Fr = 0.37$

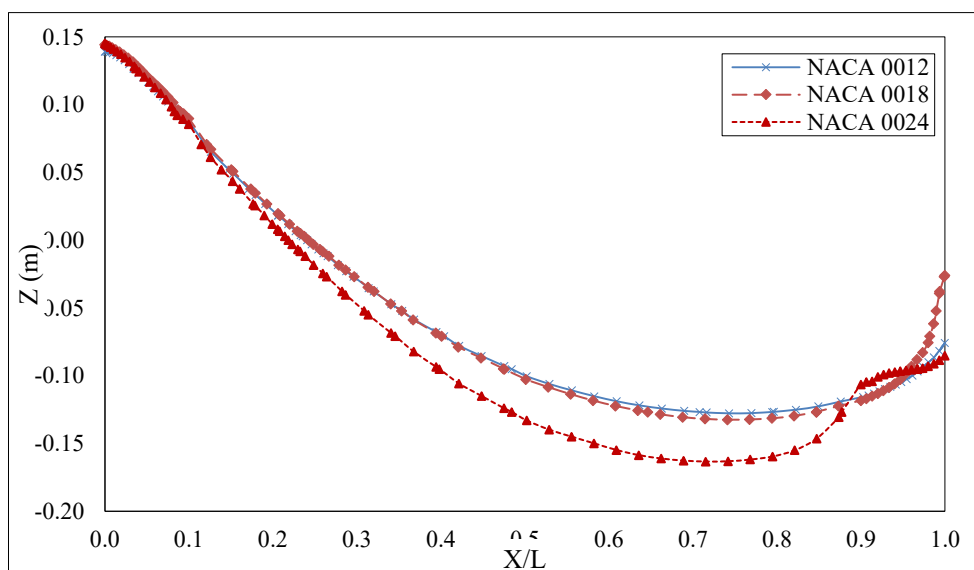


Figure 4.4.3: Comparison of thickness effects for different NACA airfoil sections at $Fr = 0.55$

The wave profile increases and it becomes more complicated for $Fr = 0.55$. The wave profile is negative in the wake section and also behind the separation region for $Fr = 0.55$. The changes in wave height and the distortion in the separation region is greater for $Fr = 0.55$ than those for $Fr = 0.19$ and $Fr = 0.37$ and dependent on Fr instead of thickness.

4.5 Comparison of Shape Effects for Different Sections

Figure 4.5.1, 4.5.2, and 4.5.3 represent the shape effects of different sections for different Froude numbers. For $Fr = 0.19$, the wave pattern is pretty much similar for all sections. For $Fr = 0.37$, the wave patterns, i.e. the wave height, wave steepness and the distortion in the separation region, are dependent on Fr . But for $Fr = 0.55$, the shape effects dominate the wave profile although primarily the wave pattern depends on Fr and the free-surface elevation increases with a constant steepness. The pressure gradients increase with the increase in Froude number.

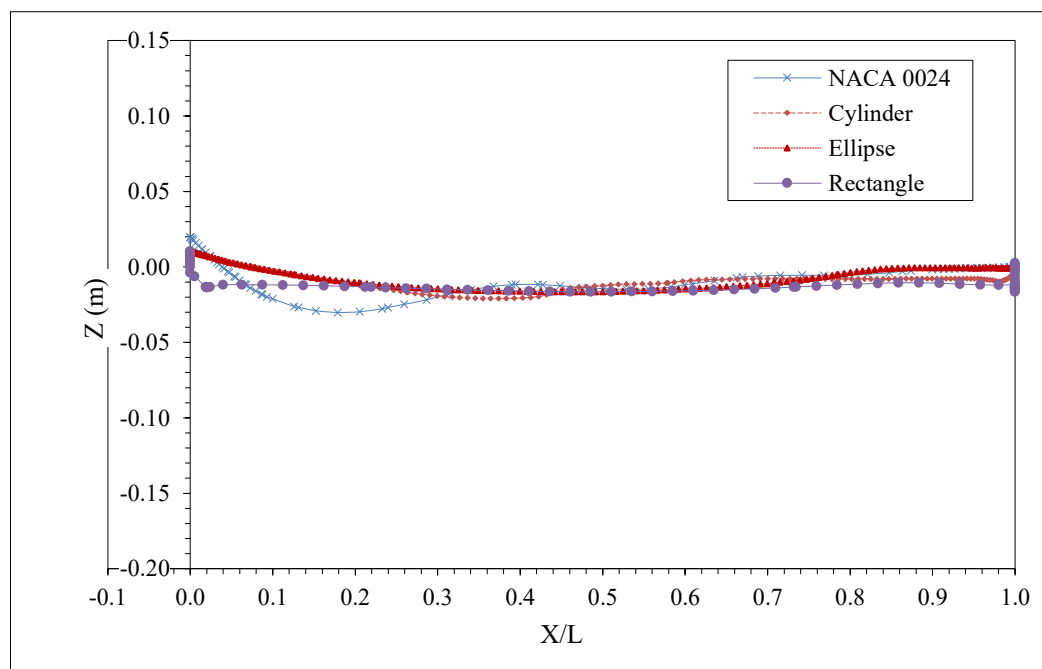


Figure 4.5.1: Comparison of shape effects for different sections at $Fr = 0.19$

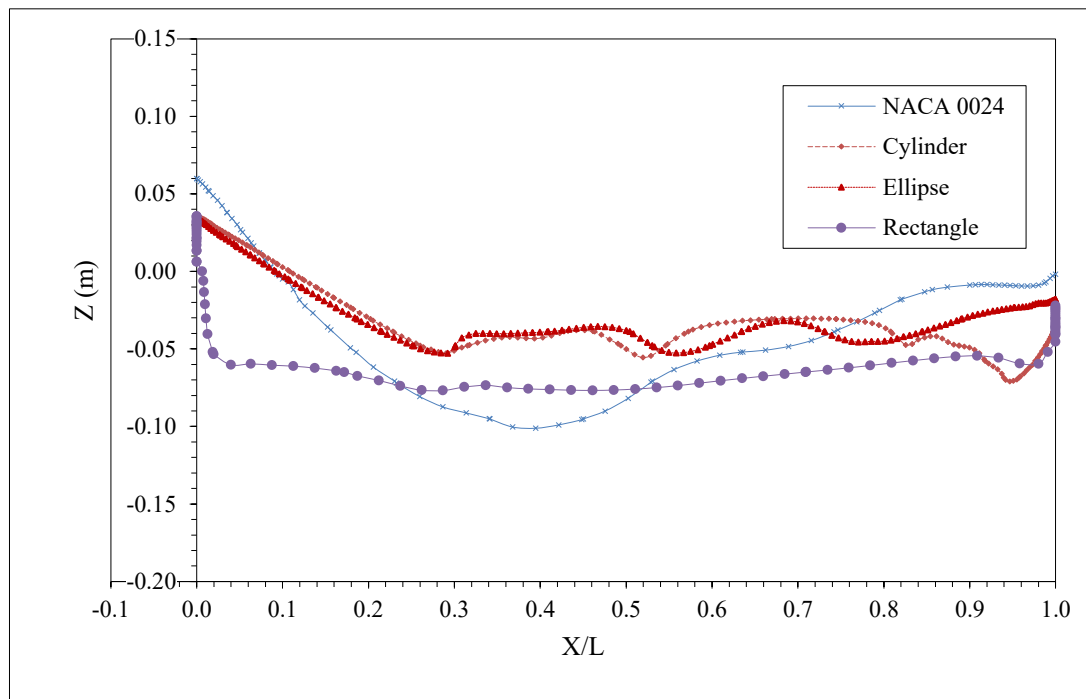


Figure 4.5.2: Comparison of shape effects for different sections at $Fr = 0.37$

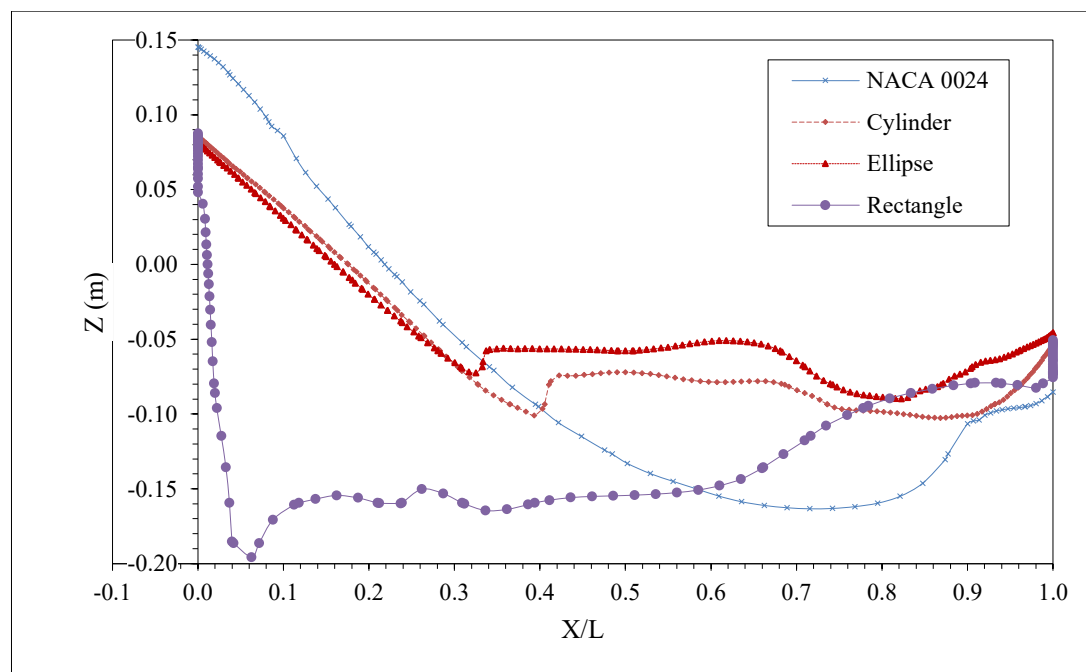


Figure 4.5.3: Comparison of shape effects for different sections at $Fr = 0.55$

4.6 Free Surface Elevation Contour

Figure 4.6.1 – 4.6.18 represent the free surface elevation contour for different surface piercing bodies. It is seen that the pattern is symmetrical about the center line. For lower Froude number the wave profile is almost likely to the kelvin wave. But when the Froude number is increase, the wave profile becomes greater than the kelvin wave profile.

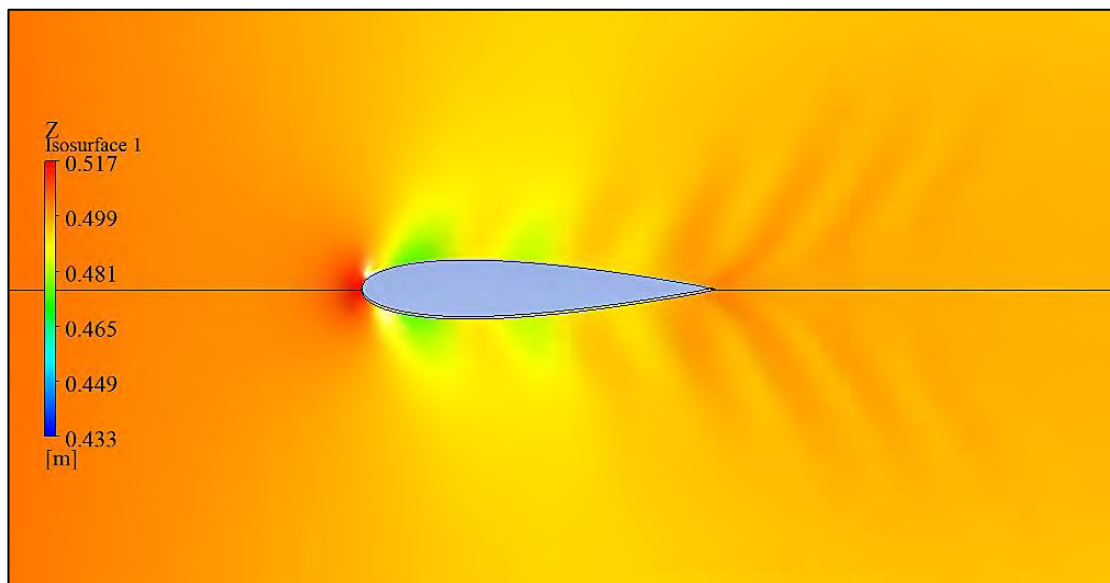


Figure 4.6.1: Free surface elevation contour along NACA 0012 airfoil section with $Fr = 0.19$

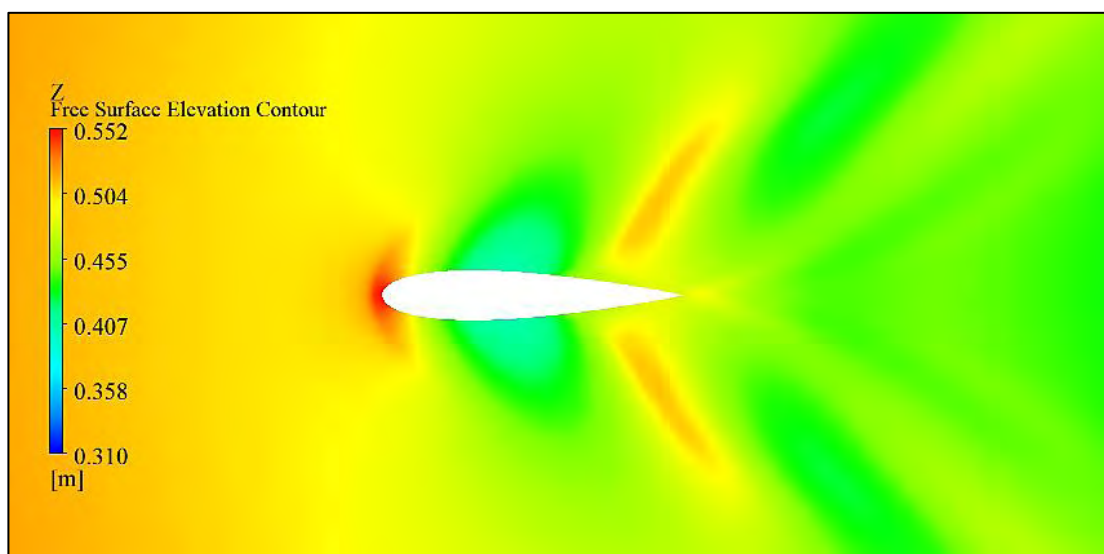


Figure 4.6.2: Free surface elevation contour along NACA 0012 airfoil section with $Fr = 0.37$

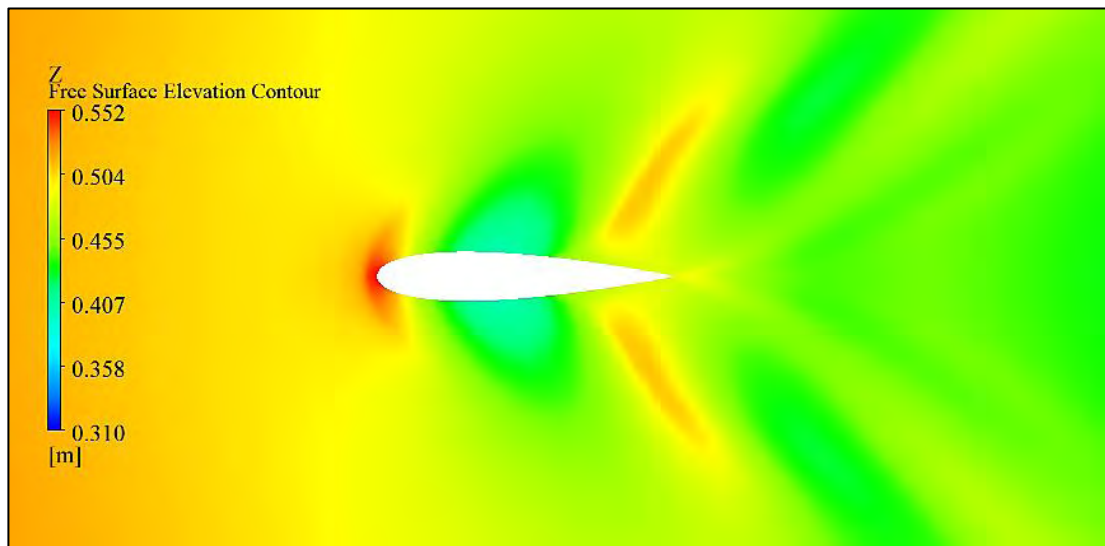


Figure 4.6.3: Free surface elevation contour along NACA 0012 airfoil section with $Fr = 0.55$

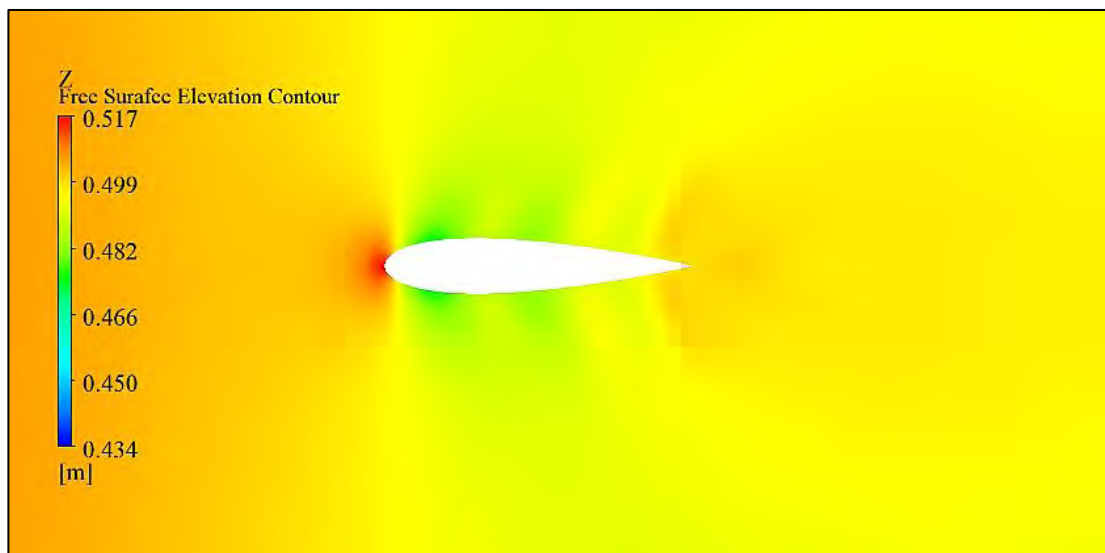


Figure 4.6.4: Free surface elevation contour along NACA 0018 airfoil section with $Fr = 0.19$

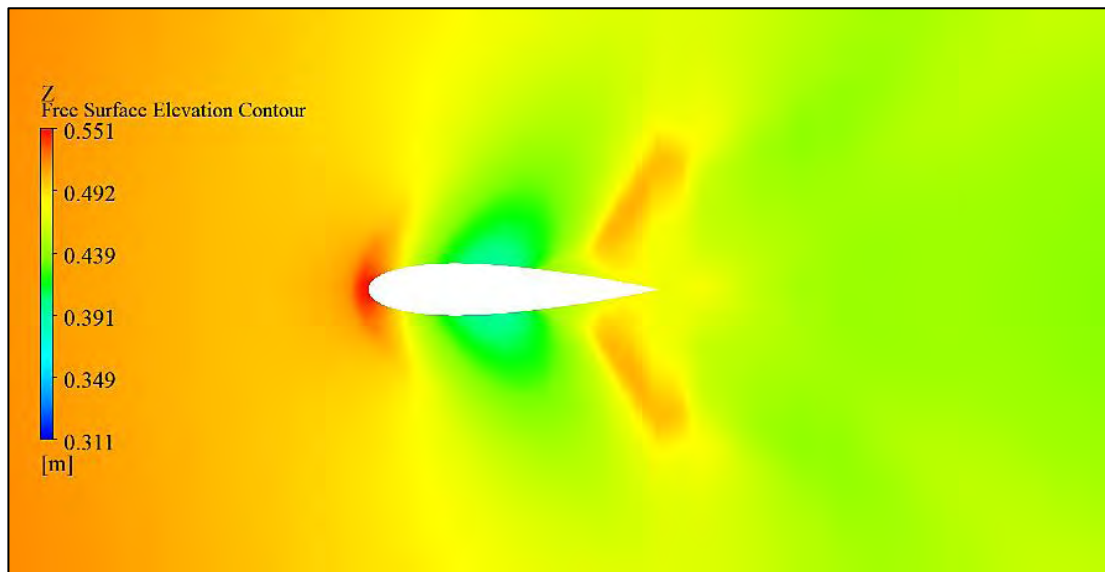


Figure 4.6.5: Free surface elevation contour along NACA 0018 airfoil section with $Fr = 0.37$

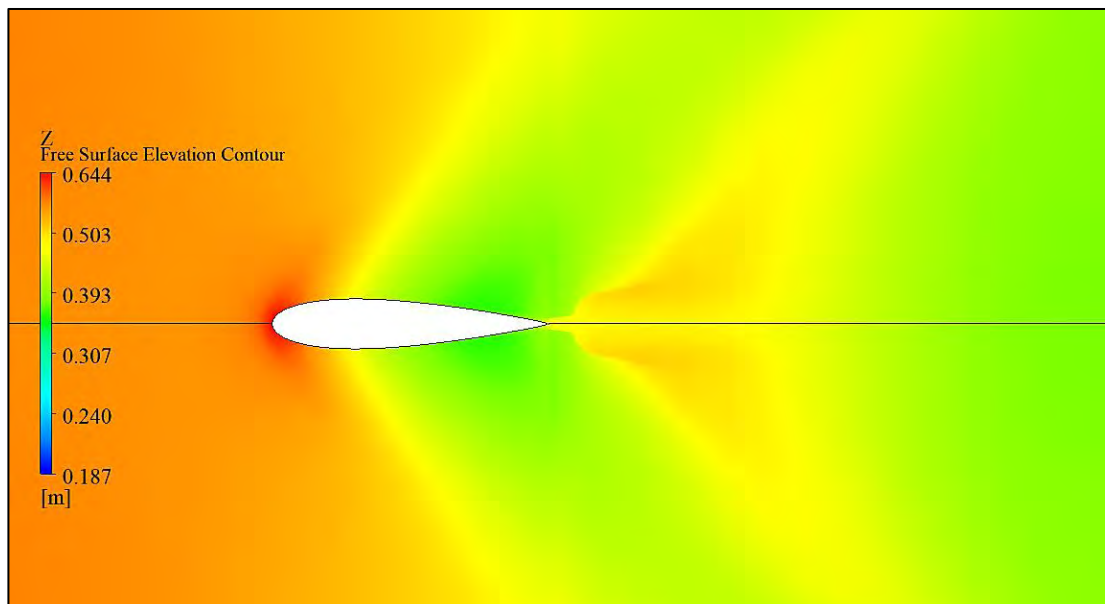


Figure 4.6.6: Free surface elevation contour along NACA 0018 airfoil section with $Fr = 0.55$

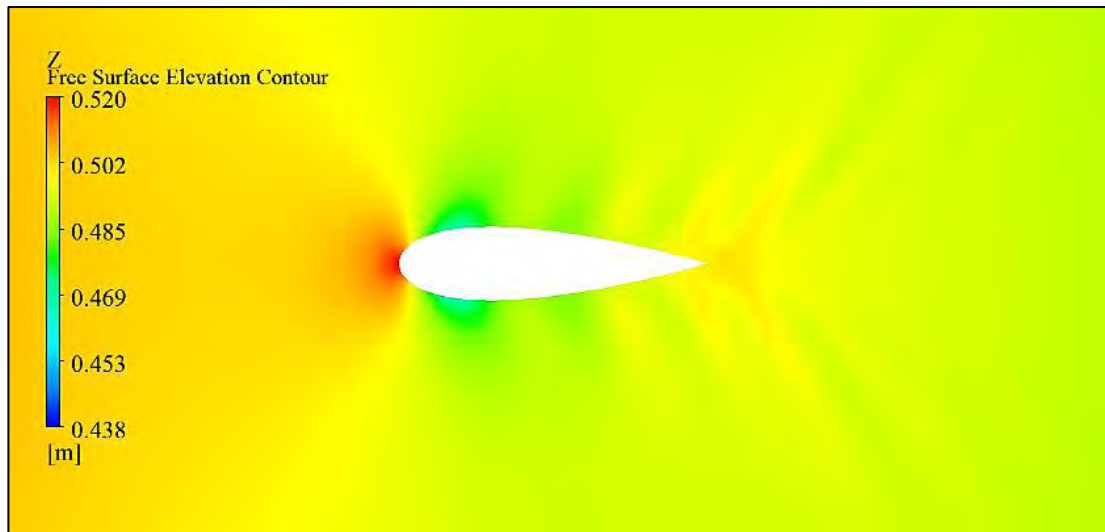


Figure 4.6.7: Free surface elevation contour along NACA 0024 airfoil section with $Fr = 0.19$

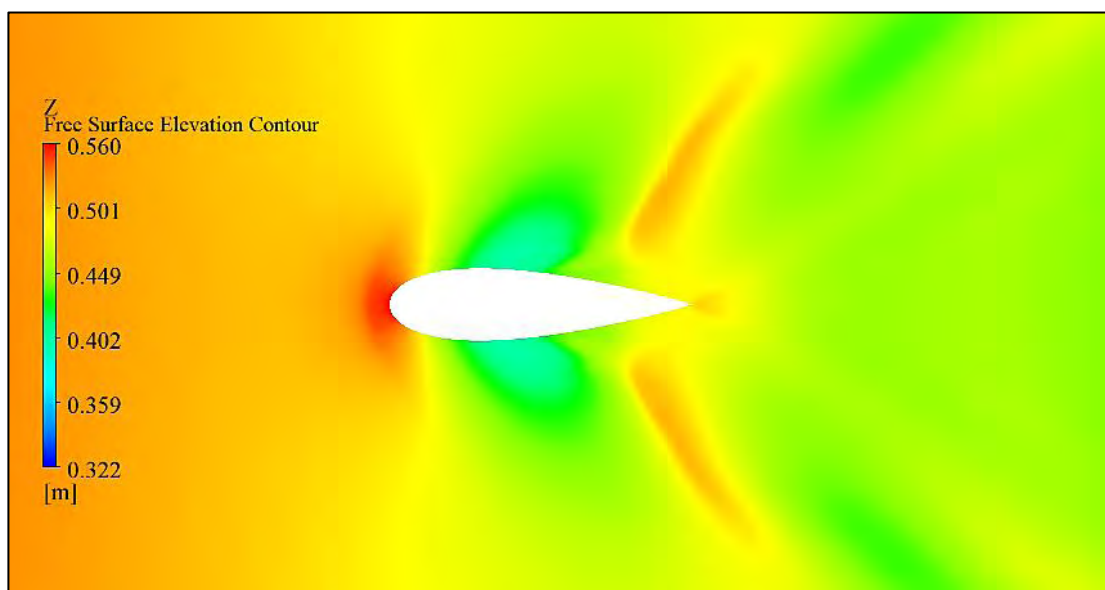


Figure 4.6.8: Free surface elevation contour along NACA 0024 airfoil section with $Fr = 0.37$

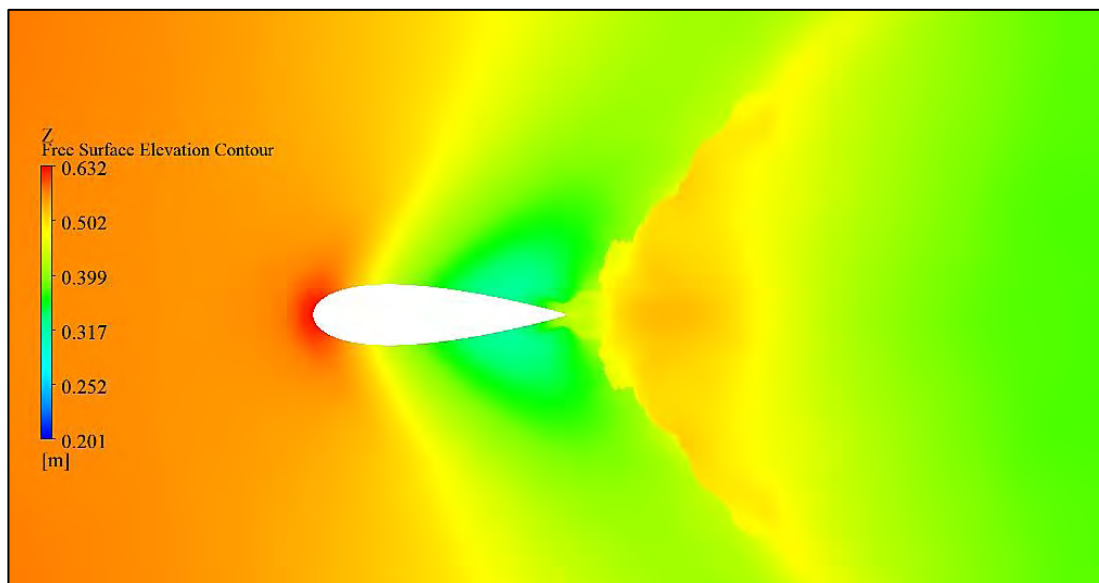


Figure 4.6.9: Free surface elevation contour along NACA 0024 airfoil section with $Fr = 0.55$

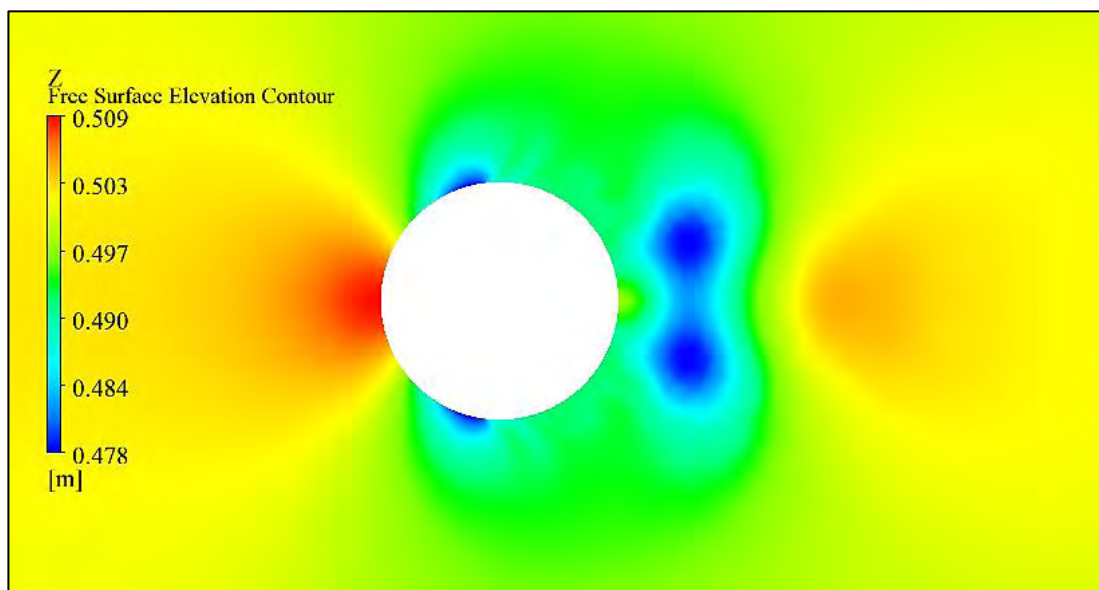


Figure 4.6.10: Free surface elevation contour along circular cylindrical section with $Fr = 0.19$

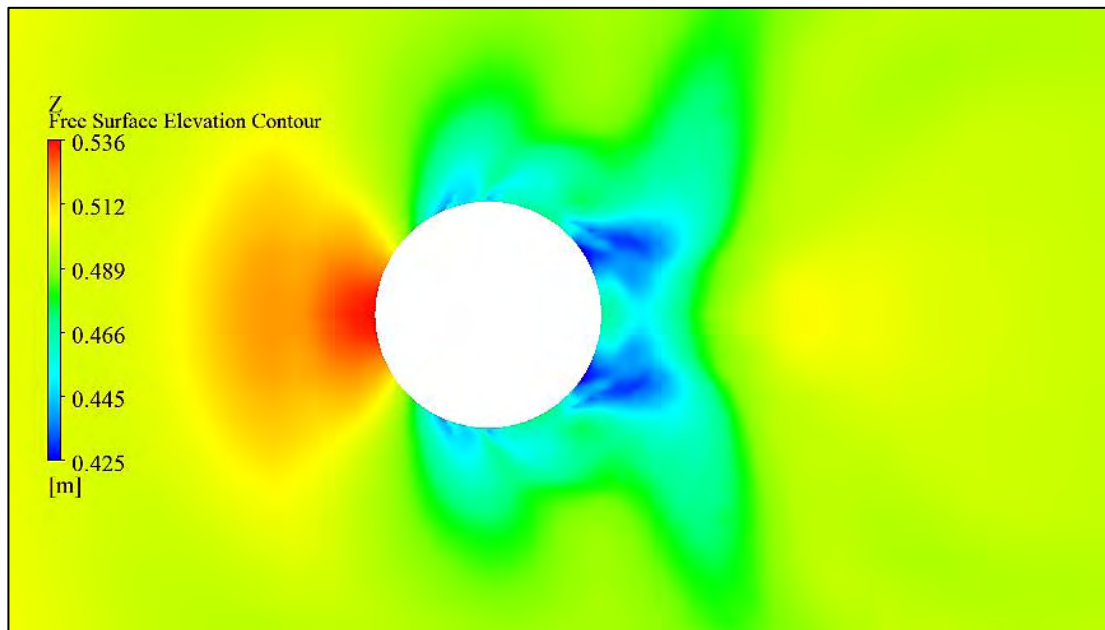


Figure 4.6.11: Free surface elevation contour along circular cylindrical section with $Fr = 0.37$

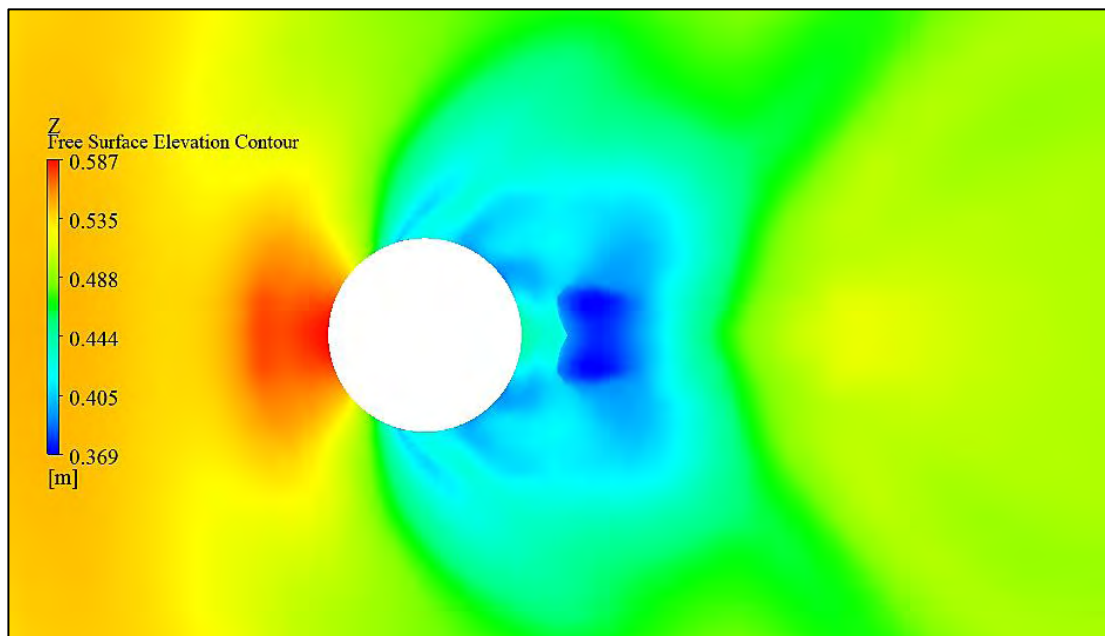


Figure 4.6.12: Free surface elevation contour along circular cylindrical section with $Fr = 0.55$

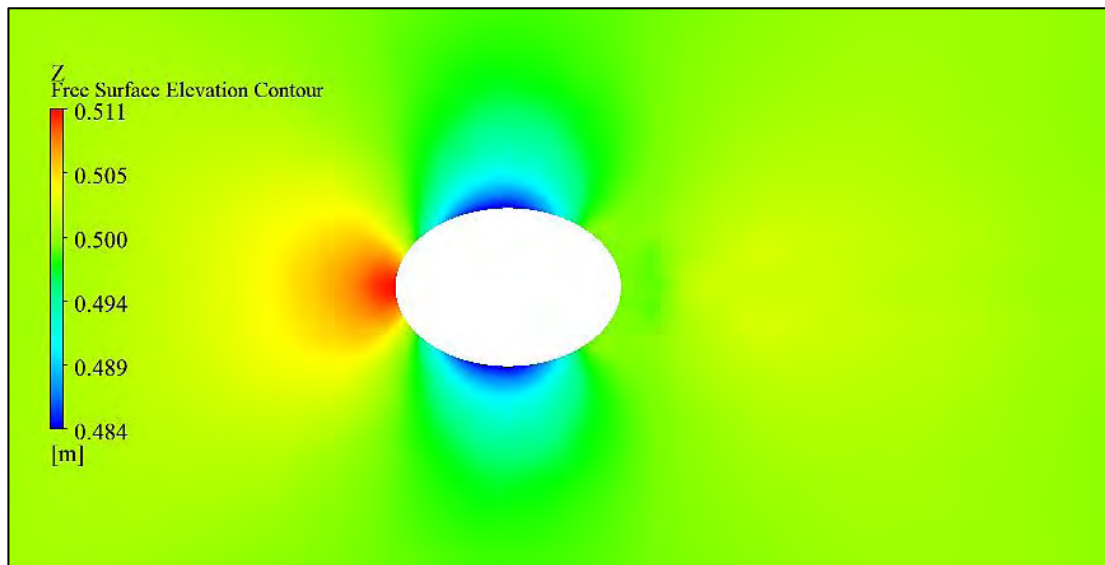


Figure 4.6.13: Free surface elevation contour along elliptical section with $Fr = 0.19$

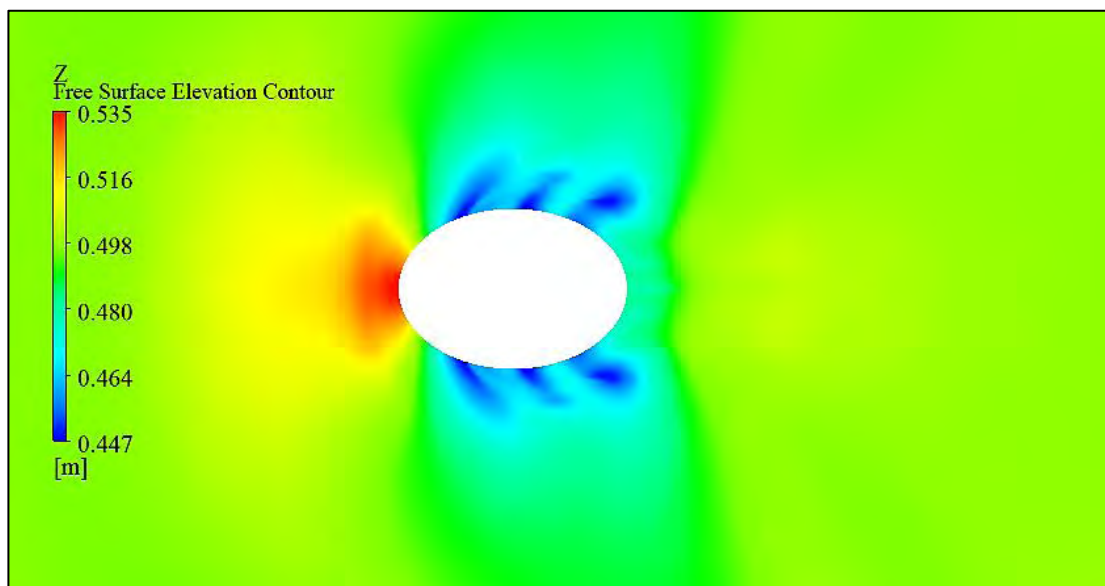


Figure 4.6.14: Free surface elevation contour along elliptical section with $Fr = 0.37$

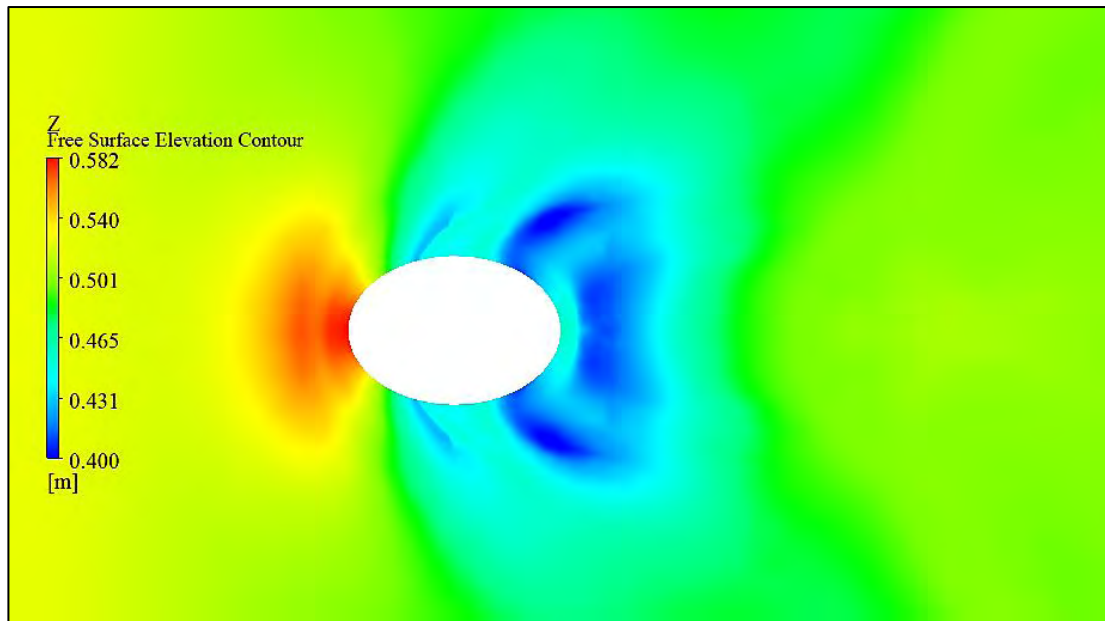


Figure 4.6.15: Free surface elevation contour along elliptical section with $Fr = 0.55$

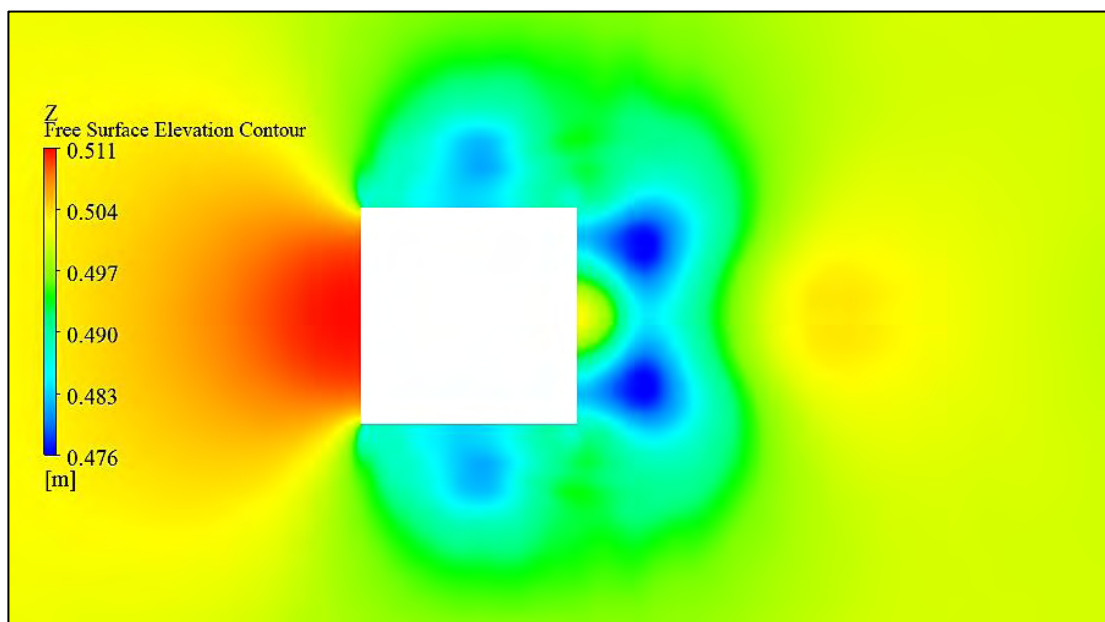


Figure 4.6.16: Free surface elevation contour along rectangular section with $Fr = 0.19$

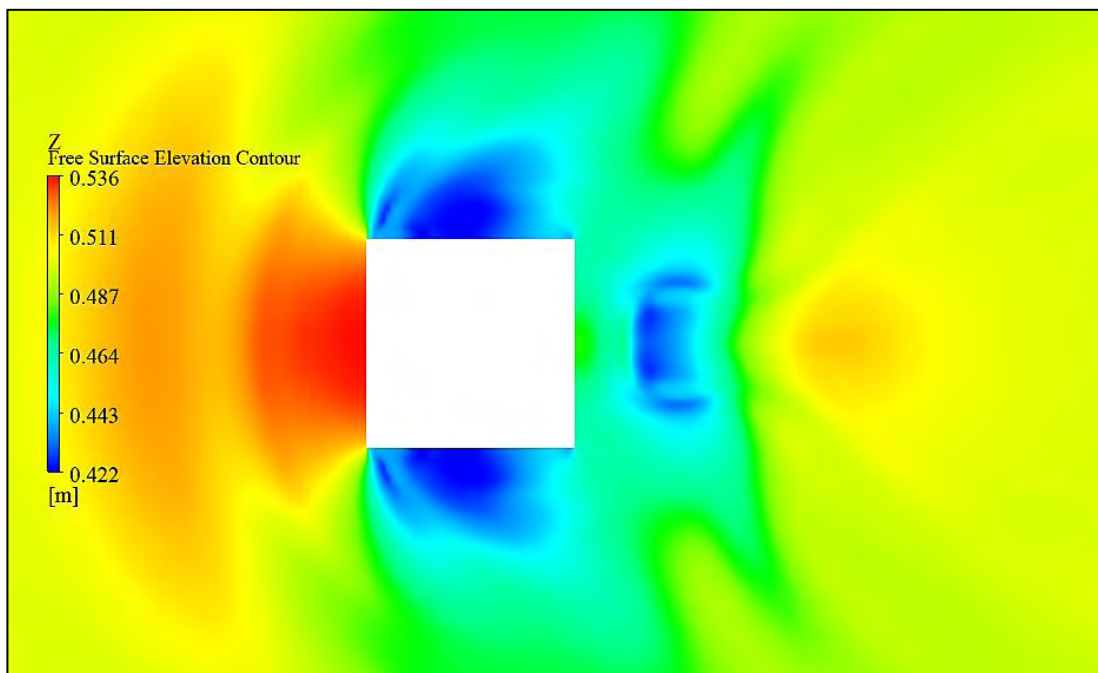


Figure 4.6.17: Free surface elevation contour along rectangular section with $Fr = 0.37$

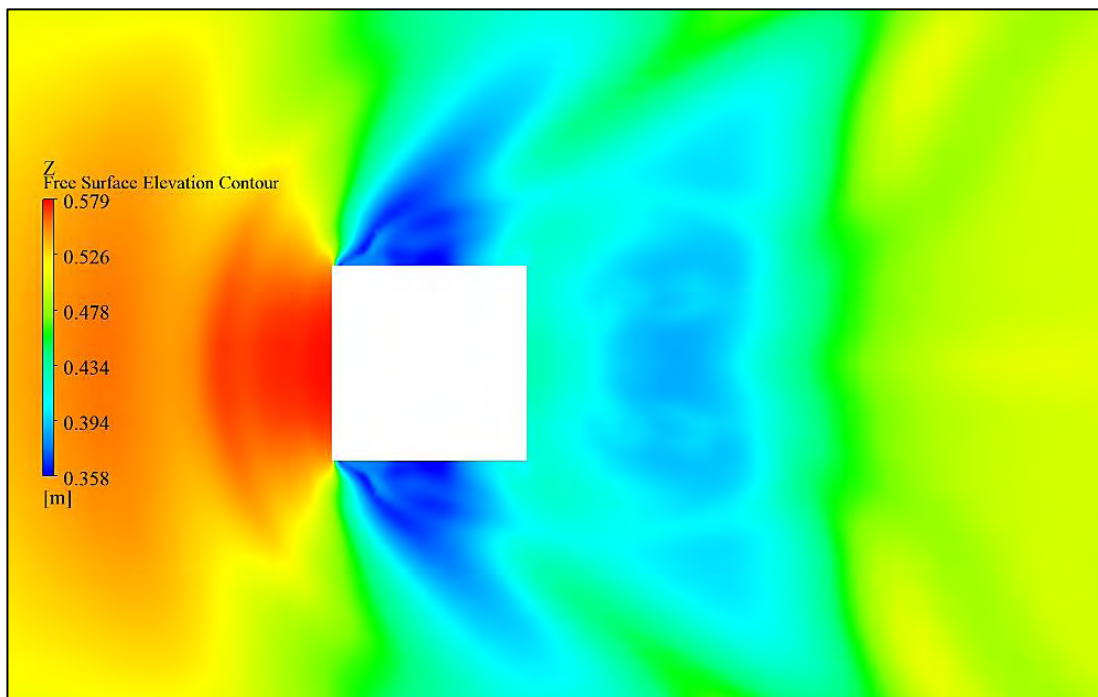


Figure 4.6.18: Free surface elevation contour along rectangular section with $Fr = 0.55$

4.7 Contour of Pressure

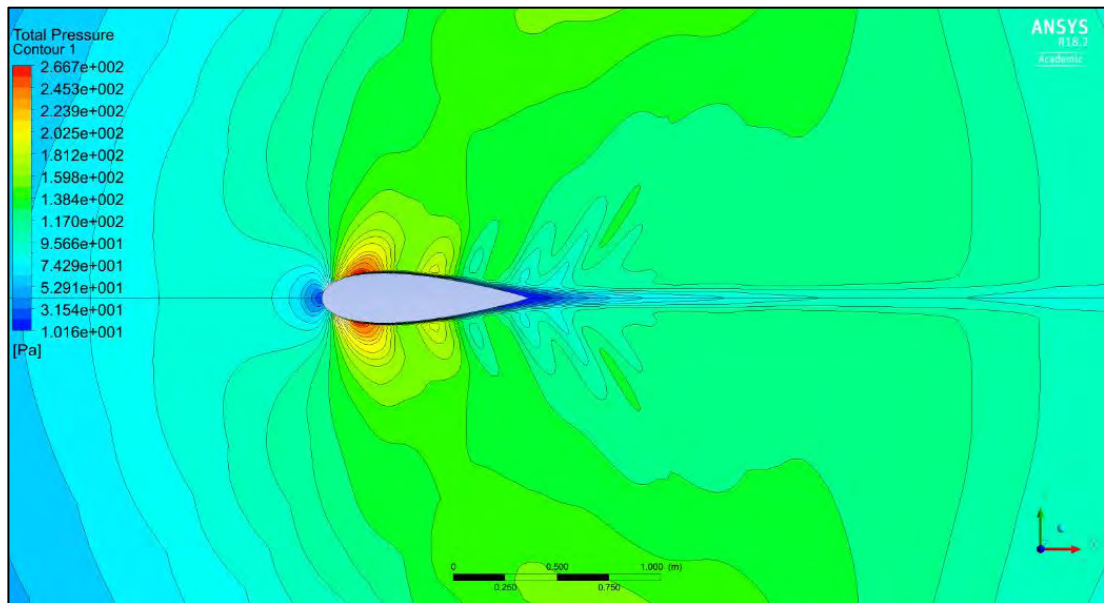


Figure 4.7.1: Pressure contour on the free surface along NACA 0024 airfoil section with $Fr = 0.19$

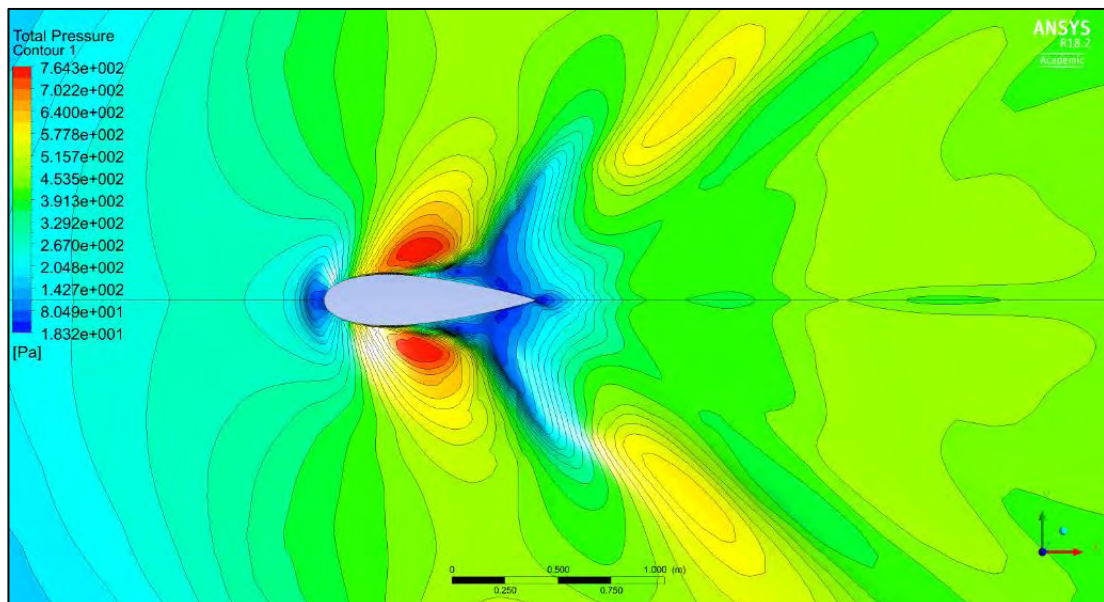


Figure 4.7.2: Pressure contour on the free surface along NACA 0024 airfoil section with $Fr = 0.37$

Figure 4.7.1, 4.7.2, and 4.7.3 represent the contours of pressure for NACA 0024 airfoil section at different Froude number. $Fr = 0.19$, the maximum pressure contour occurs

in the region between $x/L = 0.14$ and $x/L = 0.23$. The waves are found to be insignificant far from the body. The boundary layer is too small for low Froude numbers. The pressure gradient becomes steeper for higher Froude numbers. At $Fr = 0.37$ and $Fr = 0.55$, the maximum pressure occurs from $x/L = 0.35$ to $x/L = 0.56$ and from $x/L = 0.61$ to $x/L = 0.99$ respectively.

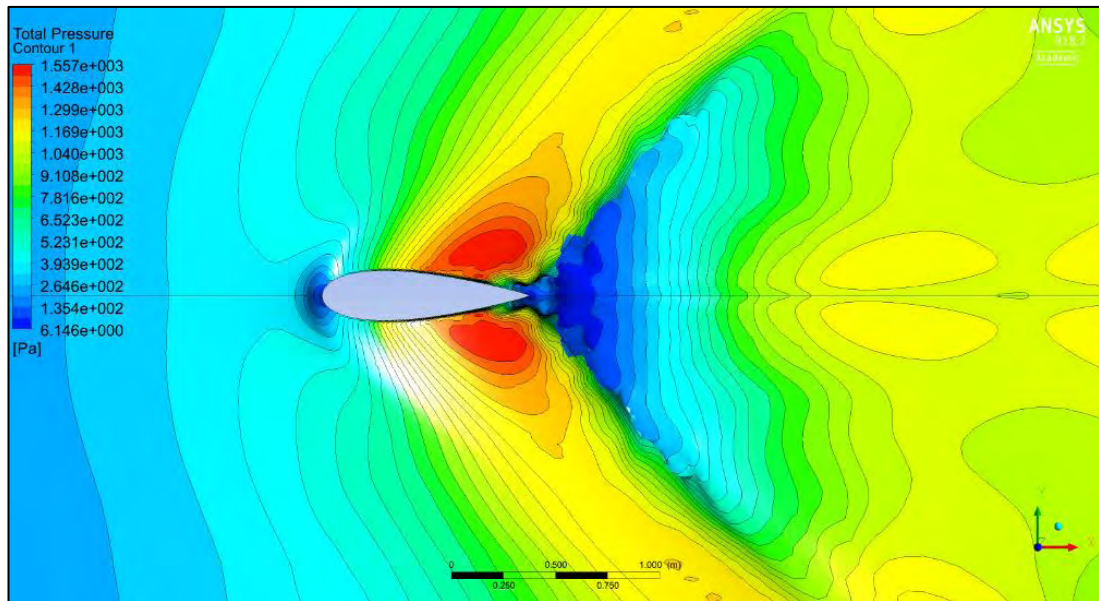


Figure 4.7.3: Pressure contour on the free surface along NACA 0024 airfoil section with $Fr = 0.55$

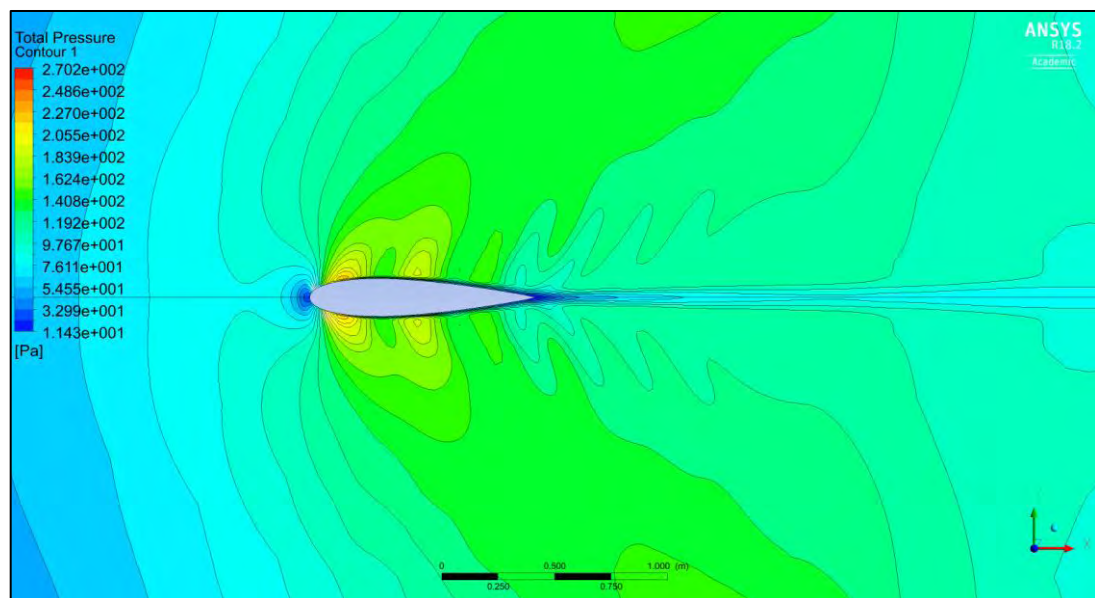


Figure 4.7.4: Pressure contour on the free surface along NACA 0012 airfoil section with $Fr = 0.19$

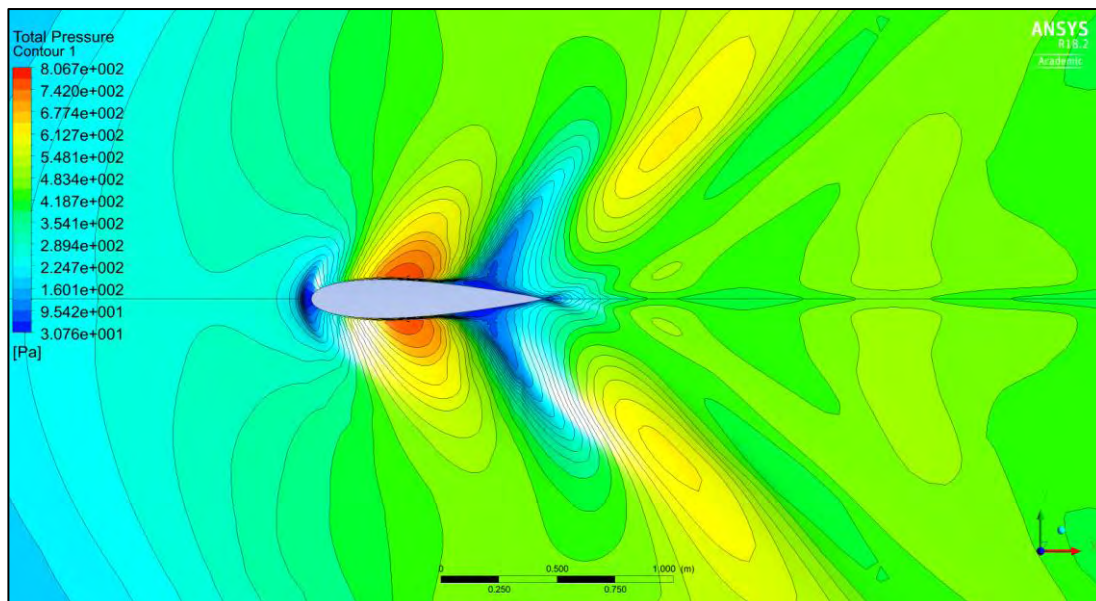


Figure 4.7.5: Pressure contour on the free surface along NACA 0012 airfoil section with $Fr = 0.37$

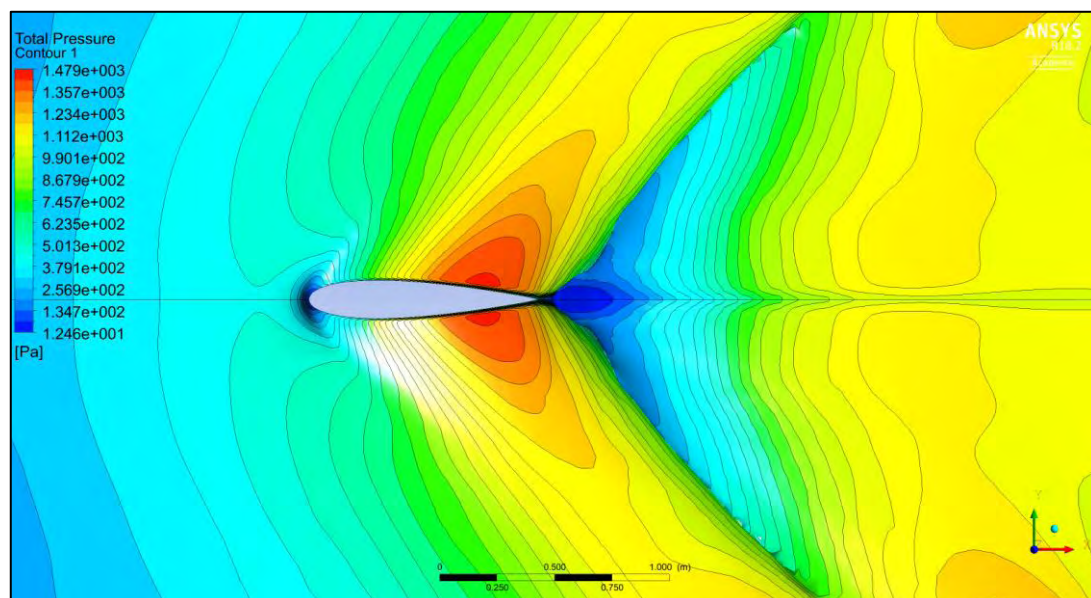


Figure 4.7.6: Pressure contour on the free surface along NACA 0012 airfoil section with $Fr = 0.55$

Figure 4.7.4, 4.7.5, and 4.7.6 show the pressure contours for NACA 0012 airfoil sections at different Froude numbers. For $Fr = 0.19$, the maximum pressure occurs in the region between $x/L = 0.12$ to $x/L = 0.17$. The pressure gradient increases with the increase in Froude number. At $Fr = 0.37$, the maximum pressure occurs between $x/L = 0.32$ to $x/L = 0.48$ and for $Fr = 0.55$, the maximum pressure occurs in the region from $x/L = 0.68$ to $x/L = 0.84$.

Figure 4.7.7, 4.7.8, and 4.7.9 show the pressure contours of NACA0018 airfoil section at different numbers. The maximum occurs from $x/L = 0.12$ to $x/L = 0.18$ for $Fr = 0.19$, from $x/L = 0.34$ to $x/L = 0.48$ for $Fr = 0.37$ and from $x/L = 0.64$ to $x/L = 0.84$ for $Fr = 0.88$. The thickness effect is negligible for low Froude number, but with the increase of Froude number the wave deforms gradually and becomes Fr dependent.

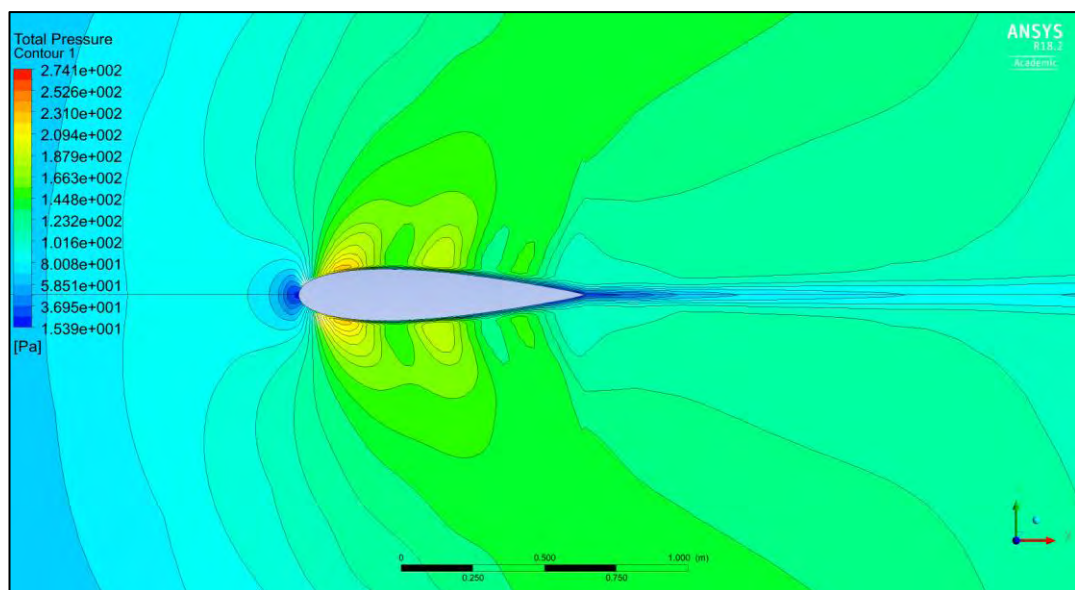


Figure 4.7.7: Pressure contour on the free surface along NACA 0018 airfoil section with $Fr = 0.19$

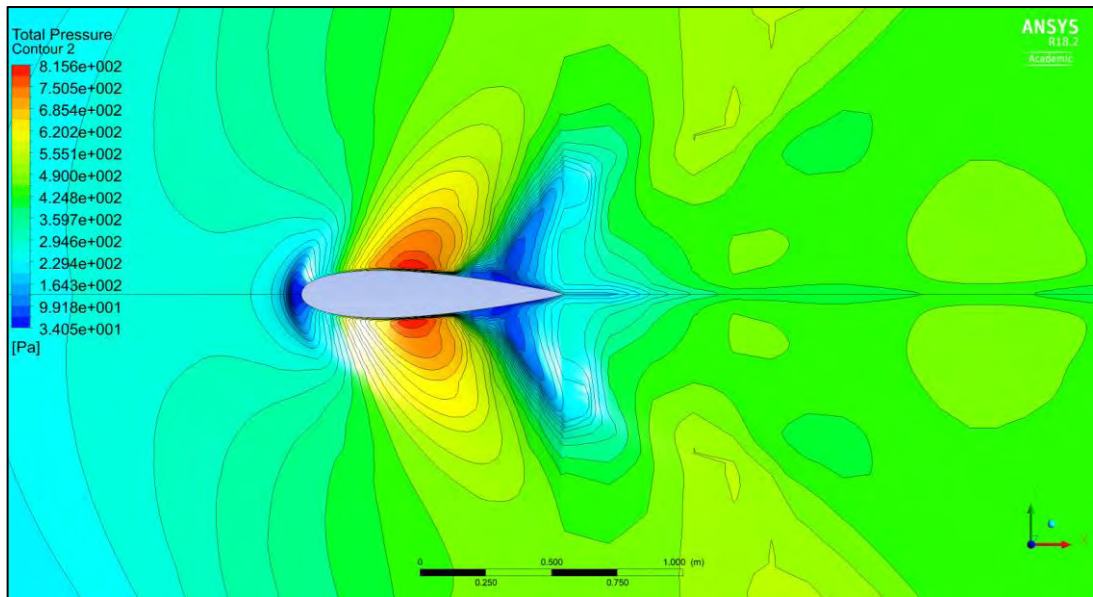


Figure 4.7.8: Pressure contour on the free surface along NACA 0018 airfoil section with $Fr = 0.37$

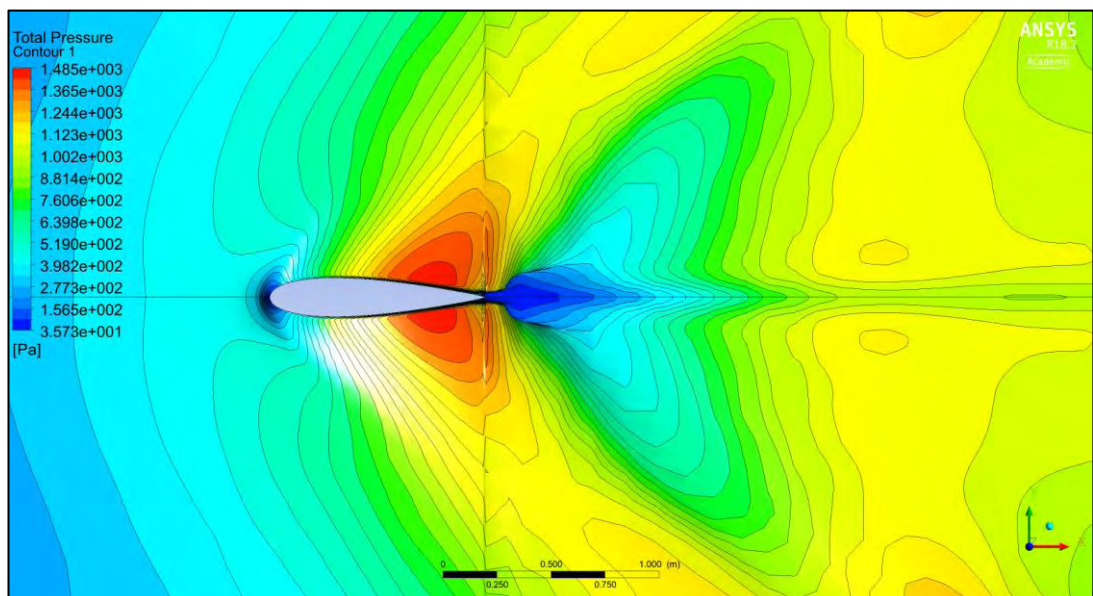


Figure 4.7.9: Pressure contour on the free surface along NACA 0018 airfoil section with $Fr = 0.55$

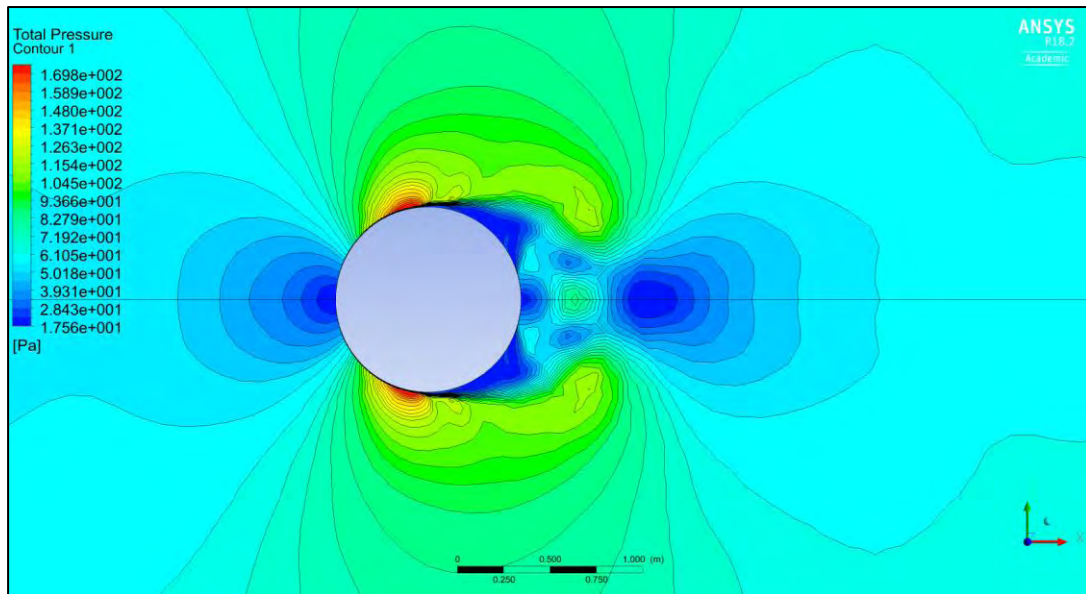


Figure 4.7.10: Pressure contour on the free surface along circular cylinder section with $Fr = 0.19$

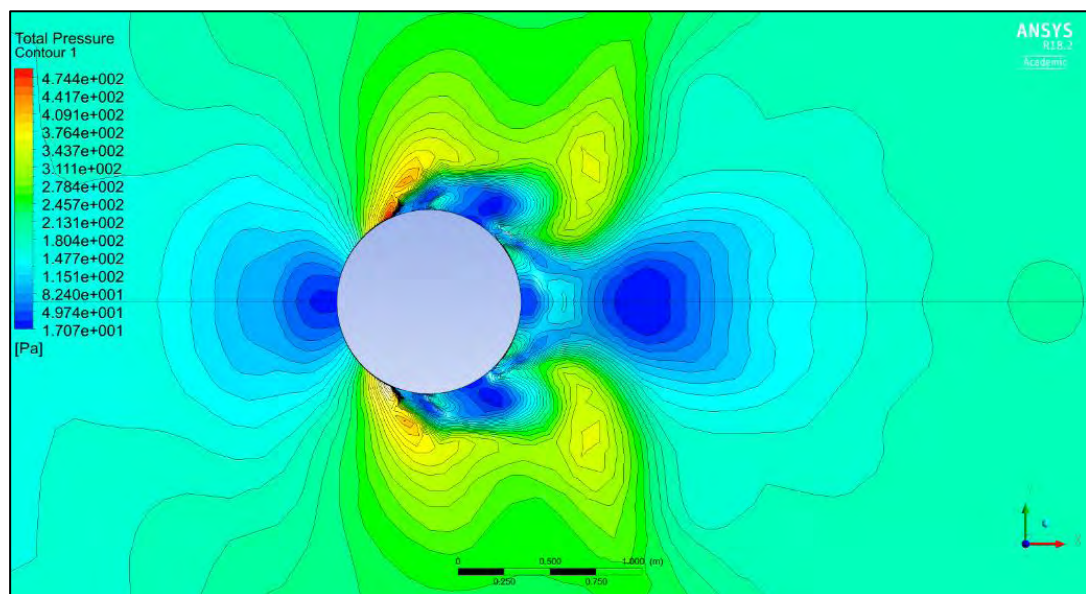


Figure 4.7.11: Pressure contour on the free surface along circular cylinder section with $Fr = 0.37$

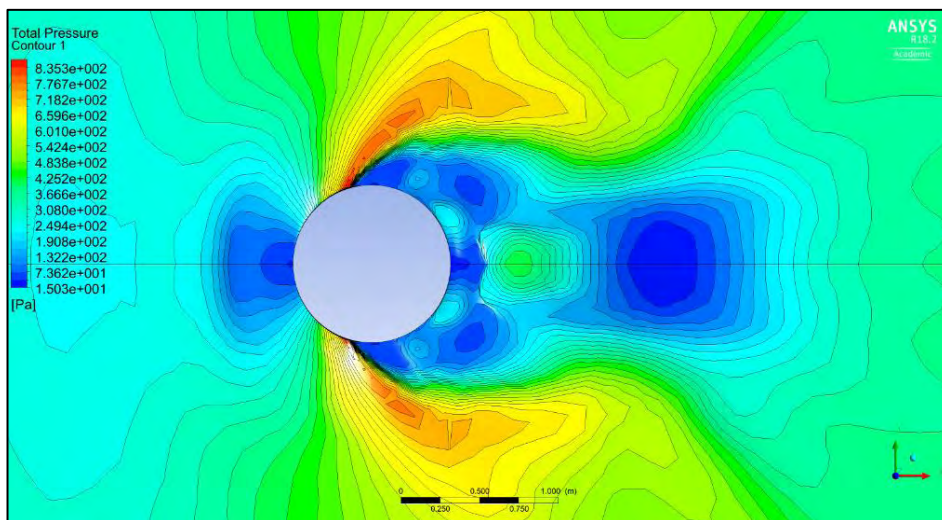


Figure 4.7.12: Pressure contour on the free surface along circular cylinder section with $Fr = 0.55$

Figure 4.7.10, 4.7.11, and 4.7.12 represent the pressure contours for the circular cylinder section at different Froude numbers. The separation of water extends with the increase of Froude number. For $Fr = 0.19$, the maximum pressure occurs in the region from $x/L = 0.32$ to $x/L = 0.44$. The maximum pressure in case of $Fr = 0.37$ and $Fr = 0.55$ are from $x/L = 0.27$ to $x/L = 0.29$ and $x/L = 0.33$ to $x/L = 0.37$ respectively. Figure shows that at Froude number $Fr = 0.55$, the water deformation is very high. Thus with the change in shape, we can see that at low Froude number the wave deformation is dependent on the shape of the body but on Fr for higher Froude number.

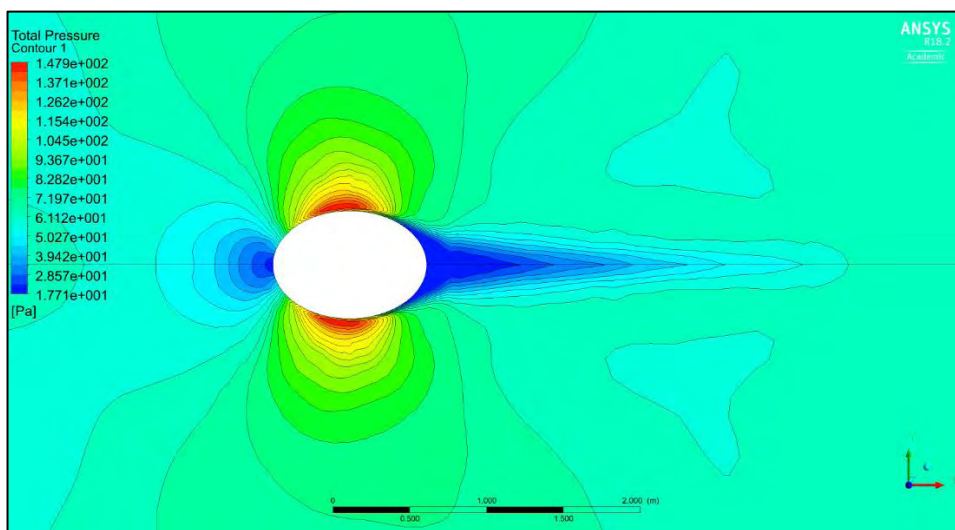


Figure 4.7.13: Pressure contour on the free surface along elliptical section with $Fr = 0.19$

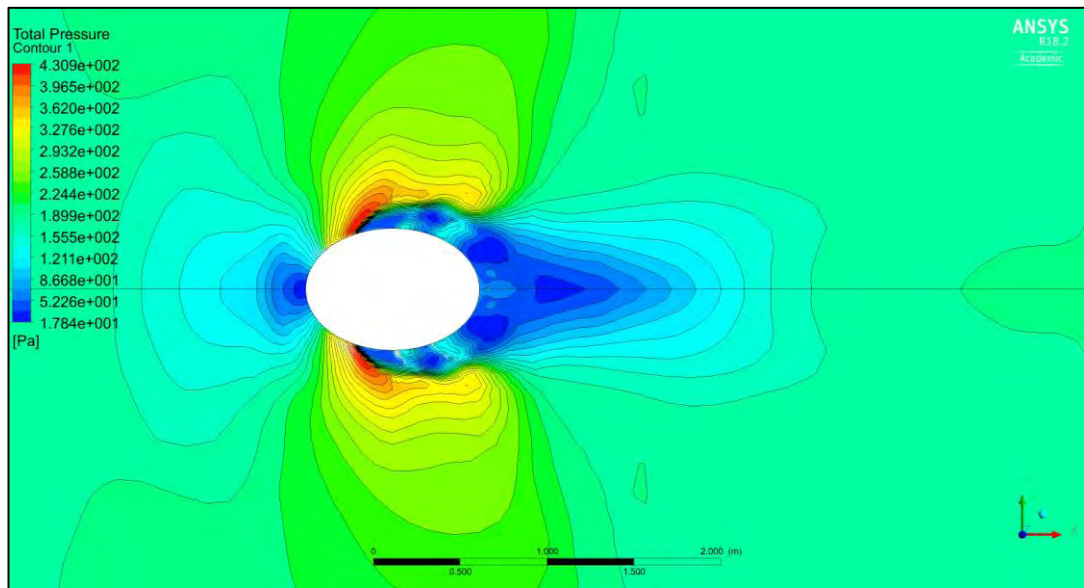


Figure 4.7.14: Pressure contour on the free surface along elliptical section with $Fr = 0.37$

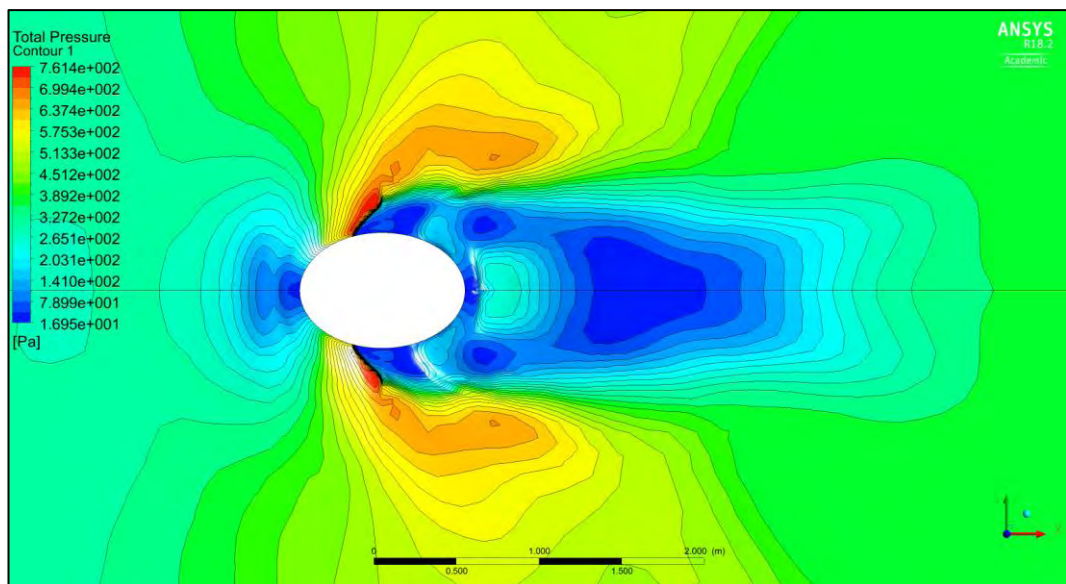


Figure 4.7.15: Pressure contour on the free surface along elliptical section with $Fr = 0.55$

Figure 4.7.13, 4.7.14, and 4.7.15 show the pressure contours for elliptical section at different Froude numbers. At low Froude number, the boundary layer is too small and the waves are found to be insignificant. For $Fr = 0.19$, the maximum pressure is about 1.479×10^2 and it is in the region from $x/L = 0.30$ to $x/L = 0.57$. The pressure gradient

increases with the increase in Froude number and the wave deformation becomes very high. Thus at low Froude numbers, the wave deformation is dependent on shape of the body but on Fr at higher Froude numbers. The maximum pressures for $Fr = 0.37$ and $Fr = 0.55$ are 4.309×10^2 and 7.614×10^2 respectively.

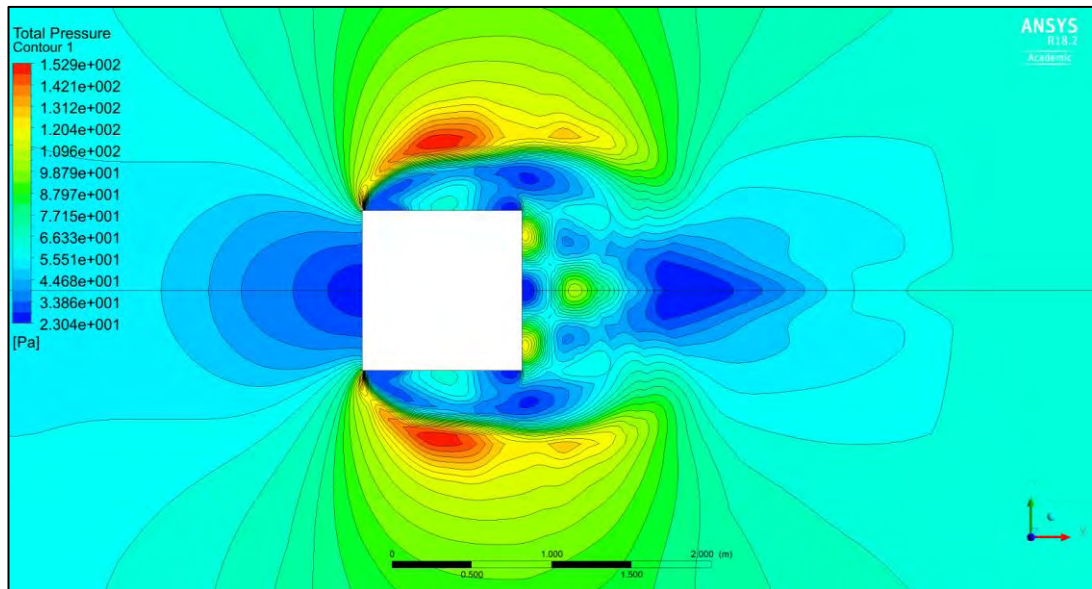


Figure 4.7.16: Pressure contour on the free surface along rectangular section with $Fr = 0.19$

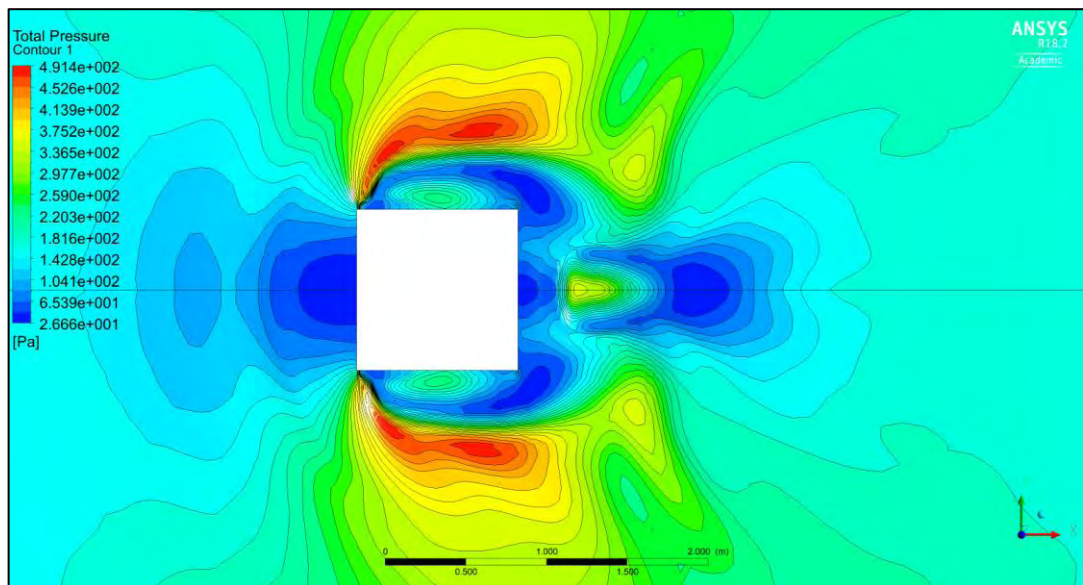


Figure 4.7.17: Pressure contour on the free surface along rectangular section with $Fr = 0.37$

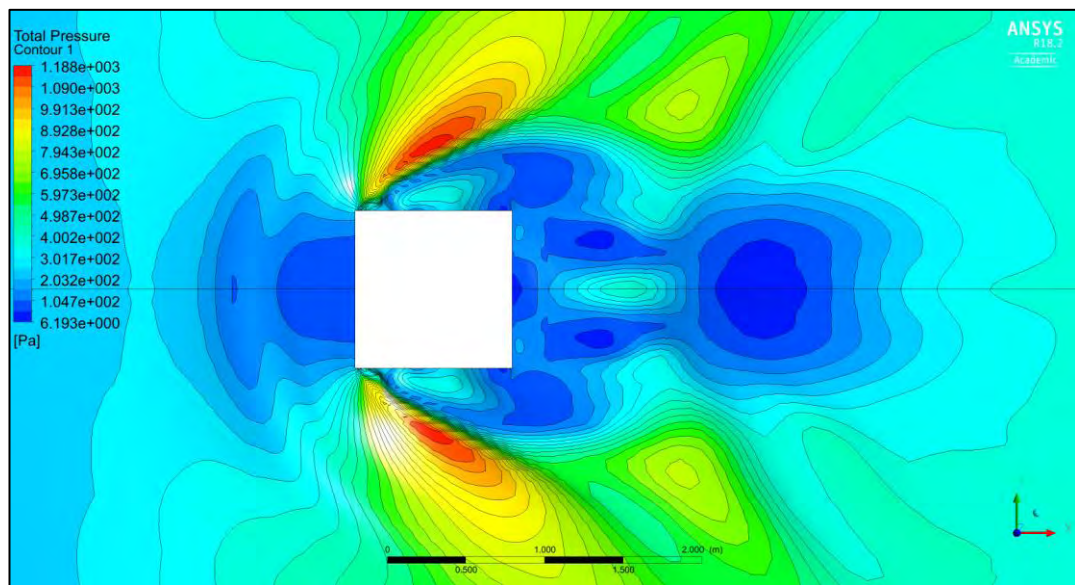


Figure 4.7.18: Pressure contour on the free surface along rectangular section with $Fr = 0.55$

Figure 4.7.16, 4.7.17, and 4.7.18 represent the contours of pressure for rectangular section at different Froude numbers. For $Fr = 0.19$, the maximum pressure is about 1.529×10^2 which dominates the flow in the region from $x/L = 0.34$ to $x/L = 0.63$. With the increase in Froude number, the pressure gradient also increases due to the high – pressure stagnation point and the free surface effects dominate the wave profile. The maximum pressure for $Fr = 0.37$ is 4.914×10^2 in the region from $x/L = 0.13$ to $x/L = 0.90$. The water deformation is very high for $Fr = 0.55$ and the maximum pressure is about 1.188×10^3 in the region from $x/L = 0.35$ to $x/L = 0.63$. For $Fr = 0.19$, shape effects dominate the wave profile due to the sharp edge of the body, but at higher Froude numbers, the flow is dependent on Fr but not on shape.

From the figures above we can see that, it shows the pressure distribution on the free surface along with the surface piercing bodies. Thus the pressure is minimum at the bow wave peak but when the air interacts with the water, the pressure becomes dominant at this interaction point. Again, the air-water separates from each other in the separation region, so the pressure becomes minimum at the separation region.

Figure 4.7.19 – 4.7.36 show the pressure contour at $z = 0.5$ m along difference surface piercing body for Froude number $Fr = 0.19, 0.37$ and 0.55 .

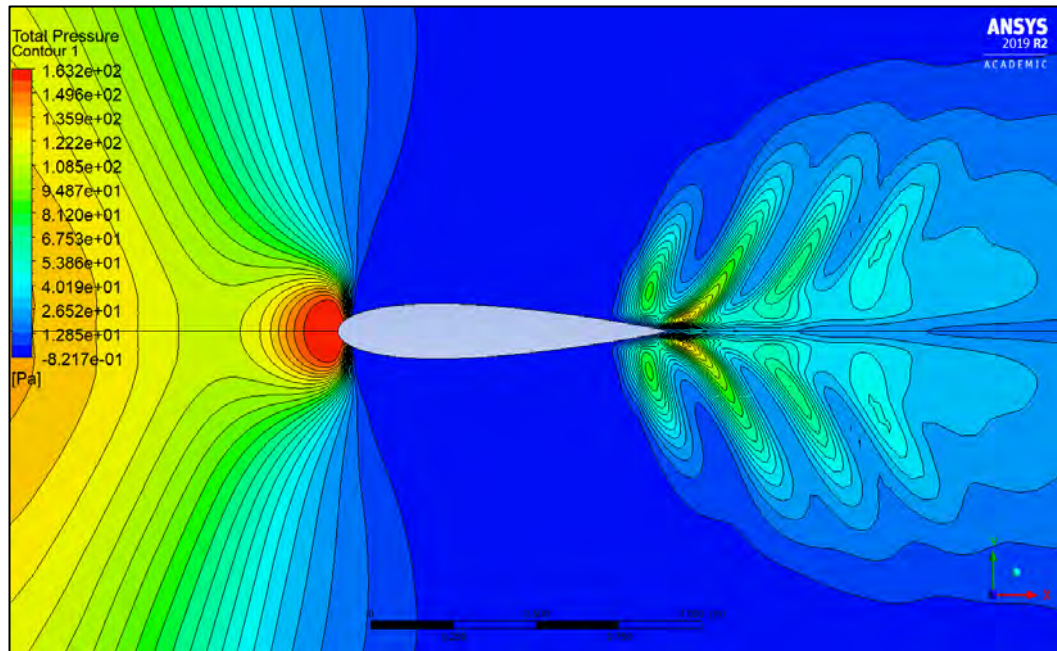


Figure 4.7.19: Pressure contour at $z = 0.5$ m along NACA 0012 airfoil section with $Fr = 0.19$

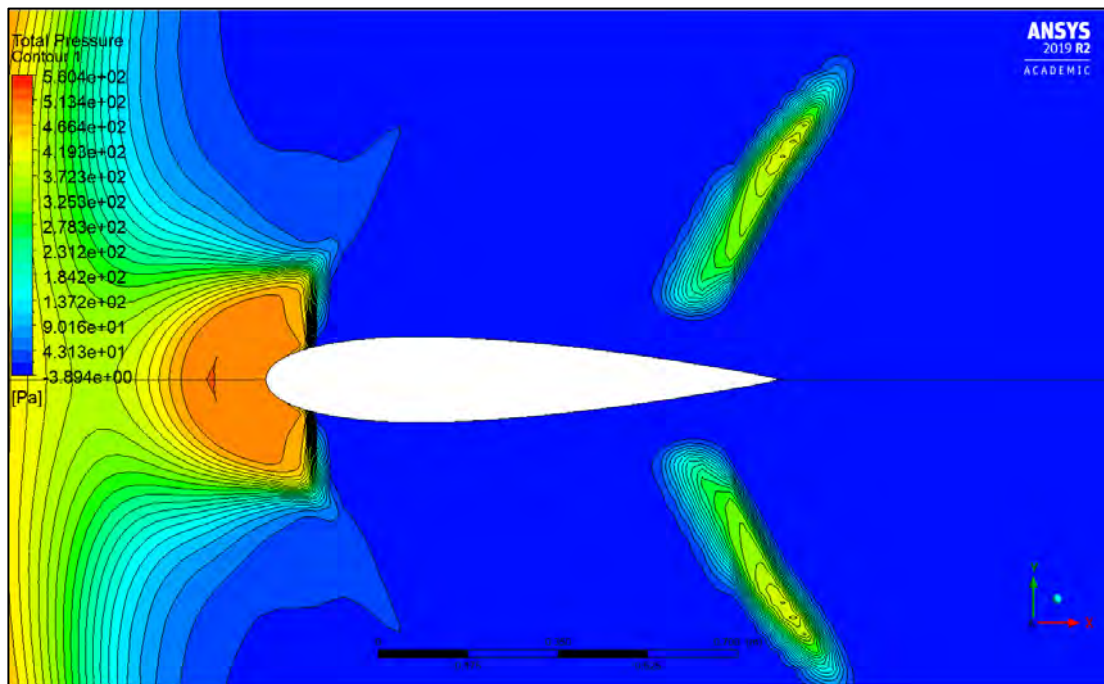


Figure 4.7.20: Pressure contour at $z = 0.5$ m along NACA 0012 airfoil section with $Fr = 0.37$

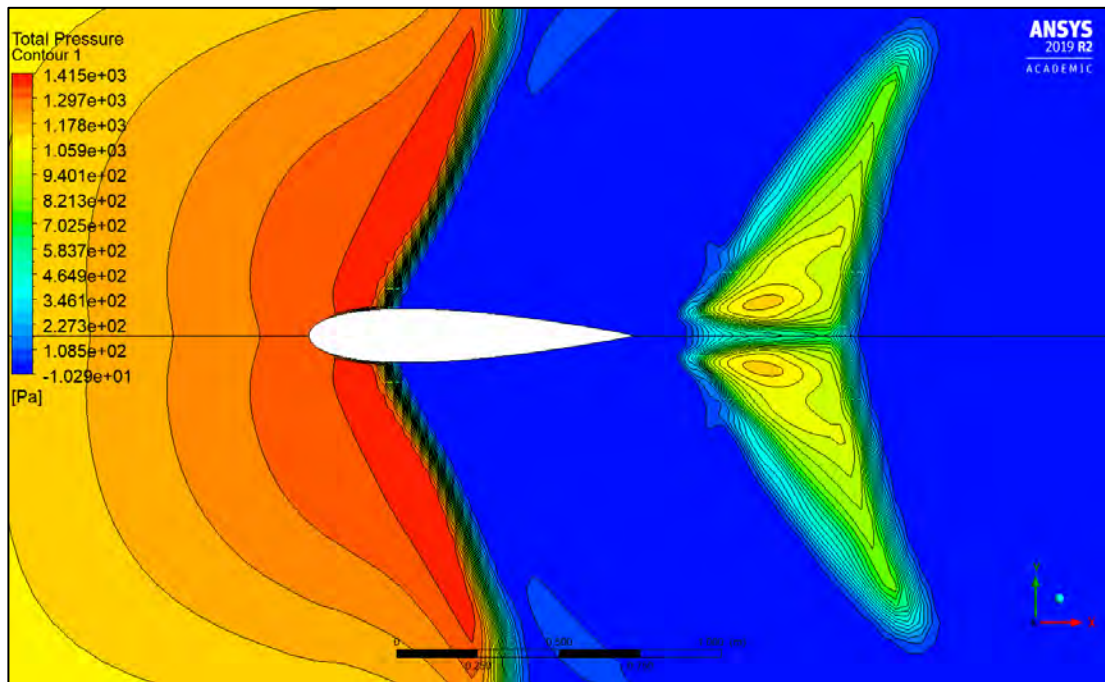


Figure 4.7.21: Pressure contour at $z = 0.5$ m along NACA 0012 airfoil section with $Fr = 0.55$

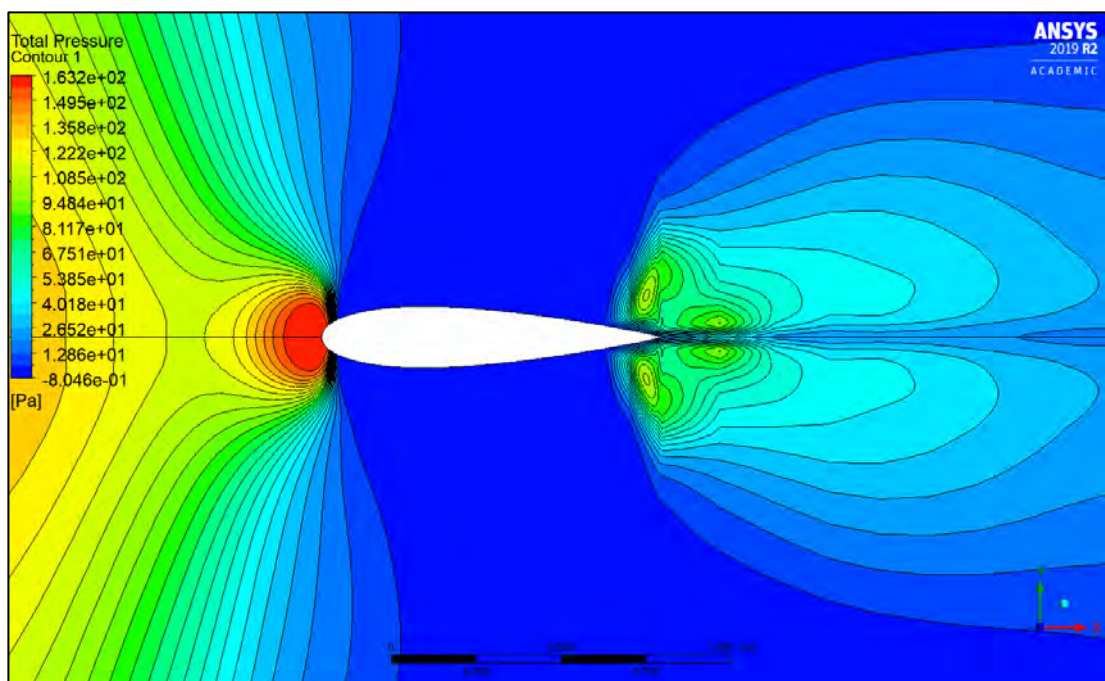


Figure 4.7.22: Pressure contour at $z = 0.5$ m along NACA 0018 airfoil section with $Fr = 0.19$

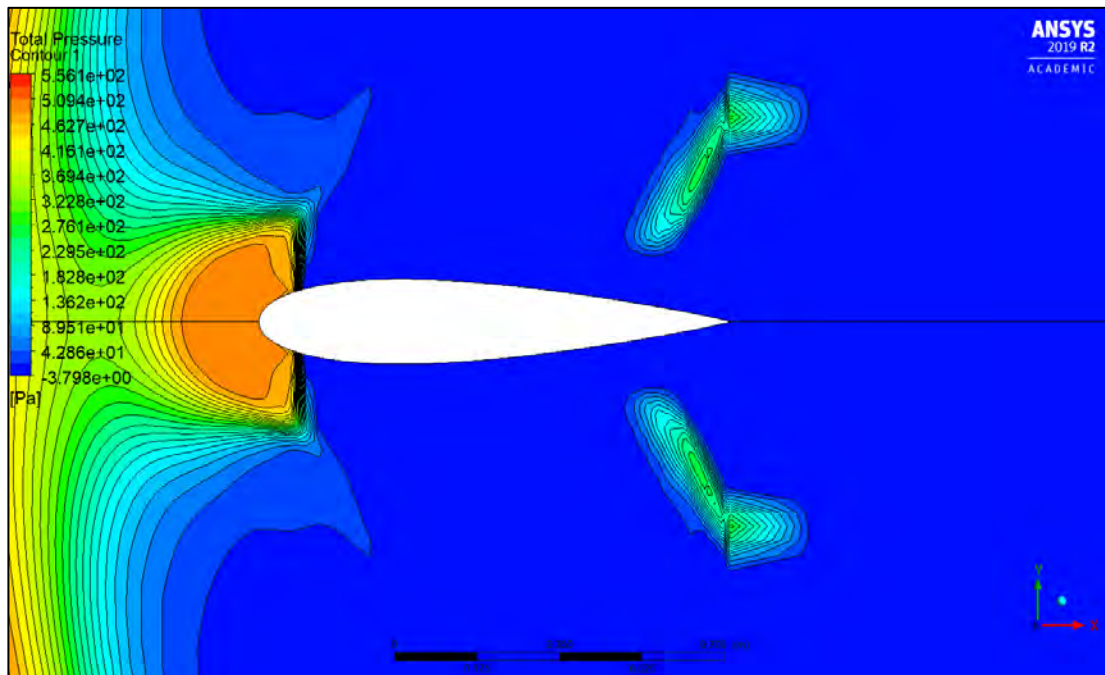


Figure 4.7.23: Pressure contour at $z = 0.5$ m along NACA 0018 airfoil section with $Fr = 0.37$

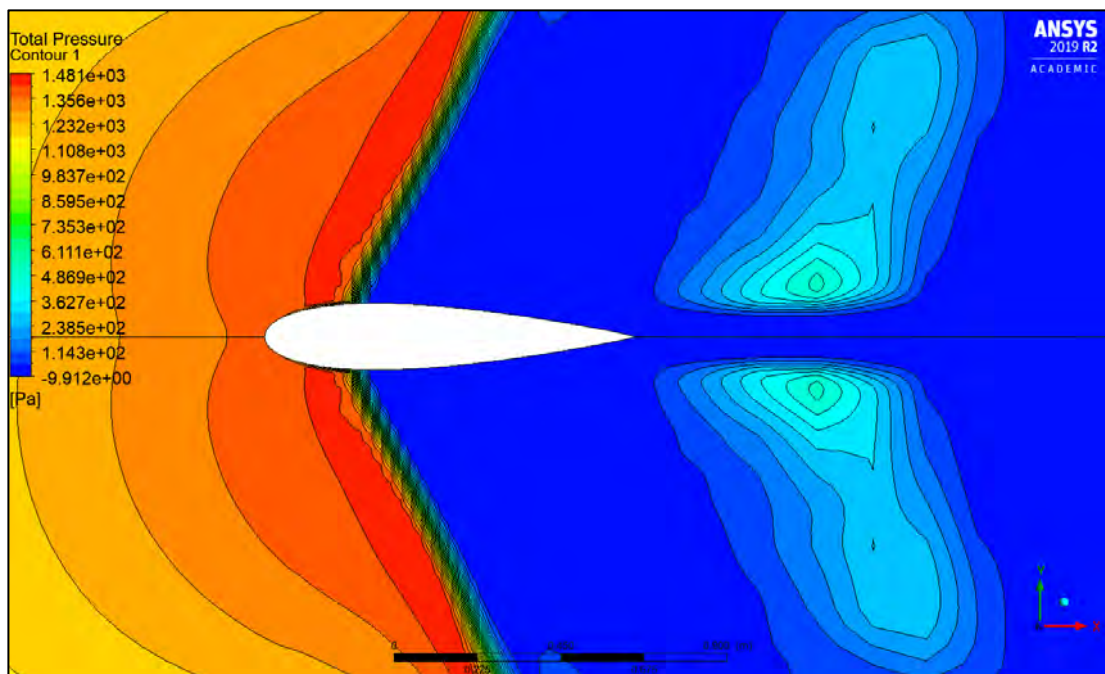


Figure 4.7.24: Pressure contour at $z = 0.5$ m along NACA 0018 airfoil section with $Fr = 0.55$

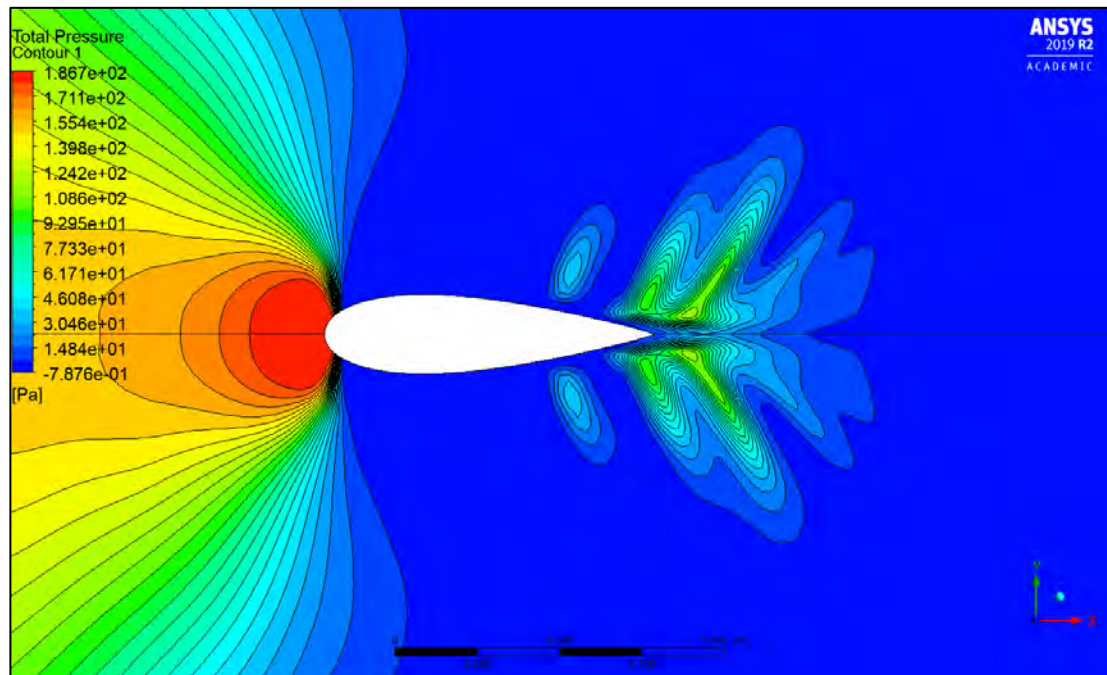


Figure 4.7.25: Pressure contour at $z = 0.5$ m along NACA 0024 airfoil section with $Fr = 0.19$

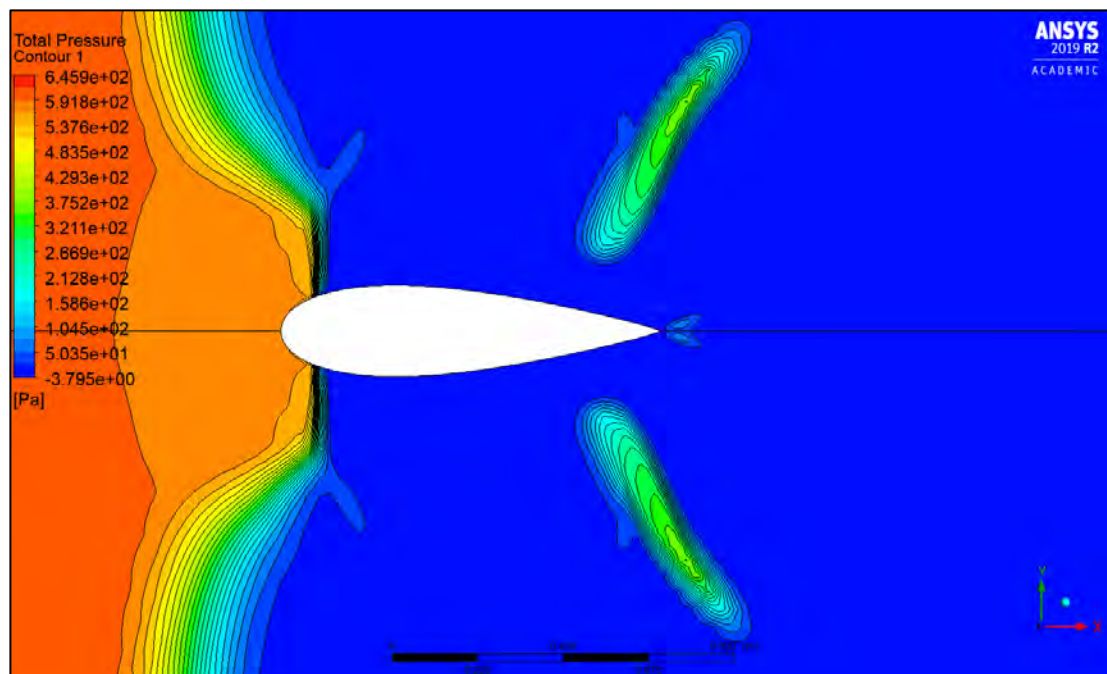


Figure 4.7.26: Pressure contour at $z = 0.5$ m along NACA 0024 airfoil section with $Fr = 0.37$

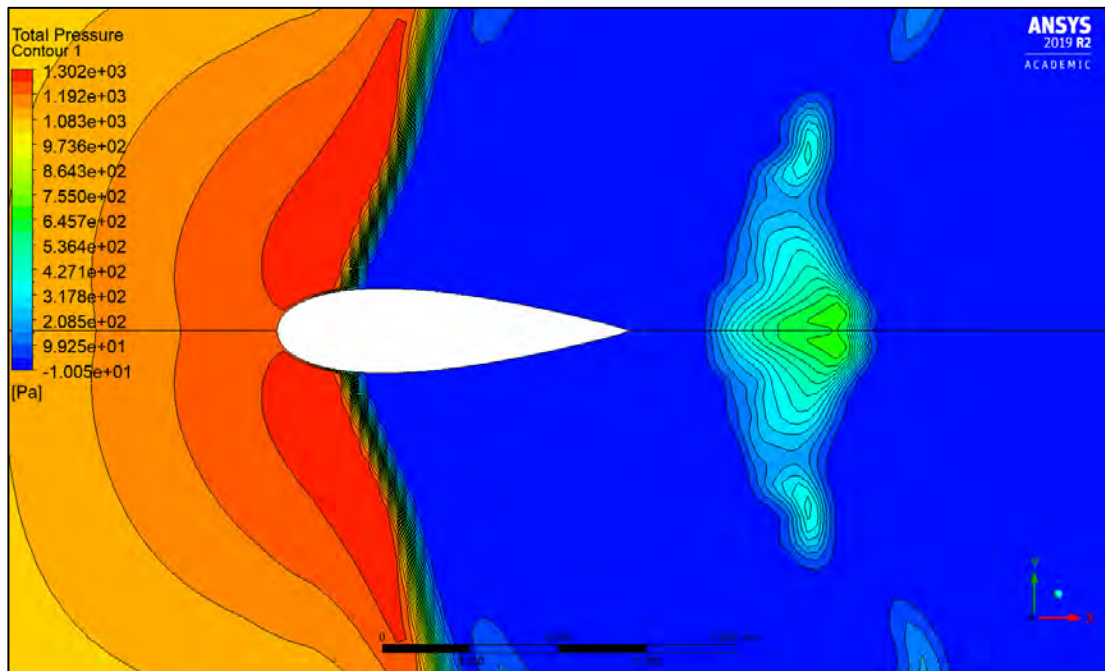


Figure 4.7.27: Pressure contour at $z = 0.5$ m along NACA 0024 airfoil section with $Fr = 0.55$

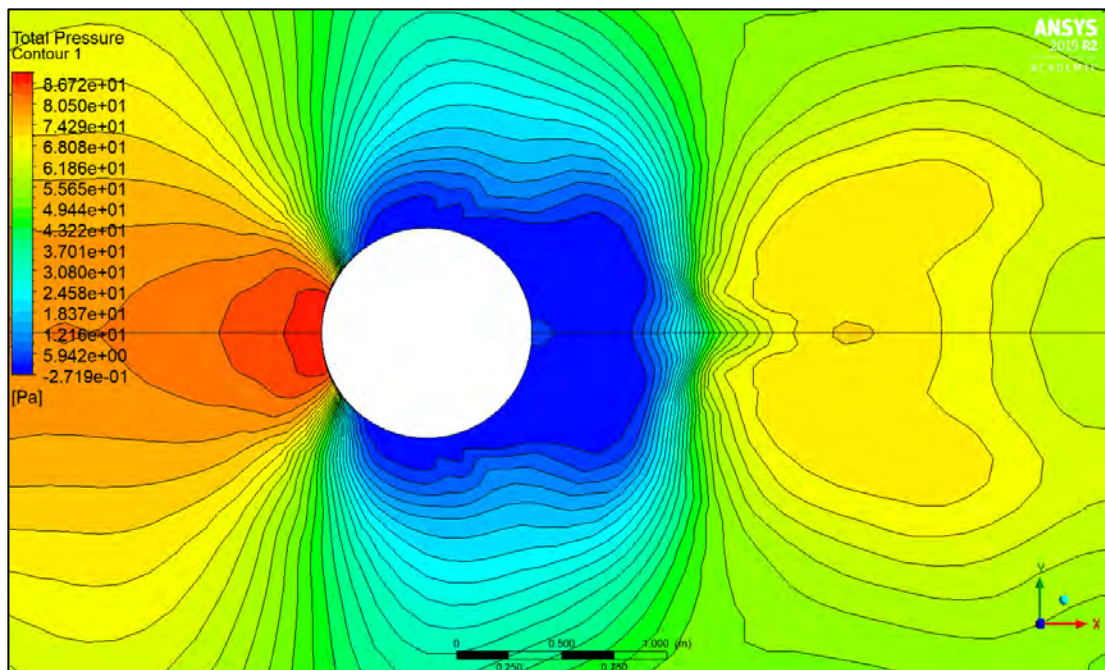


Figure 4.7.28: Pressure contour at $z = 0.5$ m along circular cylinder section with $Fr = 0.19$

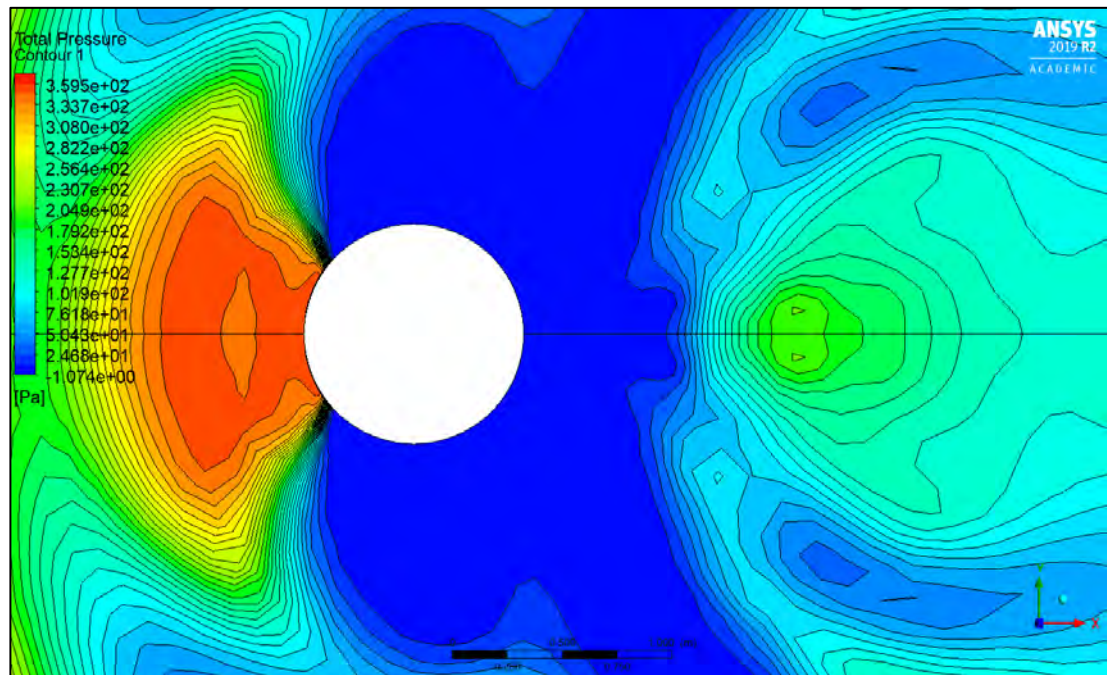


Figure 4.7.29: Pressure contour at $z = 0.5$ m along circular cylinder section with $Fr = 0.37$

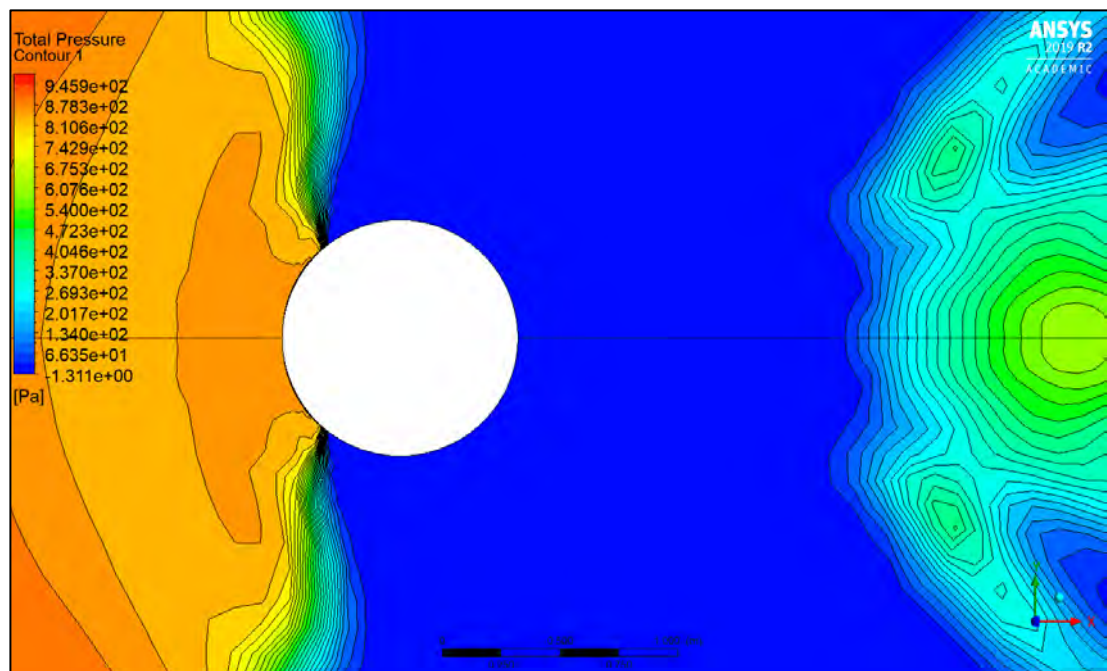


Figure 4.7.30: Pressure contour at $z = 0.5$ m along circular cylinder section with $Fr = 0.55$

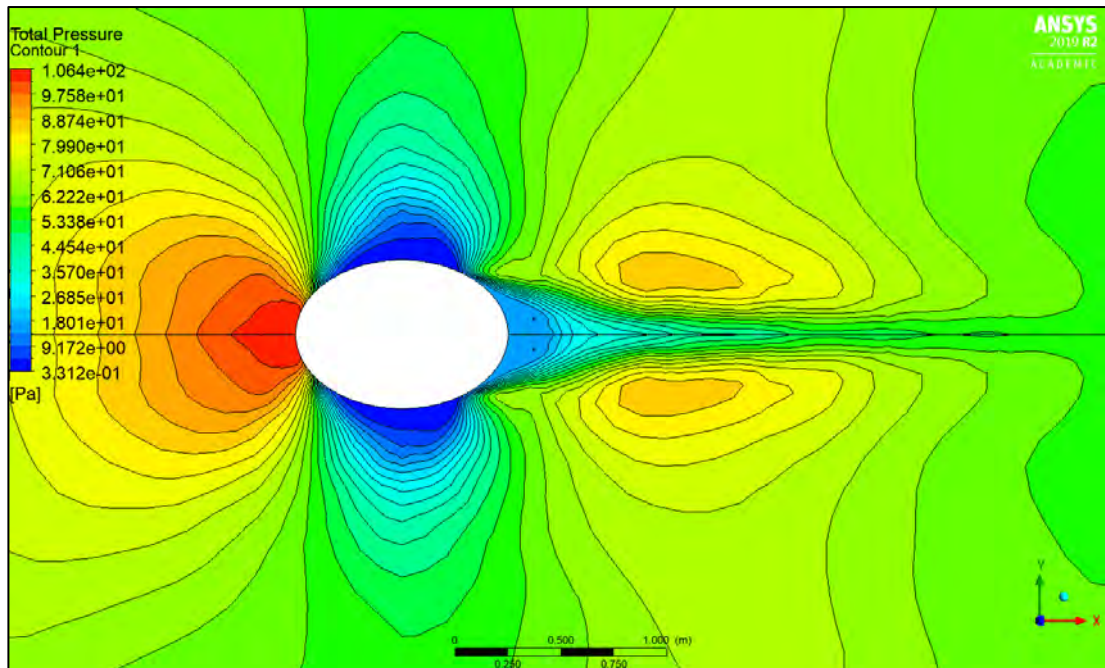


Figure 4.7.31: Pressure contour at $z = 0.5$ m along elliptical section with $Fr = 0.19$

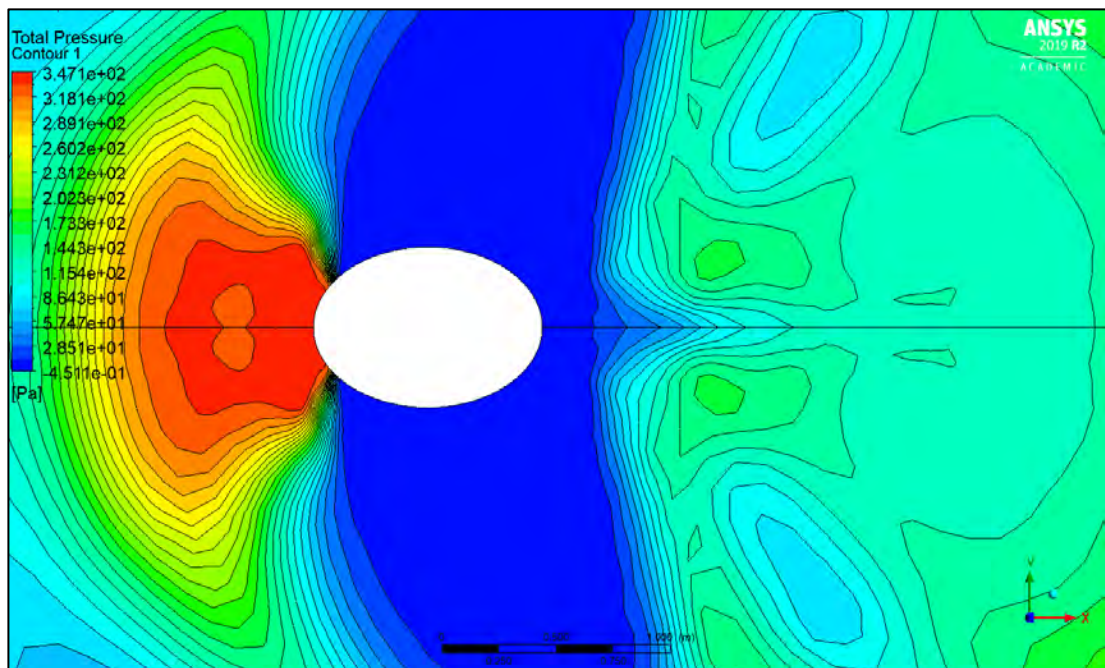


Figure 4.7.32: Pressure contour at $z = 0.5$ m along elliptical section with $Fr = 0.37$

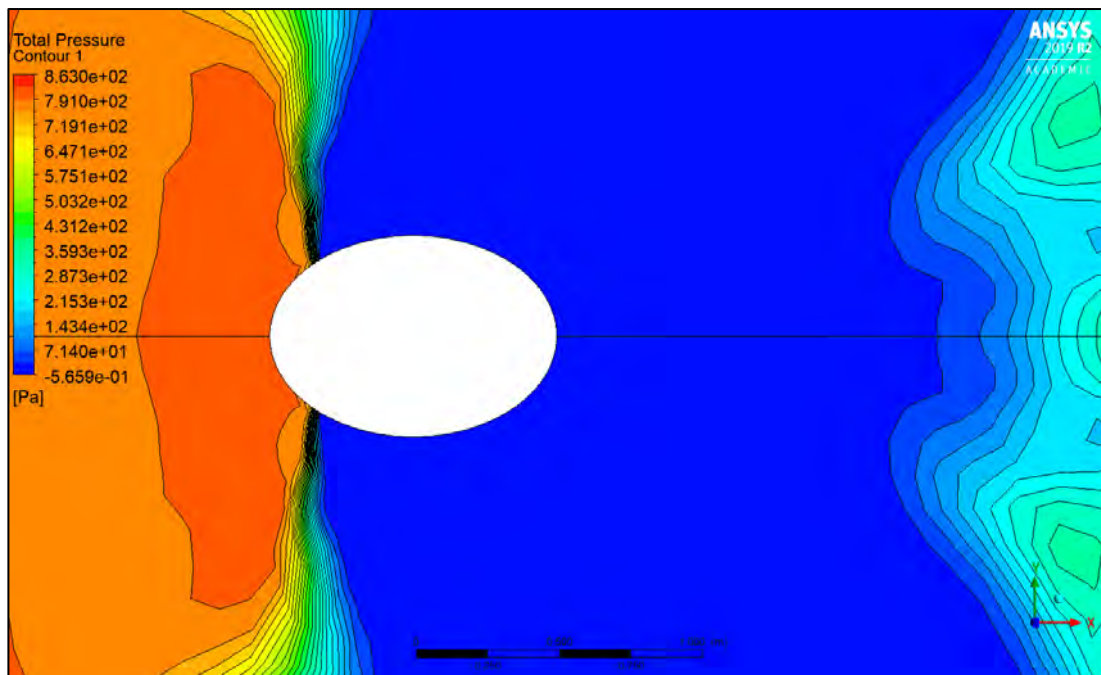


Figure 4.7.33: Pressure contour at $z = 0.5$ m along elliptical section with $Fr = 0.55$

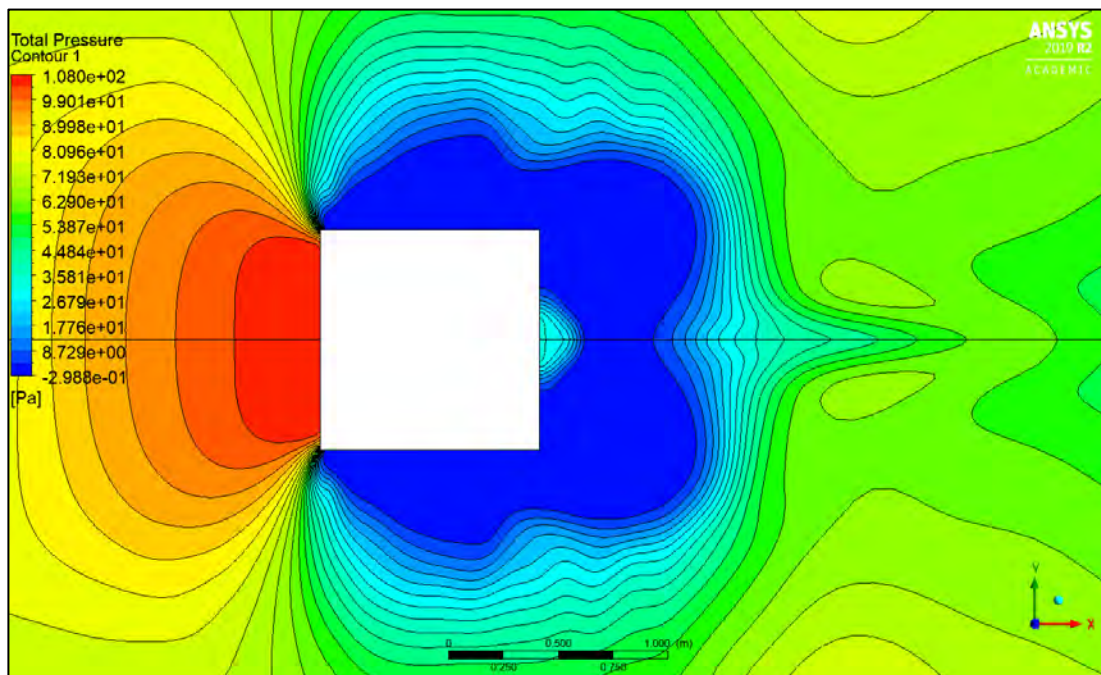


Figure 4.7.34: Pressure contour at $z = 0.5$ m along rectangular section with $Fr = 0.19$

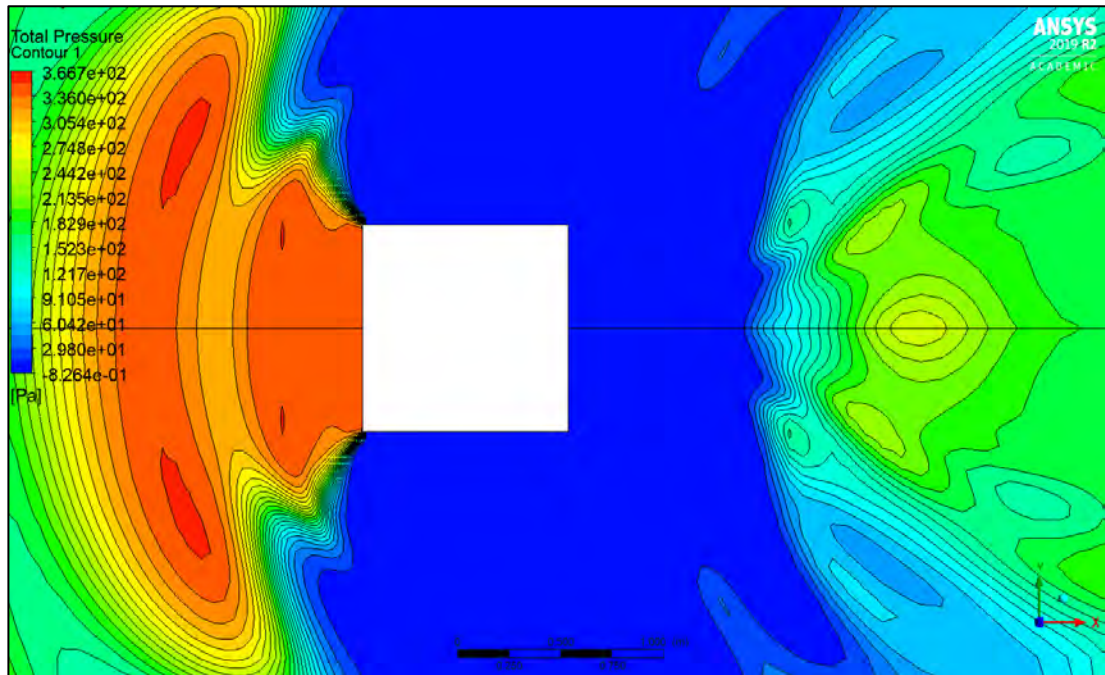


Figure 4.7.35: Pressure contour at $z = 0.5$ m along rectangular section with $Fr = 0.37$

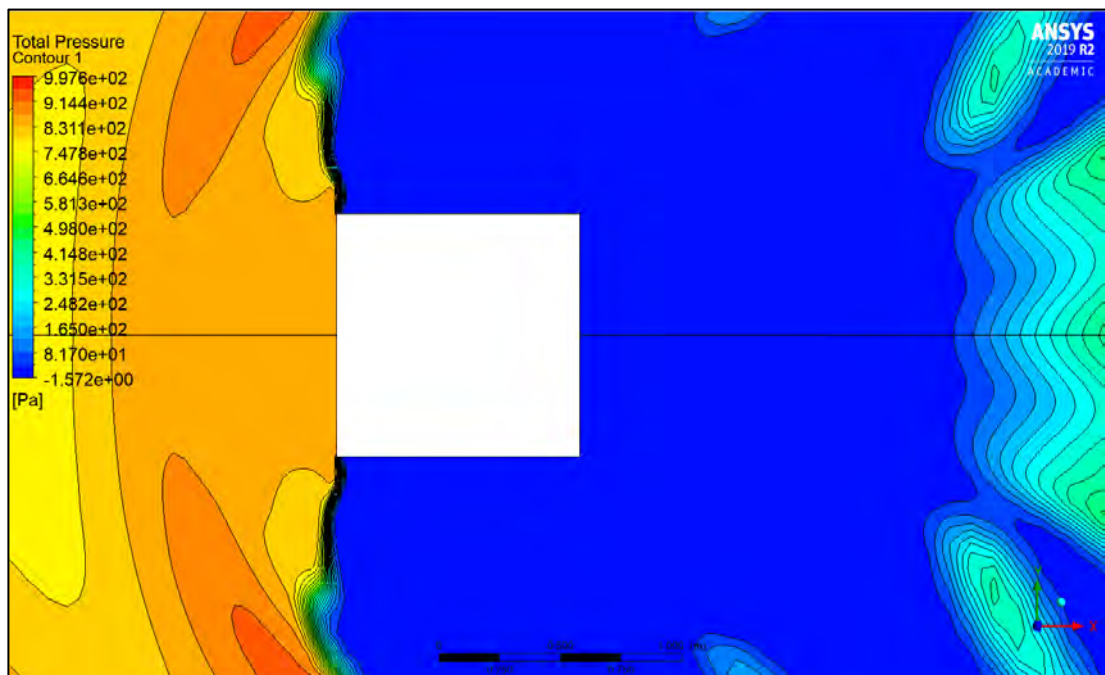


Figure 4.7.36: Pressure contour at $z = 0.5$ m along rectangular section with $Fr = 0.55$

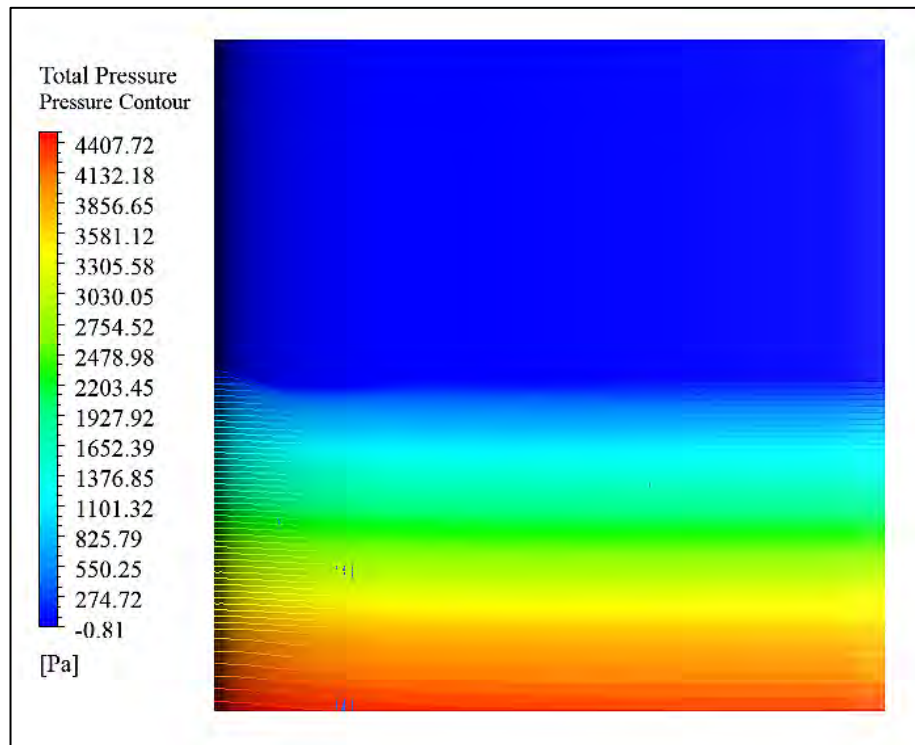


Figure 4.7.37: Pressure contour on the surface of NACA 0012 airfoil section at $Fr = 0.19$

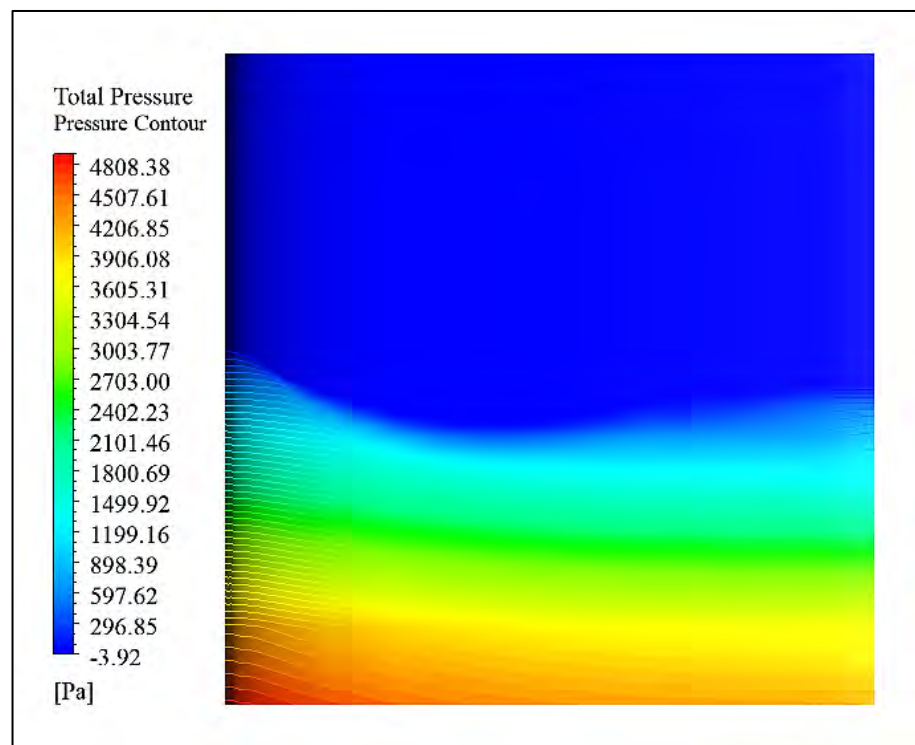


Figure 4.7.38: Pressure contour on the surface of NACA 0012 airfoil section at $Fr = 0.37$

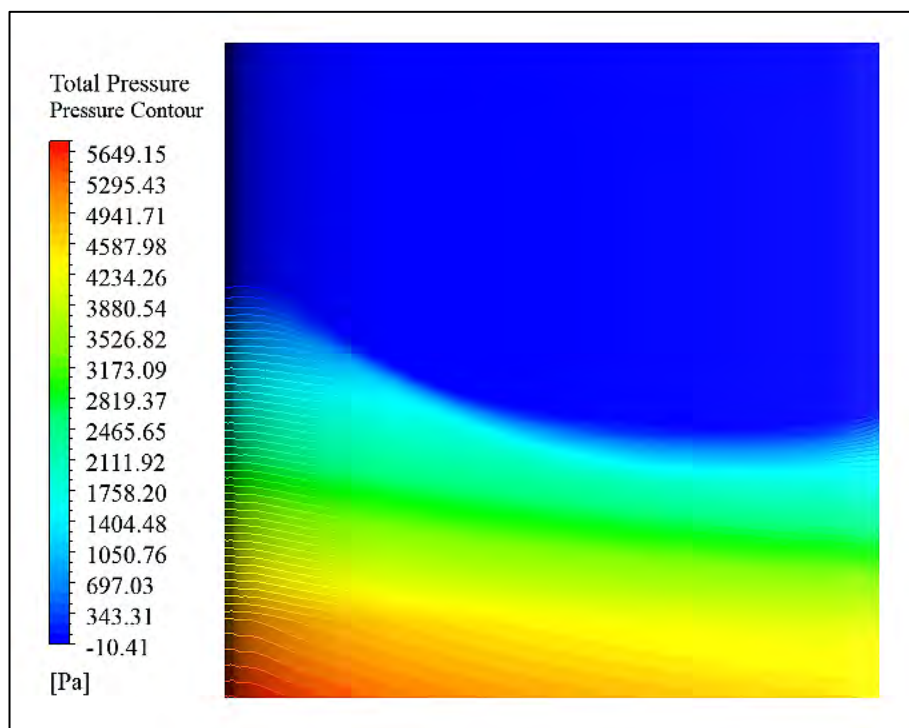


Figure 4.7.39: Pressure contour on the surface of NACA 0012 airfoil section at $Fr = 0.55$

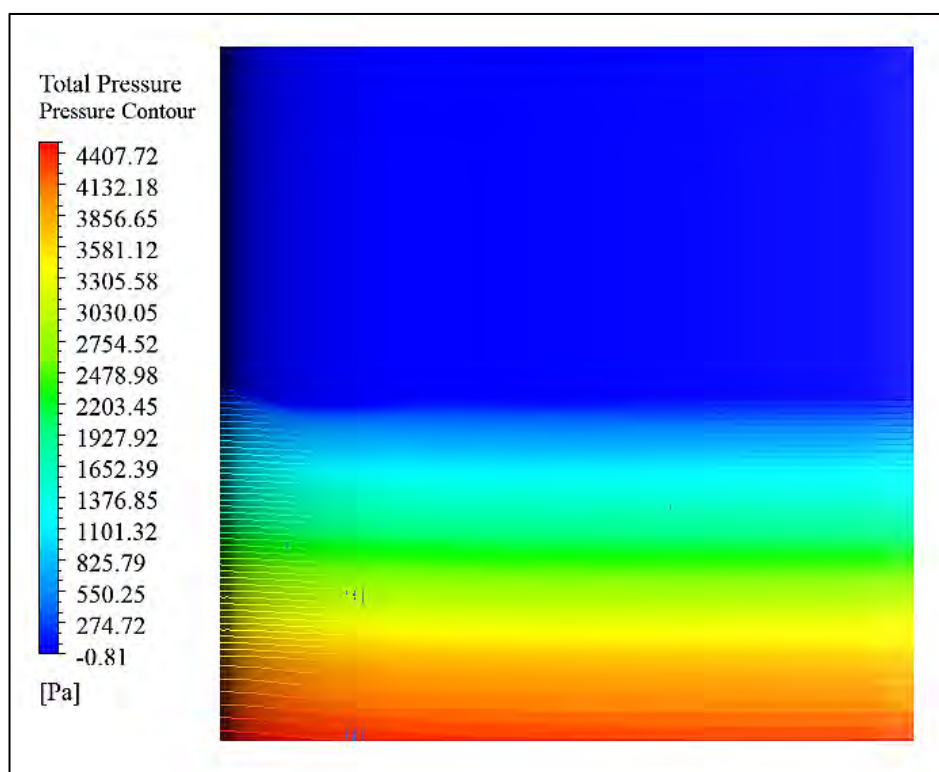


Figure 4.7.40: Pressure contour on the surface of NACA 0018 airfoil section at $Fr = 0.19$

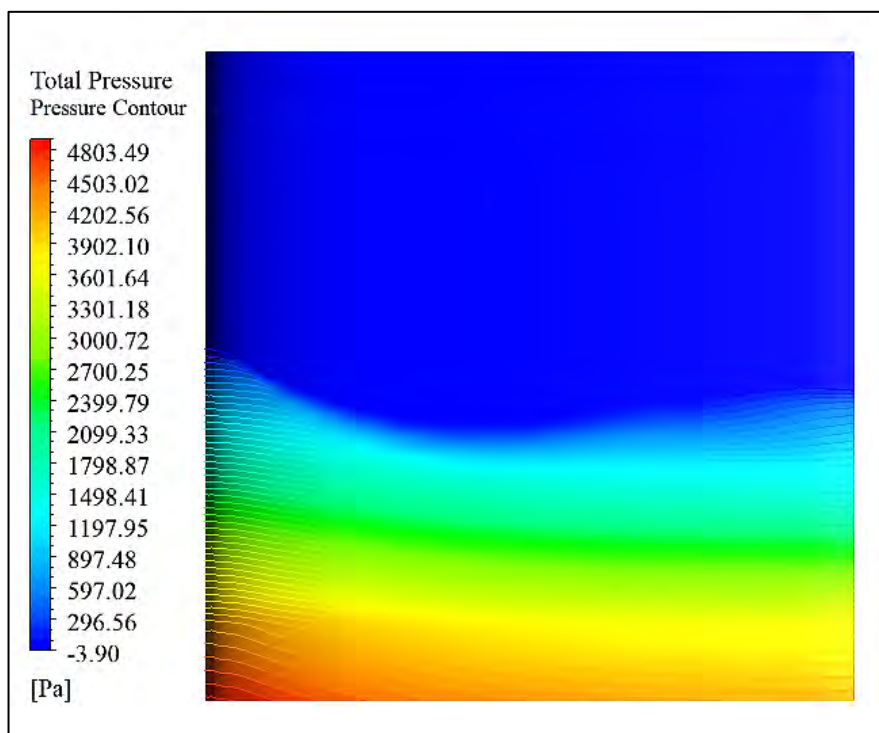


Figure 4.7.41: Pressure contour on the surface of NACA 0018 airfoil section at $Fr = 0.37$

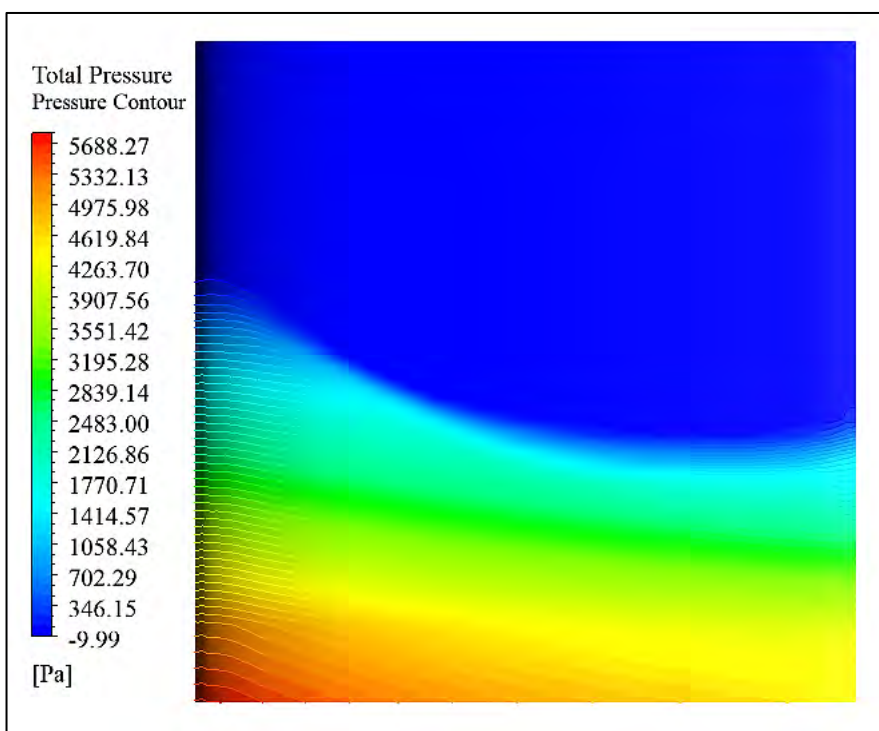


Figure 4.7.42: Pressure contour on the surface of NACA 0018 airfoil section at $Fr = 0.55$

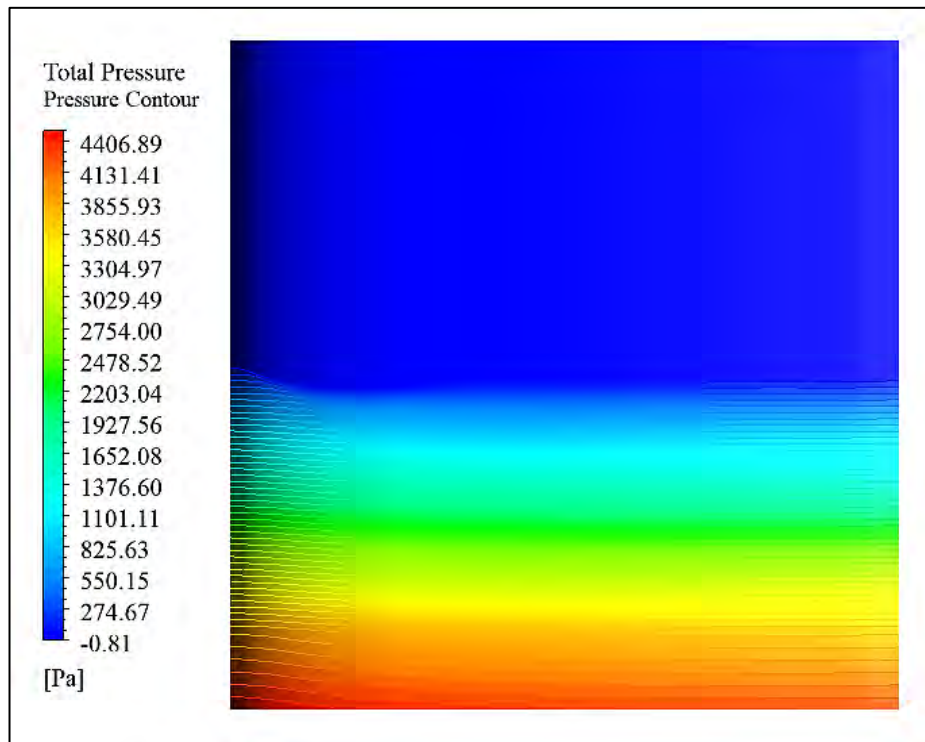


Figure 4.7.43: Pressure contour on the surface of NACA 0024 airfoil section at $Fr = 0.19$

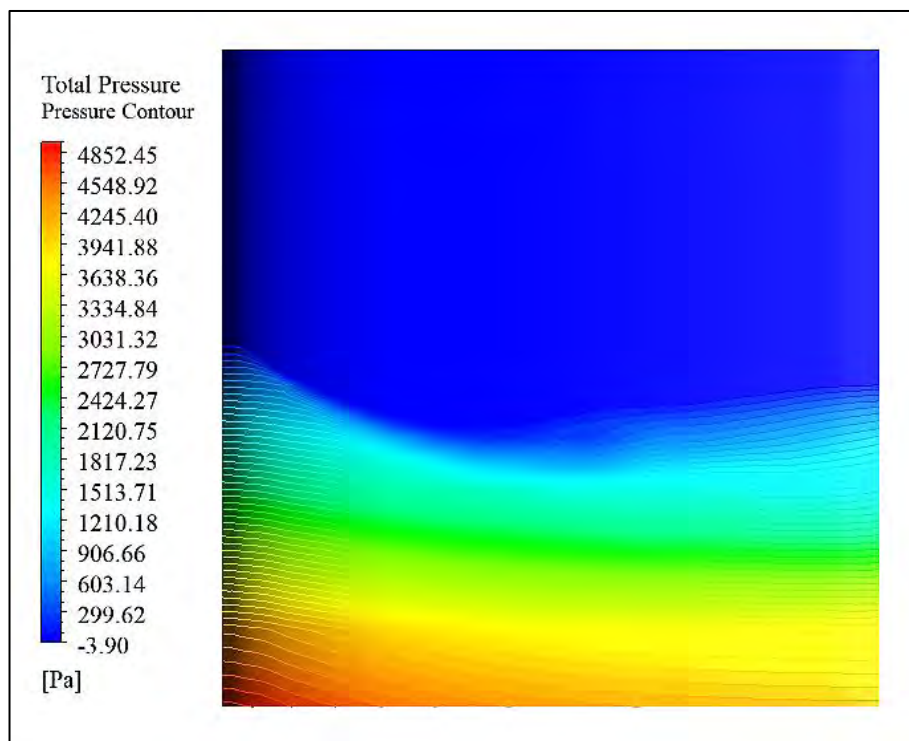


Figure 4.7.44: Pressure contour on the surface of NACA 0024 airfoil section at $Fr = 0.37$

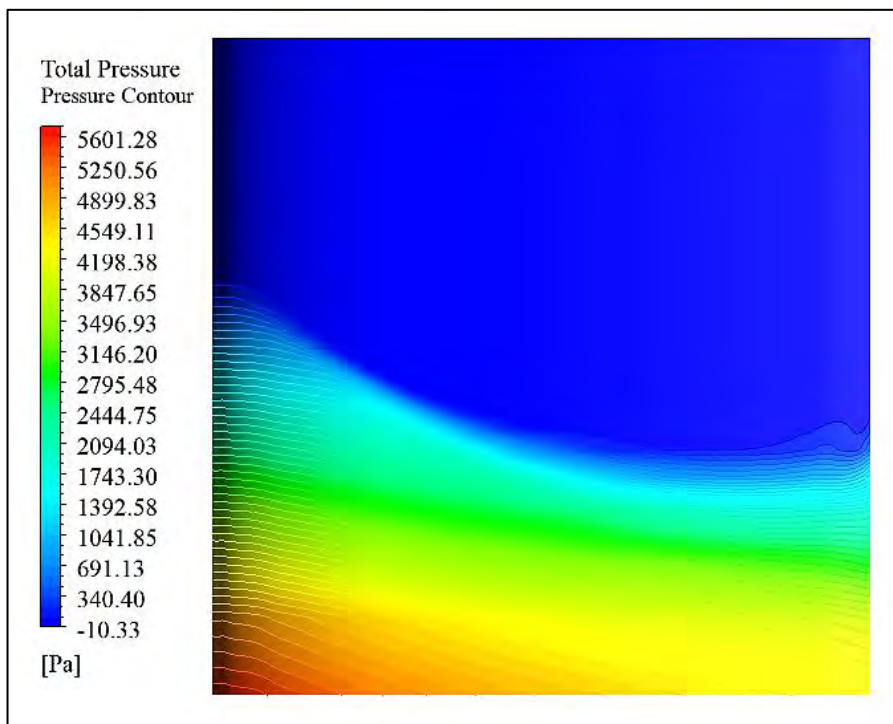


Figure 4.7.45 Pressure contour on the surface of NACA 0024 airfoil section at $Fr = 0.55$

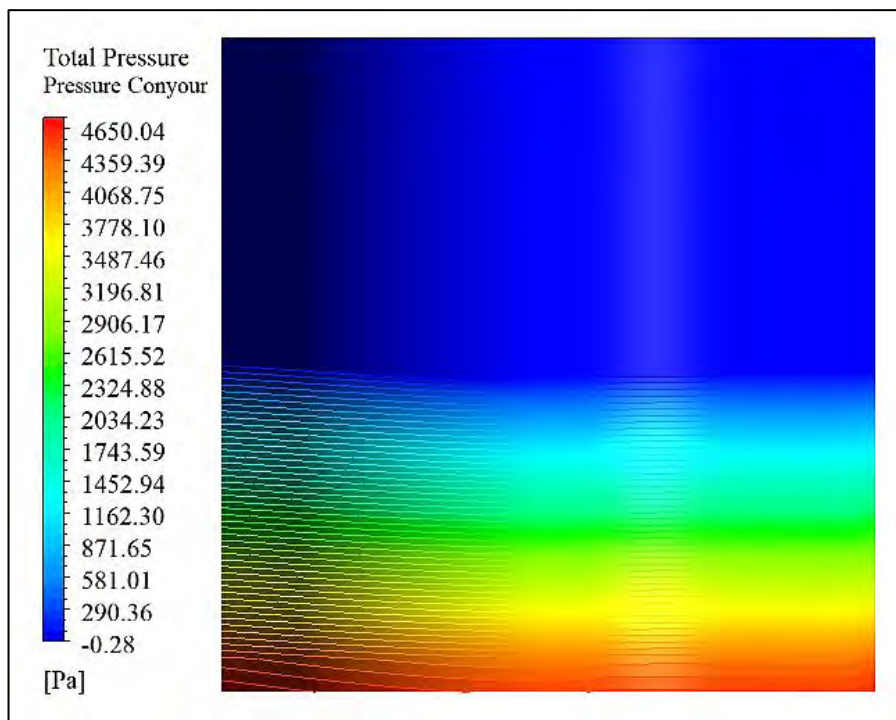


Figure 4.7.46: Pressure contour on the surface of circular cylindrical section at $Fr = 0.19$

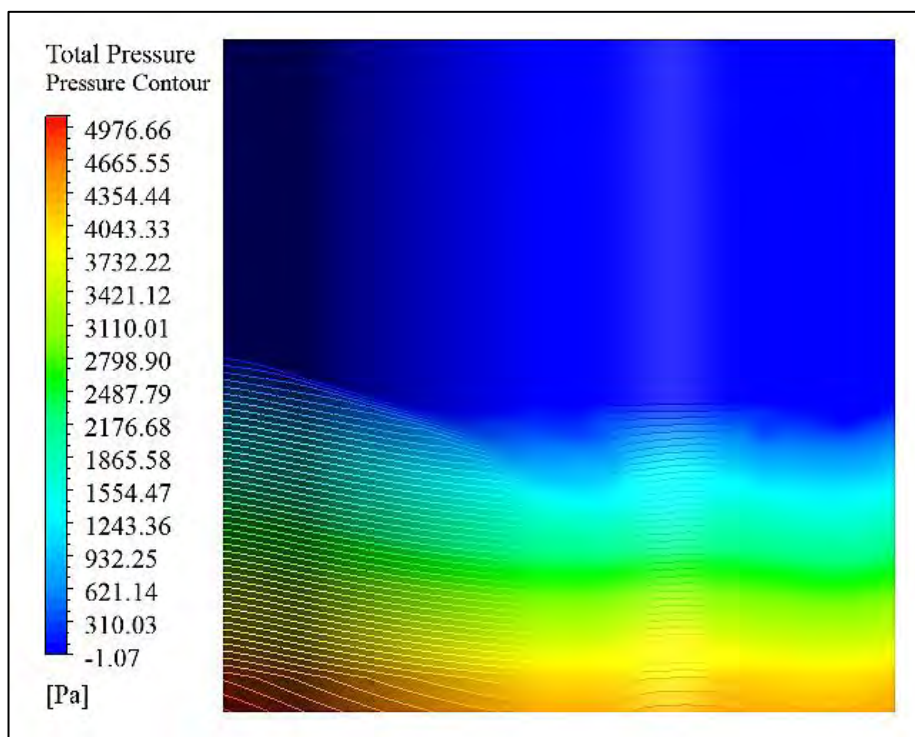


Figure 4.7.47: Pressure contour on the surface of circular cylindrical section at $Fr = 0.37$

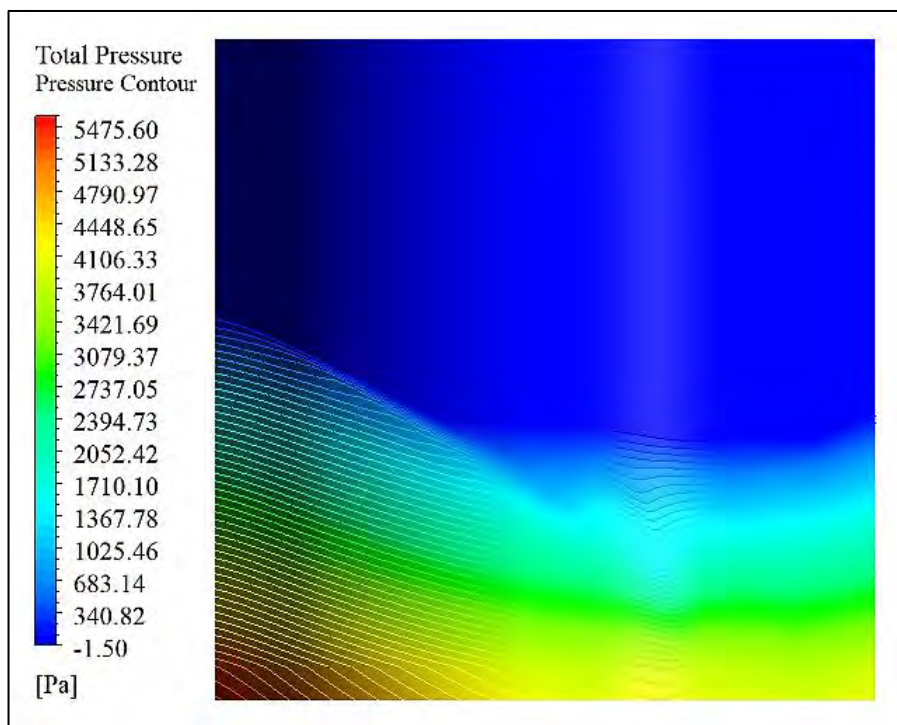


Figure 4.7.48: Pressure contour on the surface of circular cylindrical section at $Fr = 0.55$

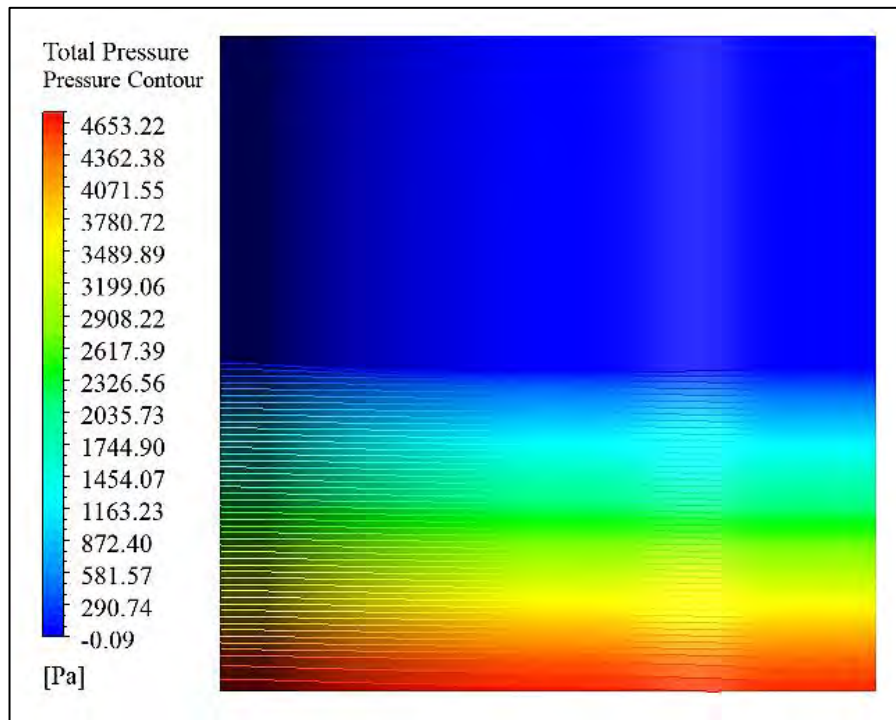


Figure 4.7.49: Pressure contour on the surface of elliptical section at $Fr = 0.19$

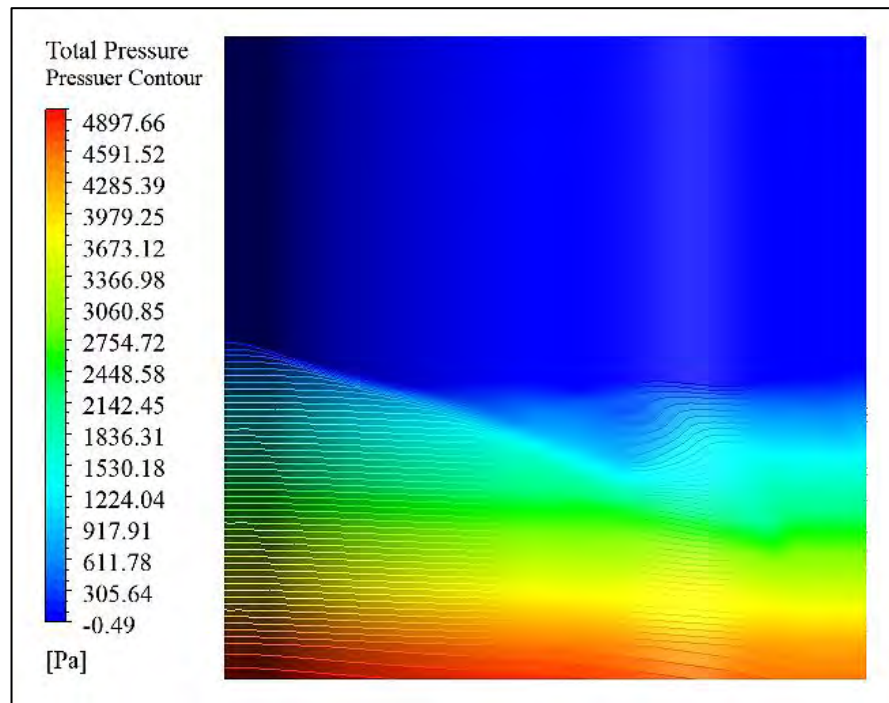


Figure 4.7.50: Pressure contour on the surface of elliptical section at $Fr = 0.37$

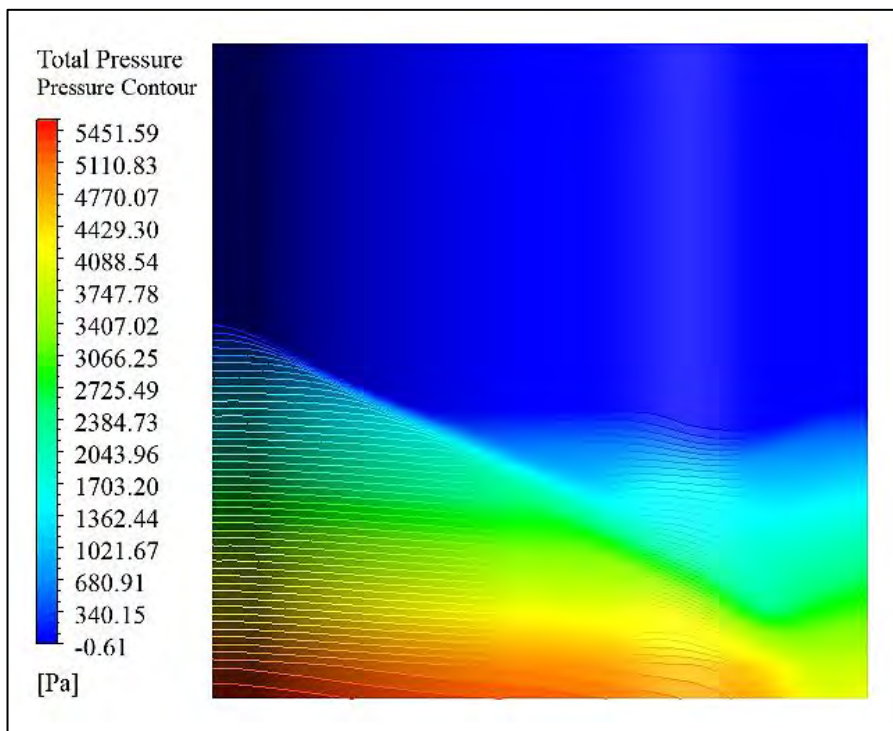


Figure 4.7.51: Pressure contour on the surface of elliptical section at $Fr = 0.55$

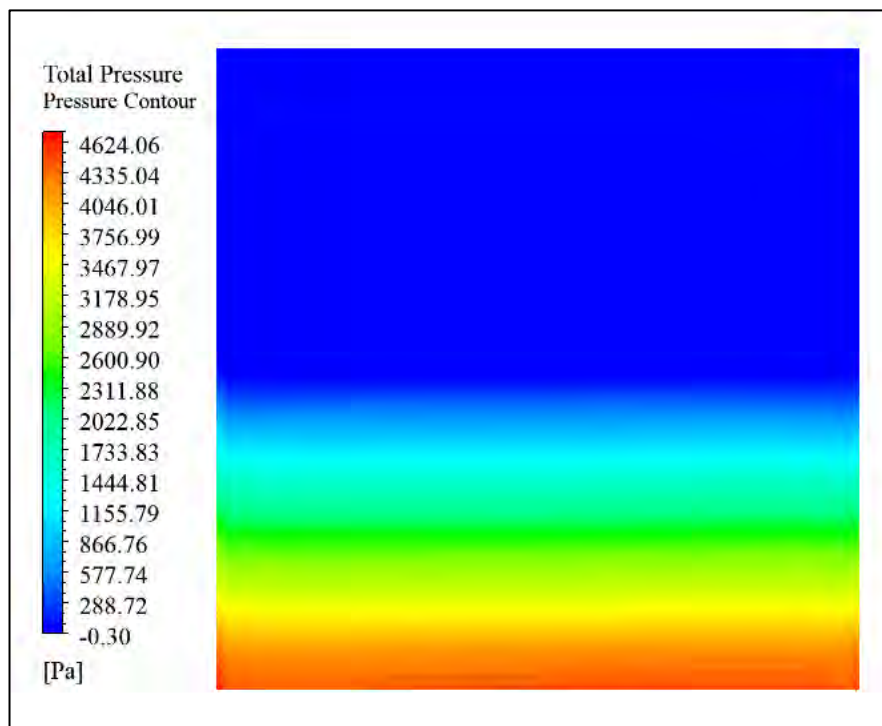


Figure 4.7.52: Pressure contour on the surface of rectangular section at $Fr = 0.19$

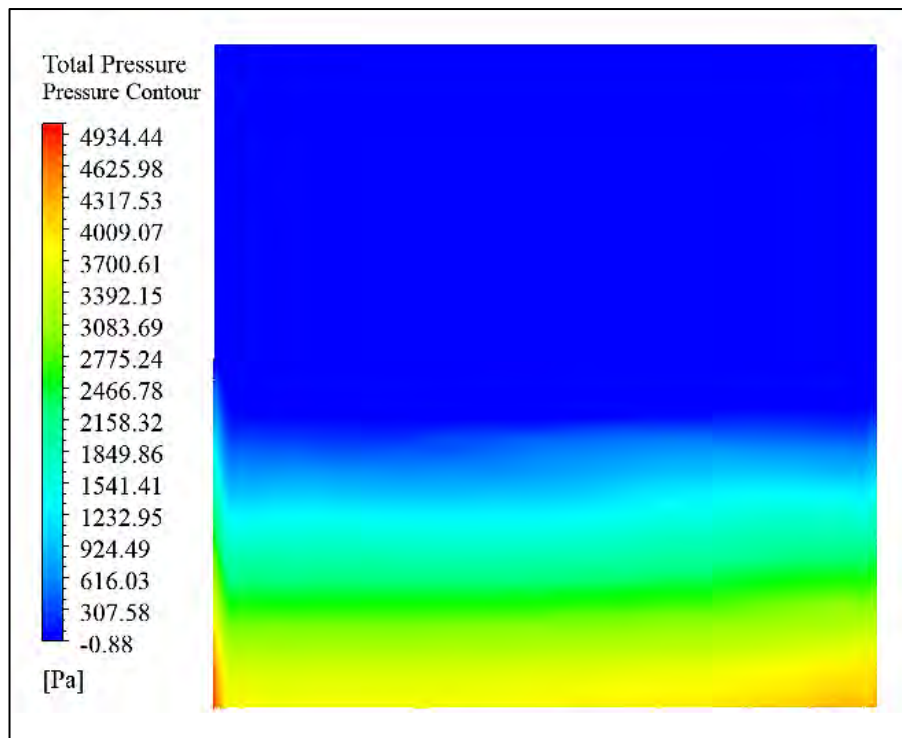


Figure 4.7.53: Pressure contour on the surface of rectangular section at $Fr = 0.37$

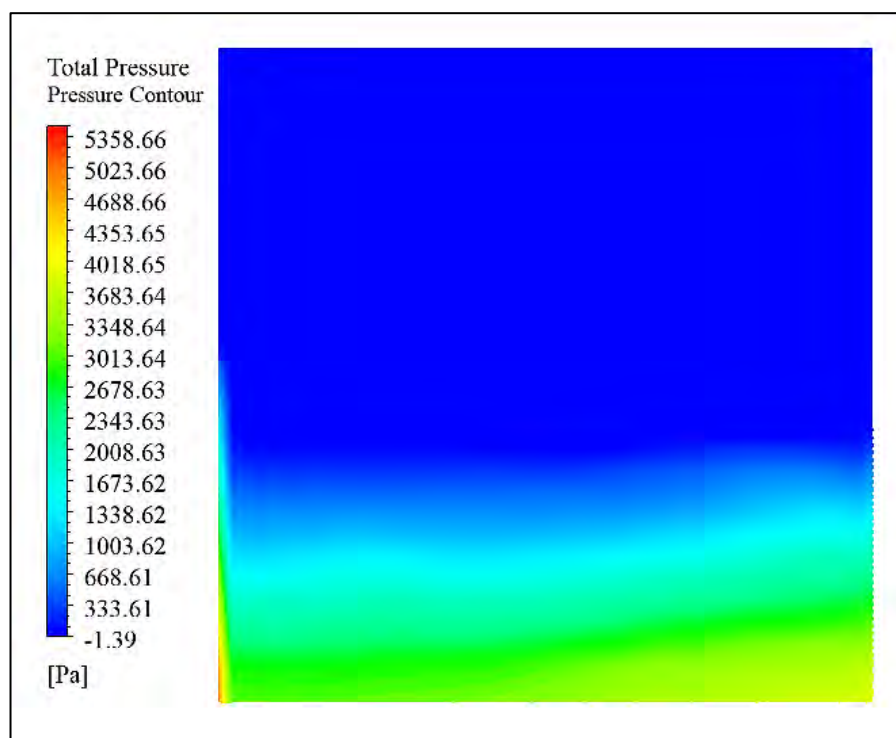


Figure 4.7.54: Pressure contour on the surface of rectangular section at $Fr = 0.55$

4.8 Contour of X-Wall Shear Stress

Figure 4.8.1, 4.8.2, and 4.8.3 represent the X-wall shear stresses along NACA 0024 airfoil section at different Froude numbers. The separation regions are also marked where the shear stress values are negative. For $Fr = 0.19$, the separation occurs at about $x/L = 0.87$ around the foil and the separation zone is very small and the wave effects are insignificant. But with the increase in Froude number, the wave effects become significant and the separation zone extended. For $Fr = 0.37$, the separation occurs at about $x/L = 0.25$ and at about $x/L = 0.62$ for $Fr = 0.55$.

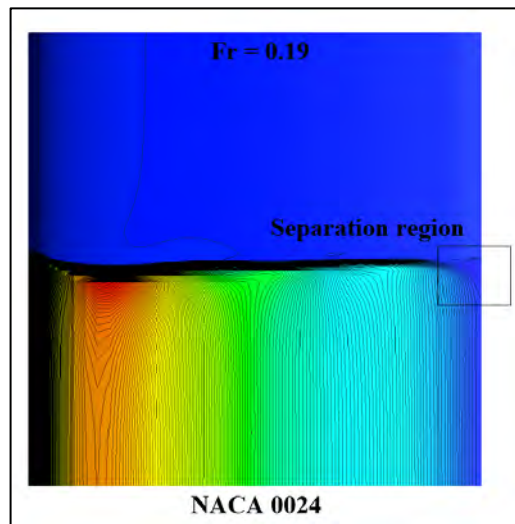


Figure 4.8.1: X-wall shear stress along NACA 0024 airfoil section at $Fr = 0.19$

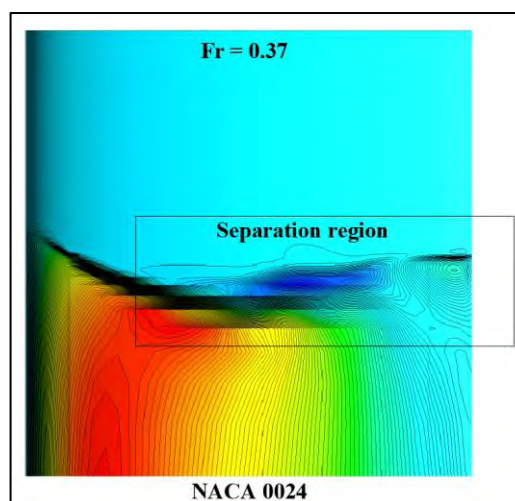


Figure 4.8.2: X-wall shear stress along NACA 0024 airfoil section at $Fr = 0.37$

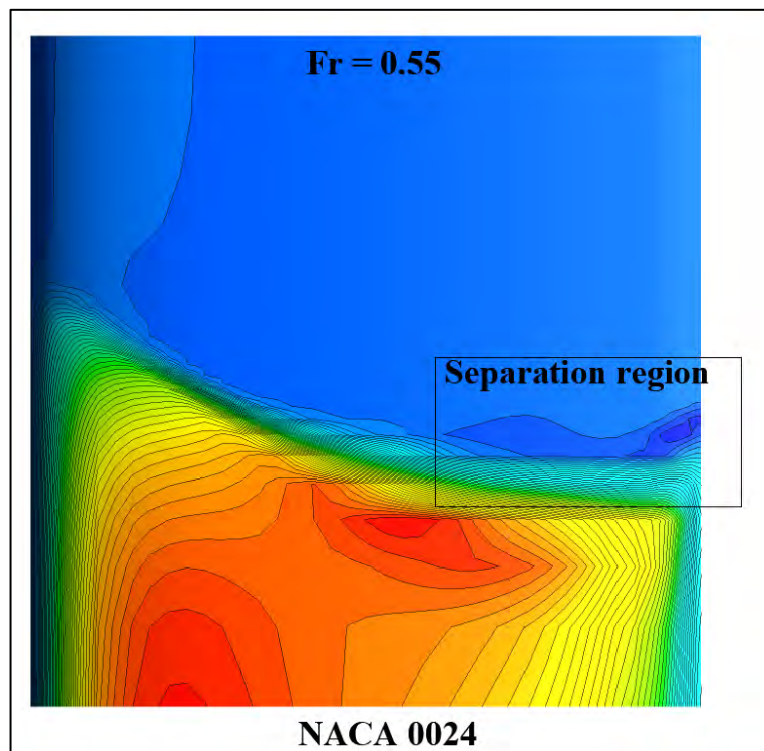


Figure 4.8.3: X-wall shear stress along NACA 0024 airfoil section at $Fr = 0.55$

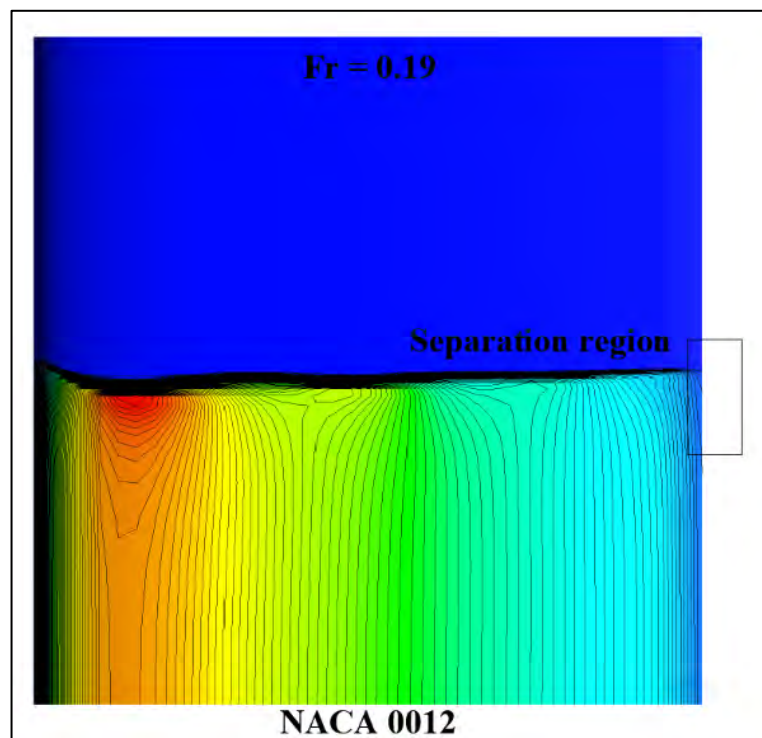


Figure 4.8.4: X-wall shear stress along NACA 0012 airfoil section at $Fr = 0.19$

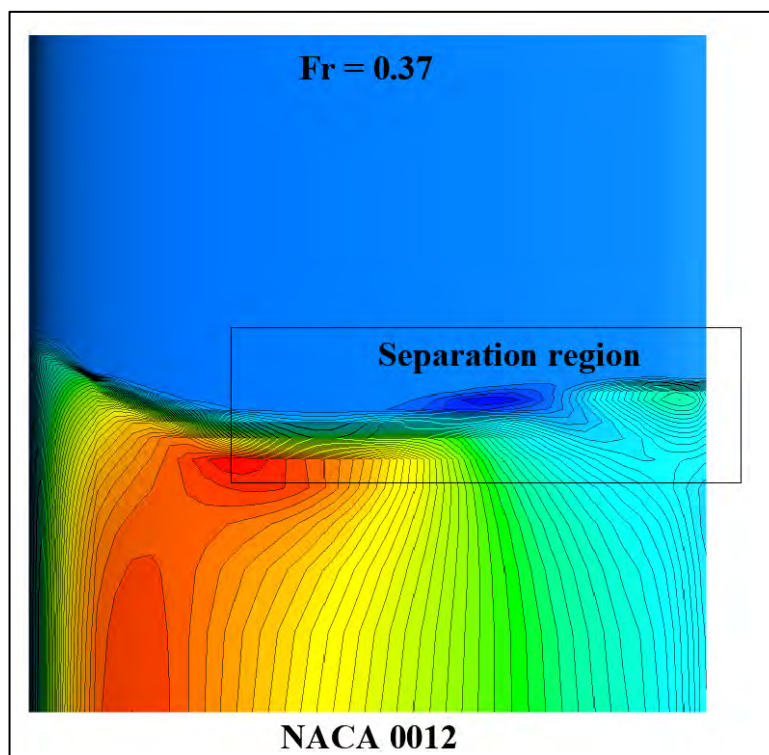


Figure 4.8.5: X-wall shear stress along NACA 0012 airfoil section at $Fr = 0.37$

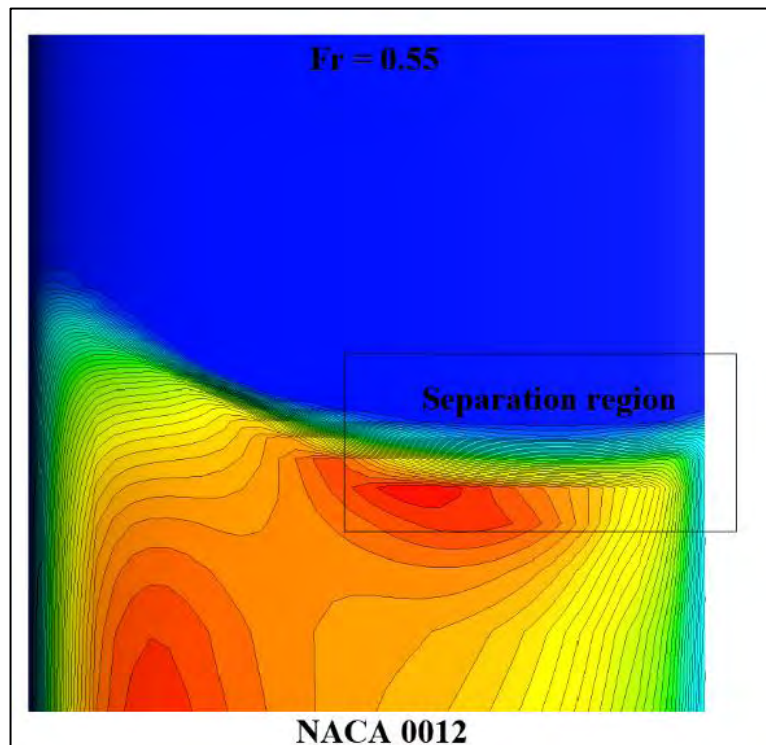


Figure 4.8.6: X-wall shear stress along NACA 0012 airfoil section at $Fr = 0.55$

Figure 4.8.4, 4.8.5, and 4.8.6 show the X-wall shear stresses along NACA 0012 foil at different Froude numbers. The separation occurs at about $x/L = 0.92$ for $Fr = 0.19$. The separation is very little for low Froude numbers but it becomes significant for higher Froude numbers and the separation zone extends. Thus the X-wall shear stress is pretty much similar regardless of the thickness and dependent on Fr instead of thickness of the body. For $Fr = 0.37$ and $Fr = 0.55$, the separation regions begin from about $x/L = 0.31$ and $x/L = 0.49$ respectively.

Figure 4.8.7, 4.8.8, and 4.8.9 represent the X-wall shear stresses along NACA 0018 foil at different Froude numbers. For $Fr = 0.19$, the separation occurs at about $x/L = 0.96$ and the separation region is too small. For higher Froude numbers, the separation region extends and becomes dependent of Fr regardless of the thickness. The separations occur for $Fr = 0.37$ and $Fr = 0.55$ at about $x/L = 0.32$ and $x/L = 0.53$ respectively.

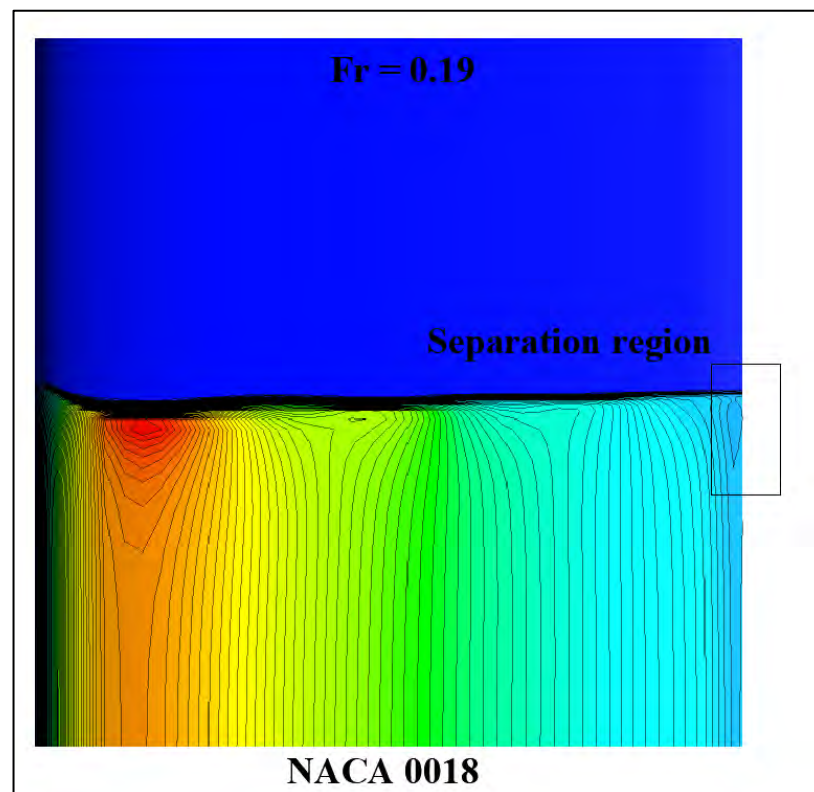


Figure 4.8.7: X-wall shear stress along NACA 0018 airfoil section at $Fr = 0.19$

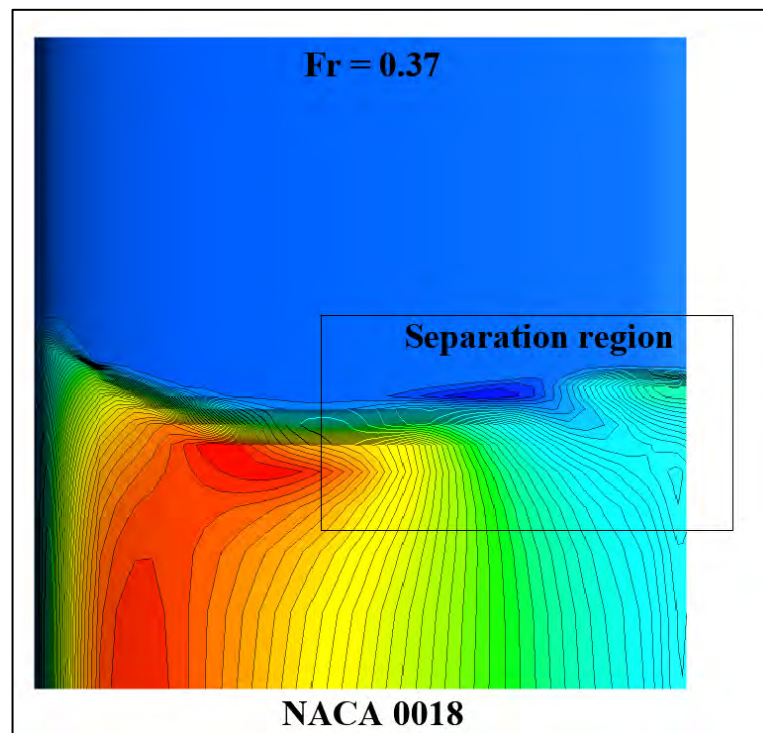


Figure 4.8.8: X-wall shear stress along NACA 0018 airfoil section at $Fr = 0.37$

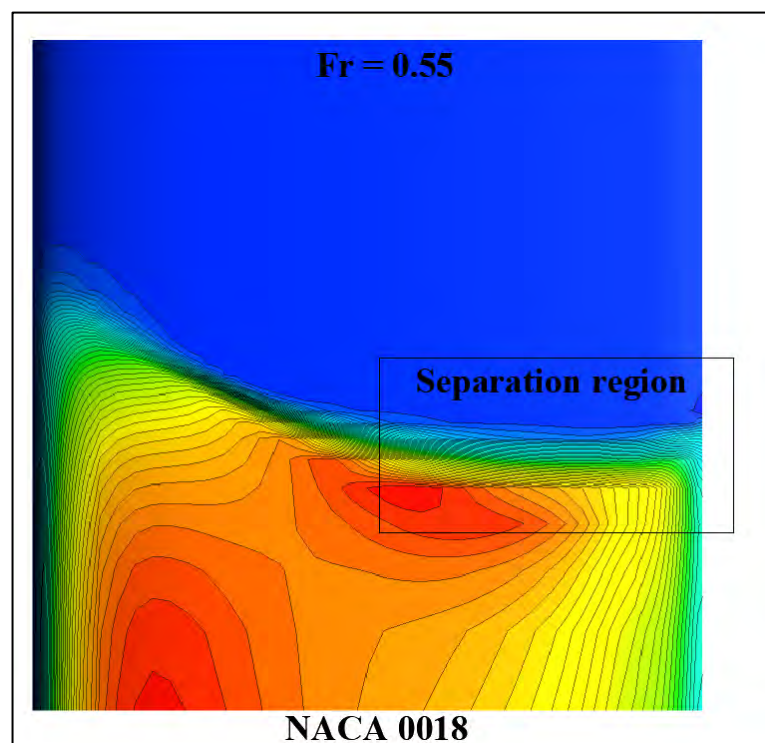


Figure 4.8.9: X-wall shear stress along NACA 0018 airfoil section at $Fr = 0.55$

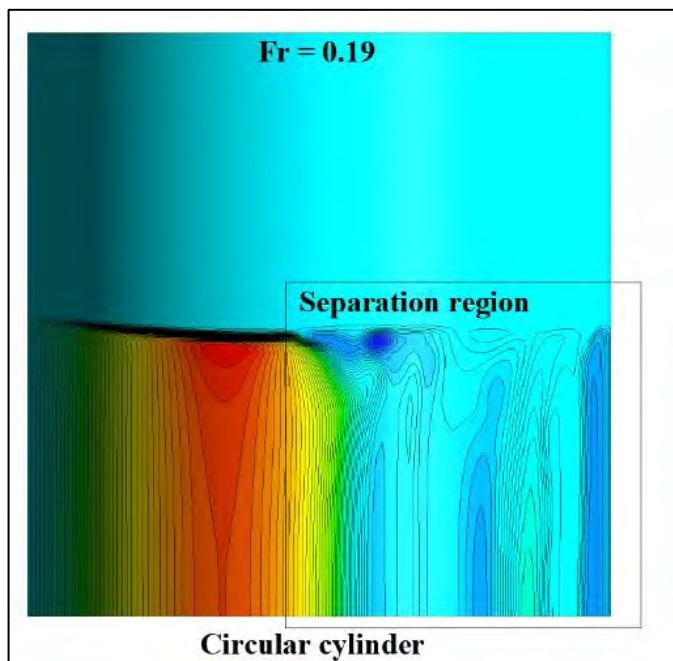


Figure 4.8.10: X-wall shear stress along circular cylinder section at $Fr = 0.19$

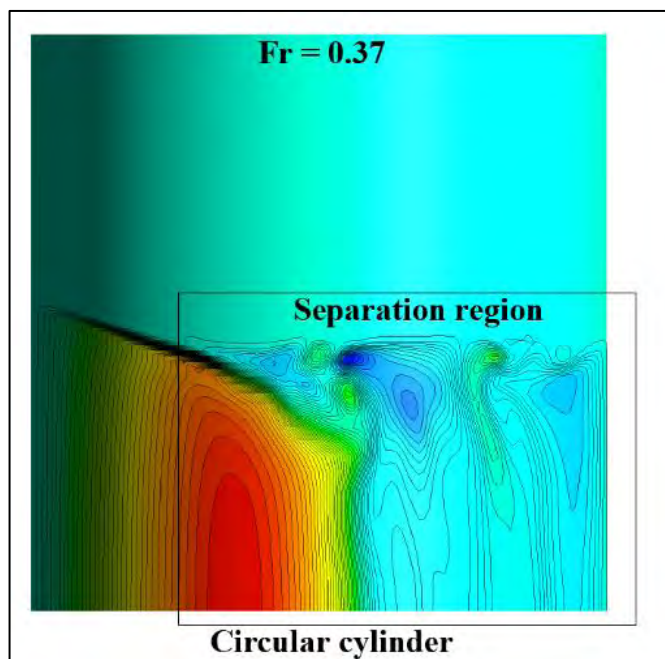


Figure 4.8.11: X-wall shear stress along circular cylinder section at $Fr = 0.37$

Figure 4.8.10, 4.8.11, and 4.8.12 show the X-wall shear stresses for circular cylinder section at different Froude numbers. For $Fr = 0.19$, the separation occurs at $x/L = 0.46$. It shows that the separation region and the effects of wave depend on shape instead of

Froude number at low Froude numbers due to the blunt shape of the cylinder. But with the increase in Froude number, the wave effects are dependent on Fr and the separation region extends. For $Fr = 0.37$ and for $Fr = 0.55$, the separation occurs at $x/L = 0.27$ and $x/L = 0.41$ respectively.

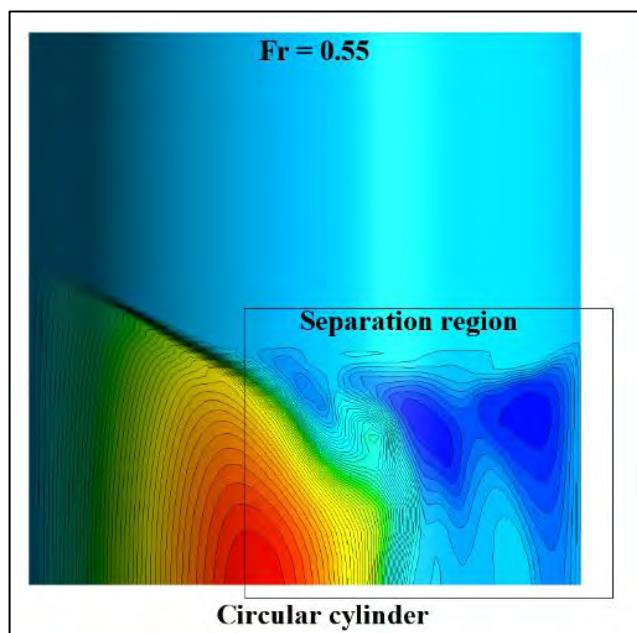


Figure 4.8.12: X-wall shear stress along circular cylinder section at $Fr = 0.55$

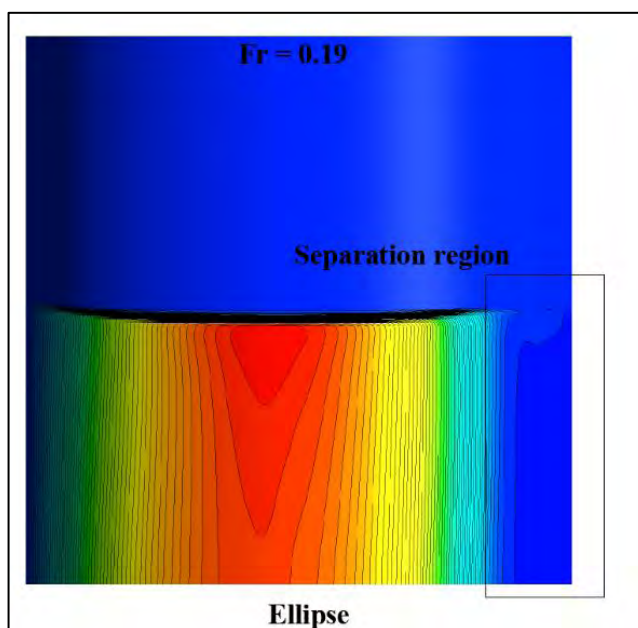


Figure 4.8.13: X-wall shear stress along elliptical section at $Fr = 0.19$

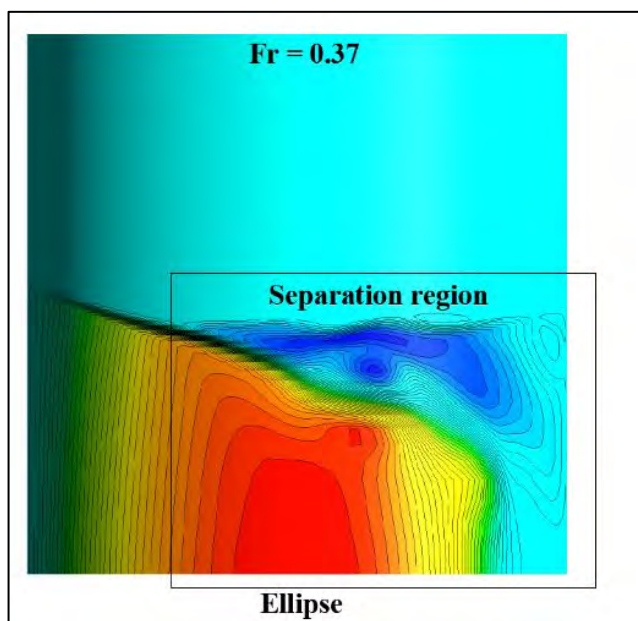


Figure 4.8.14: X-wall shear stress along elliptical section at $Fr = 0.37$

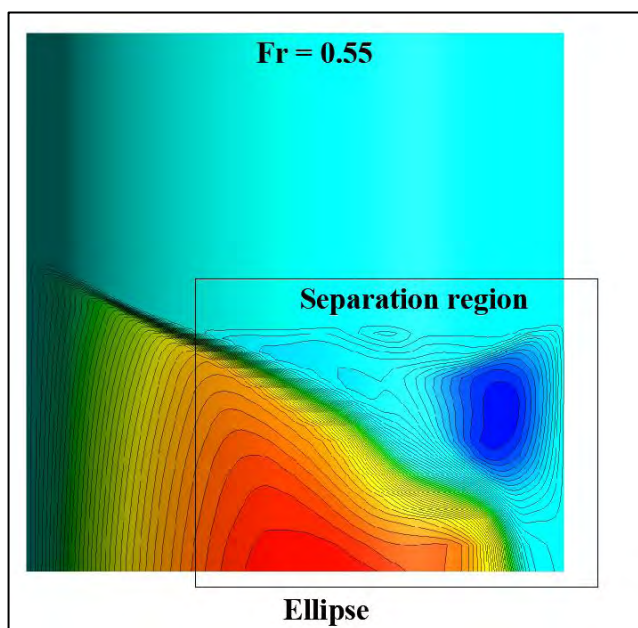


Figure 4.8.15: X-wall shear stress along elliptical section at $Fr = 0.55$

Figure 4.8.13, 4.8.14, and 4.8.15 represent the X-wall shear stresses along elliptical section at different Froude numbers. For $Fr = 0.19$, the separation region is very small and it occurs at about $x/L = 0.87$. The separation region and the water deformation depend on shape of the body at low Froude numbers. But with the increase in Froude number, the separation region also increases. The wave effects become more

complicated and dependent of Fr . The separation occurs at about $x/L = 0.29$ and $x/L = 0.33$ for $Fr = 0.37$ and $Fr = 0.55$ respectively.

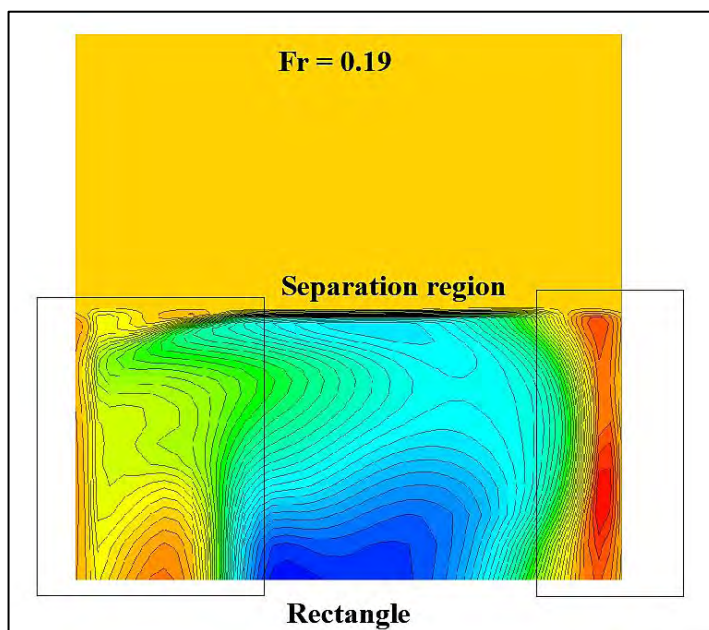


Figure 4.8.16: X-wall shear stress along rectangular section at $Fr = 0.19$

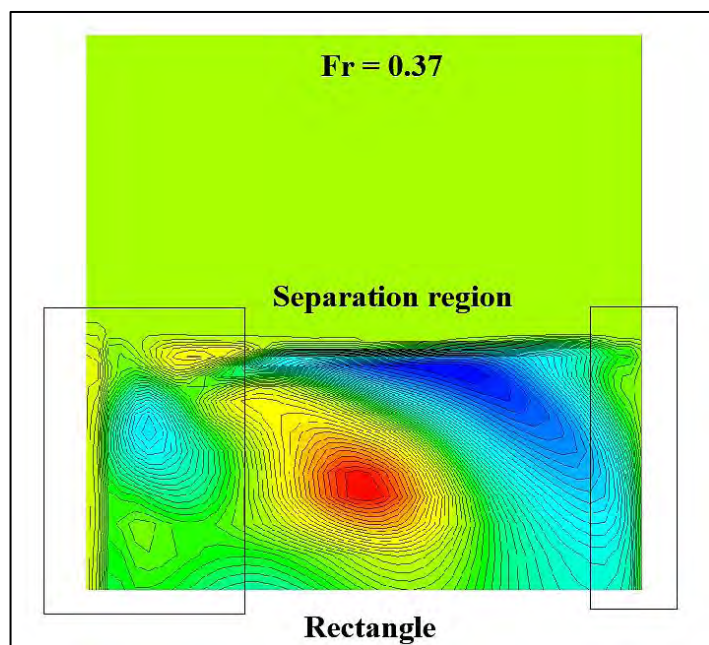


Figure 4.8.17: X-wall shear stress along rectangular section at $Fr = 0.37$

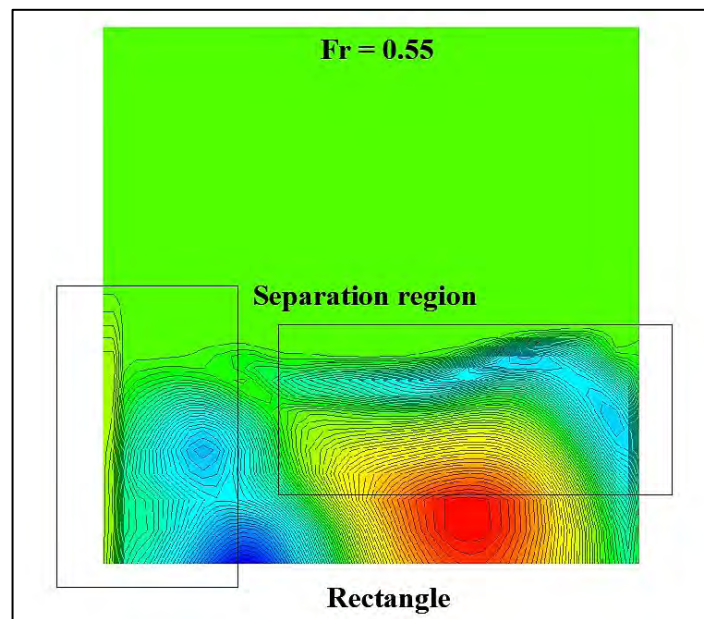


Figure 4.8.18: X-wall shear stress along rectangular section at $Fr = 0.55$

Figure 4.8.16, 4.8.17, and 4.8.18 represent the X-wall shear stresses at different Froude numbers ($Fr = 0.19, 0.37,$ and 0.55) in case of a surface piercing body with rectangular cross – section. At low Froude number, $Fr = 0.19$, the separation occurs at $x/L = 0.022$ and at $x/L = 0.88$. Thus at low Froude number, the wave effects become a function of shape instead of Froude number. But with the increase in Froude number, $Fr = 0.55$, the separation region expands and the wave effects become a function of Froude number. At $Fr = 0.55$, the separation region occurs at $x/L = 0.039$ and $x/L = 0.33$.

4.9 Velocity Vector

After simulation, from the velocity vector (Figure 4.9.1 – 4.9.18), it is clearly seen that the velocity vector is symmetrical about the center line. From the figures, we can see that backflow occurs in case of circular cylinder, elliptical and rectangular section and thus vortex is created. It is also seen that for $Fr = 0.19$, the pattern is pretty much similar for all airfoil sections and depends on thickness or shape but on Froude number. For higher Froude number, the pattern shows distinct separation at the end of the body and depends on Fr instead of thickness or shape and the gravity effects dominates the pattern. The pressure distribution is limited to the free – surface only.

The thickness and shape effects are noticeable in the bow wave peak, extent of the free – surface, at the wake region, and also in the separation region.

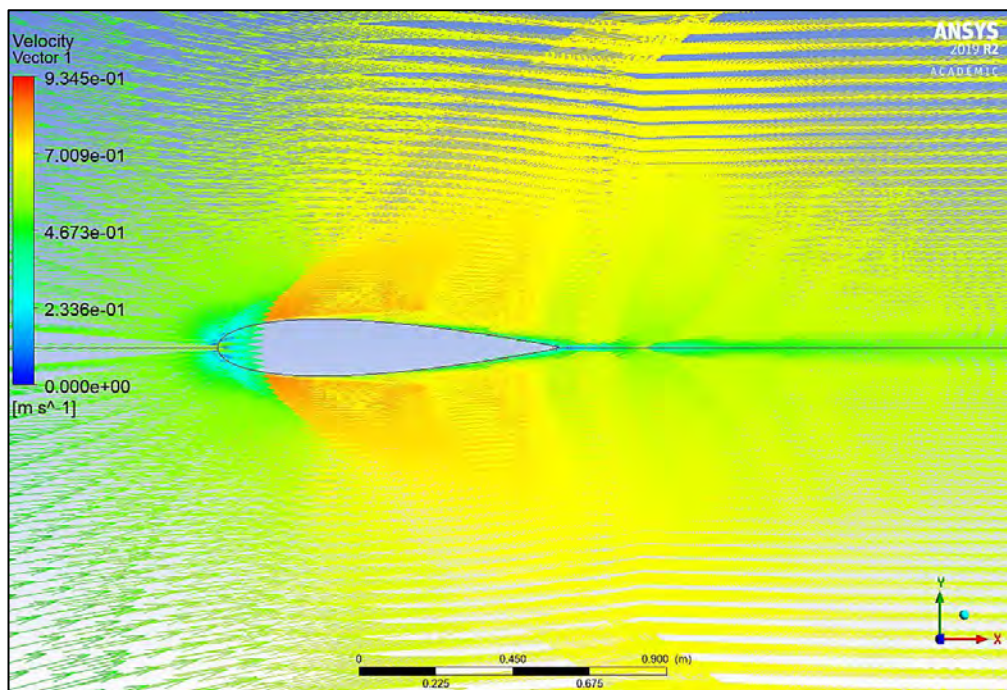


Figure 4.9.1: Velocity vector for surface piercing body with NACA 0012 airfoil section at $Fr = 0.19$

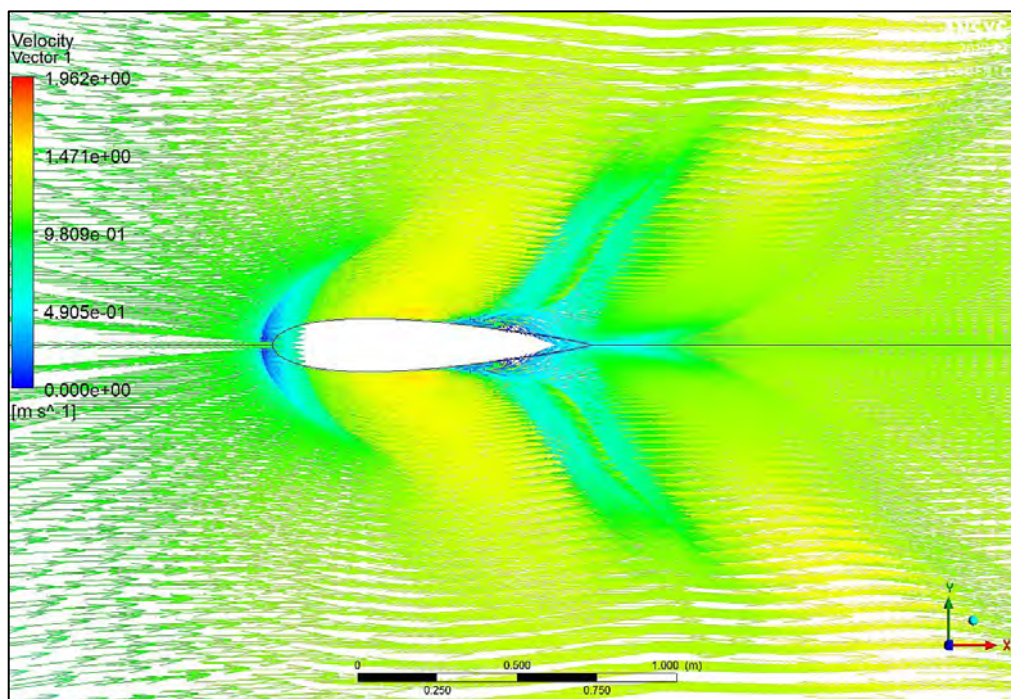


Figure 4.9.2: Velocity vector for surface piercing body with NACA 0012 airfoil section at $Fr = 0.37$

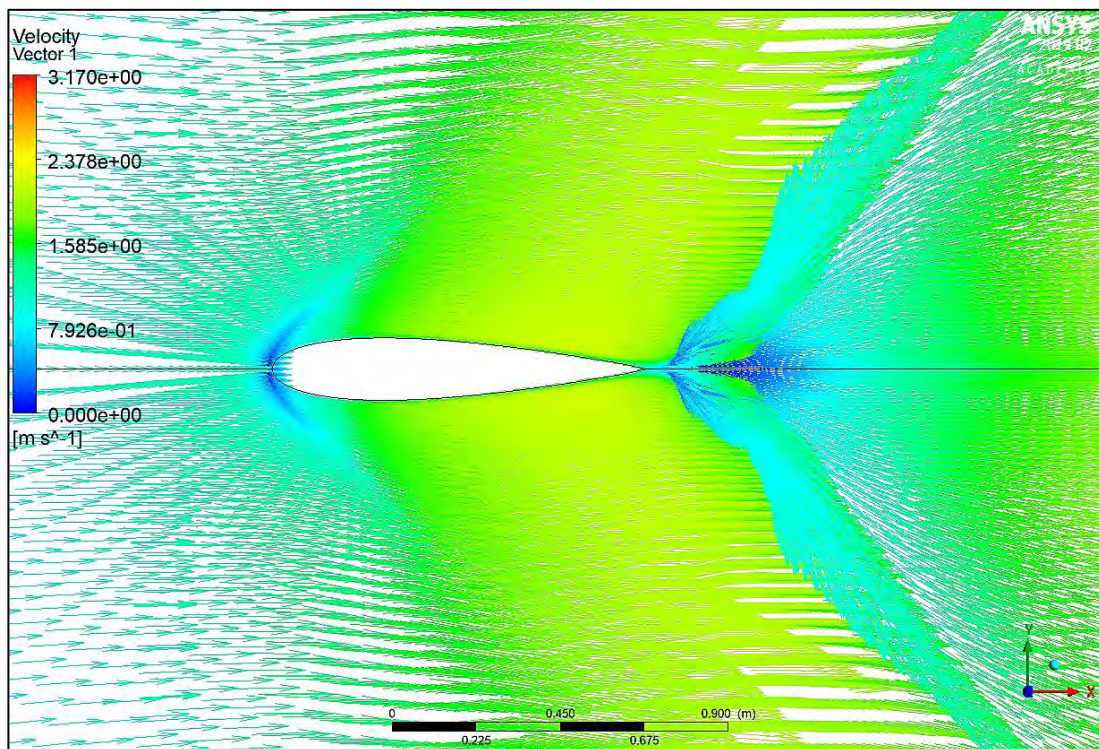


Figure 4.9.3: Velocity vector for surface piercing body with NACA 0012 airfoil section at $Fr = 0.55$

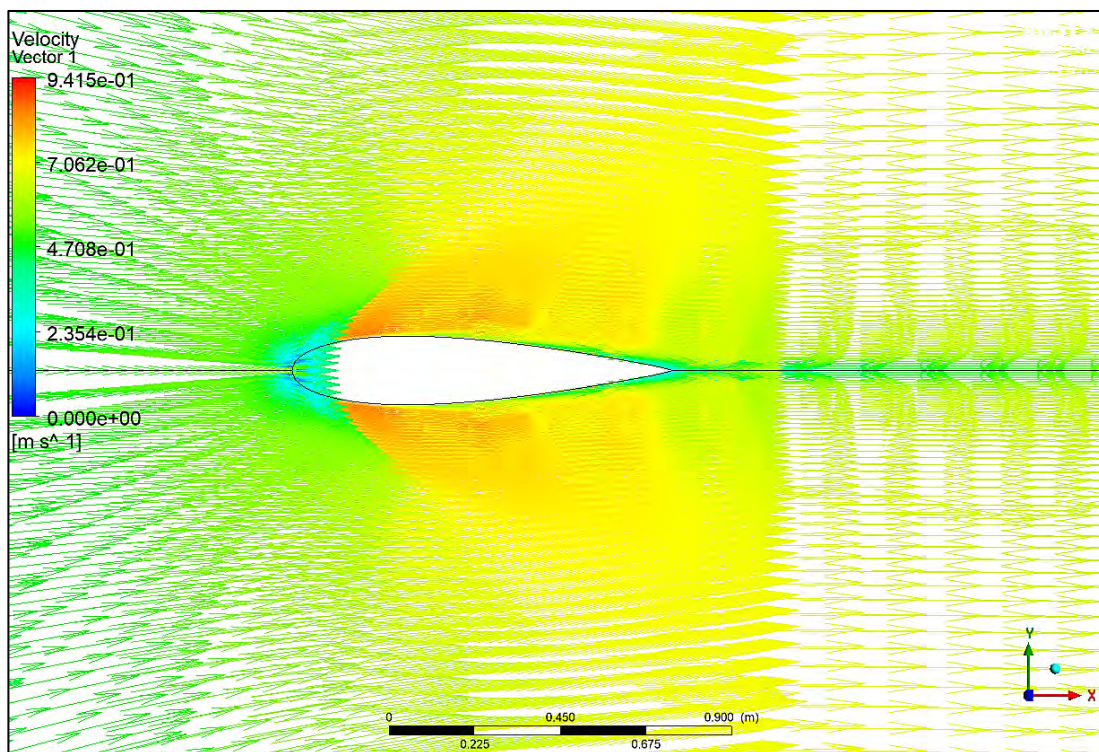


Figure 4.9.4: Velocity vector for surface piercing body with NACA 0018 airfoil section at $Fr = 0.19$

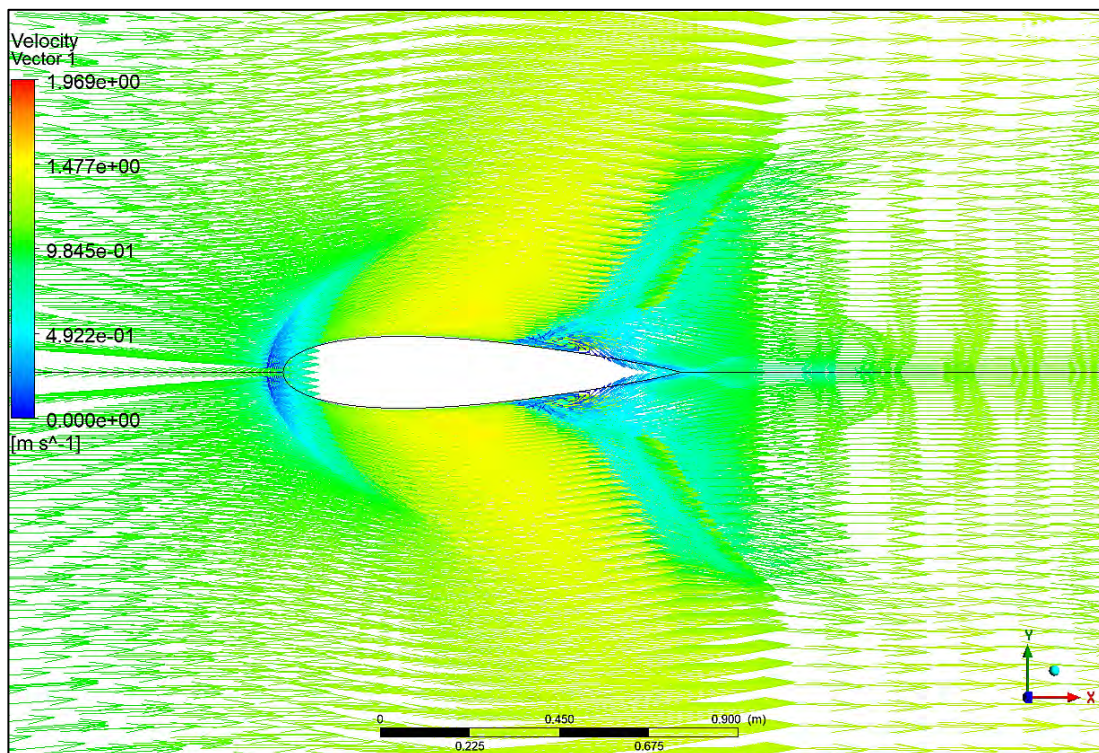


Figure 4.9.5: Velocity vector for surface piercing body with NACA 0018 airfoil section at $Fr = 0.37$

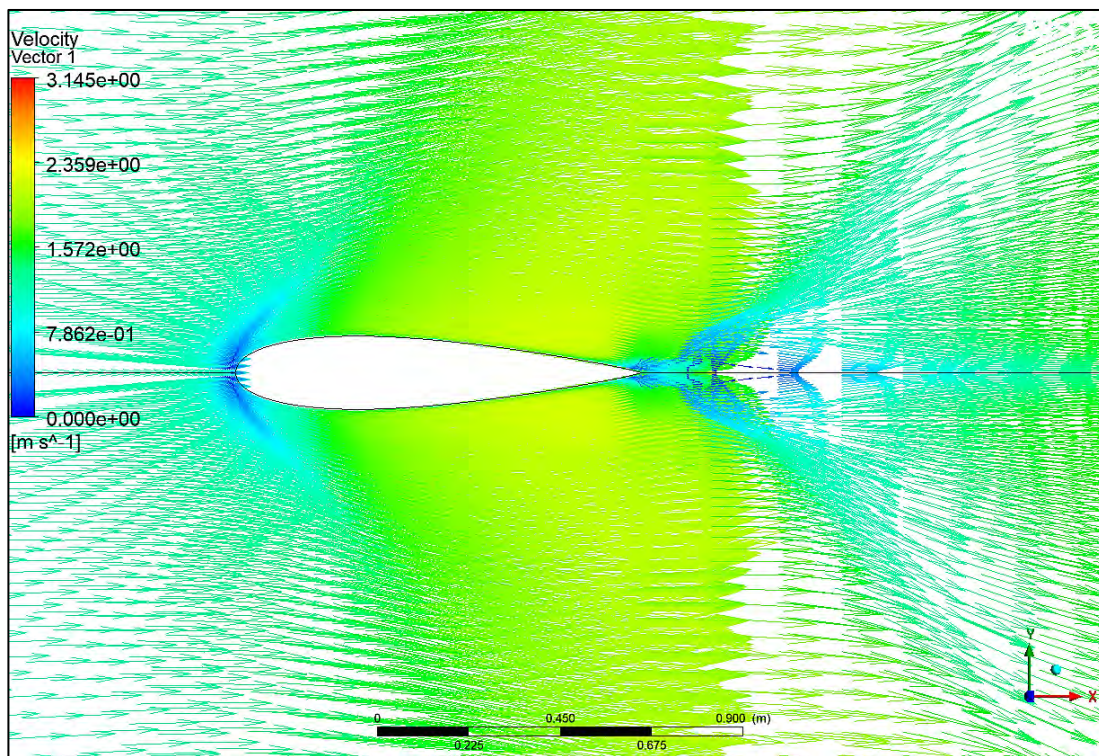


Figure 4.9.6: Velocity vector for surface piercing body with NACA 0018 airfoil section at $Fr = 0.55$

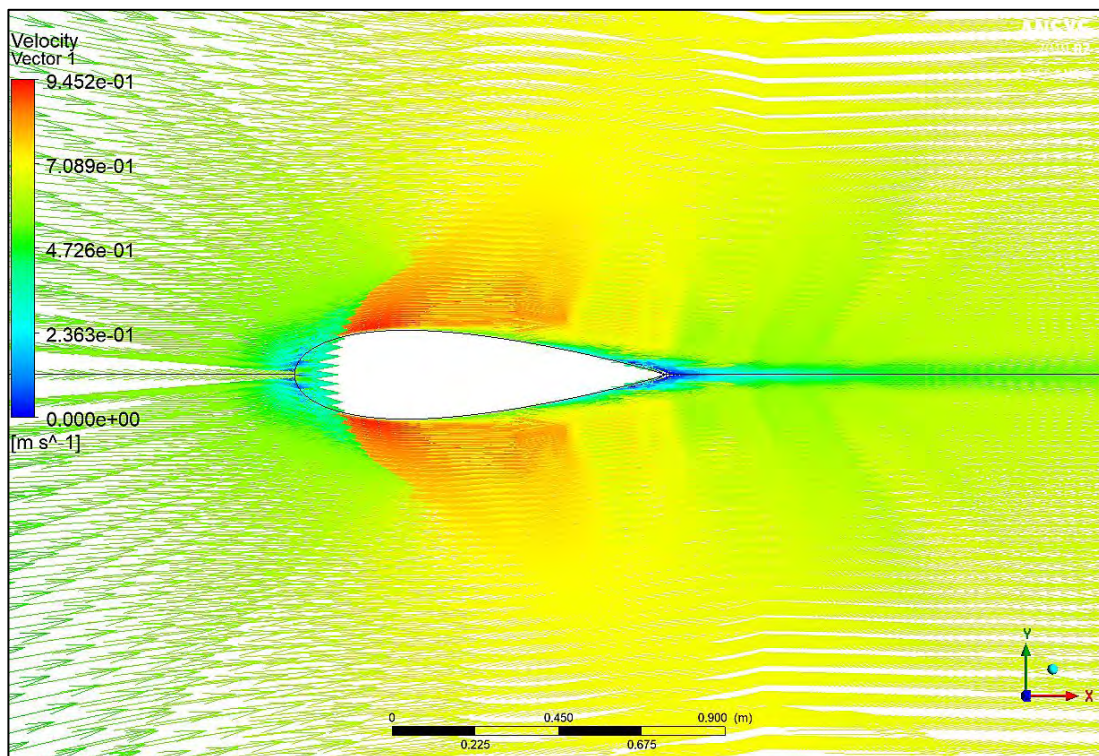


Figure 4.9.7: Velocity vector for surface piercing body with NACA 0024 airfoil section at $Fr = 0.19$

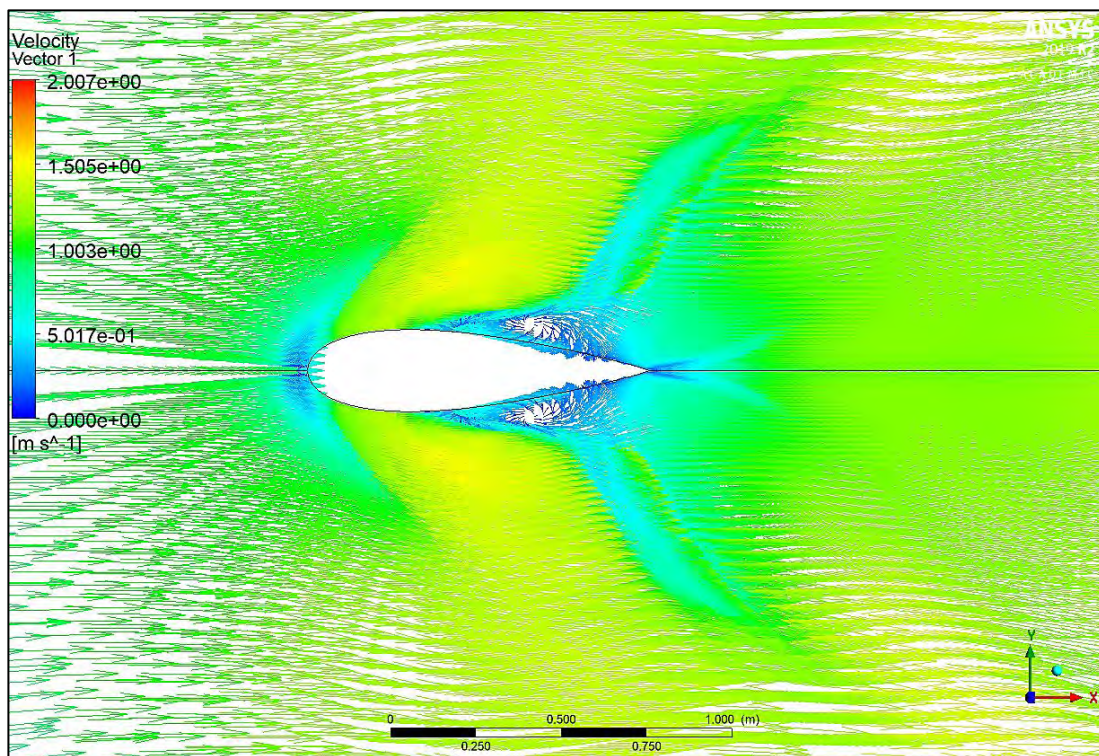


Figure 4.9.8: Velocity vector for surface piercing body with NACA 0024 airfoil section at $Fr = 0.37$

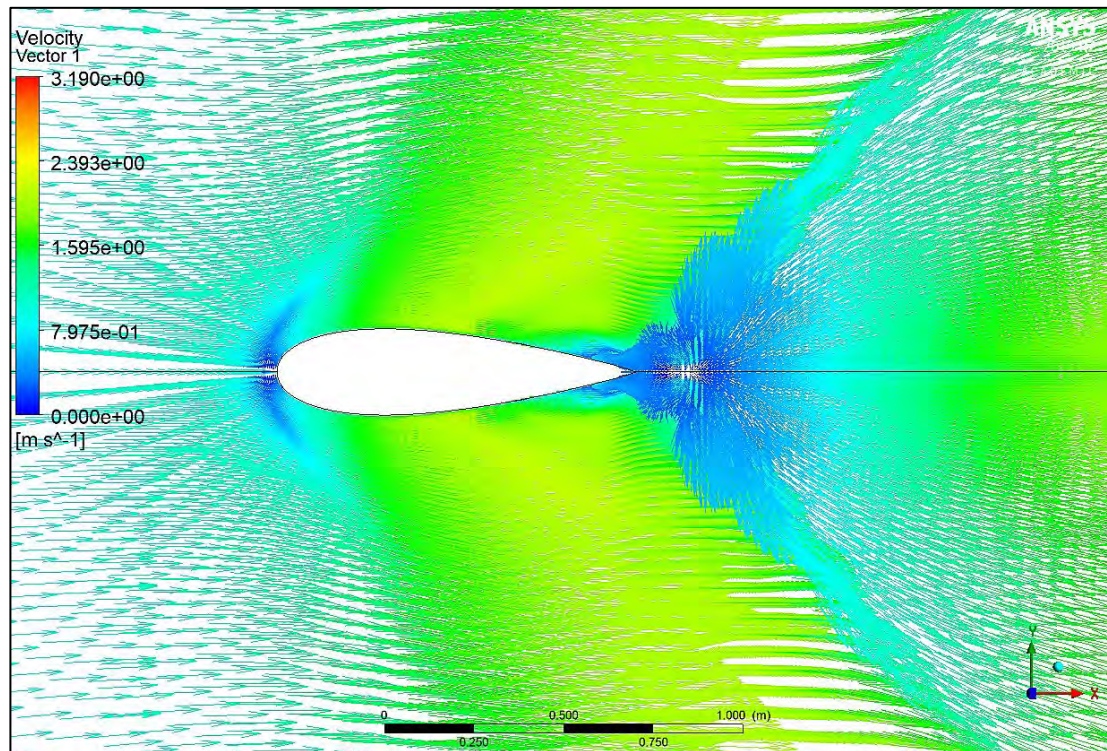


Figure 4.9.9: Velocity vector for surface piercing body with NACA 0024 airfoil section at $Fr = 0.55$

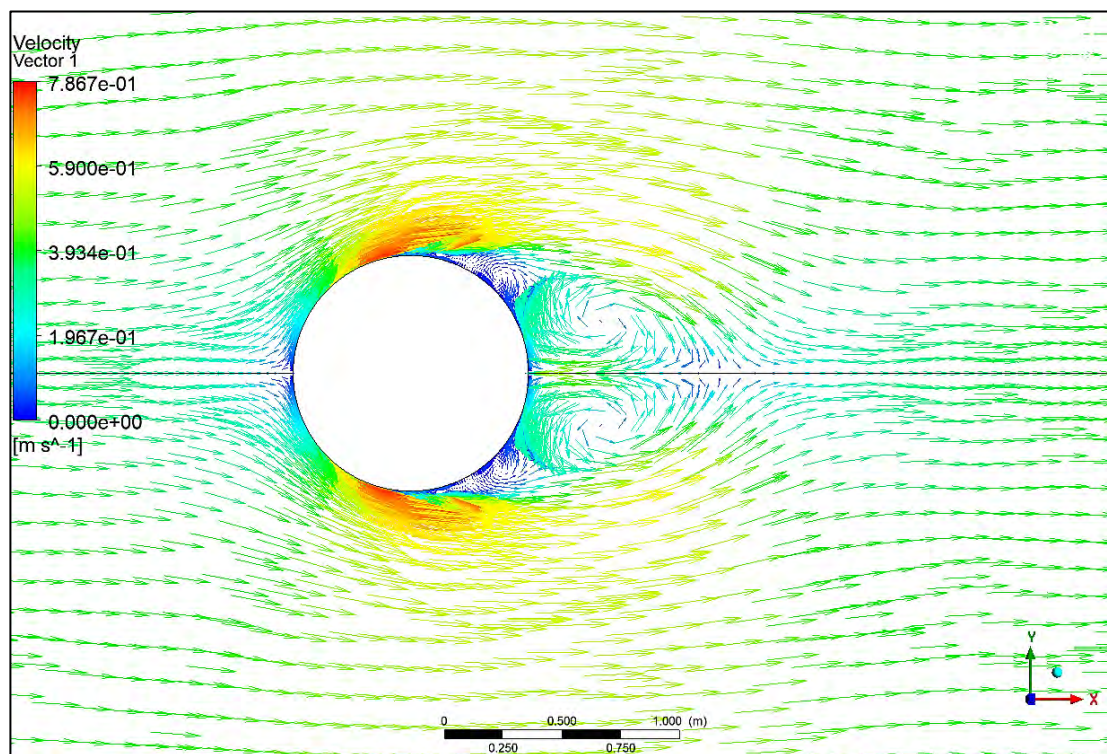


Figure 4.9.10: Velocity vector for surface piercing body with cylindrical cross – section at $Fr = 0.19$

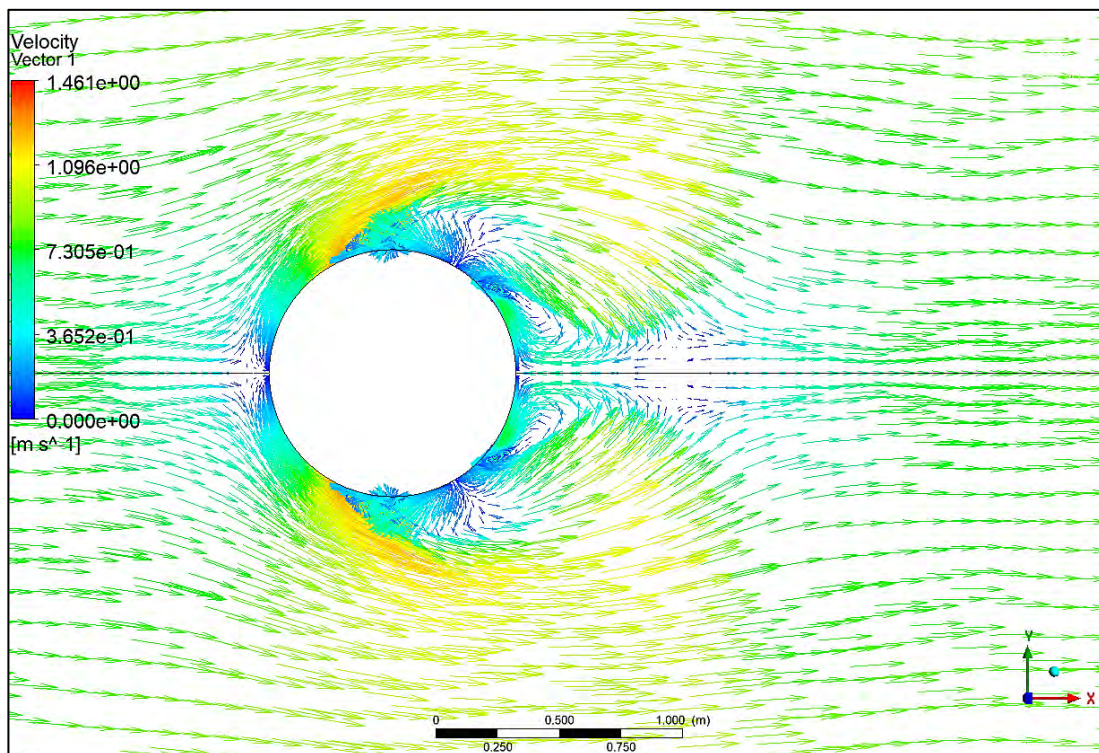


Figure 4.9.11: Velocity vector for surface piercing body with cylindrical cross – section at $Fr = 0.37$

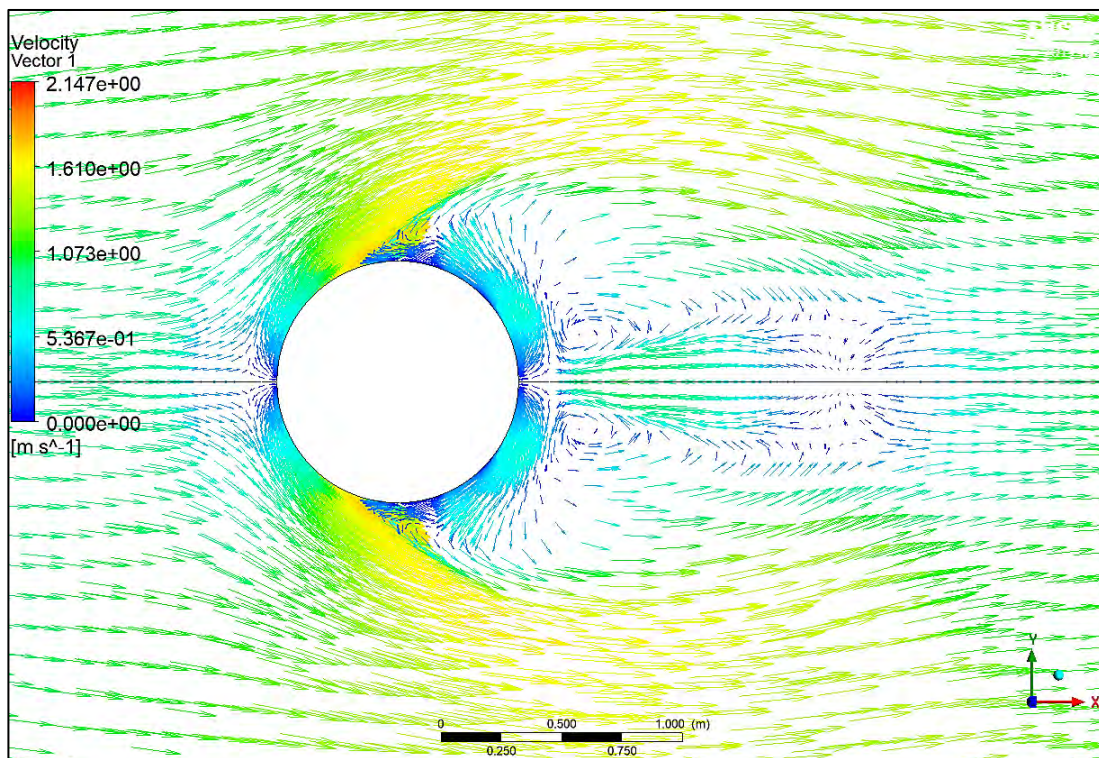


Figure 4.9.12: Velocity vector for surface piercing body with cylindrical cross – section at $Fr = 0.55$

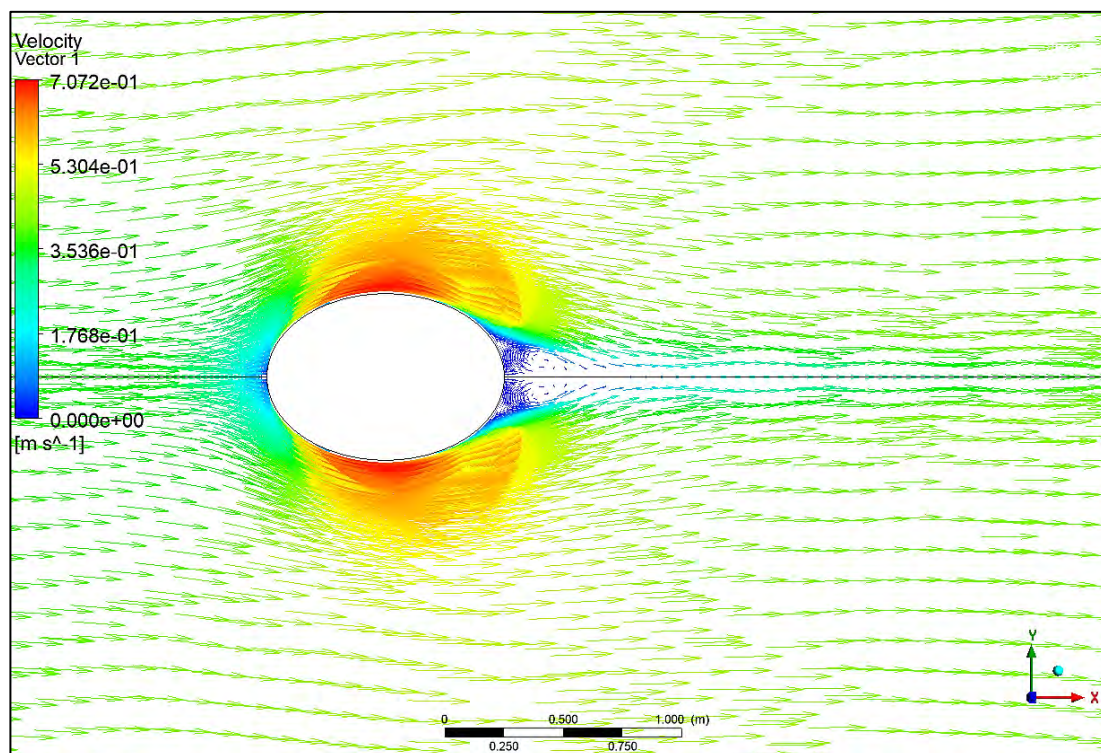


Figure 4.9.13: Velocity vector for surface piercing body with elliptical cross – section at $Fr = 0.19$

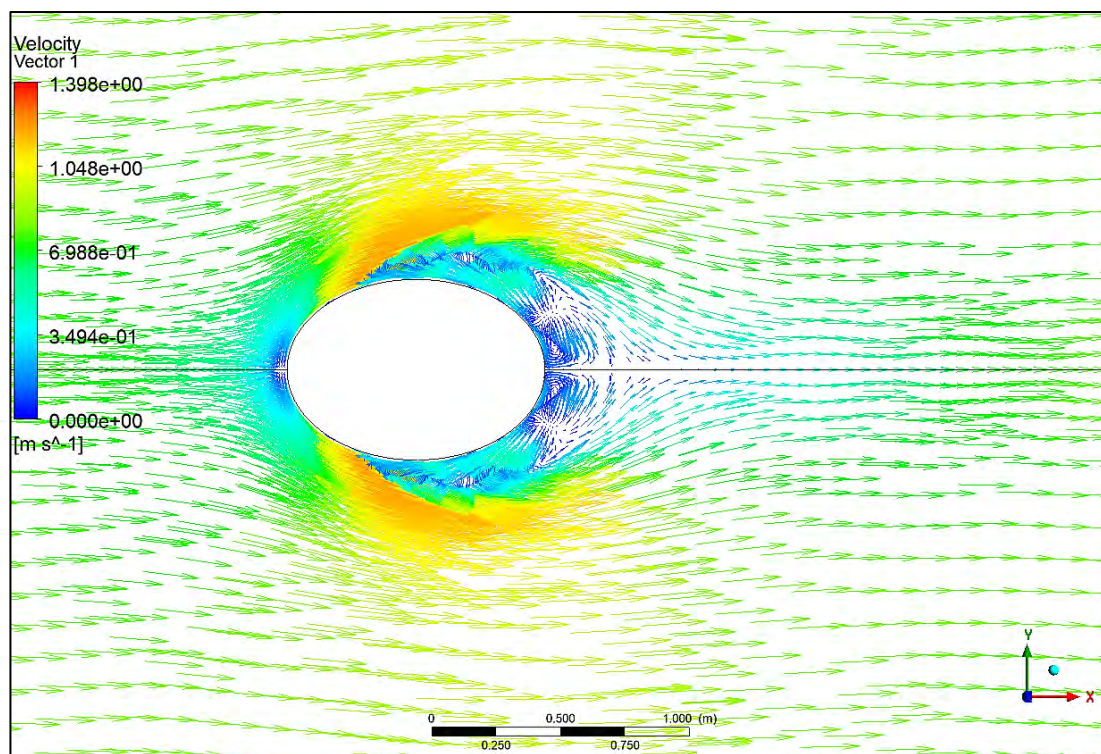


Figure 4.9.14: Velocity vector for surface piercing body with elliptical cross – section at $Fr = 0.37$

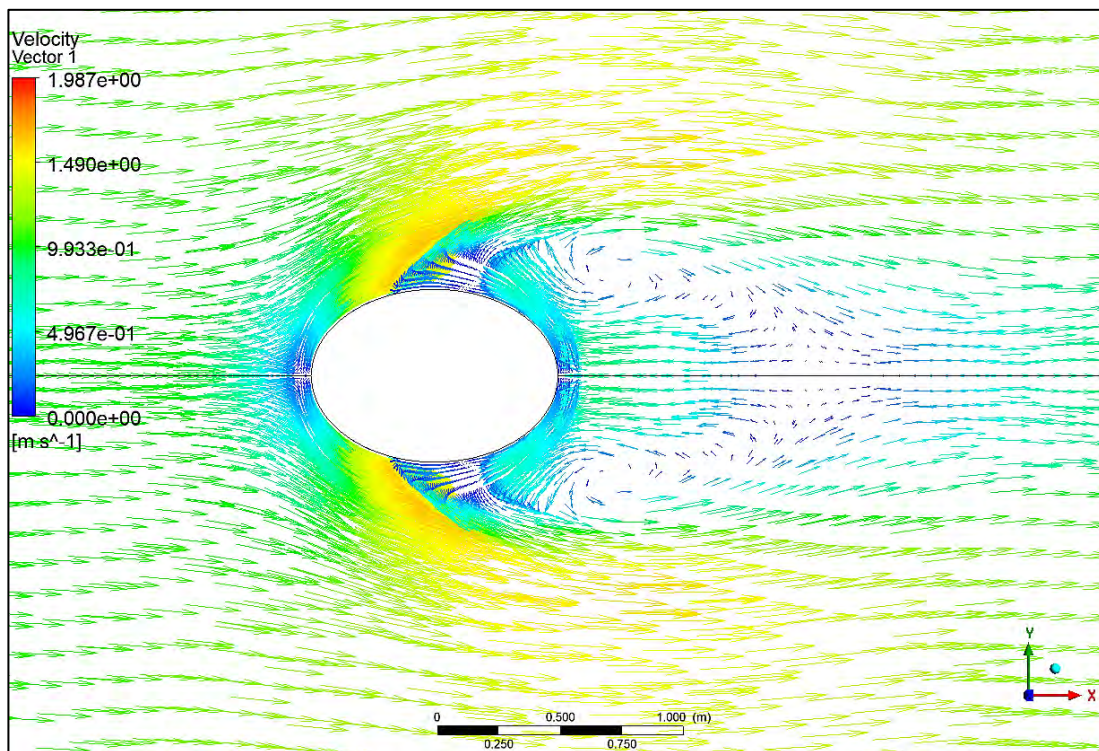


Figure 4.9.15: Velocity vector for surface piercing body with elliptical cross – section at $Fr = 0.55$

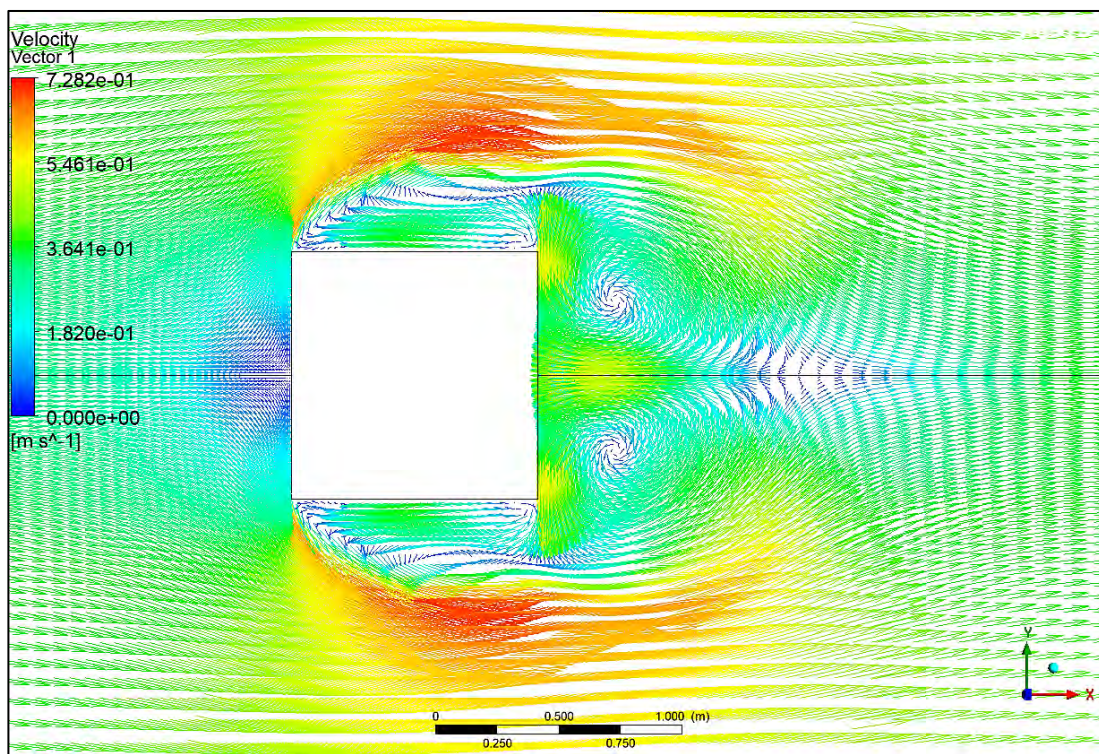


Figure 4.9.16: Velocity vector for surface piercing body with rectangular cross – section at $Fr = 0.19$

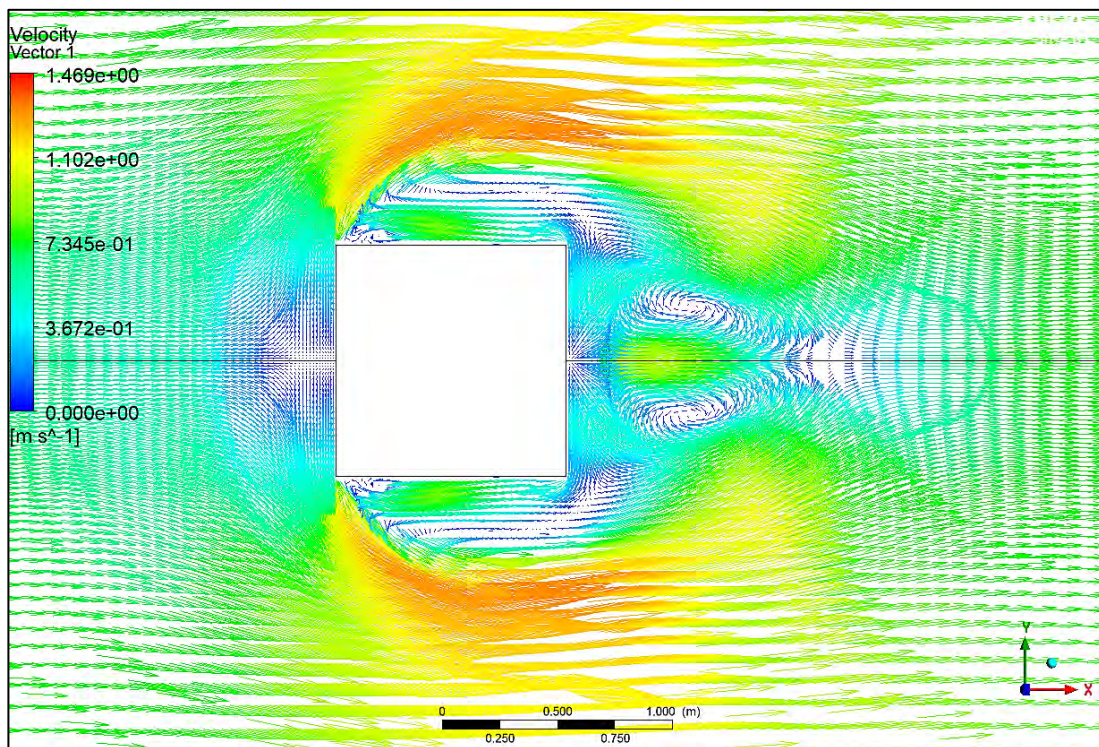


Figure 4.9.17: Velocity vector for surface piercing body with rectangular cross – section at $Fr = 0.37$

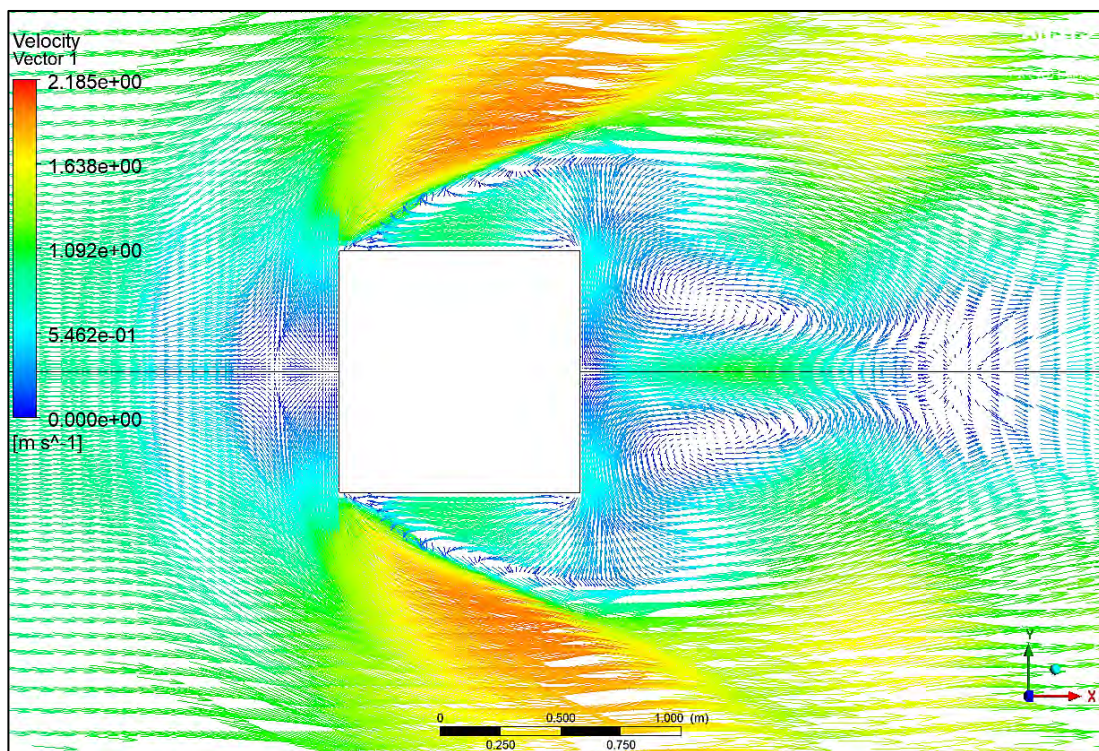


Figure 4.9.18: Velocity vector for surface piercing body with rectangular cross – section at $Fr = 0.55$

4.10 Streamline along Different Bodies

Figure 4.10.1 – 4.10.18 represent the streamline along different vertical surface piercing bodies. From these figures, we can see that when the Froude number is lower ($Fr = 0.19$), the flow around the bodies is laminar. But the flow starts to fluctuates gradually with the increase in Froude number and becomes turbulent for higher Froude number ($Fr = 0.55$).

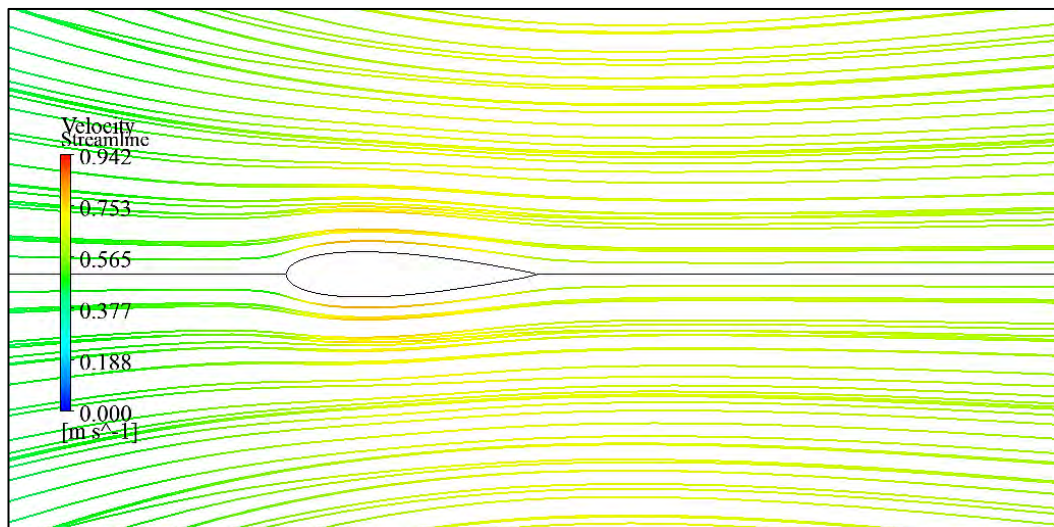


Figure 4.10.1: Streamline along NACA 0012 airfoil section with $Fr = 0.19$

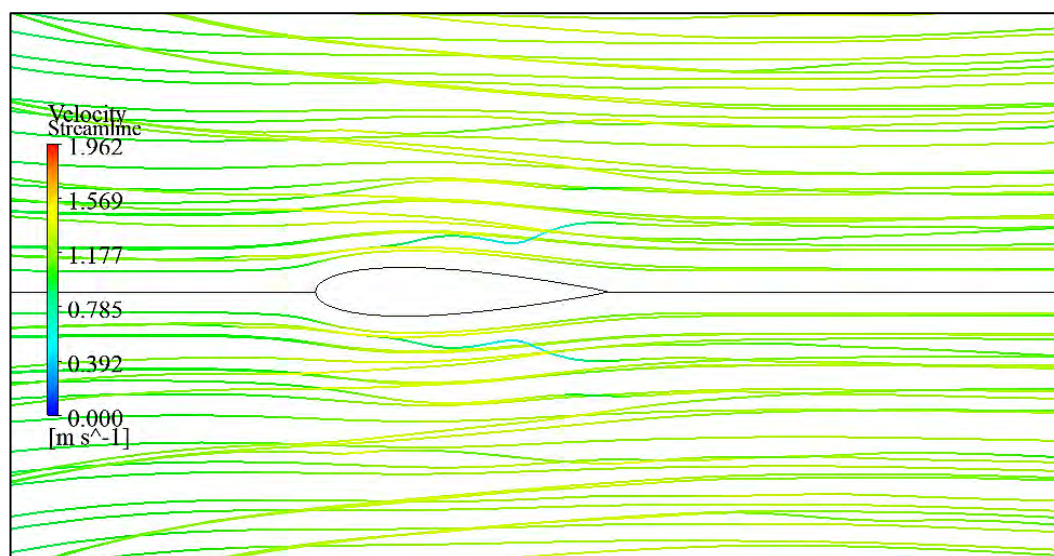


Figure 4.10.2: Streamline along NACA 0012 airfoil section with $Fr = 0.37$

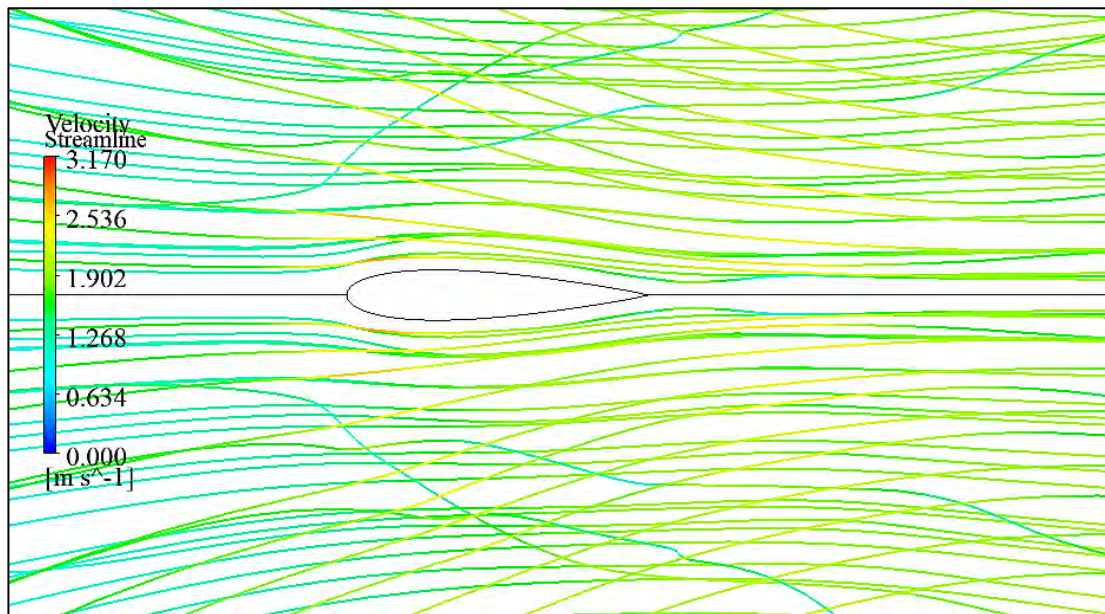


Figure 4.10.3: Streamline along NACA 0012 airfoil section with $Fr = 0.55$

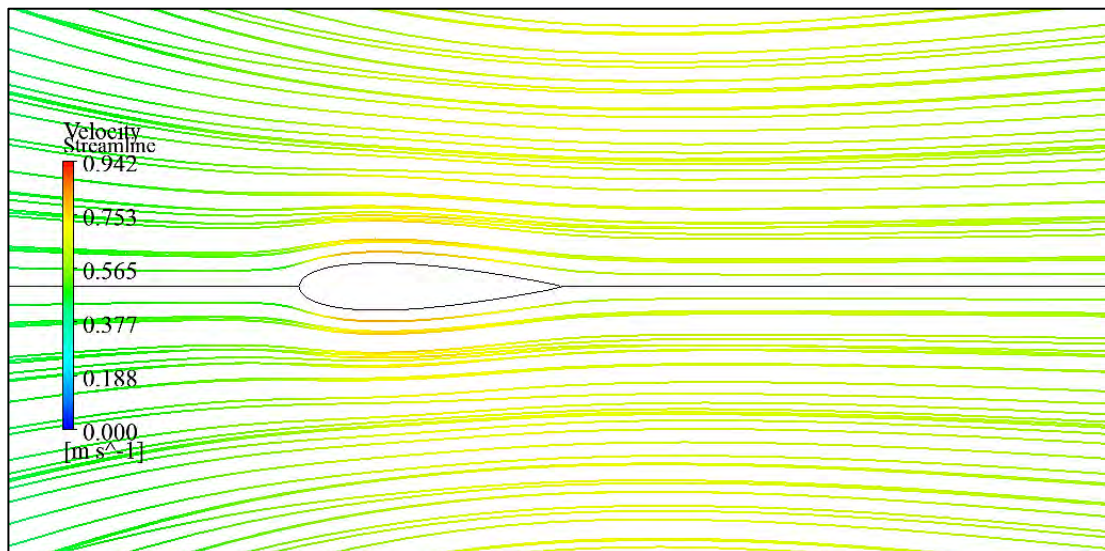


Figure 4.10.4: Streamline along NACA 0018 airfoil section with $Fr = 0.19$

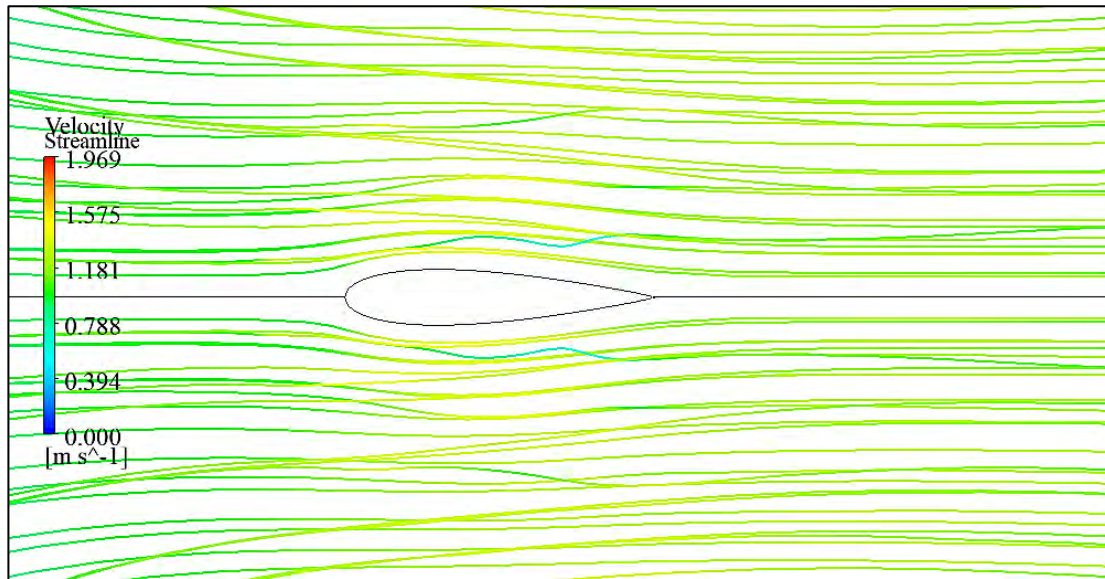


Figure 4.10.5: Streamline along NACA 0018 airfoil section with $Fr = 0.37$

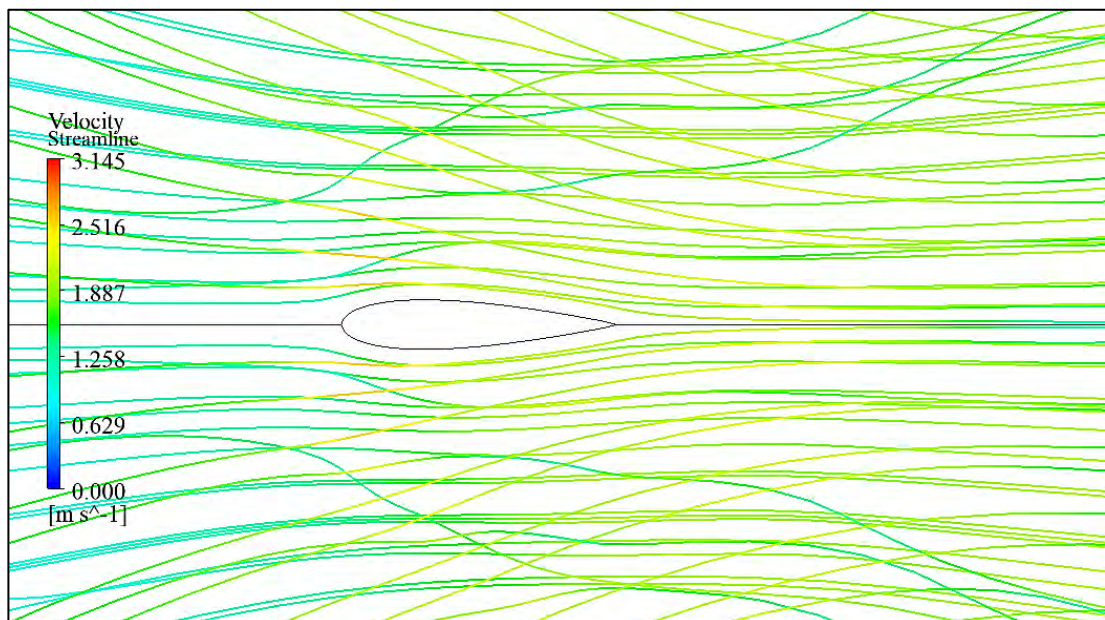


Figure 4.10.6: Streamline along NACA 0018 airfoil section with $Fr = 0.55$

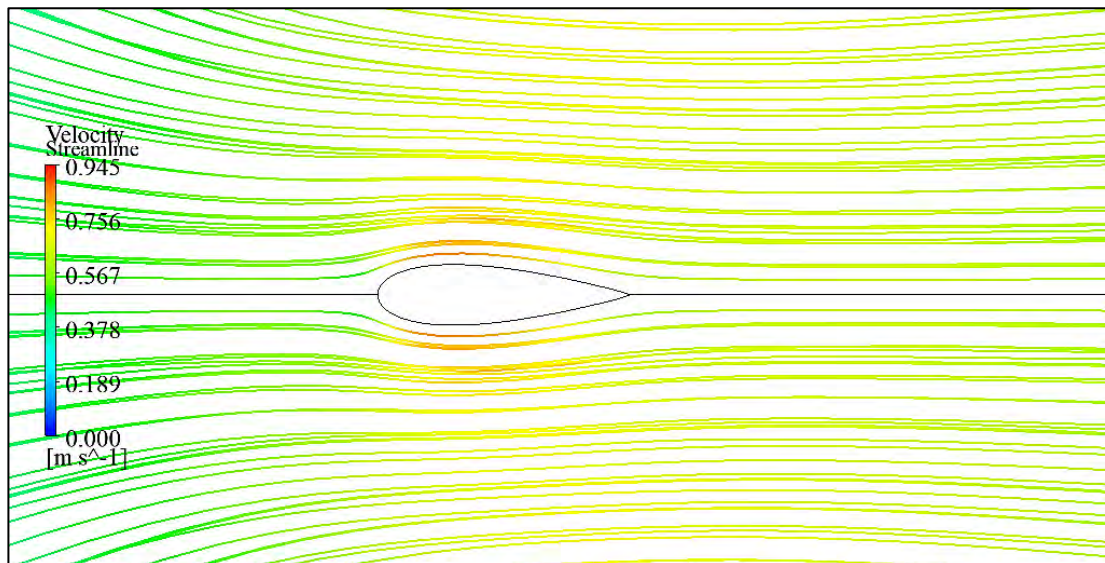


Figure 4.10.7: Streamline along NACA 0024 airfoil section with $Fr = 0.19$

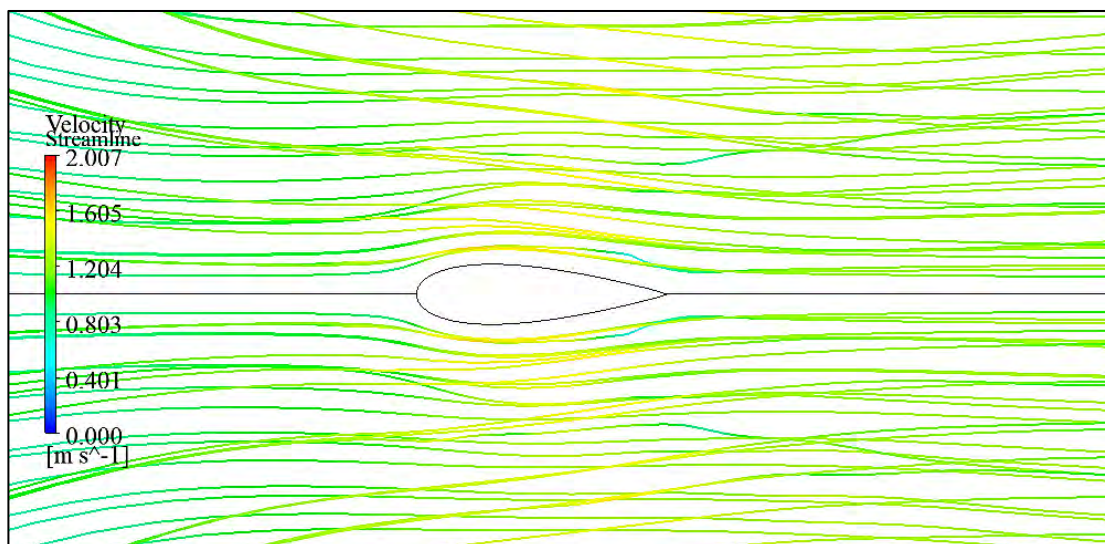


Figure 4.10.8: Streamline along NACA 0024 airfoil section with $Fr = 0.37$



Figure 4.10.9: Streamline along NACA 0024 airfoil section with $Fr = 0.55$

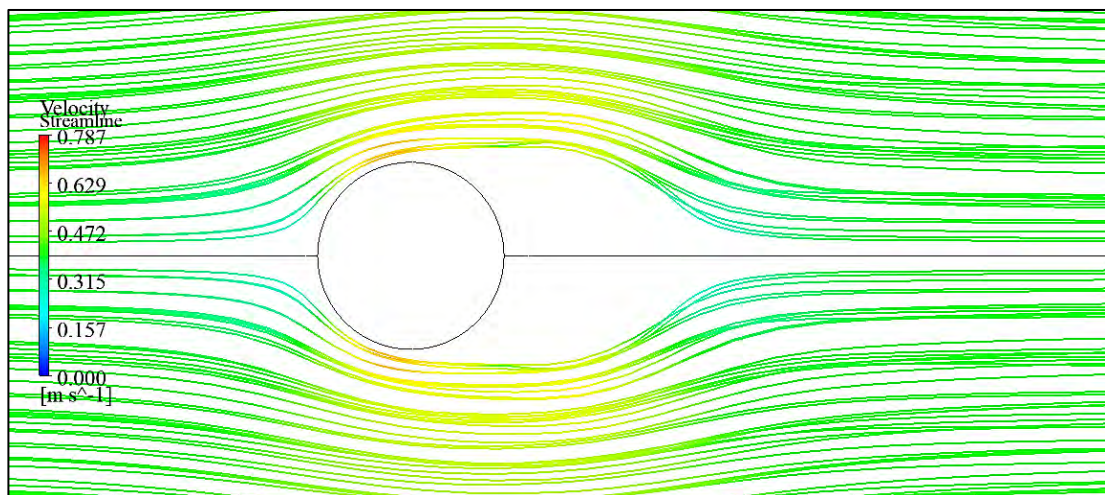


Figure 4.10.10: Streamline along circular cylindrical section with $Fr = 0.19$

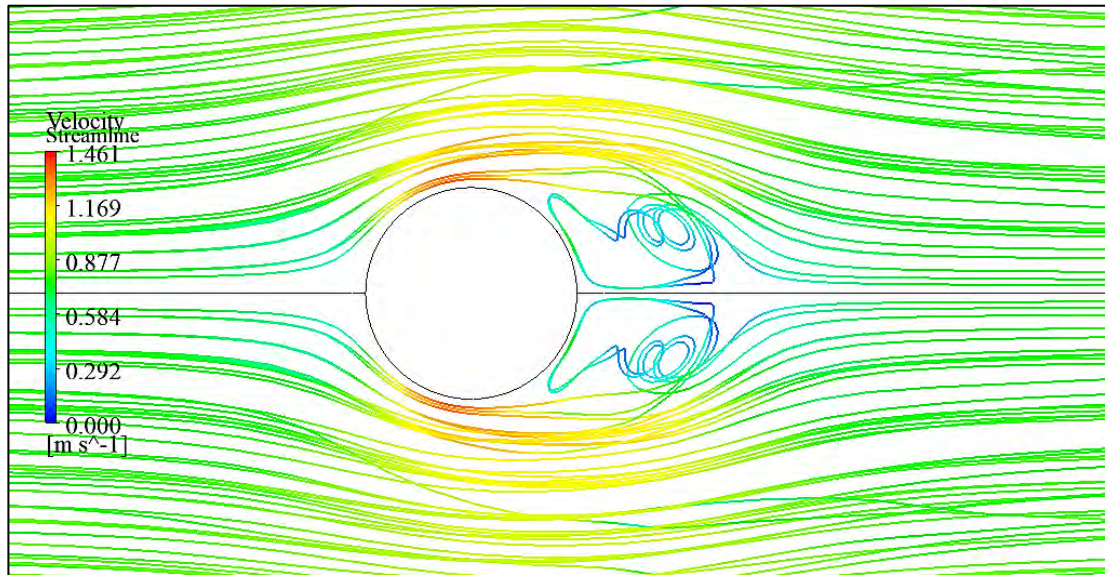


Figure 4.10.11: Streamline along circular cylindrical section with $Fr = 0.37$

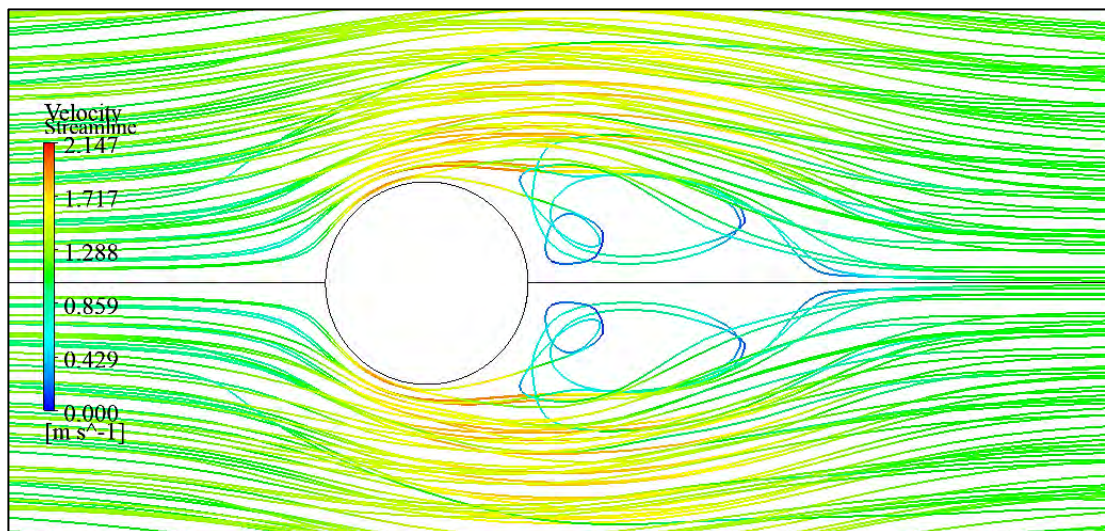


Figure 4.10.12: Streamline along circular cylindrical section with $Fr = 0.55$

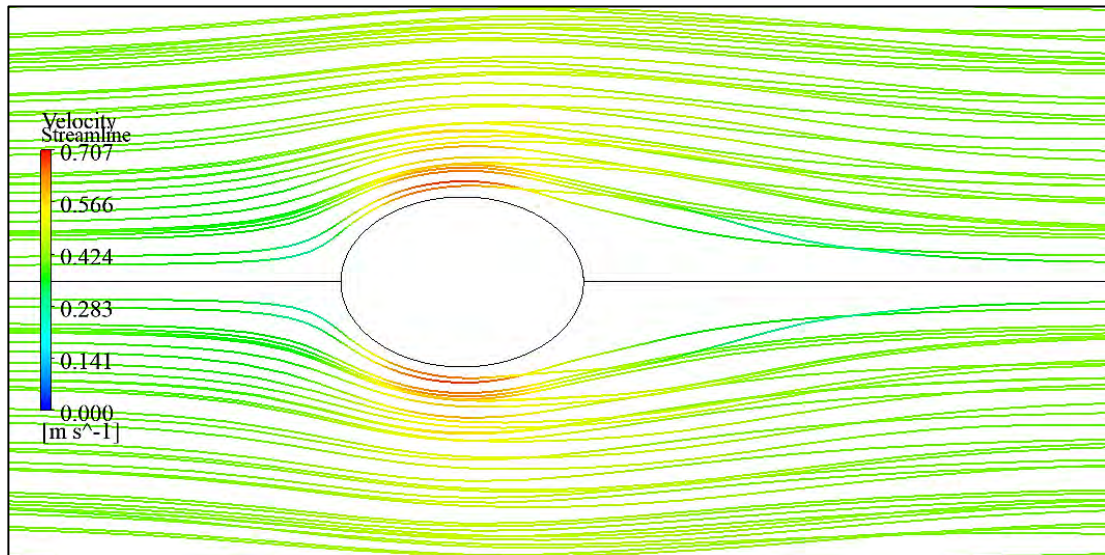


Figure 4.10.13: Streamline along elliptical section with $Fr = 0.19$

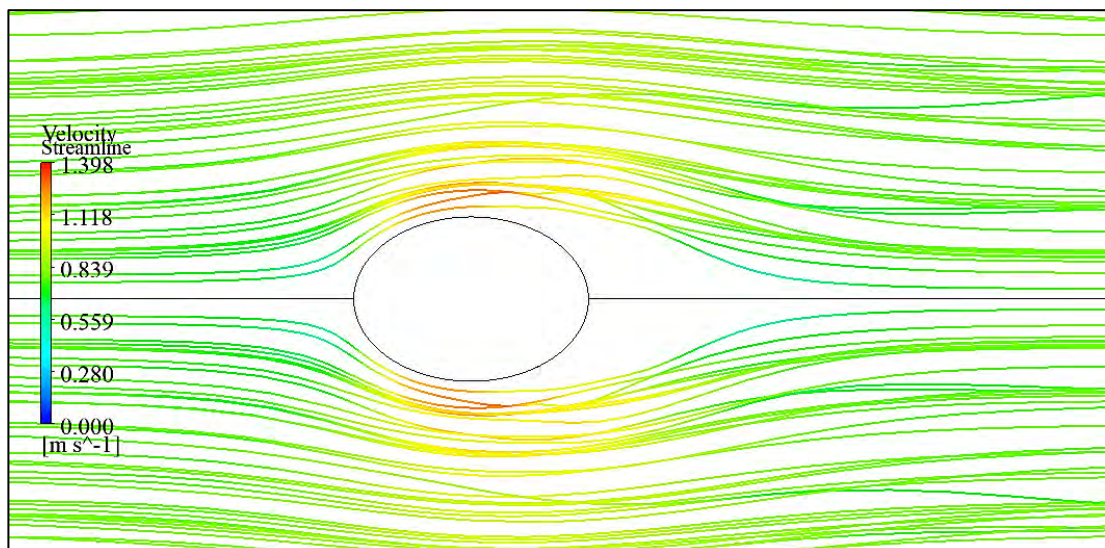


Figure 4.10.14: Streamline along elliptical section with $Fr = 0.37$

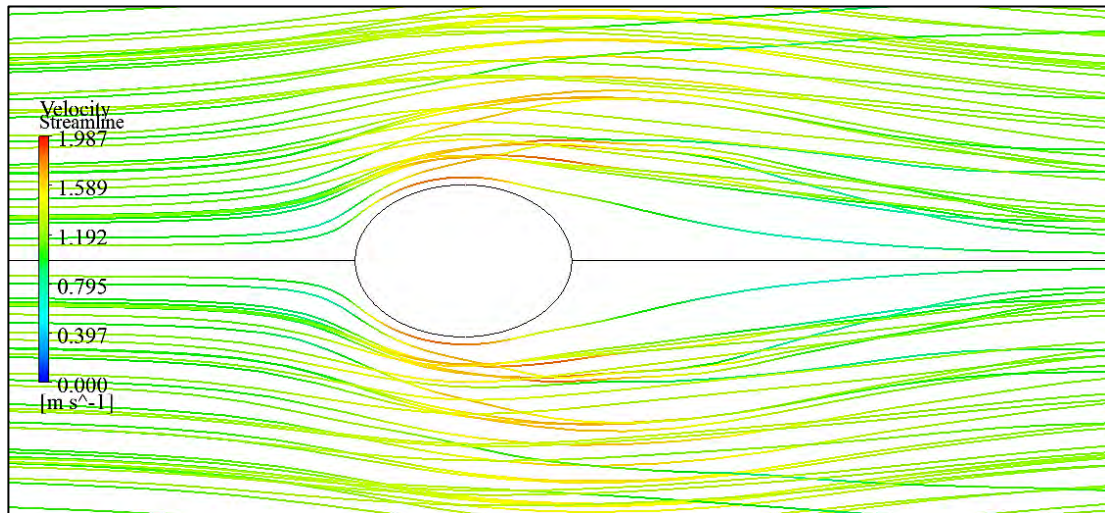


Figure 4.10.15: Streamline along elliptical section with $Fr = 0.55$

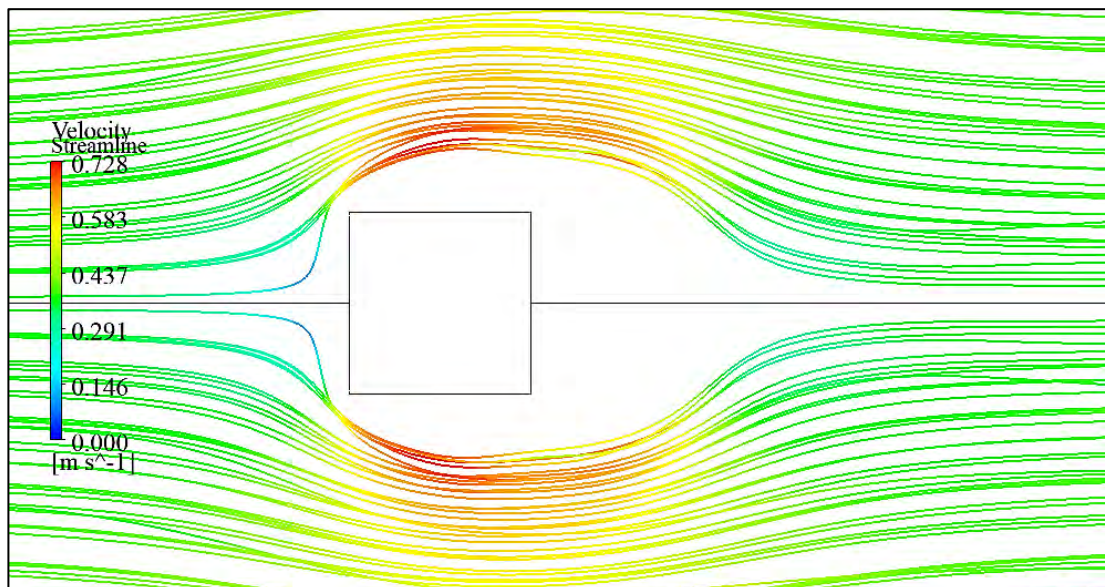


Figure 4.10.16: Streamline along rectangular section with $Fr = 0.19$

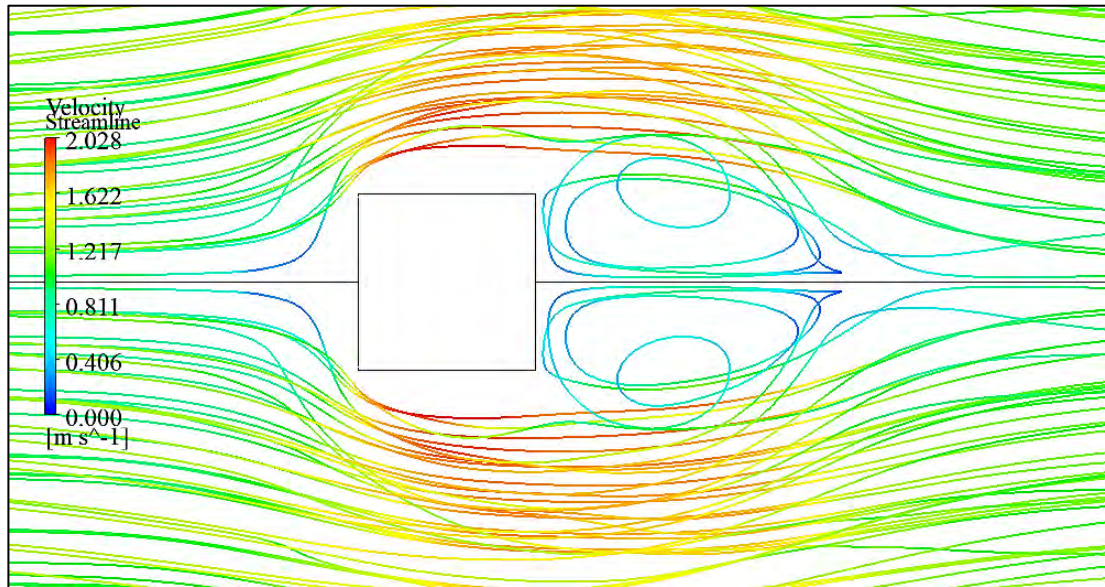


Figure 4.10.17: Streamline along rectangular section with $Fr = 0.37$

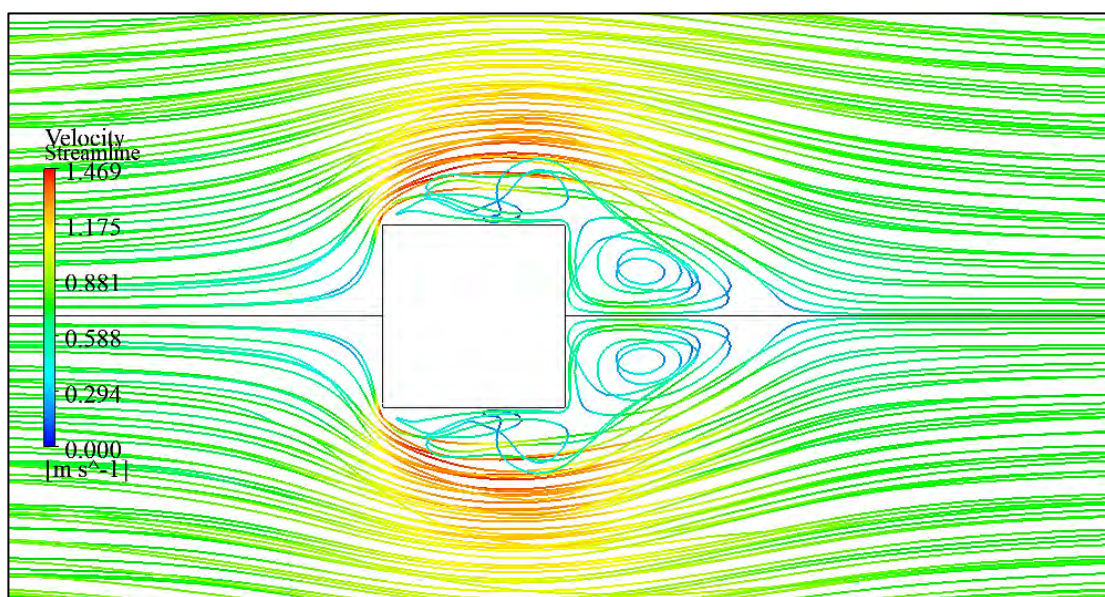


Figure 4.10.18: Streamline along rectangular section with $Fr = 0.55$

4.11 3D Views of Free Surface of Different Bodies

Figure 4.11.1 – 4.11.6 shows the 3D views of the free-surface for surface piercing bodies with NACA 0012, NACA 0018, NACA 0024 airfoil sections, cylindrical, elliptical and rectangular cross – sections at $Fr = 0.55$. The bow wave peak increases with the increase in thickness or with the change of the shape. The separation around the body, free-surface elevation, wave height, and the wave steepness is discernible in the figures.

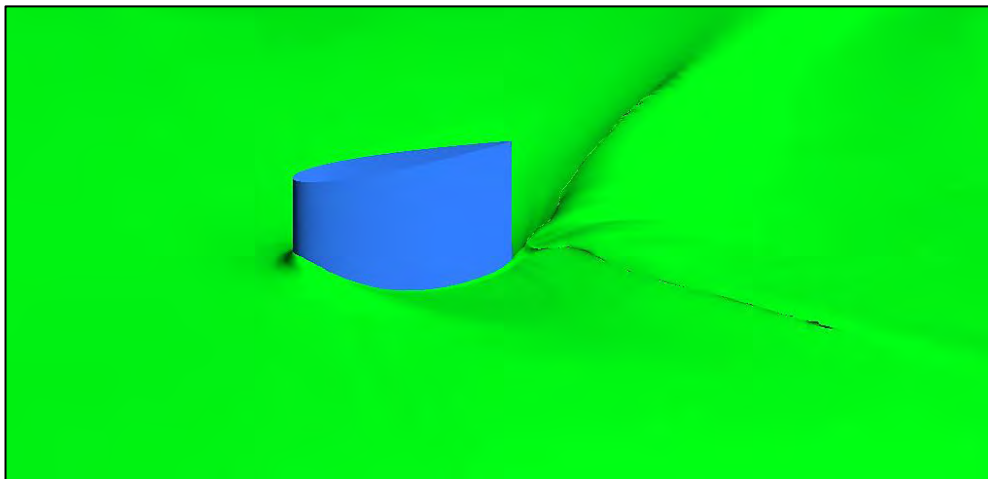


Figure 4.11.1: 3D view of free surface for surface piercing body with NACA 0012 airfoil section at $Fr = 0.55$

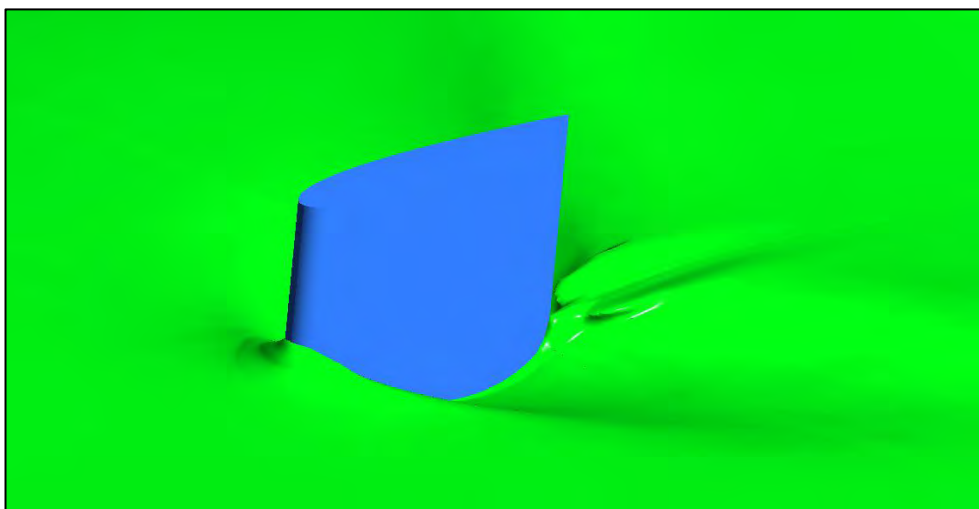


Figure 4.11.2: 3D view of free surface for surface piercing body with NACA 0018 airfoil section at $Fr = 0.55$

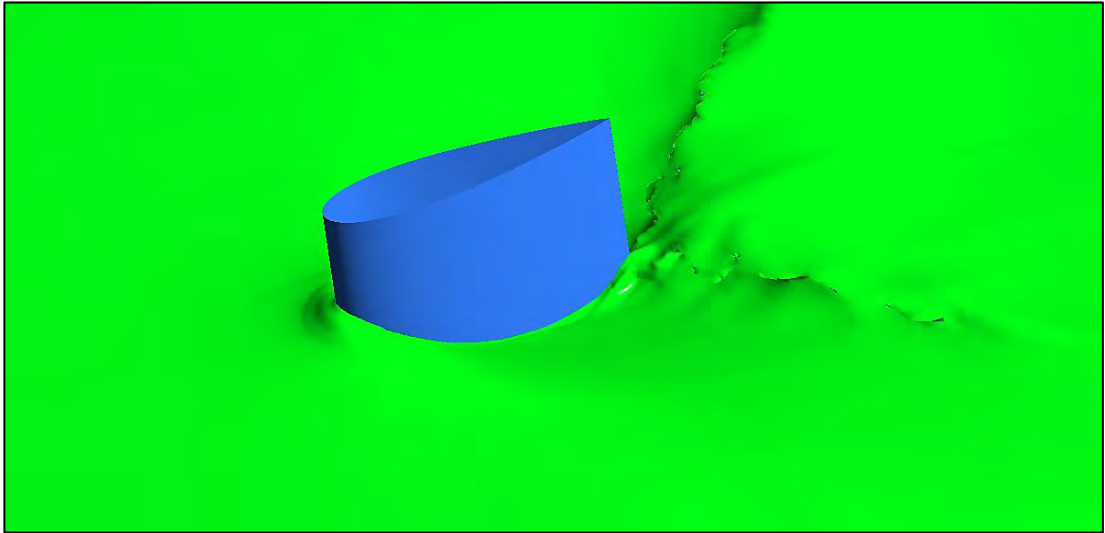


Figure 4.11.3: 3D view of free surface for surface piercing body with NACA 0024 airfoil section at $Fr = 0.55$

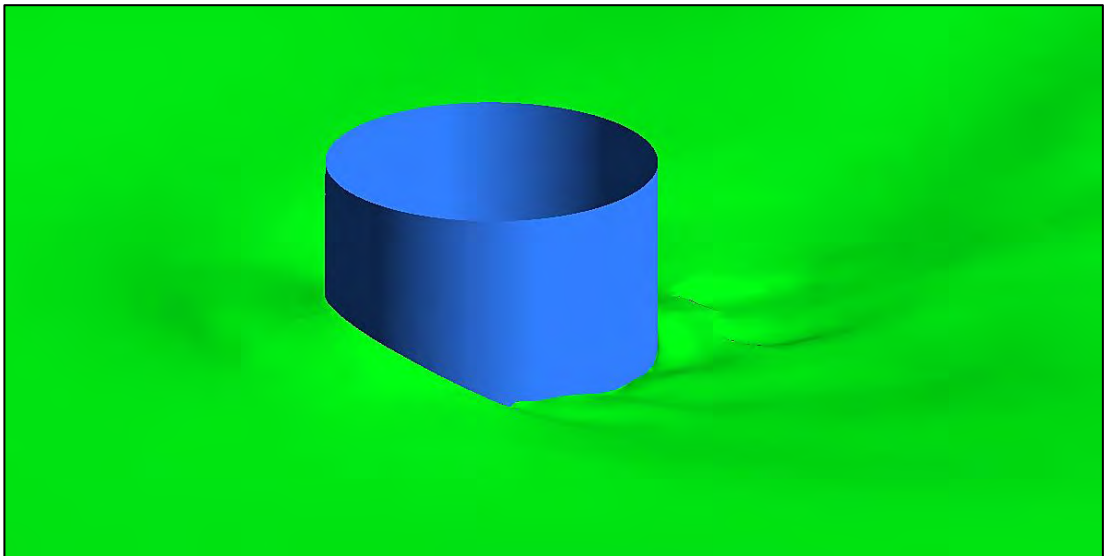


Figure 4.11.4: 3D view of free surface for surface piercing body with cylindrical cross – section at $Fr = 0.55$

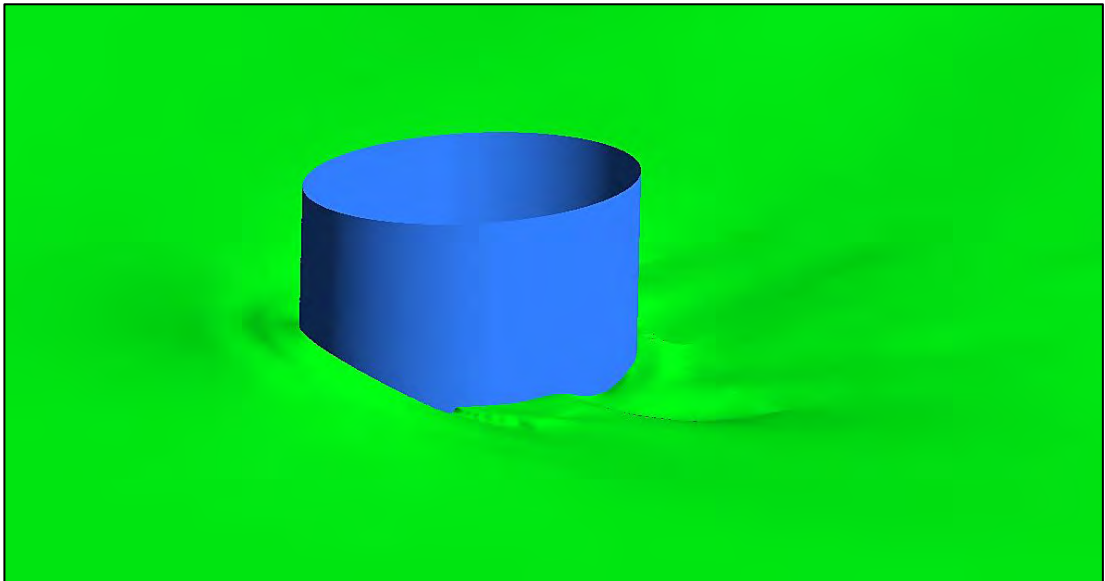


Figure 4.11.5: 3D view of free surface for surface piercing body with elliptical cross
– section at $Fr = 0.55$

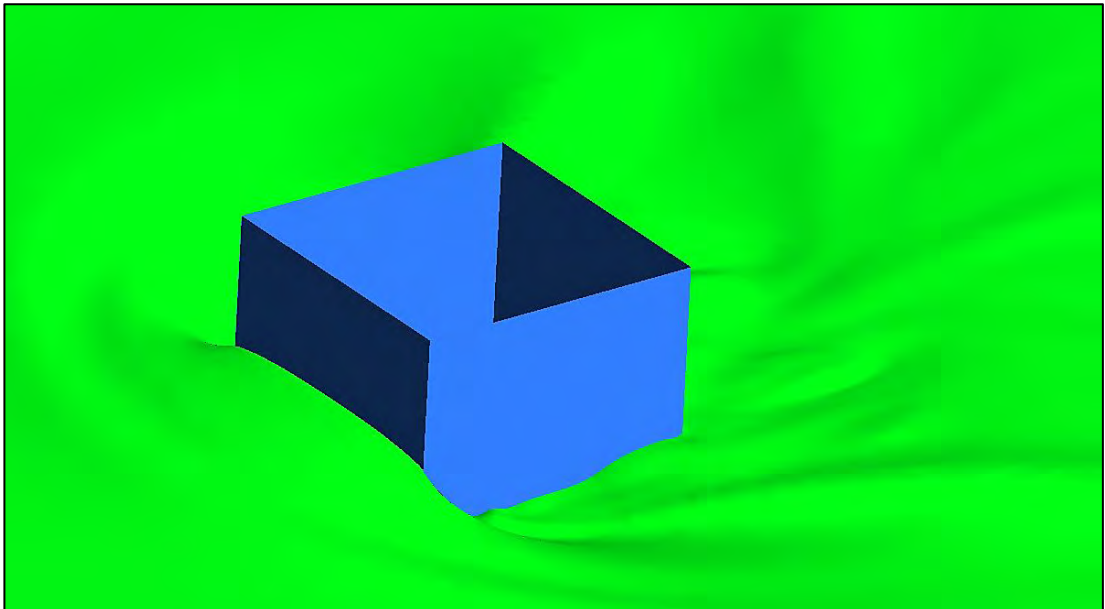


Figure 4.11.6: 3D view of free surface for surface piercing body with rectangular
cross – section at $Fr = 0.55$

CONCLUSIONS

In this study, Finite Volume Method (FVM) has been used to analyze the flow around the surface piercing floating bodies. The Shear-Stress Transport (SST) $k-\omega$ turbulence model is used to capture the boundary layer and the Volume of Fluid (VOF) technique is adopted to track the free-surface of water. The numerical results are validated by comparing with the experimental data and the previous numerical results. The following conclusions can be drawn from this study:

- The Finite Volume Method (FVM) has successfully analyzed the flow past 3D surface piercing floating body.
- The numerical results show excellent agreement with the experimental data and the previous numerical results.
- The separation of the flow due to the free – surface wave can be clearly understood.
- The wave patterns are dependent on Froude number rather than thickness or shape of the floating body at higher Froude number.
- The thickness or shape effects become dominant at lower Froude number.
- The thickness of shape effects is noticeable in the bow wave peak, extent of the free – surface, at the wake region, and also in the separation region.
- The present simulation results can be applicable to the design of hydrofoil boat, rudder, bridge pier, legs of offshore structure etc.

REFERENCES

Abbott, I. H. and Doenhoff A. E. V. (1959): Theory of Wing Sections Including a Summary of Airfoil Data, Dover Publications, Inc., New York.

Adjali, S., Belkadi, M., Aounallah, M. and Imine, O. (2015): A numerical study of steady 2D flow around 0015 and NACA 0012 hydrofoil with free surface using VOF method, EPJ Web of Conference, 92, 02001.

Ahmed, T., Amin, M. T., Islam, S. M. R. and Ahmed, S. (2013): Computational Study of Flow Around a NACA 0012 Wing Flapped at Different Angles with Varying Mach Numbers, Global Journals Inc. (USA), Vol 13, No 4-J.

Banks, J., Phillips, A. B., Bull, P. W. and Turnock, S. R. (2010): RANS Simulations of the Multiphase Flow around the KCS Hullform, A Workshop on CFD in Ship Hydrodynamics, Gothenburg, Sweden.

Chow, S. K. (1967): Free – surface effects on boundary – layer separation on vertical struts, PhD Thesis, University of Iowa, USA.

Fluent Inc. (2015): ANSYS Fluent Theory Guide 15.

Iafrati, A. (2017): Flow around ships and underwater vehicles, Encyclopedia of Maritime and Offshore Engineering, Vol. 01, pp 169-180.

Karim, M. M., Prasad, B. and Rahman, N. (2014): Numerical simulation of free surface water wave for the flow around NACA 0015 hydrofoil using the volume of fluid (VOF) method, Ocean Engineering, Vol. 78, pp 89-94.

Kandasamy, M., Xing, T. and Stern, F. (2008): Unsteady free surface wave-induced separation: Vortical structures and instabilities, Journal of Fluids and Structures, Vol. 25, No. 2, pp 343-363.

Koo, B., Yang, J. and Stern, F. (2013), Reynolds and Froude number effect on the flow past an interface – piercing circular cylinder, *International Journal of Naval Architecture and Ocean Engineering*, Vol. 6, No. 3, pp 529-561.

Liu, I. H., Riglin, J., Schleicher, W. C. and Oztekin, A. (2016): Flow past a plate in the vicinity of a free surface, *Ocean Engineering*, Vol. 111, pp 323-334.

Metcalf, B., Longo, J., Ghosh, S. and Stern, F. (2005): Unsteady free-surface wave-induced boundary-layer separation for a surface-piercing NACA 0024 foil: Towing tank experiments, *Journal of Fluids and Structures*, Vol. 22, Issue 1, pp 77-98.

Pogozelski, E., Katz, J. and Huang, T. (1997): The flow structure around a surface-piercing strut, *Physics of Fluids*, Vol. 9, No. 5, pp 1387-1399.

Rahman, M. H., Tasif, T. H. Fazle, A.B. (2016): Computational Study of Flow Past a 3D Rudder with NACA 0012 Airfoil Section, Undergraduate thesis, BUET, Dhaka, Bangladesh.

Raza, N., Mehmood, I., Rafiuddin, H., Bilal, D. S. and Rafique, D. M. (2013): Numerical Simulation of Free Surface Effect on Moving Hydrofoil Near Free Surface, 10th International Bhurban Conference on Applied Science & Technology, Islamabad, Pakistan, pp 249-255.

Rhee, S. H. (2009): Unsteady Reynolds Averaged Navier – Stokes Method for Free – Surface Wave Flows around Surface – Piercing Cylindrical Structures, *Journal of Waterway, Port, Coastal, and Ocean Engineering*, Vol. 135, No. 4, pp 135-143.

Stern, F., Hwang, W. S. and Jaw, S. Y. (1989): Free – surface effects on the boundary layer of a surface – piercing flat plate: experimental and theory, *Journal of Ship Research*, Vol. 33, No. 1, pp 63-80.

Sadathosseini, S. H., Mousaviraad, S. M., Firoozabadi, B. and Ahmadi, G. (2008): Numerical Simulation of Free – Surface Waves and Wave Induced Separation, *Science Iranica*, Vol. 15, No. 3, pp 232-331.

Stenmark, E. (2013): On Multiphase Flow Models in ANSYS CFD Software, Department of Applied Mechanics, Chalmers University of Technology, Goteborg.

Uslu, Y. and Bal, S. (2008): Numerical Prediction of Wave Drag of 2 – D and 3 – D Bodies under or on a Free Surface, Turkish Journal of Engineering and Environmental Sciences, Vol. 32, No. 3, pp 177-188.

Wei, Z. and Ao-de, H. (2007): Numerical study of the turbulent flow around a circular pier, Journal of Shanghai University (English Edition), Vol. 11, No. 1, pp 17-21.

Zhang, Z. and Stern, F. (1996): Free-surface wave-induced separation, Journal of Fluid Engineering, Vol. 118, pp 546-554.

Appendix A

Basic profile of NACA 0024 airfoil of chord length 1.0 m

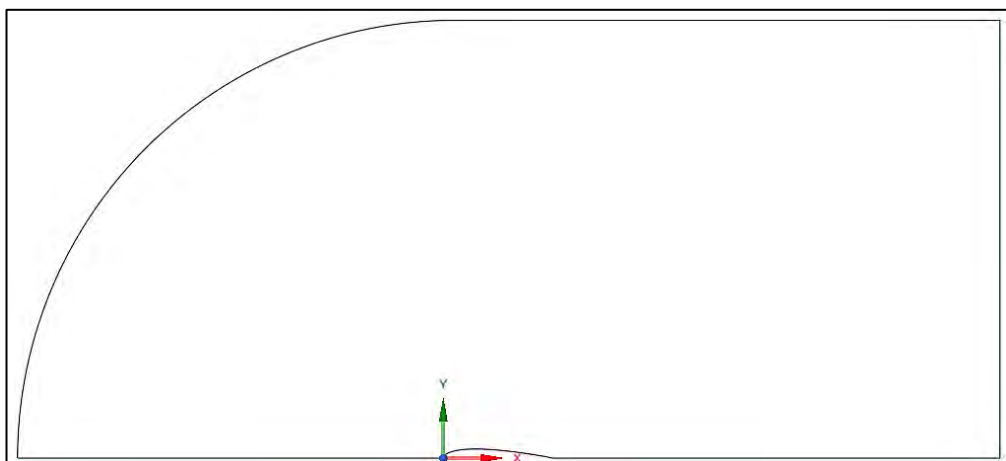
X co-ordinate (m)	Y co-ordinate (m)
0	0
0.0125	0.038
0.0250	0.052
0.0500	0.071
0.0750	0.084
0.1000	0.094
0.1500	0.107
0.2000	0.115
0.2500	0.119
0.3000	0.120
0.4000	0.116
0.5000	0.106
0.6000	0.091
0.7000	0.073
0.8000	0.053
0.9000	0.029
0.9500	0.016
1.0000	0.003

Appendix B

Detailed procedure to simulate flow around a surface piercing body

Step 1: Creating the Geometry

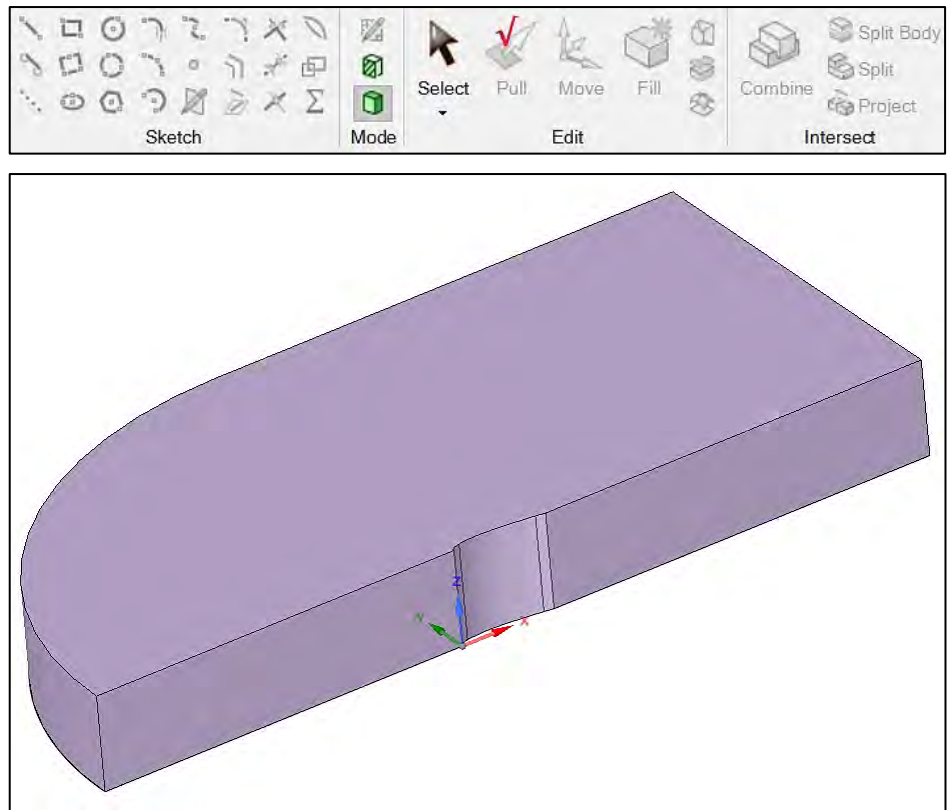
1. Open SpaceClaim modeler.
2. Draw the object and create a box around it.



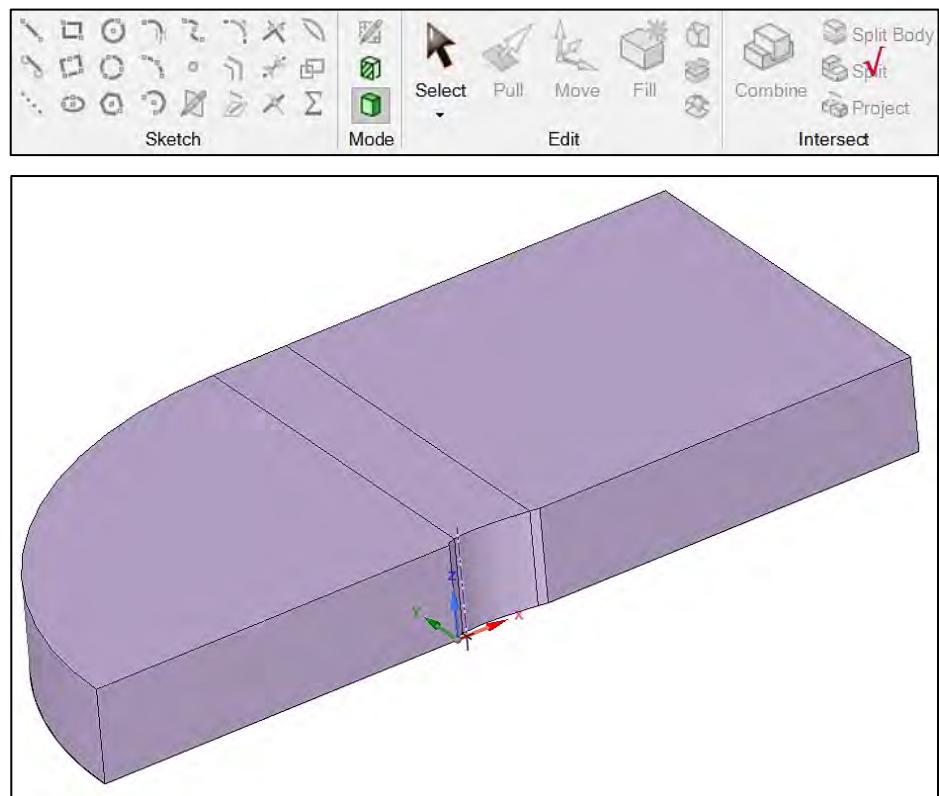
3. Create surface using 'Fill' command.



4. Extrude the surface using 'Pull' to create a 3D geometry.



5. Use 'Split' command to create region.



Step 1: Creating the Mesh

1. Open mesh modeler.
2. Generate the mesh using different settings as shown in the tables below.

Table 1
Model > Geometry

Object Name	<i>Geometry</i>
State	Fully Defined
Definition	
Source	E:\MSc
Type	SpaceClaim
Length Unit	Meters
Bounding Box	
Length X	9.0 m
Length Y	4.0 m
Length Z	1.0 m
Properties	
Volume	32.508 m ³
Scale Factor Value	1.0
Statistics	
Bodies	1
Active Bodies	1
Nodes	343356
Elements	325500
Mesh Metric	None
Update Options	
Assign Default Material	No
Basic Geometry	
Solid Bodies	Yes
Surface Bodies	Yes
Line Bodies	Yes
Parameters	Independent
Parameter Key	
Attributes	Yes
Attributes Key	
Name Selections	Yes
Name Selection Key	
Material Properties	Yes
Advanced Geometry	
Use Associativity	Yes
Coordinate Systems	Yes
Coordinate System Key	
Reader Mode Saves Updated File	No
Use Instances	Yes
Smart CAD Update	Yes
Compare Parts on Update	No
Analysis Type	3-D

Mixed Import Resolution	None
Clean Bodies on Import	No
Stitch Surfaces on Import	None
Decompose Disjoint Geometry	Yes
Enclosure and Symmetry	No

Table 2
Model > Geometry > Parts

Object Name	<i>FFF\Solid</i>
State	Meshed
Graphics Properties	
Visible	Yes
Transparency	1
Definition	
Suppressed	No
Coordinate	Default Coordinate
Treatment	Nope
Reference Frame	Lagrangian
Material	
Assignment	
Fluid/Solid	Fluid
Bounding	
Length X	9.0 m
Length Y	4.0 m
Length Z	1.0 m
Properties	
Volume	32.508 m ³
Centroid X	0.98398 m
Centroid Y	1.8859 m
Centroid Z	0.5 m
Statistics	
Nodes	343356
Elements	325500
Mesh Metric	None
CAD Attributes	
Part Tolerance	0.00000001
Color	159:143:175

Table 3
Model > Materials

Object Name	<i>Materials</i>
State	Fully Defined
Graphics Properties	
Visible	0
Transparency	0

Table 4
Model > Coordinate Systems > Coordinate System

Object Name	<i>Global Coordinate System</i>
State	Fully Defined
Definition	
Type	Cartesian
Coordinate System ID	0
Origin	
Origin X	0.0 m
Origin Y	0.0 m
Origin Z	0.0 m
Directional Vectors	
X Axis Data	[1, 0, 0]
Y Axis Data	[0, 1, 0]
Z Axis Data	[0, 0, 1]

Table 5
Model > Mesh

Object Name	<i>Mesh</i>
State	Solved
Display	
Display Style	Use Geometry Setting
Defaults	
Physics Preference	CFD
Solver Preference	Fluent
Element Order	Linear
Element Size	Default (0.49497 m)
Export Format	Standard
Export Preview Surface Mesh	No
Sizing	
Use Adaptive Sizing	No
Growth Rate	Default (1.2)
Max Size	Default (0.98995 m)
Mesh Defeaturing	Yes
Defeature Size	Default (2.4749e-003 m)
Capture Curvature	Yes
Curvature Min Size	Default (4.9497e-003 m)
Curvature Normal Angle	Default (18.0°)
Capture Proximity	No
Bounding Box Diagonal	9.8995 m
Average Surface Area	6.3773 m ²
Minimum Edge Length	2.1184e-002 m
Quality	
Check Mesh Quality	Yes
Target Skewness	Default (0.900000)
Smoothing	Medium
Mesh Metric	None
Inflation	
Use Automatic Inflation	None

Inflation Option	Smooth Transition
Transition Ratio	0.272
Maximum Layers	5
Growth Rate	1.2
Inflation Algorithm	Pre
View Advanced Options	No
Assembly Meshing	
Method	None
Advanced	
Number of CPUs for Parallel Part Meshing	Program Controlled
Straight Sided Elements	
Rigid Body Behavior	Dimensionally Reduced
Triangle Surface Mesher	Program Controlled
Topology Checking	No
Pinch Tolerance	Default (4.4548e-003 m)
Generate Pinch on Refresh	No

Table 6
Model > Mesh > Mesh Controls

Object Name	MultiZone	Edge Sizing	Edge Sizing 2	Edge Sizing 3	Edge Sizing 4	Edge Sizing 5	Edge Sizing 6
State	Fully Defined						
Scope							
Scoping Method	Geometry Selection						
Geometry	1 Body	1 Edge					
Definition							
Suppressed	No						
Method	MultiZone						
Mapped Mesh Type	Hexa						
Surface Mesh Method	Program Controlled						
Free Mesh Type	Not Allowed						
Element Order	Use Global Setting						
Src/Trg Selection	Automatic						
Source Scoping Method	Program Controlled						
Source	Program Controlled						
Sweep Size Behavior	Sweep Element Size						
Sweep Element Size	Default						
Type	Number of Divisions						
Number of Divisions		30	70	90	20	15	30
Advance							
Preserve Boundaries	Protected						

Mesh Based Defeaturing	Off				
Minimum Edge Length	2.1181e-002 m				
Write ICFM CFD Files	No				
Behavior		Hard		Soft	Hard
Capture Curvature		No			
Capture Proximity		No			
Bias Type		-	--	-	--
Bias Option		Bias Factor			
Bias Factor		40.0	55.0	40.0	
Reverse Bias		No Selection			
Growth Rate		Default (1.2)			

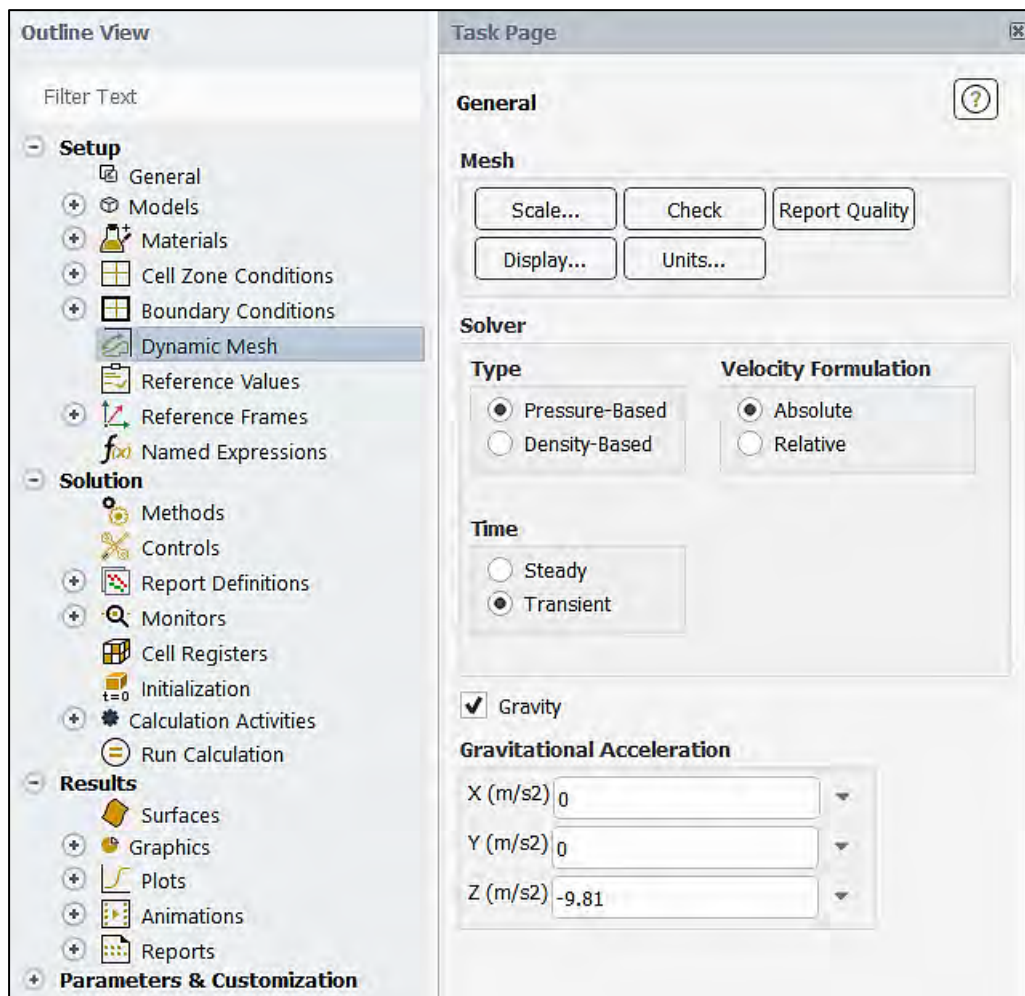
3. Create Named Selections as shown in figure 3.1.1.

Table 6
Model > Named Selections > Named Selections

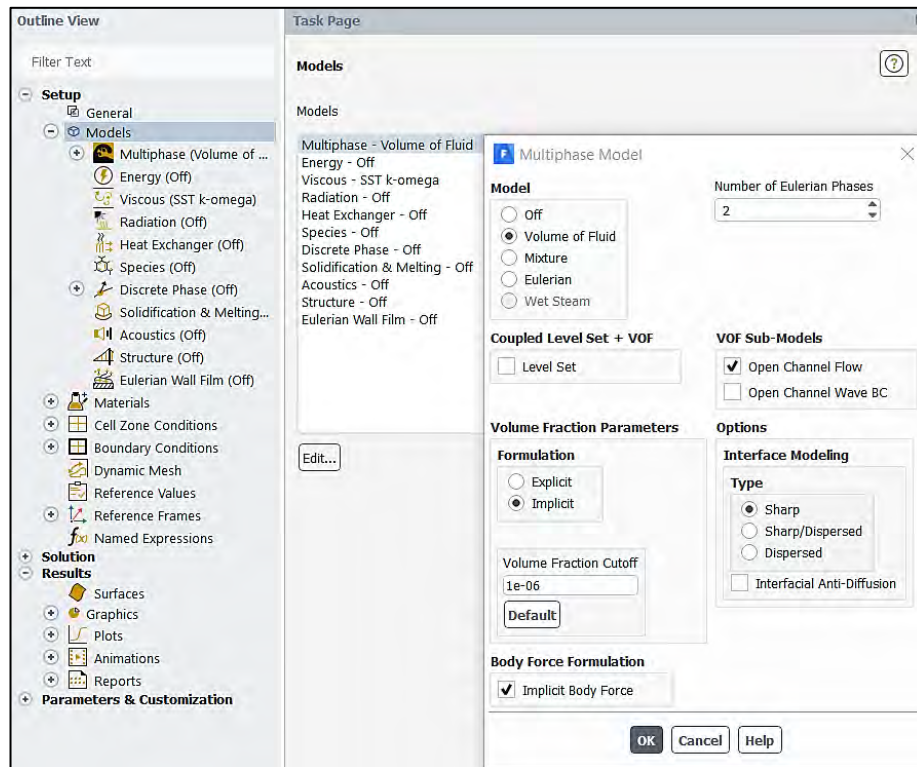
Object Name	<i>Inlet</i>	<i>Outlet</i>	<i>Airfoil</i>	<i>Symmetry</i>
State				
Scope				
Scoping Method	Geometry Selection			
Geometry	1 Face		3 Faces	9 Faces
Definition				
Send to Solver	Yes			
Protected	Program Controlled			
Visible	Yes			
Program Controlled Inflation	Exclude			
Statistics				
Type	Manual			
Total Selection	1 Face		3 Faces	9 Faces
Surface Area	6.2799 m ²	4.0 m ²	1.0329 m ²	77.97 m ²
Suppressed	0			
Used by Mesh Worksheet	No			

Step 3: Setting up the Physics

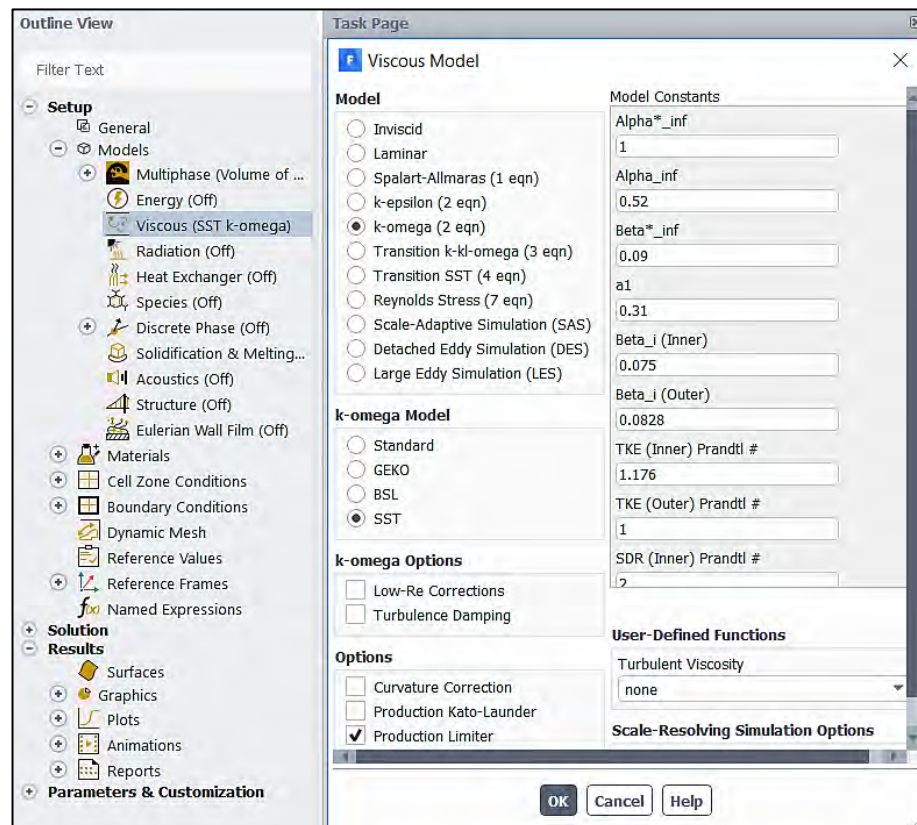
1. Open **Fluent**.
2. Check the mesh. General → Check.
3. General → Type → Pressure-Based.
4. General → Time → Transient.
5. Set the gravity as -9.81 ms^{-2} in z-direction.



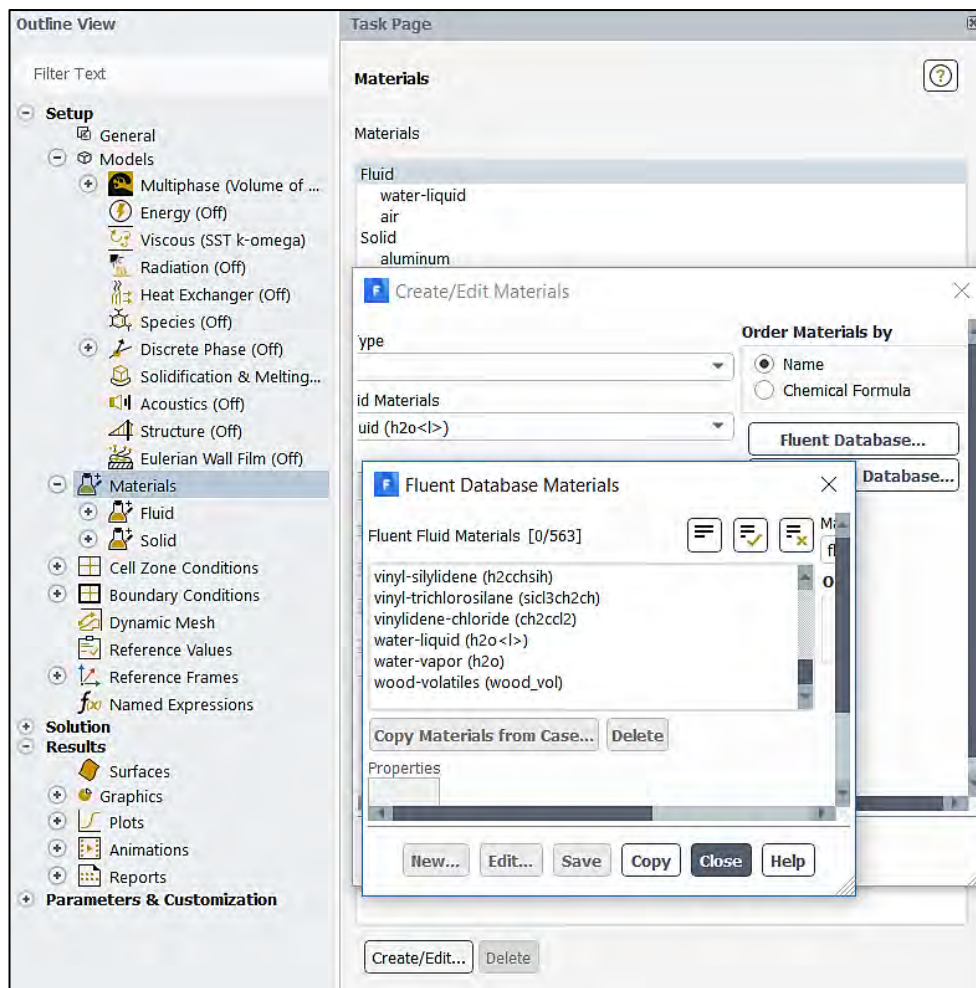
6. Models → Multiphase → Volume of Fluid (VOF). Set volume fraction parameters as **Implicit**.
7. Select the 'Open Channel Flow' and 'Implicit Body Force'.



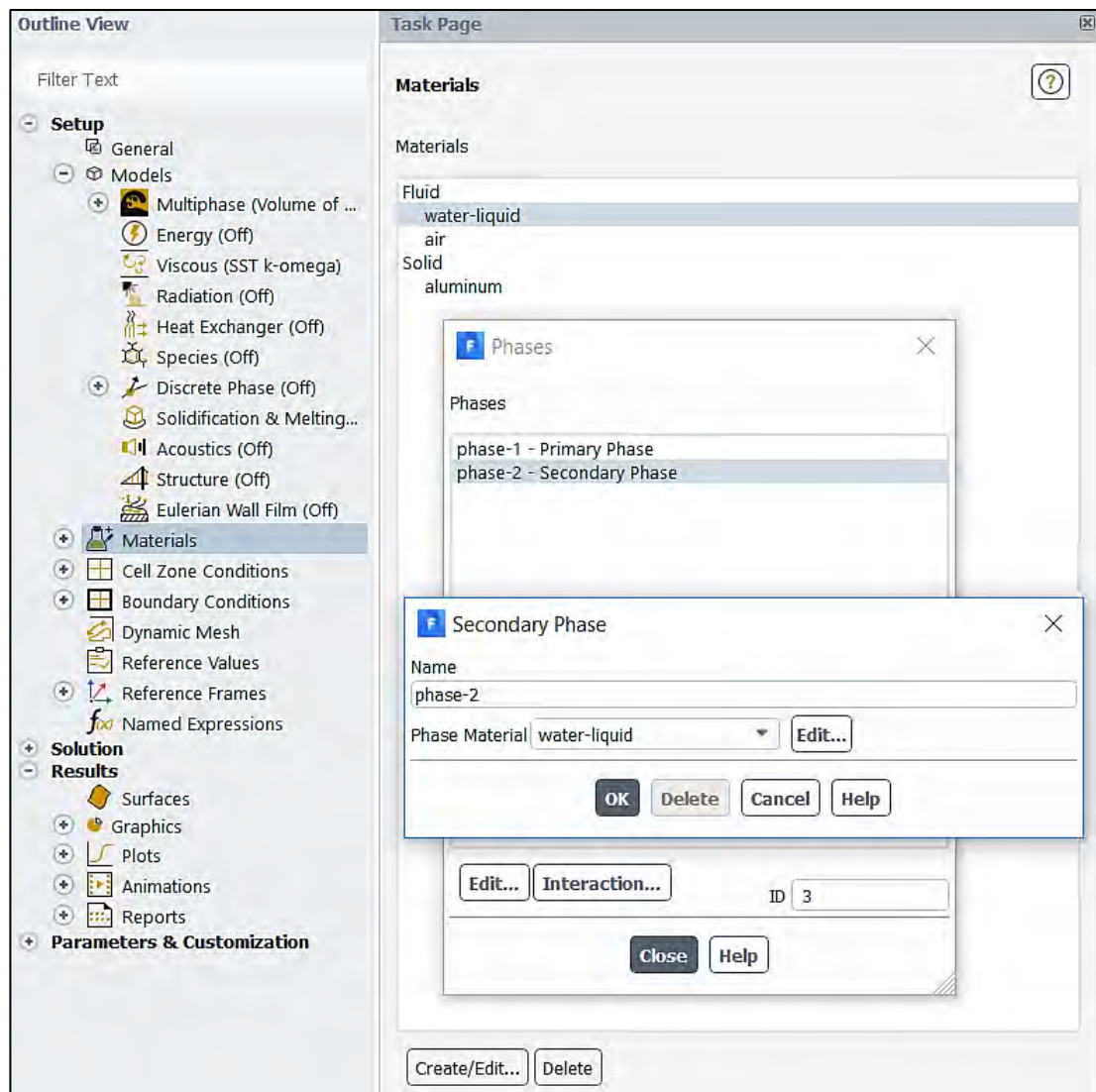
8. Models → Viscous → k - ω SST.



9. Materials → Create/Edit → Fluent Database → water-liquid (h2o <l>) → Copy.



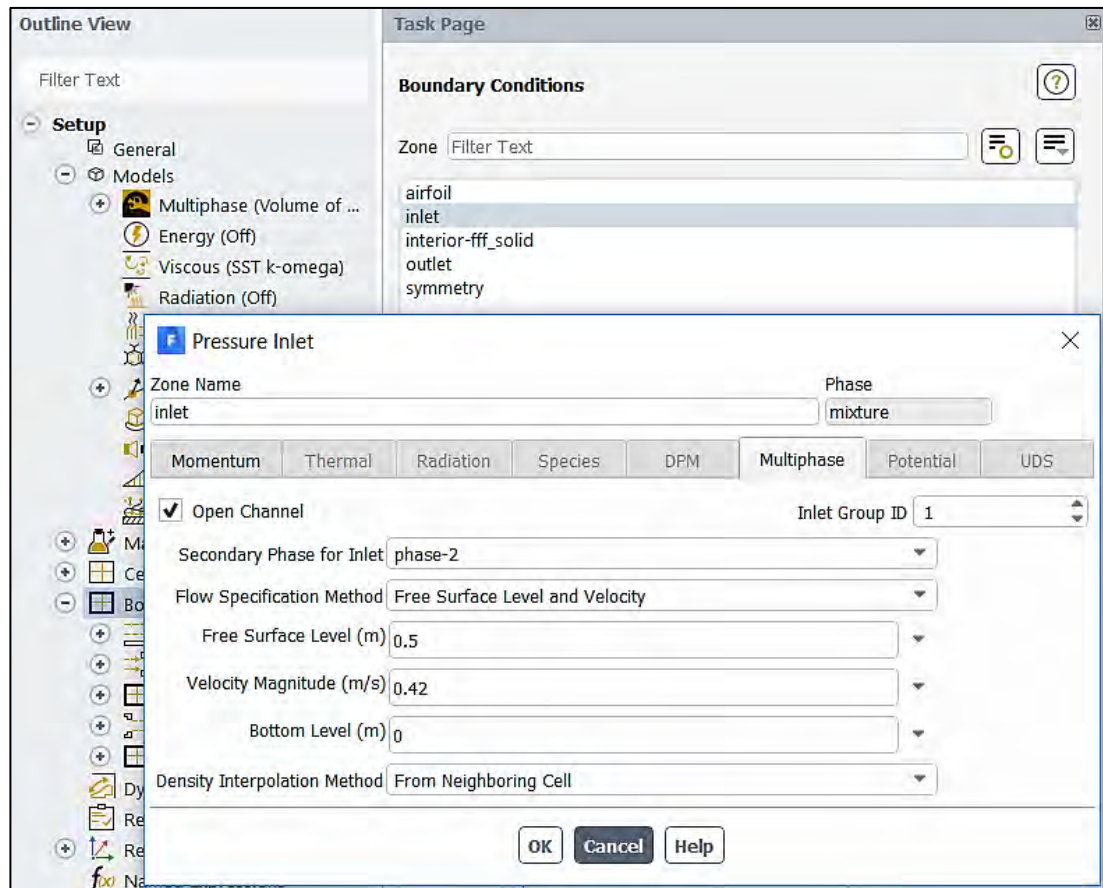
10. Physics → Phases → List/Show All Phases → Secondary Phase → water-liquid.



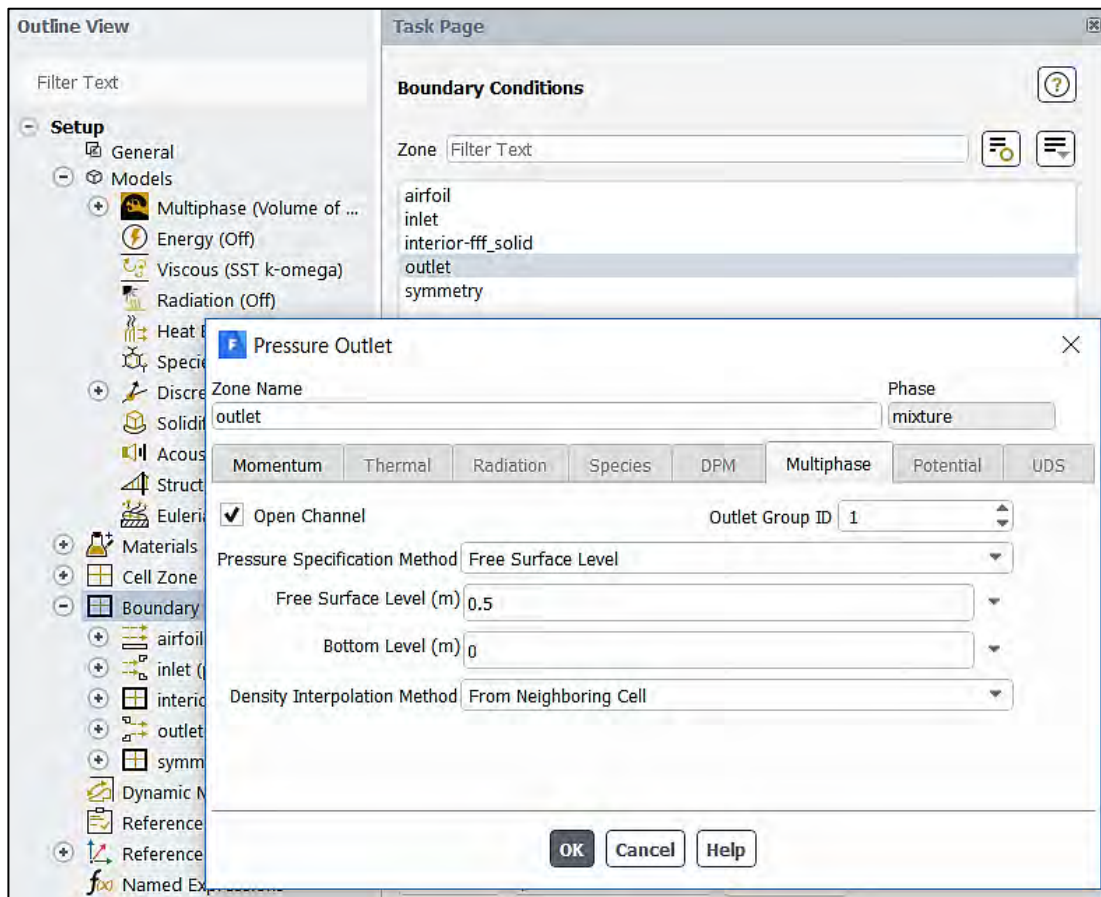
11. Select and define the boundary conditions.

Zone	Type	Phase
airfoil	wall	mixture
inlet	pressure-inlet	mixture
interior-fff-solid	interior	mixture
outlet	pressure-outlet	mixture
symmetry	symmetry	mixture

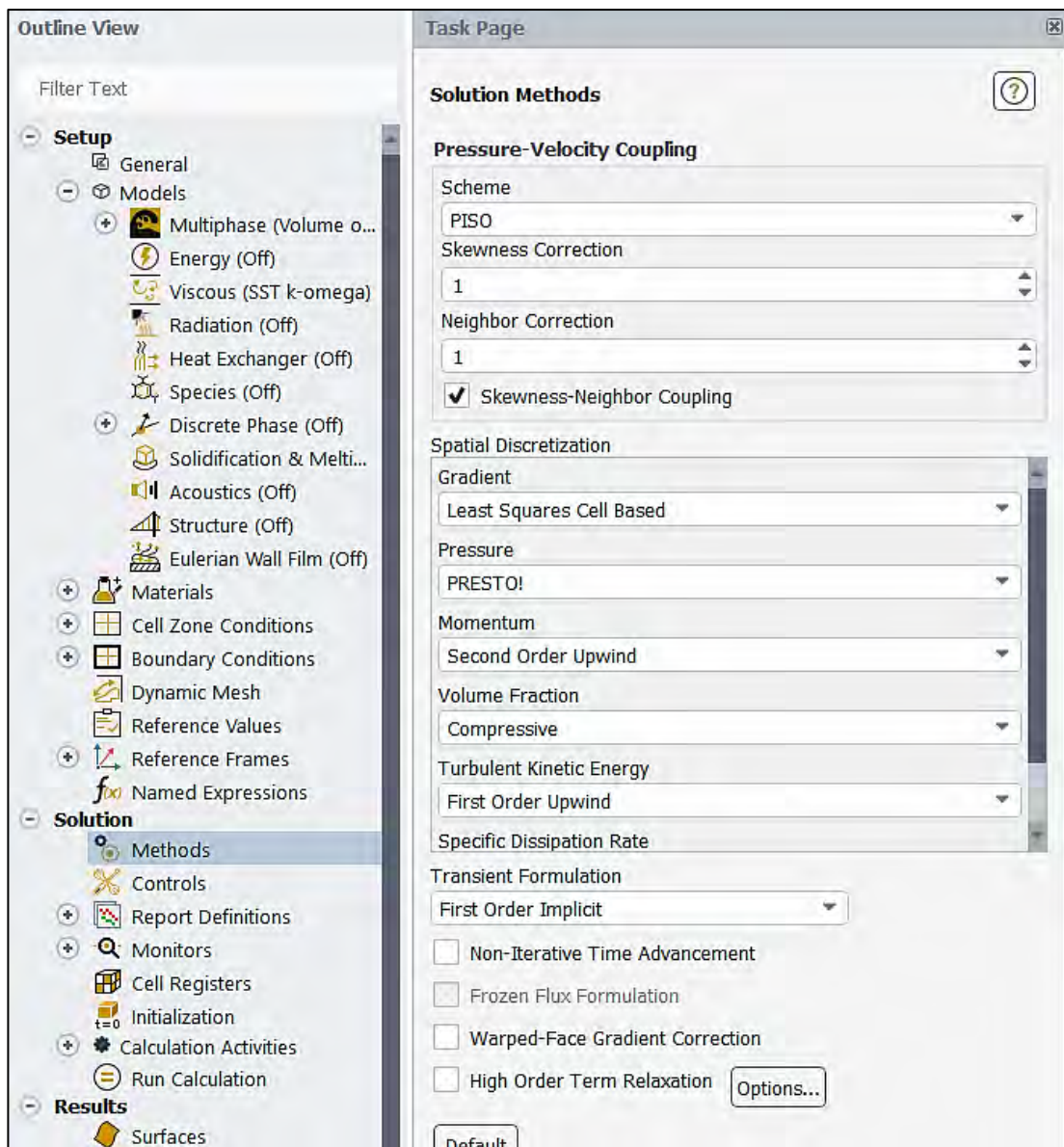
12. Boundary Conditions → inlet → edit → Multiphase. Tick ‘**Open Channel**’. Set ‘**phase-2**’ as secondary phase for inlet and ‘**Free Surface Level and Velocity**’ as flow specification method. Set the free surface level at 0.5 m from bottom and the bottom at 0 m and the velocity magnitude at 0.42 m/s. Select ‘**From Neighboring Cell**’ as density interpolation method.



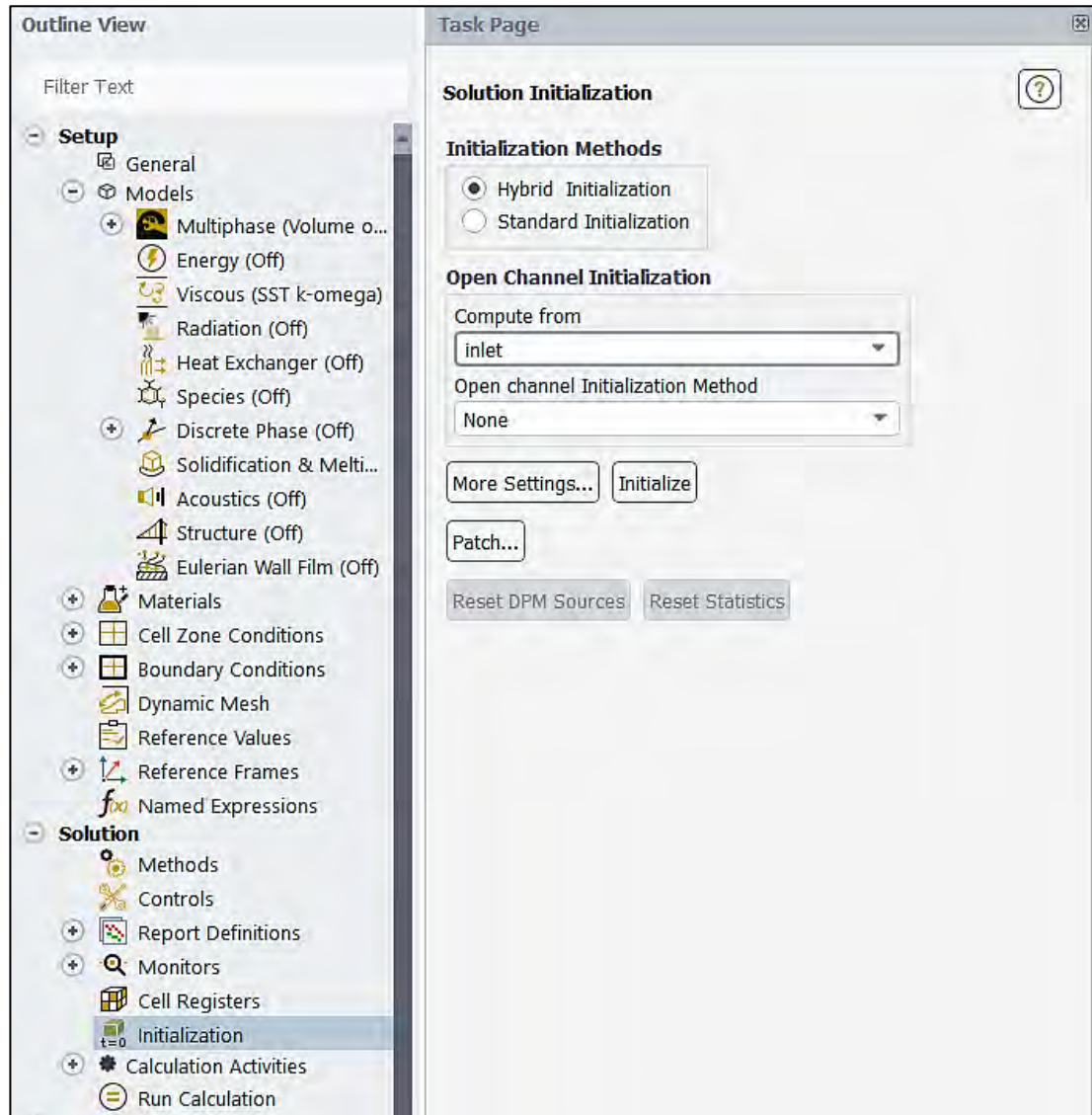
13. Boundary Conditions → outlet → edit → Multiphase. Tick 'Open Channel'. Set 'Free Surface Level' as pressure specification method. Set the free surface level at 0.5 m from bottom and the bottom at 0 m. Select 'From Neighboring Cell' as density interpolation method.



14. Solution → Methods → keep the ‘Solution Methods’ as shown in the figure.

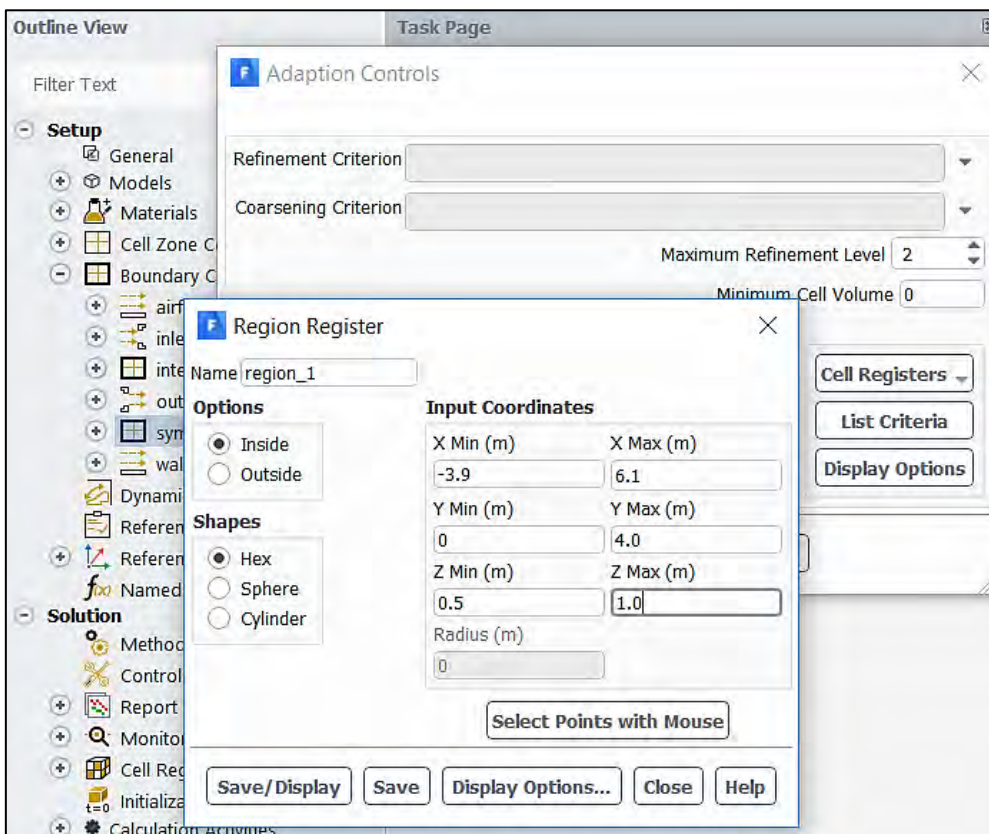
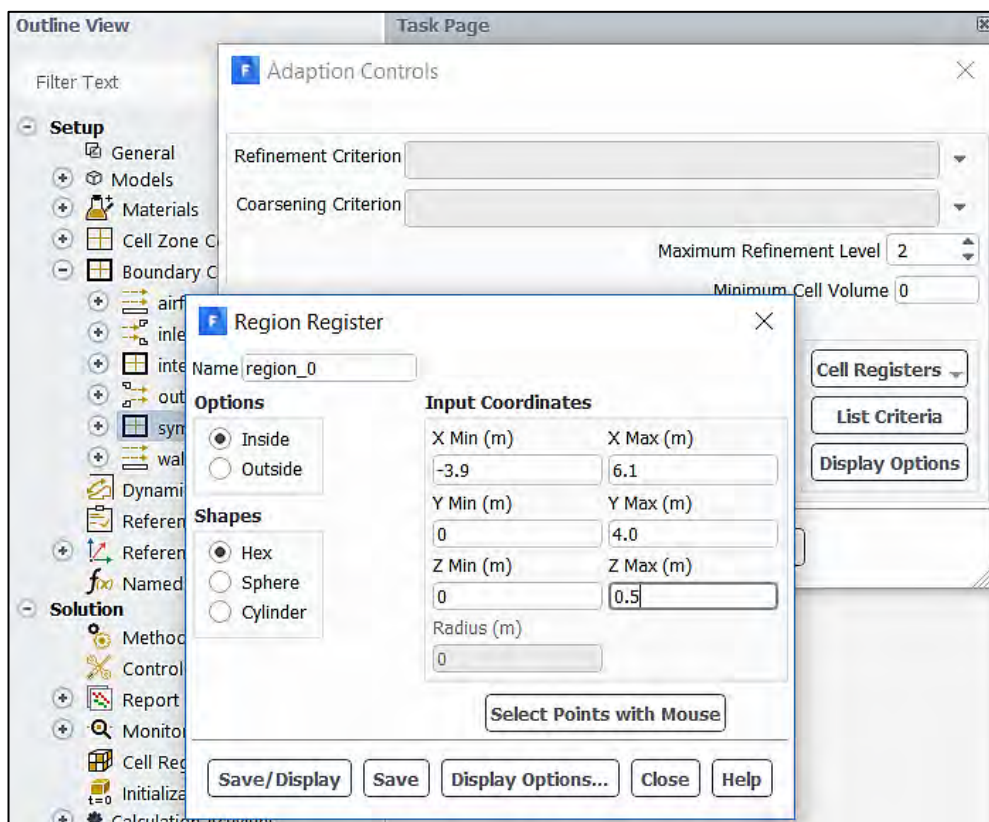


15. Solution → initialization → Hybrid initialization → Compute from (inlet) → initialize.

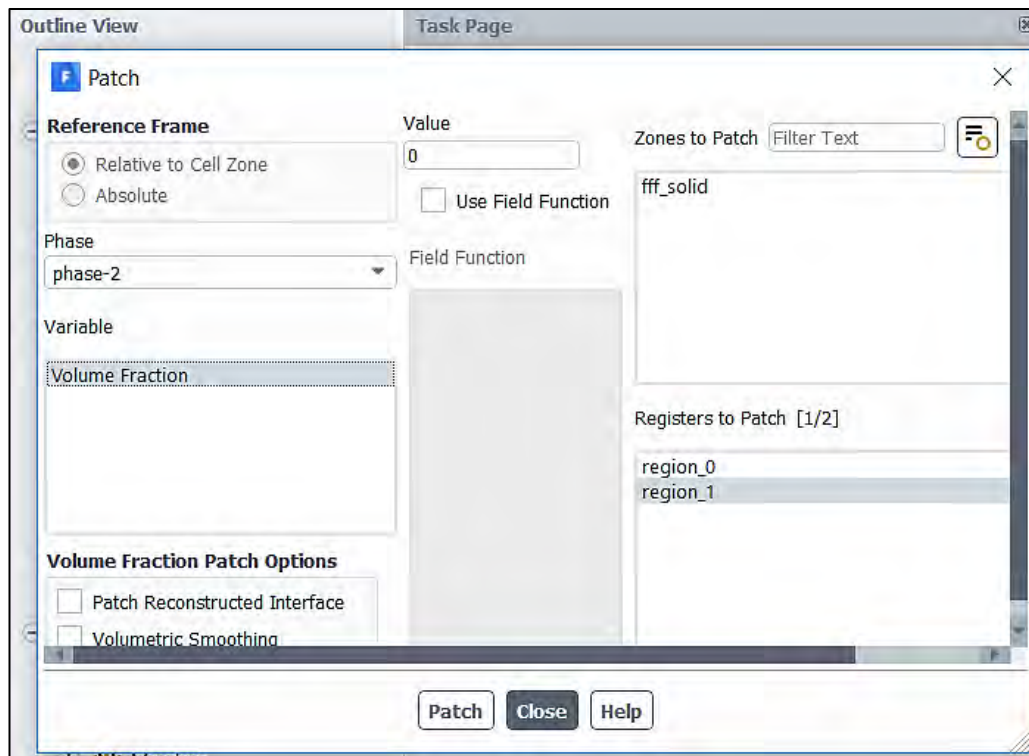
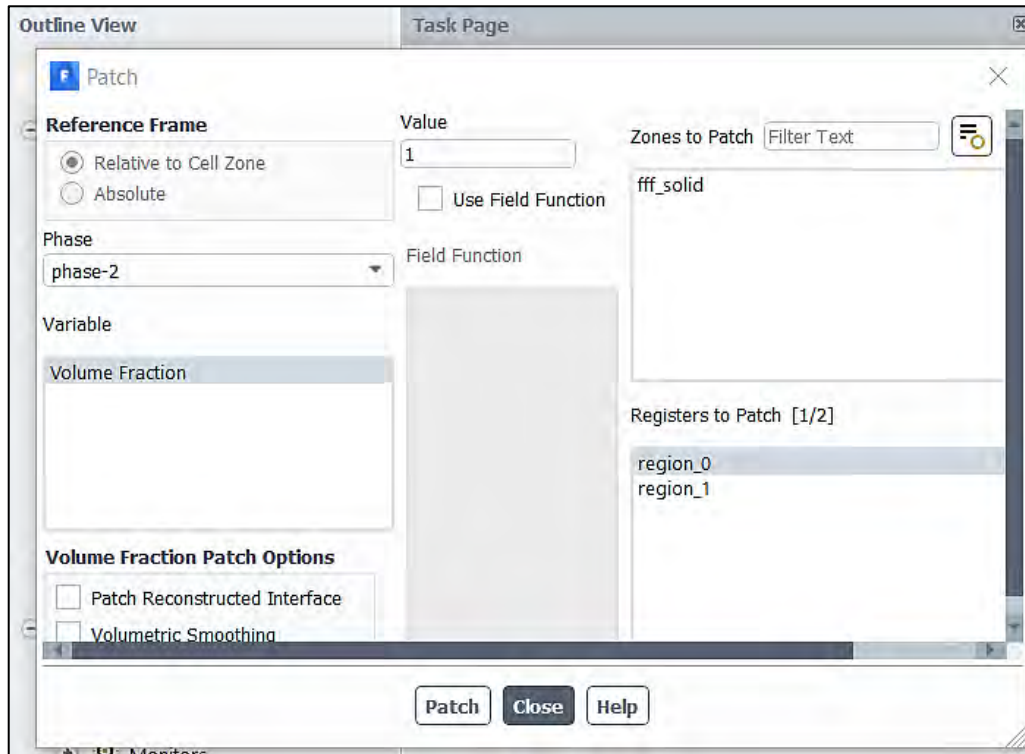


16. Adapt → Refine/Coarsen → Cell Registers → New. The following window will pop out.

The maximum and minimum of X, Y and Z should be such that the volume covers the domain of the water. Then click mark. Similarly select the domain for air and mark.



17. Solution → initialization → patch. Select the following as shown in the figure for water domain and patch. Similarly select patch for air domain.



18. Calculation activities → (Automatic export) Create → Solution export → File Type → CDAT for CFD-Post & EnSight. (This file will be required to export the result).

Select the quantities according to the requirements.

19. Run Calculation → Select proper time step and number of time step → Run Calculation.